Analysis of Multi-Component Ducted Propulsors in Unsteady Flow

by

Michael Joseph Hughes

B.S., Webb Institute of Naval Architecture (1988)
S.M., Massachusetts Institute of Technology (1990)

Submitted to the Department of Ocean Engineering
in partial fulfillment of the requirements for the degree of

Doctor of Philosophy

at the

MASSACHUSETTS INSTITUTE OF TECHNOLOGY

May 1993

Author .....
Department of Ocean Engineering
May 21, 1993

Certified by .....
Justin E. Kerwin
Professor of Naval Architecture
Thesis Supervisor

Accepted by .....
A. Douglas Carmichael
Chairman, Departmental Committee on Graduate Students

Analysis of Multi-Component Ducted Propulsors in Unsteady Flow

by

Michael Joseph Hughes

Submitted to the Department of Ocean Engineering
on May 21, 1993, in partial fulfillment of the
requirements for the degree of
Doctor of Philosophy

Abstract

The goal of this thesis is to develop a computationally efficient method for analyzing the unsteady flow past a ducted propulsor with multiple blade rows. The method models the propulsor in potential flow using a time-marching low order potential based panel method for all components. The duct and hub are represented using the generalized image model, which accounts for the effects of the duct and hub on the propeller and stator blades exactly, without solving the boundary value problem on the duct and hub at each time step. The generalized image model essentially accounts for the modification to the infinite domain Green's function due to the presence of the duct. This manifests itself in the modification to the panel influence coefficients for every propeller, stator, and wake panel. A computationally efficient method is developed for calculating these images. The generalized image model was originally developed for steady flows. In order to apply the generalized image model to solve the unsteady flow problem, a method is devised to account for the vorticity shed by the duct. This method first solves for the problem where the solution on the propeller and stators is fully unsteady, but the solution on the duct is quasi-steady. It is then demonstrated that the fully unsteady solution on the duct can be recovered from the quasi-steady duct solution. A special procedure is introduced for the flow through the clearance region between the tip of the propeller and the inner surface of the duct. Numerical results are shown for the unsteady pressure distributions, forces, and circulation distributions on the duct, propeller, and stator blades. The method is also used to predict the flow past a single component ducted propeller in uniform flow. This shows the method to be consistent with a direct panel method solution for the steady flow past a ducted propeller.

Thesis Supervisor: Justin E. Kerwin
Title: Professor of Naval Architecture

Acknowledgments

I have received a tremendous amount of assistance from many different people during the course of my studies at MIT. My greatest appreciation must go to Professor Justin E. Kerwin and Dr. Spyros A. Kinnas, whose encouragement, enthusiasm and guidance both concerning this thesis and other aspects of my life at MIT proved to be invaluable. I will always be grateful to both of them for all the help they have given me along the way, particularly during the the many frustrating moments when I ran into a research problem that seemed insurmountable. I also wish to express my gratitude to Professor J. Nicholas Newman who helped me enormously in my understanding of the use of Chebyshev polynomial expansions. Dr. Ching-Yeh Hsin was also extremely helpful and patient in helping me to figure out the workings of the PUF-10 code on which much of the work presented in this thesis is based.

I also offer my thanks to all the rest of the "propeller nuts" who worked with me in the Marine Hydrodynamics Lab at MIT. Among those deserving my acknowledgment are: Dr. Neal Fine, Dr. David Keenan, Dr. Charles Mazel, Songwoo Pyo, S. Dean Lewis, Larry Leibman, Jamie Rice, Robert Stairs, Randy Villeneuve, Beth Horwich, Greg Diggs, and Scott Black. I am sure there are many other friends and classmates whom deserve my sincerest thanks. I am fortunate to have had many of my friends from both my high school class and from my class at Webb Institute attend graduate school with me in Cambridge. In particular, I would like to thank Jeannie Sullivan, whom I've known since the first grade and who has been a terrific friend. In addition I would like to thank all of the friends I've met since coming to MIT, particularly Dave, Jen, Julie, Katy, Knut, Chris, Paul, Ted, Shane and Seamus, all of whom have made the past five years much more enjoyable. My family, particularly my sister Maria, also deserves a lot of credit for supporting and encouraging me over the years I spent working on this thesis. Finally, I would like to thank Mom and Dad for all they have done for me.

Support for this research was provided by the MIT Sea Grant College Program and Code 1544 of the Naval Surface Warfare Center, Carderock Division; Sea Grant

Project Number NA90AA-D-SG479.

Contents

List of Figures

List of Tables

Chapter 1

Introduction

Multi-component ducted propulsors are being used increasingly for both ocean vehicle propulsion and control. A multi-component ducted propulsor consists of a propeller operating inside of a duct with either one or more rows of stationary blades or another set of rotating blades. Some examples of the various types of multi-component ducted propulsors are shown in Figure 1-1. The applications for these devices range from the propulsion of large vessels which require highly loaded propellers to that of small underwater vehicles. Multi-component ducted propulsors can also be applied as thrusters to help maneuver vessels. Pre-swirl and post-swirl stator vanes are sometimes employed as a means of reducing the rotational losses which occur downstream from a propeller, thereby improving the propulsive efficiency of the system. Ducts have been used both to protect the propeller and to increase propulsive efficiency or to reduce propeller cavitation. Since ducted propellers often require struts in order to support the duct, using these struts as a set of pre-swirl or post-swirl stator blades may prove advantageous.

In the design of these propulsors it is often important to examine the unsteady forces associated with their use. Propulsors are often subjected to severe non-axisymmetric wakes from the boundary layer of the vehicle, an inclination of the propeller shaft, or the maneuvering of the vehicle. In the case of multi-component propulsors, unsteady forces will result from the interaction between the various blade row components as well. An important step in this process is the analysis of the unsteady

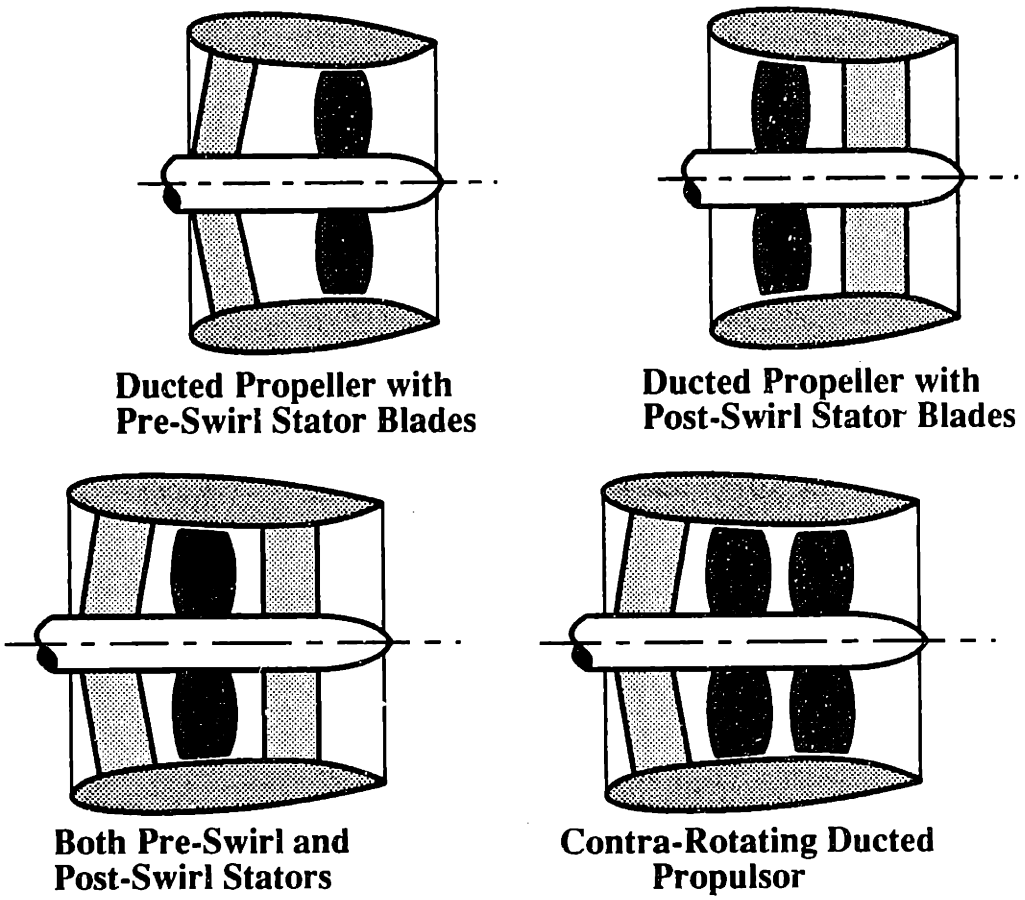

Figure 1-1: Various types of multi-component ducted propulsors

potential flow past the propulsor in the presence of a prescribed spatially non-uniform inflow. When the propulsor in question contains a duct and one or more rows of stator blades, the analysis of the propulsor in a non-uniform inflow becomes increasingly complex and computationally expensive. Accurate predictions of the unsteady pressure distributions on the duct, hub, propeller blades, and stator blades are critical in determining cavitation inception, unsteady boundary layer separation and the hydrodynamic performance of the propulsor.

1.1 Previous Research

1.1.1 Steady flow analysis methods for ducted propulsors

Significant progress has been made in predicting the steady flow past ducted propellers. In most cases the duct and propeller are examined separately, with their mutual interaction being accounted for by including the induced velocities from each component on the other in an iterative manner. For these cases the ducted propeller is usually assumed to operate in a uniform or axisymmetric inflow, and the propeller is typically treated using an actuator disk, lifting line, or lifting surface method. In the earliest models, the duct is represented in linear theory by placing ring vortices and sources on an appropriate mean surface. Among others, Morgan [34], Caster [2], and Dyne [4] have published works describing these types of models. Later methods represented the duct in non-linear theory using axisymmetric singularity distributions on the exact duct surface. Examples of these methods can be found in the works of Gibson and Lewis [11], Glover and Ryan [12], and Falcão de Campos [5]. Still later models allowed for non-axisymmetric loading on the duct by incorporating lifting surface theory to represent both the duct and propeller. Such methods are discussed by Van Houten [39] and Feng and Dong [6]. A more complete review of the various methods for the analysis of single component ducted propellers in steady flow is given by Kerwin et. al. [23] which describes a method that uses a vortex-lattice lifting surface method to model the propeller and a boundary element method (or

panel method) to model the duct and hub.

Boundary element (panel) methods are currently being used extensively in fluid dynamics. In these methods, Green's theorem is applied to the fluid dynamics problem. Singularities are distributed on the surfaces of the bodies in the problem. These singularities consist of dipoles and sources or vorticity. Panel methods were first applied by Hess and Smith [14] to solve a steady three-dimensional non-lifting body problem. They later applied this method to a three-dimensional lifting body problem [13]. Since that time the use of panel methods has flourished with many different panel methods being developed. A review of different panels methods is given by Hunt [21], and a review of their application to propellers is given by Hsin [15]. Kerwin et. al. [23] and Lee [30] developed a low-order, potential based panel method to analyze marine propellers in 1987. The propeller surface is discretized with flat quadrilateral panels. An iterative Kutta condition is applied at the trailing edge of the propeller blades. At about this same time, Kerwin et. al. [23] applied panel methods to the hydrodynamic analysis of ducted propellers in steady flow. In this method the surface of the duct and the hub were represented using panels, while the propeller was represented with a vortex lattice lifting surface method. Validation of this method through comparison with experimental results was demonstrated by Hughes et. al. [20]. This method was later extended by Hughes and Kinnas [19] to include the effects of a single row of evenly spaced pre-swirl stator blades with equal pitch distributions. In this method the interactions between the propeller and the duct and the interactions between the stators and the duct are handled in a completely three-dimensional and non-axisymmetric manner. The interactions between the propeller and the stators are handled in a three-dimensional but axisymmetric manner. This method was later extended to account for an inclined inflow and unevenly spaced stator blades with unequal pitch distributions [18]. Single component ducted propellers have also been analyzed in steady flow using a panel method for the duct and propeller simultaneously using an algorithm developed by Hsin [16].

1.1.2 Current unsteady flow algorithms for propulsors

Numerical lifting surface methods have been used extensively for the analysis of unsteady propeller flows. A review of different steady and unsteady lifting surface methods as applied to marine propellers has been given by Kerwin [22]. Feng and Dong [6] presented a method to solve for the unsteady flow past a ducted propeller using a lifting surface method for both the duct and propeller. In their method the flow past the duct and propeller were solved separately using an iterative time-marching scheme. Kinnas and Hsin [25] have developed a time-marching potential based boundary element method for the analysis of the unsteady flow around extreme propeller geometries. This method predicts accurately the unsteady blade pressures and forces for a broad range of reduced frequencies for a single component open propeller. Panel methods have also been used to model the unsteady flow past multiple bodies by Maskew [32].

A method has also been developed to analyze the unsteady flow past a single component ducted propeller using a hybrid panel method / vortex lattice lifting surface method by Kinnas et. al. [26]. Their method combines a time marching vortex lattice lifting surface method for the propeller with a potential based panel method for the duct. In [26] the effects of the duct are accounted for via the generalized images (described in the next section) of the singularities representing the propeller and its trailing wake with respect to the duct. In this thesis, methods which use a panel method to solve the boundary value problem on the combined duct and propeller surface simultaneously will be referred to as *direct* panel methods. This is to distinguish such methods from the procedure used in this thesis, which use the generalized image model to represent the duct and hub.

1.2 The Generalized Image Model

The generalized image model allows for the propeller and stators to be examined independently of the duct and hub, with the interactions between the duct and hub and the propeller and stators being accounted for accurately. One method of analyzing the

unsteady flow past a ducted propulsor is by treating all of the components as a single body and applying Green's formula to solve for the potential on all the body surfaces simultaneously using a time-marching panel method. The duct, hub, propeller, and stators would have to be paneled, with unsteady vorticity being shed from the trailing edges of the duct, propeller blades and stator blades. An alternative method is to model only the propeller and stators using a time-marching panel method, and to incorporate the duct and hub using the generalized image model. The generalized image model is analogous to the classical image concept, where the potential flow past a body near an infinite wall can be modeled by singularities distributed on the surface of the body, as if the fluid were unbounded, with the presence of the wall accounted for via the images of these singularities with respect to the wall. The generalized image idea extends this concept for the case where the wall is allowed to be a body of any shape, in our application a duct and hub. The generalized image model essentially accounts for the modification to the infinite domain Green's function due to the presence of the duct and hub. This manifests itself in the modification of the panel to panel influence coefficients which form the left hand side of the system of linear equations which are solved at each timestep.

The generalized image model was first introduced by Kinnas and Coney [27], [28], to solve for the optimum circulation distribution for a propeller operating inside of a duct in uniform flow. In their work, the generalized image model is used to accurately model the steady flow past a ducted propeller. The duct is modeled using a potential based panel method. The propeller is represented using lifting line theory, and the generalized images are calculated directly for each lifting line horseshoe element. For this steady flow problem, the duct coordinate system rotates along with the propeller, and the strength of the dipole sheet representing the duct wake is constant along the wake strips in the streamwise direction. When the modifications to the left hand side influence coefficients are calculated, the problem of the flow past the duct and hub in the absence of any inflow, but in the presence of each individual propeller singularity is solved. When solving these problems it is assumed that the strength of the vorticity in the duct wake varies only circumferentially and does not change in the streamwise

direction. This is acceptable for solving the steady flow problem. However, when these same modified coefficients are applied to the unsteady flow problem, it will result in a duct wake sheet which has a different strength at each timestep, but whose strength does not change in the streamwise direction. We have termed this solution the "quasi-steady duct" solution. This will be abbreviated as the QSD solution. In the actual unsteady solution, the duct will shed vorticity at each timestep. Therefore, the dipole sheet representing the duct wake will both change at each timestep and vary in the streamwise direction. In Chapter 4, a method is developed to account for the vorticity shed by the duct, which allows the generalized image model to be applied to the unsteady flow problem. This method is first applied to a two dimensional analog of the three dimensional problem being studied. This consists of two foils: a "smaller" foil which represents the propeller and a "larger" foil which represents the duct. The smaller foil sees a steady inflow plus a sinusoidal gust. The larger foil sees only the steady inflow, but its loading is still unsteady due to its interaction with the smaller foil. Employing this method is shown to reproduce the results from solving the full boundary value problem on both foils simultaneously. The procedure is then extended to three dimensions and incorporated into the solution on the duct.

The mathematical justification of the generalized image model was presented by Kinnas and Coney [24]. In Chapter 2, this mathematical formulation is extended to justify the use of the generalized image model for unsteady flows.

1.3 Objectives

A disadvantage to using lifting surface methods for the propeller in a ducted propeller algorithm is that these methods are not able to accurately predict the unsteady pressure distributions near the blade leading edge where the blade thickness effects are substantial. In addition, for high reduced frequencies, the wavelength of the disturbance is much smaller than the blade chord, and therefore, typical lifting-surface grids are not adequate. Accurate predictions of the unsteady forces and pressures generated at high reduced frequencies are important for the structural acoustic analysis

of propulsors. Future ducted propulsor design may incorporate thick blades, multiple blade rows and unusual section shapes and blade planforms as well. Therefore, the lifting surface representation used in current unsteady ducted propeller analysis methods needs to be replaced by a full panel representation for all components. This must be done, however, without causing the related code to require an unreasonable amount of computer time or memory, so that a large number of configurations can be examined during the design process.

To this end, this thesis will develop an analysis method for a multi-component ducted propulsor with two blade rows, which uses a full panel representation for the duct, hub, propeller, and stators. A time marching solution will be applied for the propeller and stators, where at each time step the effects of the duct and hub will be included via the generalized image of each stator and propeller singularity with respect to the duct and hub. In this way the system of linear equations which must be solved at each timestep will only be as large as the number of propeller and stator panels, and will not include the number of panels on the duct and hub. The objective is to accurately predict the forces and pressure distributions on all the components, especially those corresponding to high reduced frequencies.

The value of the generalized image for each of the influence coefficients forming the left hand side of this system of equations for the propeller and stator solution will have to be computed. For this reason, a computationally efficient method is developed for calculating these images. The generalized images are computed directly *only* at a representative set of panel and control point locations. An interpolation scheme based on a Chebyshev polynomial expansion is then utilized to evaluate the generalized image for any arbitrary panel and control point location. This procedure is discussed in Chapter 3. The propeller and stators will be modeled as one problem. The interaction between the wake of the upstream component and the blade of the downstream component is treated by allowing the downstream blade to pass through the wake without altering the wake geometry. The influence from the upstream wake panels which touch the blade of the downstream component are set to zero. This process is described in Section 3.6. A special procedure is introduced to account for

the effects of the flow through the clearance region between the tip of the propeller and the inner surface of the duct which is discussed in Chapter 5. Finally, a method is developed for obtaining the solution on the duct at each timestep after the conclusion of the time-marching solution for the propeller and stator blades. This method uses the solution on the propeller and stator blades and the "inverse" generalized images. A separate iterative pressure Kutta condition is then applied to the duct. This procedure is described in Chapter 4.

The complete method is first used to solve for the flow past a single component ducted propeller in uniform flow. These results are used to show that the method is consistent with a direct panel method solution for the steady flow past a ducted propeller. The same case is used to show that the method is convergent with number of panels. The results of these tests for convergence and consistency are shown in Chapter 6. This chapter also shows results for the unsteady pressure distributions, forces, and circulation distributions on the duct, propeller, and stator blades.

Chapter 2

Mathematical Formulation

In this chapter the problem of a ducted propulsor operating in a spatially non-uniform inflow is precisely defined and formulated. All the relevant assumptions made in the formulation of the problem are listed. Green's formula is applied to the appropriate boundaries in order to obtain the perturbation potential (which will in turn be used to obtain velocities and pressures) on the surfaces of all the propulsor components. This is first done by applying Green's Formula directly to all of the propulsor components simultaneously and solving the problem as if the propulsor was a single body. The generalized image model is then incorporated into the formulation, and it is shown that the problem can be decomposed into separate problems concerning individual components or groups of components. A discussion is given on the additional features which must be added to the generalized image model when solving an unsteady flow problem.

2.1 Fundamental Assumptions

The propulsor geometry is assumed to be known, and the propulsor components are assumed to be rigid surfaces. The propulsor consists of a propeller, duct, hub, and possibly one or more rows of stator blades. The propeller blades are assumed to be symmetrically arranged around a common axis and to rotate about that axis with a constant angular velocity. The duct and hub geometries are assumed to be axisym-

metric about this same axis, and the hub may include any axisymmetric centerbody. The stator blade geometries may be unevenly spaced, and each stator blade may have a different geometry. The fluid is assumed to be unbounded. The presence of any solid boundaries such as the ship hull are assumed to be accounted for as part of the inflow and the possible existence of a free surface is ignored. In addition, it is assumed that cavitation does not occur on any part of the propulsor.

The inflow is assumed to be known and to be inviscid and incompressible. This inflow represents the wake field behind the vehicle to which the propulsor is attached. It is assumed that this flow field is the *effective wake*, which includes the interactions between the vorticity in the inflow in the absence of the propulsor (the *nominal wake*) and the flow due to the propulsor. The flow field representing the difference between the resulting total flow and the effective wake inflow can then be treated as irrotational. This allows the resulting flow to be expressed as the superposition of the inflow velocity field and the gradient of the perturbation potential.

The stator blades, propeller blades, and duct are all lifting bodies which require a wake surface to be attached to their trailing edge when solving for the velocity potential using a boundary element formulation. These wake surfaces are infinitely thin regions, across which a discontinuity in the direction of the velocity is allowed to occur. It is assumed in this thesis that the geometry of these wakes are known and are constant. The geometry of the wakes could presumably be determined by solving the steady potential flow problem for the mean flow coupled with a free wake analysis so that the wakes will be "aligned" with the local mean flow. In applying the generalized image model, it is only important for the wake of the "imaging" body (i.e. the duct) to remain constant. The wake geometry for the "imaged" body (i.e. the propeller and stator blades) may be allowed to change; however, in this work the wakes for all of the components will be fixed. The geometry of the duct wake is assumed to be axisymmetric.

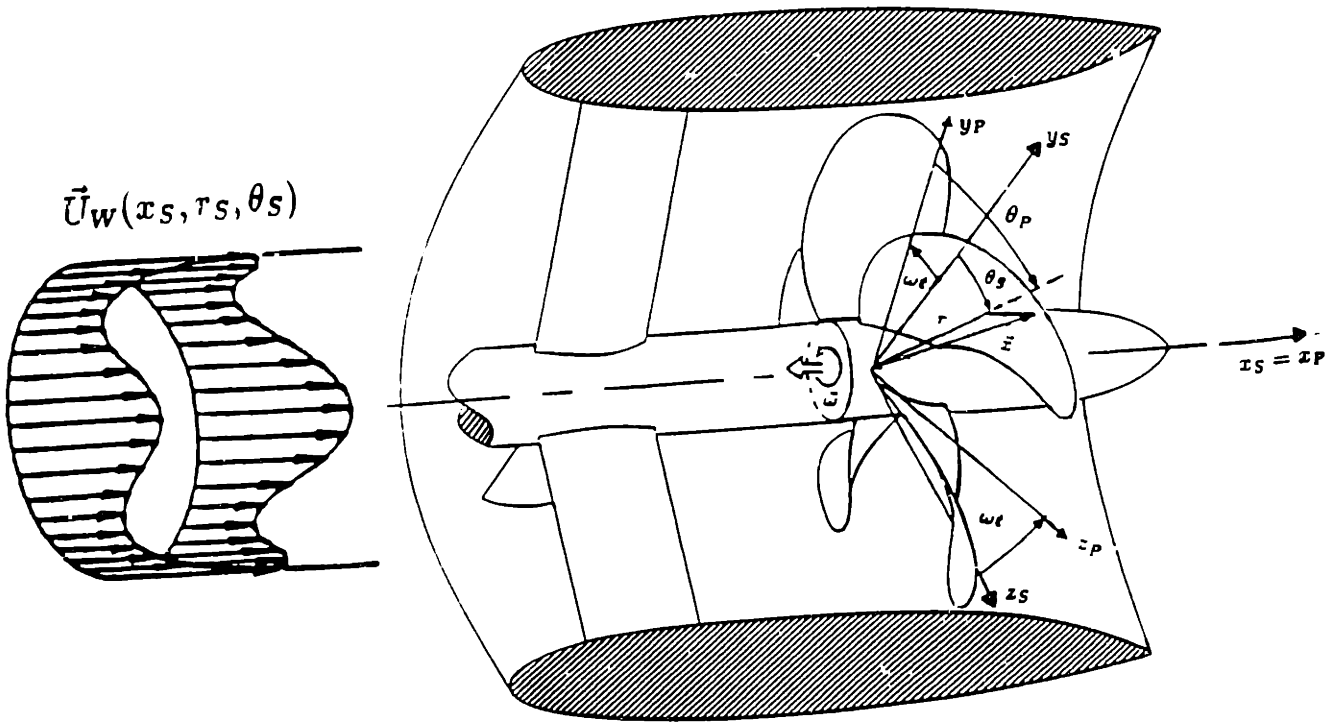

Figure 2-1: Multi-component ducted propulsor operating in a spatially non-uniform inflow

2.2 Definition of the Problem

Consider a ducted propulsor operating in the presence of a spatially non-uniform inflow $\boldsymbol{U}_W(x_S, r_S, \theta_S)$ as is shown in Figure 2-1. The subscript S refers to the fact that the inflow is defined with respect to the ship fixed coordinate system. The propulsor consists of a duct, hub, and propeller as well as one or more rows of stator blades. The duct and hub are treated as a single body and referred to using the subscript D. Any axisymmetric centerbody may be modeled as part of the hub. In the derivation shown in this chapter, the stators blades and propeller blades will be treated together using the subscript PS. The modeling of the interaction between the stators and propeller will be discussed in Chapter 3.6.

The solution is formed in terms of the perturbation potential, ϕ, on the surface of each of the propulsor components. For the propeller, the solution will be with respect to a coordinate system which rotates with the propeller so that $\phi \rightarrow \phi(x_P, y_P, z_P, t)$,

where the subscript P refers to the propeller fixed coordinate system. For the stators, duct, and hub the solution for ϕ will be with respect to the ship fixed coordinate system, $\phi \rightarrow \phi(x_S, y_S, z_S, t)$. The difference between these two coordinate systems is described by Figure 2-1. The value of ϕ at a given location at a given moment in time is, of course, independent of the coordinate system. However, when differentiating the perturbation potential in order to obtain the perturbation velocity, $\nabla\phi$, the selected coordinate system becomes important. Since ϕ is determined only on the surfaces of the propulsor components, it is necessary to differentiate along these surfaces in order to compute the pressure distribution on the component. Therefore, it is desirable to express the solution on each component in the coordinate system which is fixed to the surface of that component.

Since the inflow is spatially non-uniform, the solution for the perturbation potential on the propeller will be unsteady, as the propeller blade will see an unsteady inflow as it rotates through the variations in the flow. The solution for the potential on the duct, hub, and stator blades will also be unsteady, but only because of the interaction of these components with the propeller blades.

If the propeller rotates at a constant angular velocity ω, the inflow relative to the propeller will be time dependent and expressed as:

$$\boldsymbol{U}_{P_{in}}(x_P, y_P, z_P, t) = \boldsymbol{U}_W(x_P, r_P, \theta_P - \omega t) + \boldsymbol{\omega} \times \mathbf{x} \tag{2.1}$$

where $r_P = \sqrt{y_P^2 + z_P^2}$, $\theta_P = \arctan(z_P/y_P)$, and $\mathbf{x} = (x_P, y_P, z_P)$. The total flow at a point on the surface of the propeller, $\boldsymbol{q}(x_P, y_P, z_P, t)$, may then be expressed in terms of this local inflow velocity and the perturbation potential:

$$\boldsymbol{q}(x_P, y_P, z_P, t) = \boldsymbol{U}_{P_{in}}(x_P, y_P, z_P, t) + \nabla_P\phi(x_P, y_P, z_P, t) \tag{2.2}$$

where ∇_P is gradient operator with respect to the propeller fixed coordinate system. The total time dependent velocity on the duct, hub, and stator blades with respect to the ship fixed coordinate system may also be expressed in terms of the perturbation

potential,

$$q(x_S, y_S, z_S, t) = U_W(x_S, y_S, z_S) + \nabla_S \phi(x_S, y_S, z_S, t) \tag{2.3}$$

where ∇_S is the gradient operator with respect to the ship fixed coordinate system. For simplicity in defining the inflow, it is assumed that the effective inflow, U_W, does not vary in the axial direction through the propulsor. This assumption is not a necessary part of the formulation, but allows the inflow velocity to be defined as a harmonic function of radial and angular location, r_S and θ_S.

$$U_W(x_S, y_S, z_S) = \mathbf{A}_0(r_S) + \sum_{n=1}^{\infty} \mathbf{A}_n(r_S)\cos(n\theta_S) + \sum_{n=1}^{\infty} \mathbf{B}_n(r_S)\sin(n\theta_S) \tag{2.4}$$

2.3 Application of Green's Formula

This problem could be formulated using the same procedure as used by Hsin [15] to solve the problem of the open propeller in unsteady flow. Namely, by applying Green's formula for $\phi(\mathbf{x}, t)$ at any time t, we obtain the following integral equation for the perturbation potential ϕ at every point $\mathbf{x}$ on the surfaces of the propulsor components, S_{PS} and S_D.

$$\begin{aligned} 4\pi\epsilon\phi(\mathbf{x}, t) \;=\; & \int_{S_D} \phi(\boldsymbol{\xi}, t)\frac{\partial G(\mathbf{x}, \boldsymbol{\xi})}{\partial n_D}\, dS(\boldsymbol{\xi}) + \int_{S_{PS}} \phi(\boldsymbol{\xi}, t)\frac{\partial G(\mathbf{x}, \boldsymbol{\xi})}{\partial n_{PS}}\, dS(\boldsymbol{\xi}) \\ & - \int_{S_D} G(\mathbf{x}, \boldsymbol{\xi})(-\boldsymbol{U}_{in} \cdot \boldsymbol{n}_D)\, dS(\boldsymbol{\xi}) \\ & - \int_{S_{PS}} G(\mathbf{x}, \boldsymbol{\xi})(-\boldsymbol{U}_{in} \cdot \boldsymbol{n}_{PS})\, dS(\boldsymbol{\xi}) \\ & + \int_{W_D} \Delta\phi_{duct}(\boldsymbol{\xi}, t)\frac{\partial G(\mathbf{x}, \boldsymbol{\xi})}{\partial n_{W_D}}\, dS(\boldsymbol{\xi}) \\ & + \int_{W_{PS}} \Delta\phi_{PS}(\boldsymbol{\xi}, t)\frac{\partial G(\mathbf{x}, \boldsymbol{\xi})}{\partial n_{W_{PS}}}\, dS(\boldsymbol{\xi}) \end{aligned} \tag{2.5}$$

where:

- S_D is the surface of the duct and hub.
- W_D is the surface of the wake from the duct.
- S_{PS} is the surface of the propeller and stator blades.

- W_{PS} is the surface of the wakes from the propeller and stator blades.
- n_D and n_{PS} are the normal vectors to the duct/hub surface and propeller/stator blade surfaces respectively.
- U_{in} is the local inflow velocity, which will be equal to $U_{P_{in}}$ on the propeller blade surface and U_W on all other component surfaces.
- $\Delta\phi_{duct}$ is the jump in the potential across the duct wake.
- $\Delta\phi_{PS}$ is the jump in the potential across propeller and stator blade wake sheets. Its value is equal to ϕ_{prop} on the propeller wake and ϕ_{stat} on the stator wake.
- G is the infinite domain Green's function which in three dimensions is given by:

$$G(\mathbf{x},\boldsymbol{\xi}) = G(\boldsymbol{\xi},\mathbf{x}) = \frac{1}{\|\mathbf{x}-\boldsymbol{\xi}\|} \tag{2.6}$$

where $\|\mathbf{x}-\boldsymbol{\xi}\|$ is the distance between points $\mathbf{x}$ and $\boldsymbol{\xi}$. $G(\mathbf{x},\boldsymbol{\xi})$ corresponds to the potential at a point $\mathbf{x}$ induced by a point source of strength -4π located at a point $\boldsymbol{\xi}$.

The coordinate system used in equation (2.5) is dependent upon the surface on which ϕ is integrated. This is acceptable since the values for ϕ and the relative distance between $\mathbf{x}$ and $\boldsymbol{\xi}$ at a given instant in time are independent of whether the coordinate system is rotating or stationary. Only the local inflow velocity U_{in} is dependent upon the relative motion of the coordinate system which is why this value is defined differently on the propeller surface.

Equation (2.5) expresses the potential on the propulsor as the superposition of the potentials induced by a continuous source distribution, G, on the propulsor component surfaces, and a continuous dipole distribution, $\frac{\partial G}{\partial n}$, on the propulsor component surfaces and wake surfaces. The strength of the source distribution is obtained from the kinematic boundary condition:

$$\frac{\partial \phi_{\boldsymbol{\xi}}}{\partial n_{\xi}} = U_{in}(\boldsymbol{\xi},t)\cdot n_{\xi} \tag{2.7}$$

The strength of the dipole distribution is unknown and equal to the perturbation potential on the surface of the propulsor or to the jump in potential across the wake surface. These dipole strengths can be determined by inverting equation (2.5) at each time step.

In the case of steady flow, the jump in the potential across the propeller, stator and duct wakes would remain invariant along the mean streamlines in the wake sheets. In the case where the solution is unsteady, however, the wakes no longer remain invariant as vorticity will be shed into the wake as the solution varies with time. It is assumed that the geometry of the wakes remains invariant with time, even for the unsteady case; however, the dipole strength along the wakes, $\Delta\phi_{duct}$ and $\Delta\phi_{PS}$ will be convected along the assumed wake model. For the case of the propeller, $\Delta\phi_{prop}$ will be convected downstream with angular velocity ω relative to the propeller in order to ensure that there is no jump in pressure across the wake surface.

$$\begin{aligned} \Delta\phi_{prop}(r,\theta,t) &= \Delta\phi^T_{prop}\left(r, t - \tfrac{\theta-\theta_T(r)}{\omega}\right); \quad t \geq \frac{\theta-\theta_T(r)}{\omega} \\ &= \Delta\phi^S_{prop}(r); \qquad\qquad t < \frac{\theta-\theta_T(r)}{\omega} \end{aligned} \tag{2.8}$$

where r and θ are the cylindrical coordinates of the propeller wake surface, and $\theta_T(r)$ is the θ coordinate of the propeller blade trailing edge at radius r. Since the formula depends only on the relative angle between the propeller trailing edge and a point in the propeller wake, it will be valid in either coordinate system. $\Delta\phi^S_{prop}(r)$ is the steady flow potential jump across the propeller wake. It is assumed that for $t < 0$ the propulsor operates in the circumferentially averaged inflow, and then begins to operate in the unsteady inflow at $t = 0$. The value of the dipole strength, $\Delta\phi^T_{prop}(r,t)$, at the trailing edge of the blade at any time t, will be given by:

$$\Delta\phi^T_{prop}(r,t) = \phi^+_T(r,t) - \phi^-_T(r,t) = \Gamma_{prop}(r,t) \tag{2.9}$$

where $\phi^+_T(r,t)$ and $\phi^-_T(r,t)$ are the values of the potential on the upper (suction side) and lower (pressure side) of the blade trailing edge, respectively at time t. The

difference in these potentials is equal to the circulation, Γ_{prop}, at time t around the blade section at radius r. This condition is equivalent to requiring the shed vorticity from the blade trailing edge to be proportional to the time rate of change of the circulation around the blade (Kelvin's law).

The dipole strengths along the wakes behind the stators and duct will be convected downstream with a velocity based on the mean velocity field. The variance in the dipole strength along these wakes is due solely to the interaction of the stator blades and duct with the rotating propeller blades. Therefore, the period of the fluctuation in dipole strength along these wakes will still be based on the angular velocity of the propeller. The jump in potential across the stator blade wake surface, $\Delta\phi_{stat}$, can be expressed as:

$$\begin{aligned} \Delta\phi_{stat}(x,r,t) &= \Delta\phi^T_{stat}\left(r, t - \tfrac{x-x_T(r)}{V_a(r)}\right); \quad t \geq \frac{x-x_T(r)}{V_a(r)} \\ &= \Delta\phi^S_{stat}(r); \qquad\qquad t < \frac{x-x_T(r)}{V_a(r)} \end{aligned} \tag{2.10}$$

where x and r are the axial and radial coordinates of the stator blade wake surfaces, and $x_T(r)$ is the axial coordinate of stator blade trailing edge at radius r. $V_a(r)$ is the mean axial velocity at radius r. Similarly, the potential jump across the duct wake surface, $\Delta\phi_{duct}$, can be expressed as:

$$\begin{aligned} \Delta\phi_{duct}(x,\theta,t) &= \Delta\phi^T_{duct}\left(\theta, t - \tfrac{x-x_T}{V_a}\right); \quad t \geq \frac{x-x_T}{V_a} \\ &= \Delta\phi^S_{duct}; \qquad\qquad t < \frac{x-x_T}{V_a} \end{aligned} \tag{2.11}$$

where x and θ are the axial and circumferential coordinates in the duct wake, x_T is the axial location of the duct trailing edge, and V_a is the circumferential mean axial velocity at the duct trailing edge. The value of the dipole strength, $\Delta\phi^T_{stat}(r,t)$, at the trailing edge of the stator blades at any time t, will be given by:

$$\Delta\phi^T_{stat}(r,t) = \phi^+_T(r,t) - \phi^-_T(r,t) = \Gamma_{stat}(r,t) \tag{2.12}$$

where $\phi_T^+(r,t)$ and $\phi_T^-(r,t)$ are the values of the potential on the upper (suction side) and lower (pressure side) of the stator blade trailing edge, respectively at time t. The value of the dipole strength, $\Delta\phi_{duct}^T(r,t)$ at, at the trailing edge of the duct at any time t, will be given by:

$$\Delta\phi_{duct}^T(\theta,t) = \phi_T^+(\theta,t) - \phi_T^-(\theta,t) = \Gamma_{duct}(\theta,t) \tag{2.13}$$

where $\phi_T^+(\theta,t)$ and $\phi_T^-(\theta,t)$ are the values of the potential on the upper and lower sides of the duct trailing edge, respectively at time t.

As with the propeller, the difference in these potentials at the trailing edges of the stator blades and duct are equal to the circulation around the stator blades, Γ_{stat}, and duct, Γ_{duct}, respectively. This again satisfy's Kelvin's law which requires the shed vorticity from the trailing edge to be proportional to the time rate of change of the circulation.

2.4 The Generalized Image Model

Equation (2.5) can be solved numerically by approximating the component and wake surfaces with panels on which the potential and source distributions are assumed constant. This procedure is described in detail in [23], [15]. In this section, an alternative method is formulated to solve for the perturbation potential on the stator and propeller blade surfaces using the generalized image model. The method used to obtain the solution for the potential on the duct and hub surface is discussed in Chapter 4. The generalized image model was first introduced by Kinnas and Coney [27], [28]. In these works, the generalized image model is used to accurately model the steady flow past a single component ducted propeller. In order to apply the generalized image model in the case where the "imaging" body (i.e. the duct) is both lifting and unsteady, an additional assumption must be made. This is to assume that when solving for the potential on the surface of the "imaged" bodies (i.e. the propeller and stator blades), the dipole strength in the wake of the imaging body (i.e.

the duct wake) can be taken as being invariant along the mean streamlines on the wake surface. The dipole strength along the duct wake still varies with time and in the circumferential direction. In mathematical terms, this is equivalent to replacing the condition specified by equation (2.11) with the following condition:

$$\Delta\phi_{duct}(x,\theta,t) = \Delta\phi^{T}_{duct}(\theta_T,t) \tag{2.14}$$

where θ_T is the θ location at the duct trailing edge which lies on the streamline which passes through the point of interest on the duct wake. This is expected to have a small effect on the solution for the potential on the stators and propeller, particularly at high reduced frequencies. The effect of this assumption on the propeller/stator solution is discussed in Chapter 4. The correct duct wake strength as specified by equation (2.11) is recovered from the quasi-steady duct (QSD) solution and used when determining the solution for the perturbation potential on the duct surface. This is discussed in detail in Chapter 4.

For the steady problem, the duct coordinate system rotates along with the propeller, and the strength of the dipole sheet representing the vorticity in the duct wake is constant along streamlines in the duct wake. Therefore, equation (2.14) is the correct expression for the duct wake strength in steady flow, and no additional assumption is necessary. The mathematical justification for the generalized image model in steady flow is given by Kinnas and Coney [24]. The mathematical formulation for the generalized image in unsteady flow is shown below. This formulation is for the QSD solution on the internal blade row components.

With the assumption discussed above, equation (2.5) becomes:

$$\begin{aligned} 4\pi\epsilon\phi(\mathbf{x},t) \;=\; & \int_{S_D} \phi(\boldsymbol{\xi},t)\frac{\partial G(\mathbf{x},\boldsymbol{\xi})}{\partial n_D}\,dS(\boldsymbol{\xi}) + \int_{S_{PS}} \phi(\boldsymbol{\xi},t)\frac{\partial G(\mathbf{x},\boldsymbol{\xi})}{\partial n_{PS}}\,dS(\boldsymbol{\xi}) \\ & - \int_{S_D} G(\mathbf{x},\boldsymbol{\xi})(-\boldsymbol{U}_{in}\cdot\boldsymbol{n}_D)\,dS(\boldsymbol{\xi}) \\ & - \int_{S_{PS}} G(\mathbf{x},\boldsymbol{\xi})(-\boldsymbol{U}_{in}\cdot\boldsymbol{n}_{PS})\,dS(\boldsymbol{\xi}) \\ & + \int_{W_D} \Delta\phi^{T}_{duct}(\theta,t)\frac{\partial G(\mathbf{x},\boldsymbol{\xi})}{\partial n_{W_D}}\,dS(\boldsymbol{\xi}) \end{aligned}$$

$$+\int_{W_{PS}} \Delta\phi_{PS}(\xi,t)\frac{\partial G(\mathbf{x},\boldsymbol{\xi})}{\partial n_{W_{PS}}}\,dS(\boldsymbol{\xi}) \tag{2.15}$$

By introducing the Green's function $\tilde{G}$, an alternative way of expressing ϕ can be established. $\tilde{G}$ must satisfy the following equations:

$$\nabla^2\tilde{G}(\mathbf{x},\boldsymbol{\xi}) = -4\pi\delta(\mathbf{x}-\boldsymbol{\xi});\ \text{ for } \mathbf{x},\boldsymbol{\xi} \text{ not on the duct surface, } S_D \tag{2.16}$$

$$\frac{\partial\tilde{G}(\mathbf{x},\boldsymbol{\xi})}{\partial n_D(\mathbf{x})} = 0;\ \text{ for } \mathbf{x} \text{ on the duct surface, } S_D \tag{2.17}$$

$$\nabla_{\mathbf{x}}\tilde{G}(\mathbf{x},\boldsymbol{\xi}) \to 0 \ \text{ as } \mathbf{x}\to\infty \tag{2.18}$$

$$\nabla_{\mathbf{x}}\tilde{G}(\mathbf{x},\boldsymbol{\xi}) = \text{finite at the duct trailing edge} \tag{2.19}$$

where δ is the generalized *delta* function. The Green's function $\tilde{G}(\mathbf{x},\boldsymbol{\xi})$ represents the potential induced at $\mathbf{x}$ by a point source of strength -4π, placed at ξ, in the presence of the duct and hub. This is shown schematically in Figure 2-2. $\tilde{G}$ satisfies the Kutta condition at the duct trailing edge. By applying Green's formula to the duct and hub surface with a point source in the fluid domain at ξ, it follows that $\tilde{G}(x,\xi)$ must satisfy the following integral equation:

$$\begin{aligned} 2\pi\tilde{G}(\mathbf{x}',\mathbf{x}) &= \int_{S_D}\tilde{G}(\mathbf{x}',\mathbf{x})\frac{\partial G(\mathbf{x}',\mathbf{x})}{\partial n_D}\,dS(\mathbf{x}') \\ &- \int_{W_D}(\Delta\tilde{G})^D(\theta)\frac{\partial G(\mathbf{x}',\mathbf{x})}{\partial n_W}\,dS(\mathbf{x}') + 4\pi G(\mathbf{x},\boldsymbol{\xi}) \end{aligned} \tag{2.20}$$

Note that the jump in potential across the duct wake surface, $\Delta\tilde{G}^D(\theta)$, is invariant along the assumed streamlines in the duct wake. The strength of $(\Delta\tilde{G})^D(\theta)$ is determined from the application of the Kutta condition at the duct trailing edge. The geometry of the duct wake W_D is taken to be identical to the geometry assumed when the complete propulsor is present. The value of $\tilde{G}$ in the fluid domain off the duct surface can be expressed as:

$$\tilde{G}(\mathbf{x},\boldsymbol{\xi}) = G(\mathbf{x},\boldsymbol{\xi}) + G_I(\mathbf{x},\boldsymbol{\xi}) \tag{2.21}$$

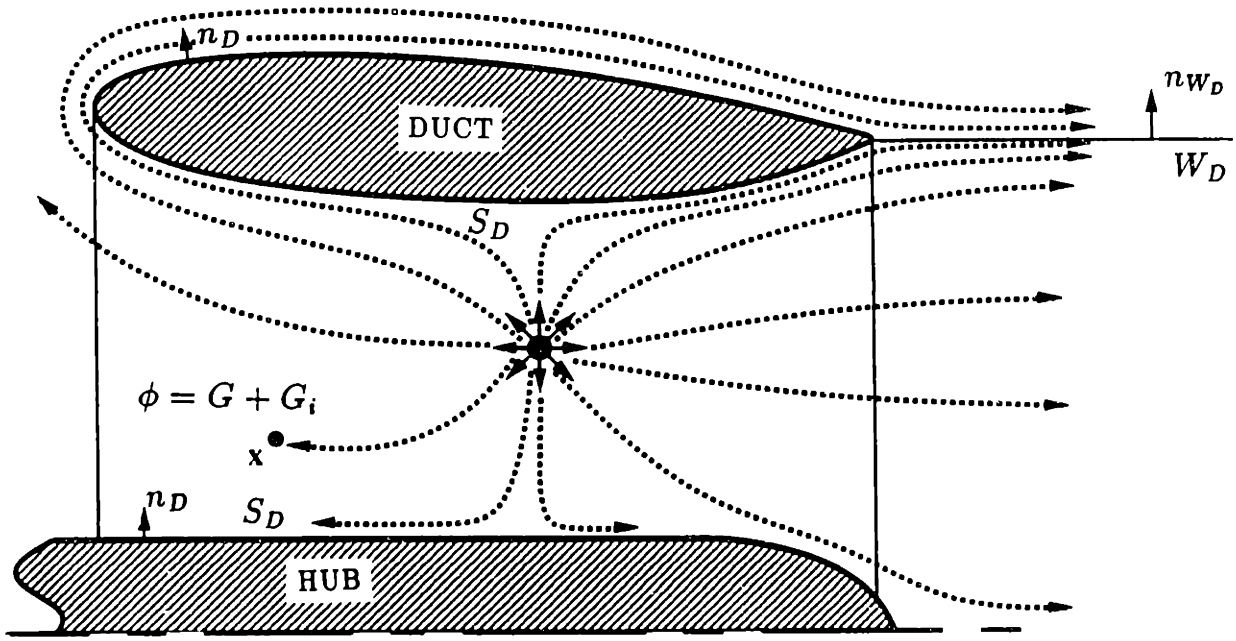

Figure 2-2: Potential flow through a duct and hub in the presence of a point source. The combined flow field due to the source, G, and its generalized image, G_I, with respect to the duct and hub is shown schematically with the dashed lines. Note that a Kutta condition is applied at the trailing edge of the duct.

where G_I is the *generalized image* of the source G with respect to the duct and hub and is defined as:

$$G_I(\mathbf{x},\boldsymbol{\xi}) = \frac{1}{4\pi}\left[\int_{S_D} \tilde{G}(\mathbf{x}',\boldsymbol{\xi})\frac{\partial G(\mathbf{x}',\mathbf{x})}{\partial n_D}\,dS(\mathbf{x}') + \int_{W_D} (\Delta\tilde{G})^D \frac{\partial G(\mathbf{x}',\mathbf{x})}{\partial n_W}\,dS(\mathbf{x}')\right] \quad (2.22)$$

G_I is the modification to the infinite fluid domain Green's function which accounts for the presence of the duct and hub. The perturbation potential ϕ in the presence of the complete propulsor can be expressed as:

$$\phi = \phi_D + \tilde{\phi}_{PS} \quad (2.23)$$

A proof of equation (2.23) is given in [24]. ϕ_D is defined as the perturbation potential outside of the duct and hub in the presence of the inflow velocity field, $\boldsymbol{U}_W$, but in the absence of the propeller and stators. From its definition, ϕ_D can be expressed as

follows:

$$
\begin{aligned}
4\pi\epsilon\phi_D(\mathbf{x}) &= \int_{S_D} \phi_D \frac{\partial G(\mathbf{x},\boldsymbol{\xi})}{\partial n_D}\, dS(\xi) + \int_{W_D} (\Delta\phi_D) \frac{\partial G(\mathbf{x},\boldsymbol{\xi})}{\partial n_{W_D}}\, dS(\xi) \\
&- \int_{S_D} G(\mathbf{x},\boldsymbol{\xi})(-U_{in}\cdot n_D)\, dS(\xi) \qquad (2.24)
\end{aligned}
$$

where $\epsilon = 1/2$ when $\mathbf{x} \in S_D$ and $\epsilon = 1$ when $\mathbf{x}$ is outside the duct/hub surface S_D. The value for ϕ_D on S_D is determined by solving equation (2.24) where $\mathbf{x} \in S_D, (\epsilon = 1/2)$. Since the propeller geometry is not involved in this expression, ϕ_D, will not vary in time. Therefore, the jump in potential across the duct wake used for solving equation (2.24), $\Delta\phi_D$, will be invariant along the assumed wake geometry without the need for any assumptions. In this case, the conditions set by equations 2.11 and 2.14 are equivalent, and the value of $\Delta\phi_D$ can be set according to equation (2.14). This will satisfy the Kutta condition at the trailing edge of the duct. The wake geometry, W_D, is the same as that used when the complete propulsor is present.

The potential $\tilde{\phi}_{PS}$ is defined as follows:

$$
\begin{aligned}
4\pi\epsilon\tilde{\phi}_{PS}(\mathbf{x},t) &= \int_{S_{PS}} \tilde{\phi}_{PS}(\xi,t) \frac{\partial \tilde{G}(\mathbf{x},\boldsymbol{\xi})}{\partial n_{PS}}\, dS(\xi) + \int_{W_{PS}} \Delta\tilde{\phi}_{PS}(\xi,t) \frac{\partial \tilde{G}(\mathbf{x},\boldsymbol{\xi})}{\partial n_{W_{PS}}}\, dS(\xi) \\
&- \int_{S_{PS}} \tilde{G}(\mathbf{x},\boldsymbol{\xi})\left[-(\boldsymbol{U}_{in} + \nabla\phi_D)\cdot n_{PS}\right]\, dS(\xi) \qquad (2.25)
\end{aligned}
$$

where $\epsilon = 1/2$ when $\mathbf{x} \in S_{PS}$ and $\epsilon = 1$ when $\mathbf{x}$ is outside of S_{PS}. The value of $\tilde{\phi}_{PS}$ on the surface of the propeller and stator blades, S_{PS}, is determined by solving equation (2.25) when $\mathbf{x} \in S_{PS}, (\epsilon = 1/2)$. The geometries for the propeller and stator blade wakes, W_{PS} are taken to be identical to those assumed in the presence of the complete propulsor. The Kutta condition is satisfied at the trailing edge of the propeller and stator blades by setting the jump in potential across the propeller blade and stator blade wakes, $\Delta\tilde{\phi}_{PS}$, according to equations 2.8 and 2.10 respectively.

Equation (2.23) shows that the flow through a ducted propulsor can be decomposed into two parts:

- The flow through the duct/hub in the presence of the inflow, $\boldsymbol{U}_W$.

- The disturbance to this flow resulting from the presence of the internal blade row components. This disturbance can be examined as the flow past the internal blades with the presence of the duct and hub accounted for via the modified inflow, $\boldsymbol{U}_W + \nabla\phi_D$, and the generalized sources and dipoles distributed on the blade surfaces.

By using the conditions specified by equations 2.17 and 2.19, The modified dipole distribution, $\frac{\partial\tilde{G}}{\partial n_{PS}}$, can be shown to satisfy the kinematic boundary condition on the duct and hub surface and the Kutta condition at the trailing edge of the duct. It can be decomposed as:

$$\begin{aligned}\frac{\partial\tilde{G}(\mathbf{x},\boldsymbol{\xi})}{\partial n_{PS}(\boldsymbol{\xi})} &\equiv \boldsymbol{n}_{PS}(\boldsymbol{\xi})\cdot\nabla_{\xi}\tilde{G}(\mathbf{x},\boldsymbol{\xi}) \\ &= \frac{\partial G(\mathbf{x},\boldsymbol{\xi})}{\partial n_{PS}(\boldsymbol{\xi})}\frac{\partial G_I(\mathbf{x},\boldsymbol{\xi})}{\partial n_{PS}(\boldsymbol{\xi})};\ \boldsymbol{\xi}\in S_{PS} \qquad (2.26)\end{aligned}$$

where $\partial G/\partial n_{PS}$ is the infinite fluid domain dipole, and $\partial G_I/\partial n_{PS}$ is the generalized image of the dipole with respect to the duct and hub.

Chapter 3

Numerical Implementation

This chapter describes the numerical implementation of the scheme for obtaining the solution for the flow past the internal blade row components of a ducted propulsor using the process formulated in Chapter 2. This process involves many steps. Therefore, the first section gives an overview of the method to describe how all of these steps fit together. Then the discrete forms of the equations used to obtain the solution on the propeller are presented. These discrete equations contain coefficients related to the generalized image of source and dipole distributions with respect to the duct and hub. The remaining parts of the chapter discuss the numerical computation of these coefficients and their incorporation into the procedure for determining the solution on the propeller. The implementation is initially discussed only for a single component ducted propeller. This will be extended to two rows of internal blades in Section 3.6. However, the procedure used to obtain and incorporate the generalized images are identical for both the propeller and stator blades.

The procedure used to numerically compute the value of the generalized image of a source with respect to the duct and hub directly is first discussed. The properties of the generalized image are examined and a simplified image is determined which closely approximates the singular properties of the generalized image. The simplified image is used to form the *image factor*, which is a "smoothed out" function of the generalized image. This is done in order to make the generalized image more suitable to interpolation. An interpolation scheme based on a Chebyshev polynomial expan-

sion is then developed to evaluate the generalized image for any arbitrary panel and control point location. This scheme is then validated by comparing the interpolated values for the generalized image to those computed directly.

Finally a discussion is given of the incorporation of the stator blades procedure into the procedure. A separate procedure, described in Chapter 4, is used to obtain the solution on the duct after the propeller and stator solution has been obtained.

3.1 Overview

When solving the problem of an open propeller in unsteady flow using a potential based panel method such as the one used in [25], a system of linear equations is established where the left hand side consists of coefficients equal to the potential induced by a uniform dipole distribution on one panel at the control point of another panel, and the right hand side consists of source terms determined by the magnitude of the inflow velocity normal to each panel. With the application of the generalized image model, the structure of this system of equations remains the same, except that the left hand side coefficients are now the influence of a propeller panel with a uniform dipole distribution *in the presence of the duct* at the control point of another panel, and the right hand side is now determined from the velocity field existing inside of the duct in the specified inflow using source influence coefficients which also account for the presence of the duct. The modification to each of the dipole influence coefficients forming the left hand side of the system of equations for unbounded flow, the generalized images, will have to be computed. In addition, the modifications to the source influence coefficients used to form the right hand side must also be computed. Since the number of these coefficients can become quite large, a fast but accurate method of calculating these images has been developed. This method, described in Section 3.4, utilizes a Chebyshev polynomial expansion of the image factors in the region inside the duct and into the duct wake.

The flow around the duct and hub in the absence of any inflow and in the presence of a single point source is calculated multiple times. Each time the point source

is moved to a new location, with the locations determined in order to set up an Chebyshev polynomial expansion. For each solution the "image factors" are computed at a set of control points inside of the duct which again correspond to the locations required to establish a Chebyshev polynomial expansion. The image factor is defined as the ratio of the induced potential due to the duct and hub at a specified field point with a source at a specified location (the generalized image) divided by the induced potential from the simplified image of the source with respect to the duct and the hub. The simplified image consists of two point sources, one located outside the duct inner surface which models the duct as an infinite wall and the other which is located inside the hub. By converting the potentials from the generalized images to image factors, an interpolating function can be set up which is more accurate and uses fewer terms than attempting to interpolate the generalized image potentials directly. This is because the image factor is a much smoother function than the potential induced by the generalized image. In addition, as the source point approaches the duct or hub surface, the simplified image approaches the generalized image, resulting in the image factor approaching one. The direct computation of the image factors is discussed in Section 3.3.

From this expansion, the influence coefficient for a source distribution in the presence of the duct on any given panel at the control point of another panel can be computed. From the derivative of the image factor, which is calculated directly from the Chebyshev polynomial expansion, the influence coefficient from a dipole distribution on any given panel in the presence of the duct at the control point of any panel can be computed as well. This is another advantage of using the series expansion of the image factor, as if the generalized images were computed directly, the images due to a source and dipole distribution would have to be computed separately.

The implementation of this procedure consists of the following steps: This procedure is shown schematically in Figure 3-1.

Step 1: Solve for the flow through the duct with the specified inflow but in the absence of the propeller and stators using a potential based panel method. The resulting flow field will be steady but non-axisymmetric.

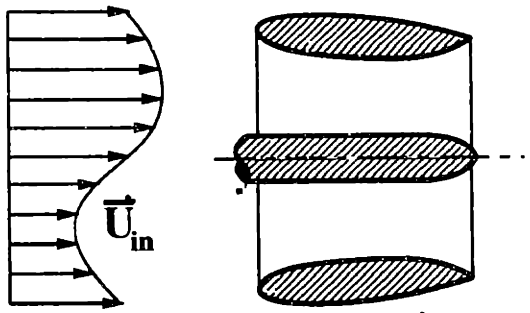

Step 1. Solve for ϕ_D and $\nabla\phi_D$

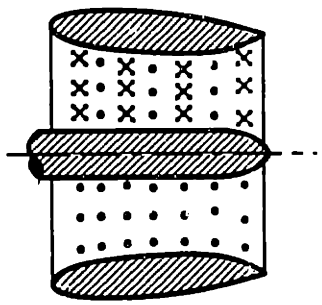

Steps 2-4. Solve for Chebyshev coefficients: c_{ijklm}

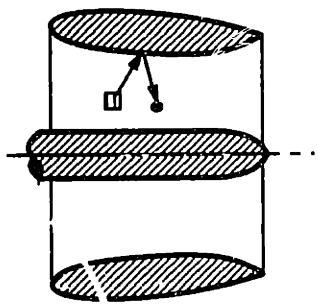

Step 5. Obtain the generalized images: $\bar{a}_{ij}$ and $\bar{b}_{ij}$

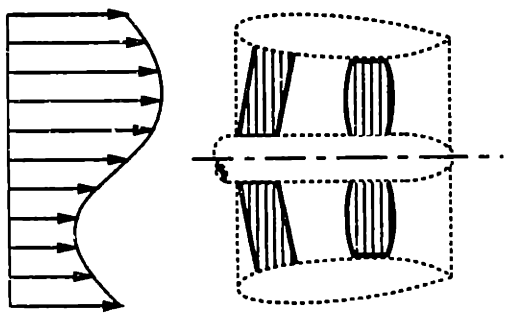

Step 6. Obtain the solution on the propeller and stator blades.

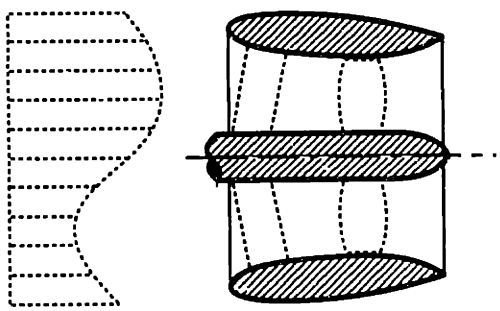

Step 7. Solve for the potential, pressure, and forces on the duct and hub.

Figure 3-1: Procedure used to obtain the solution for the flow past a multi-component ducted propulsor incorporating the generalized image model.

Solve for the velocity and potential at all of the propeller and stator control points. Store the potential on the surface of the duct and hub. This is described in Section 3.5.

Step 2: Solve for the flow past the duct and hub multiple times with zero inflow and a single point source located at various positions in the interior flow region. Solve for the potential induced by the duct and hub, defined as the generalized image, at a set of field points inside of the duct. Store the potential distribution on the duct and hub surfaces for each solution. This is discussed in Section 3.3.1

Step 3: Calculate the simplified image for the same set of source and field points. Then calculate the "image factors" for each combination of source and field points. This procedure is examined in Section 3.3.2.

Step 4: Compute the coefficients for the Chebyshev polynomial expansion based on the image factors calculated in Step 3. This is discussed in Section 3.4.2.

Step 5: Evaluate the Chebyshev polynomial expansion to determine the generalized image for each propeller, stator, and wake panel at all of the propeller and stator control points. This procedure will be described in Section 3.4.3.

Step 6: Solve the propeller and stator problem at each timestep:

- Using the modified influence coefficients which account for the presence of the duct and hub.
- Taking the inflow as being the flow field in the presence of the duct and hub in the absence of the propeller and stators from Step 1.
- Adding the potentials at the propeller and stator control points induced by the duct and hub operating in the absence of the pro-

peller and stators, calculated in Step 1, to the propeller and stator potentials.

This step is described in Section 3.2

Step 7: After solving the propeller/stator problem at all timesteps, determine the potential and pressure distribution on the duct surface from the potentials on the duct stored during Steps 1 and 2. This step is discussed in Chapter 4

Steps 2 through 4 will only have to be performed once for a given duct and hub geometry. Different propeller and stator geometries or different inflow conditions may be examined using the same set of coefficients computed during these steps. This is advantageous when many different propeller and stator configurations need to be examined for a given duct and hub. Using the method described above, the most costly part of the computations will only be performed once.

3.2 Discrete Formulation on Propeller

The method used to obtain the propeller solution is based on the unsteady panel method for open propellers developed by Hsin [15]. In [15], a complete description of the numerical formulation and implementation used for the open propeller case is given. Only a brief overview of this procedure will be given here, in order to describe the modifications necessary to incorporate the duct and hub using the generalized image model.

Recall from equation (2.23) that the solution for the potential on the propeller can be decomposed as $\phi = \phi_D + \tilde{\phi}_{PS}$. In the numerical scheme, ϕ_D and $\tilde{\phi}_{PS}$ will be obtained separately and then added together to give the total potential on the propeller. The potential $\tilde{\phi}_{PS}$ is obtained using the method based on [15] which is described in this section. A separate interpolation procedure is used to obtain ϕ_D which will be described in Section 3.5.

The potential $\tilde{\phi}_{PS}$ is defined by equation (2.25), which is a Fredholm integral of

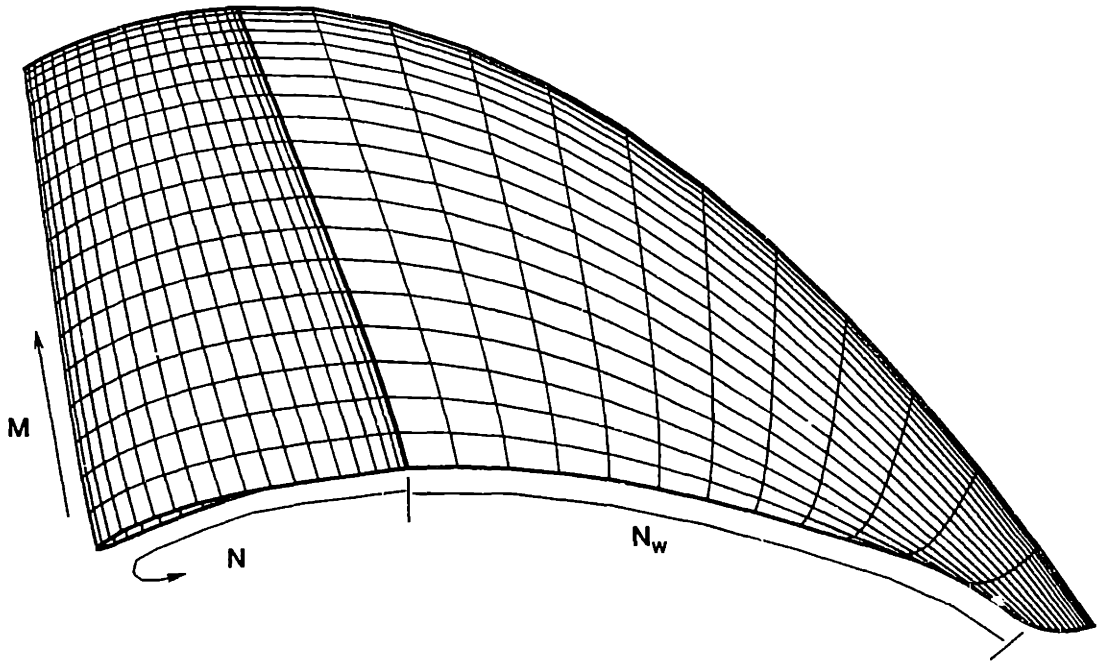

Figure 3-2: The propeller blade and wake discretization.

the second kind with respect to $\tilde{\phi}_{PS}$ over the surface of only the propeller and its wake. This equation can be solved numerically by discretizing the propeller and wake surfaces and implementing a time-marching panel method similar to the method used by Hsin [15]. Figure 3-2 shows the panel arrangement for the propeller and wake. The time domain is also discretized into equal intervals of time, Δt. The propeller wake panels start at the trailing edge of the propeller blade and are placed along the prescribed wake surface at a constant angular spacing which is related to the time step, $\Delta\theta_W = \omega\Delta t$.

Equation (2.25) can be expressed as a linear system of discretized equations which must be solved to obtain $\tilde{\phi}_{PS}$ at each time step, $n = t/\Delta t$. The PS subscript has been omitted in the remaining equations in this section for the sake of clarity. The

linear system of equations is shown below:

$$\sum_{k=1}^{N_B}\sum_{j=1}^{N_P}\tilde{a}_{ij}^{k}\tilde{\phi}_{j}^{k}(n)+\sum_{k=1}^{N_B}\sum_{m=1}^{M}\sum_{l=1}^{N_W}\tilde{W}_{ilm}^{k}\Delta\tilde{\phi}_{lm}^{k}(n) \tag{3.1}$$
$$=\sum_{k=1}^{N_B}\sum_{j=1}^{N_P}\tilde{b}_{ij}^{k}\tilde{\sigma}_{j}^{k}(n) \qquad i=1,(N_P\times N_B)$$

where:

- $\tilde{\phi}_j^k(n)$ is the solution for the dipole strength at panel j of blade k at time $t = n\Delta t$.
- N_B is the number of propeller blades
- N is the number of chordwise panels on the propeller blade
- M is the number of spanwise panels on the propeller blade
- $N_P = N \times M$ is the total number of panels on the key blade
- N_W is the number of chordwise panels in the propeller wake

The generalized influence coefficients, $\tilde{a}_{ij}^k$ and $\tilde{b}_{ij}^k$ are defined as the potentials induced at the control point of panel i by unit (constant) strength dipole and source distributions, respectively, on panel j of blade k, accounting for the presence of the duct and the hub. The generalized wake influence coefficients, $\tilde{W}_{ilm}^k$, are defined in the same manner as $\tilde{a}_{ij}^k$, except that the dipole distribution is placed on the l^{th} panel of the m^{th} wake strip. The generalized influence coefficients can be decomposed into the potential induced by the panel directly (in the absence of the duct) and the potential induced by the duct and hub due to the presence of the panel.

$$\begin{aligned}\tilde{a}_{ij}^{k} &= a_{ij}^{k}+(a_{ij}^{k})_I \\ \tilde{b}_{ij}^{k} &= b_{ij}^{k}+(b_{ij}^{k})_I \\ \tilde{W}_{ilm}^{k} &= W_{ilm}^{k}+(W_{ilm}^{k})_I\end{aligned} \tag{3.2}$$

The coefficients a_{ij}^k, b_{ij}^k and W_{ilm}^k are simply the unbounded flow influence coefficients which are the same as the influence coefficients used in the open propeller analysis

method developed by Hsin [15]. These coefficients can be calculated based on the method derived by Newman [36], in which the values of a_{ij}^k and W_{ilm}^k on each panel are computed from a closed form solution of $\int_S \frac{\partial G}{\partial n} dS$ for control points in the near field and are computed using a multipole expansion for control points in the far field. In the same manner, b_{ij}^k on each panel is computed using the analytic closed form solution or a multipole expansion of $\int_S G dS$ for control points in the near and far field respectively. The use of hyperberloidal panels was incorporated into the calculation of these coefficients by Hsin [15] in order to improve the accuracy for nonplanar panels resulting in the case of highly skewed propellers.

The coefficient $(a_{ij}^k)_I$ represents the generalized image with respect to the duct and hub of a uniform dipole distribution on panel j of blade k at the control point of panel i. Similarly, $(b_{ij})_I^k$ is the generalized image with respect to the duct and hub of a uniform source distribution on panel j of blade k at the control point of panel i. $(W_{ilm}^k)_I$ is the generalized image for a dipole panel in the propeller wake. The procedure used to obtain these coefficients will be discussed later in this chapter.

The magnitude of the source strength, $\tilde{\sigma}_j^k(n)$, is defined from equation (2.25) to be the equal the component of the velocity resulting inside the duct in the absence of the propeller at the control point of panel j which is normal to panel j.

$$\tilde{\sigma}_j^k(n) = -\left(\mathbf{U}_{P_{in}}(x_j^k, y_j^k, z_j^k, n\Delta t) + \nabla\phi_D\right) \cdot \hat{n}_j^k \tag{3.3}$$

where x_j^k, y_j^k and z_j^k are the coordinates of the centroid of panel j on blade k and $\hat{n}_j^k$ is the normal vector to that panel. All of these terms are defined in the rotating propeller coordinate system. As shown by (3.3), the source strength may be decomposed into the effect from the effective wake inflow in the absence of the duct, $\mathbf{U}_{P_{in}}$, which is defined by equation (2.1), and the effect from the velocity induced by the duct in the absence of the propeller, $\nabla\phi_D$, which will be determined using an interpolation procedure discussed in Section 3.5.

The solution is obtained at each time step only for one of the blades, which is called the *key blade*. The solution on the other blades is obtained from earlier solutions on

the key blade. Therefore, the influence from the other blades will be placed on the right hand side of the system of linear equations. In addition, the strength of the wake panels (except for the wake panels adjacent to the blade) will be known from the history of the solution. The influence of these panels should also be placed on the right hand side. Equation (3.2) can be rewritten as shown below. In these equations, the superscript 1 has been omitted for all values which refer to the key blade.

$$\sum_{j=1}^{N_P} \tilde{a}_{ij}\tilde{\phi}_j(n) + \sum_{m=1}^{M} \tilde{T}^L_{im}\Gamma_m(n) = RHS_i(n); \;\; i = 1, N_P \tag{3.4}$$

where,

$$\begin{aligned} RHS_i(n) \;=\; & \sum_{k=1}^{N_B}\sum_{j=1}^{N_P} \tilde{b}^k_{ij}\tilde{\sigma}^k_j(n) - \sum_{k=2}^{N_B}\sum_{j=1}^{N_P} \tilde{a}^k_{ij}\tilde{\phi}^k_j(n) - \sum_{m=1}^{M} \tilde{T}^R_{im}\Gamma_m(n-1) \\ & - \sum_{k=2}^{N_B}\sum_{m=1}^{M}\sum_{l=1}^{N_W} \tilde{W}^k_{ilm}\Delta\tilde{\phi}^k_{lm}(n) - \sum_{m=1}^{M}\sum_{l=2}^{N_W} \tilde{W}_{ilm}\Delta\tilde{\phi}_{lm}(n) \end{aligned} \tag{3.5}$$

$\tilde{T}^L_{im}$ and $\tilde{T}^R_{im}$ are the decomposed influence coefficients for the first wake panel in each strip on which a linear dipole distribution is specified. This is done to reduce the sensitivity of the solution to the size of the time step. These coefficients are described in [15]. Equation (3.4) forms a linear system of N_P equations for the unknown potentials $\tilde{\phi}_j(n)$ on the key blade. This system of equations is inverted at each time step n. The right hand side is then updated before solving the system at the next time step. The procedure continues until a steady state oscillatory solution is obtained which usually requires several propeller revolutions. The jump in potential across the propeller wake panels, $\Delta\tilde{\phi}^k_{l,m}(n)$, can be obtained from equations (2.8) and (2.9). The circulation at the trailing edge of the blade, $\Gamma_m(n)$, is approximated numerically by:

$$\Gamma_m(n) = \tilde{\phi}^+_m(n) - \tilde{\phi}^-_m(n) \tag{3.6}$$

where $\tilde{\phi}^+_m$ and $\tilde{\phi}^-_m$ are the potentials on the upper and lower trailing edge panels, respectively, for the m^{th} blade strip. This is an extension of Morino's Kutta condition in steady flow [35]. This approximation is improved through the use of an unsteady

iterative pressure Kutta condition which is discussed in more detail in [15]. A complete description of the numerical stepwise solution algorithm applied to solve the system of linear equations formed by equation (3.4) as well as a numerical validation of the algorithm is given by Hsin [15].

3.3 The Image Factor

In order to solve the system of linear equations formed by equation (3.4), it is necessary to obtain the modifications to the panel influence coefficients which account for the presence of the duct and hub, $(a_{ij}^k)_I$, $(b_{ij}^k)_I$ and $(W_{ilm}^k)_I$. In the next two sections, a procedure will be developed for obtaining these generalized images. These generalized images will be approximated by their far field values. In other words, the value of the generalized image of a constant unit source or dipole distribution on a panel will be approximated by the generalized image for a point source or dipole of unit strength located at the centroid of the panel multiplied by the panel area.

$$\begin{aligned} (a_{ij}^k)_I &= \int_{S_j} \frac{G_I(\mathbf{x},\boldsymbol{\xi})}{\partial n_j}\, dS \approx A_j \bar{a}_{ij}^k \\ (b_{ij}^k)_I &= \int_{S_j} G_I(\mathbf{x},\boldsymbol{\xi})\, dS \approx A_j \bar{b}_{ij}^k \end{aligned} \tag{3.7}$$

where:

A_j is the area of panel j.

S_j represents the surface of panel j.

$G_I(\mathbf{x},\boldsymbol{\xi})$ is the generalized image for a point source with respect to the duct and hub as defined by equation (2.22). $\mathbf{x}$ corresponds to the control point on panel i, and $\boldsymbol{\xi}$ corresponds to the point of integration on the surface of panel j.

$\bar{a}_{ij}^k$ is the potential induced at the control point of panel i by the duct and hub in the presence of a unit strength point dipole placed at the centroid of panel j. The dipole is aligned with, $\hat{n}_j$, the normal vector for panel j.

$\bar{b}^k_{ij}$ is the potential induced at the control point of panel i by the duct and hub in the presence a unit strength point source placed at the centroid of panel j.

This approximation should be accurate for most cases, although it may have some effect on the generalized images corresponding to panels adjacent to the duct and hub (particularly the generalized images which modify the self influence coefficients for these panels). The possible effects from this approximation on the propeller solution will be discussed in Chapter 6. The procedure used to calculate $(W^k_{ilm})_I$ is the same as that used for $(a^k_{ij})_I$ since both of these coefficients refer to panels with a unit dipole distribution. Therefore, only the procedure for determining $(a^k_{ij})_I$ and $(b^k_{ij})_I$ will be detailed in this chapter.

The coefficient $\bar{b}^k_{ij}$ is equivalent to the value $G_I(\mathbf{x}, \boldsymbol{\xi})$ defined by equation (2.22), where $\mathbf{x} = (x_i, y_i, z_i)$ is the location of the control point on panel i, and $\boldsymbol{\xi} = (x_j, y_j, z_j)$ is the location of the point source at the centroid of panel j. The value for the generalized image of a point dipole with respect to the duct and hub is the derivative of the generalized image of a point source placed at the same location with respect to the location of the source.

$$\bar{a}^k_{ij} = \frac{\partial G_I(\mathbf{x}, \boldsymbol{\xi})}{\partial n_j} = \left(\frac{\partial \bar{b}^k_{ij}}{\partial x^k_j} \hat{i} + \frac{\partial \bar{b}^k_{ij}}{\partial y^k_j} \hat{j} + \frac{\partial \bar{b}^k_{ij}}{\partial z^k_j} \hat{k} \right) \cdot \hat{n}_j \tag{3.8}$$

The present method will first compute the generalized source images, $G_I(\mathbf{x}, \boldsymbol{\xi})$, by directly solving equation (2.22). This will be done *only* for a representative set of source and control point locations inside the duct and in the duct wake. This process will be discussed in Section 3.3.1. The generalized images at these points are then converted to image factors, defined as the ratio of the generalized image divided by a simplified image, which consists of the potential induced by two point sources, one located outside the duct inner surface which models the duct as an infinite wall and the other which is located inside the hub. The simplified image will be discussed in Section 3.3.2. To find the generalized source images, $\bar{b}^k_{ij}$, at other panel and control point locations, an interpolation scheme is utilized based on a Chebyshev polynomial expansion of the image factors in the region bounded by the duct and

hub and their wakes. The generalized dipole images, $\bar{a}_{ij}^k$, can then be determined by differentiating the polynomial expansion of the generalized source image. By converting the generalized images to image factors, an interpolating function can be set up which is more accurate and uses fewer terms than attempting to interpolate the generalized images directly. The interpolation scheme will be discussed in Section 3.4.

3.3.1 The generalized image

Calculating the generalized image directly involves two steps. The first step is to solve the discretized form of equation (2.20), which is equivalent to solving for the potential, $\tilde{G}$, on the surface of the duct and hub in the absence of an inflow but in the presence of a point source placed at $\boldsymbol{\xi}$. This problem is shown schematically in Figure 2-2. Equation (2.20) is a Fredholm integral of the second kind with respect to $\tilde{G}$ over the surface of the duct, hub, and duct wake. This equation can be solved numerically by discretizing the duct, hub and duct wake surfaces and implementing a panel method in similar manner as was used for the propeller in Section 3.2. The panel arrangement for the duct, hub and duct wake is shown in Figure 3-3. Notice that straight, rectangular panels are used on the both the duct and hub. Since this problem is solved in the absence of the propeller and in the presence of only a single point source, it is not necessary to align the panels on the duct, hub with any part of the propeller or propeller wake. The second step is to use this potential distribution on the duct, hub and duct wake to calculate the potential, $G_I(\mathbf{x}, \boldsymbol{\xi})$, induced by the duct and hub at a field point $\mathbf{x}$. This is equivalent to solving the discretized form of equation (2.22).

The generalized image in its most general form is a function of all six coordinates of the source and field points. It can be reduced, however, to a function of five variables by taking advantage of the axisymmetry of the duct and hub geometry.

$$G_I(x_i, y_i, z_i | x_j, y_j, z_j) \rightarrow G_I(x_i, r_i, | x_j, r_j, \theta'), \tag{3.9}$$

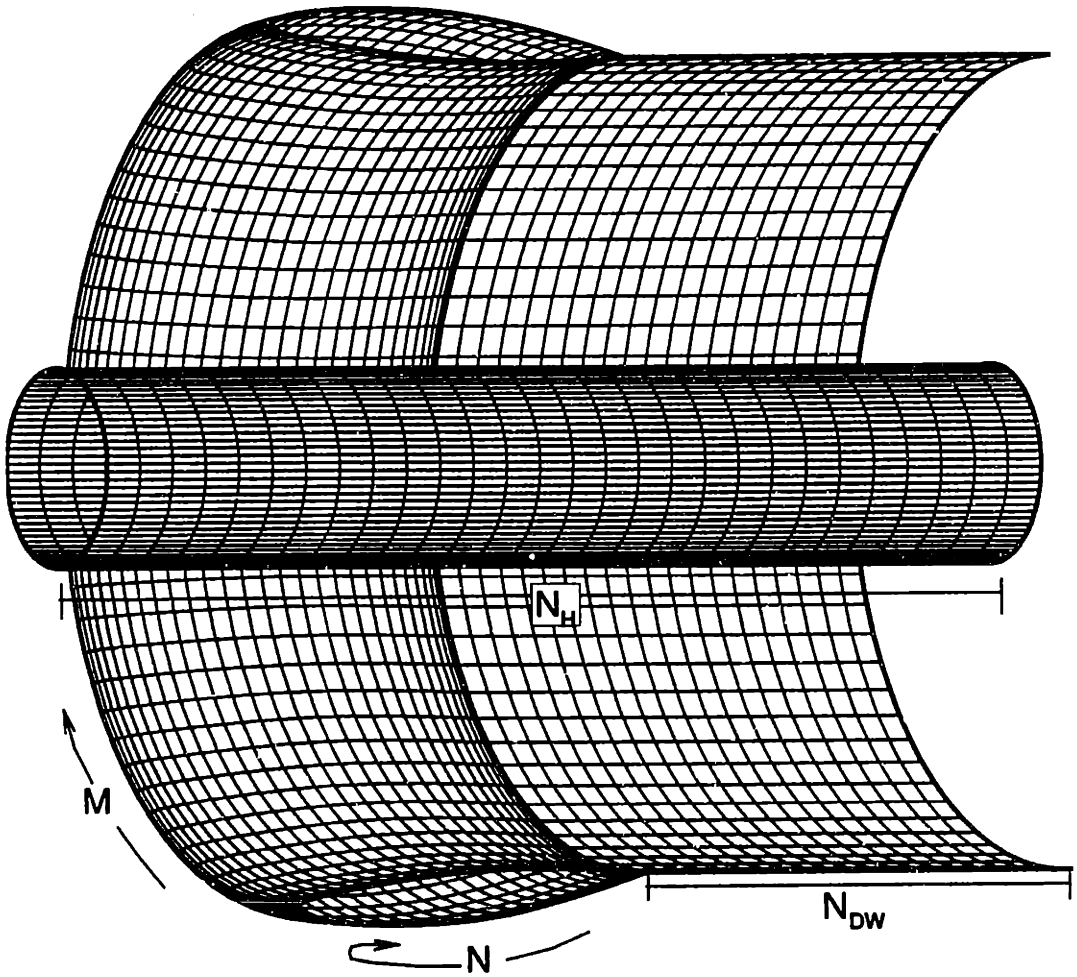

Figure 3-3: The duct, hub and duct wake discretization. N=60, M=80, only half the duct is shown.

where

$$\theta' = \theta_i - \theta_j \tag{3.10}$$

where $r_i = \sqrt{y_i^2 + z_i^2}$ and $r_j = \sqrt{y_j^2 + z_j^2}$ are the radial positions of the field and source points respectively; and $\theta_i = \arctan(z_i/y_i)$ and $\theta_j = \arctan(z_j/y_j)$ are the angular positions of the field and source points respectively. These positions are shown schematically in Figures 3-4 and 3-5. In addition, it turns out that the function is also symmetrical about $\theta' = 0$.

$$G_I(x_i, r_i, |x_j, r_j, \theta') = G_I(x_i, r_i, |x_j, r_j, -\theta') \tag{3.11}$$

The axisymmetry of the duct and hub geometry allows the generalized image to be represented by calculating G_I directly for a set of sources located only on the $\theta = 0$ plane inside the duct and in the duct wake. The field points must still be placed throughout the region inside the duct. However, since the solution is symmetric about $\theta' = 0$, G_I can be adequately represented using field points only in the region covering half of the duct, (i.e. from $\theta' = 0°$ to $180°$). The procedure to obtain a representative set of values for G_I will solve the duct and hub problem N_S times, where N_S is the number of source locations required to represent the generalized image. For each solution, the source will be placed at a different location, $\boldsymbol{\xi}_j$, with these locations being distributed over the $\theta = 0$ plane inside the duct and in the duct wake. For each solution, the potential, $G_I(\mathbf{x}_i, \boldsymbol{\xi}_j)$, induced by the duct and hub will be calculated at set of N_{FP} field points, $\mathbf{x}_i$. The placement and number of the source points, $\boldsymbol{\xi}_j$, and the field points, $\mathbf{x}_i$, will be discussed when describing the interpolation scheme in Section 3.4.

The first step in solving for the generalized image is to obtain the potential $\tilde{G}(\boldsymbol{\chi}, \boldsymbol{\xi}_j)$ on the duct and hub surface in the presence of a point source located at $\boldsymbol{\xi}_j$, where $\boldsymbol{\chi} = (x_d, r_d, \theta_d)$ refers to the position of a point on the duct or hub surface. This will be done by solving equation (2.20) numerically. Since $\boldsymbol{\xi}_j$ lies in the $\theta = 0$ plane, $\tilde{G}(\boldsymbol{\chi}, \boldsymbol{\xi})$ will be symmetrical about $\theta_d = 0$. Therefore, when solving the discretized form of equation (2.20), it is only necessary to solve for the strengths

of the panels on half of the duct. Expressing $\tilde{G}(\chi, \xi)$ in its discretized form, this is equivalent to:

$$\tilde{G}^j_{n,m} = \tilde{G}^j_{n,m'} \tag{3.12}$$

where $\tilde{G}^j_{n,m}$ is the potential on the n^{th} panel of the m_{th} circumferential strip on the duct in the presence of a point source at ξ_j. The index m' corresponds to the circumferential duct strip on the opposite side of the $\theta = 0$ plane. In other words, if the duct is paneled with M_D circumferential strips of panels, the potential will be computed only on the first $M_D/2$ strips. The potential on the remaining strips will be obtained from symmetry. In this case the circumferential indexes on the opposite side of the duct are defined as:

$$m' = M_D + 1 - m. \tag{3.13}$$

Figure 3-3 shows only the panels on the half of the duct on which the solution is obtained from symmetry. In the actual implementation, the duct grid is rotated so that a panel is centered over the source at $\theta = 0$. This requires the duct potential to be solved on $M_D/2 + 1$ strips; however, this simple modification has been left out of this derivation for clarity. The linear system of equations formed by equation (2.20) for a single point source at ξ_j is shown below:

$$\sum_{m=1}^{M_D/2} \sum_{n=1}^{N_D} (a_{i,n,m} + a_{i,n,m'}) \tilde{G}^j_{n,m} + \sum_{m=1}^{M_D/2} \sum_{n=N_D+1}^{N_D+N_H} (a_{i,n,m} + a_{i,n,m'}) \tilde{G}^j_{n,m} \tag{3.14}$$
$$+ \sum_{m=1}^{M_D/2} \sum_{n=1}^{N_{WD}} (W_{i,n,m} + W_{i,n,m'}) \Delta \tilde{G}^j_m = \frac{1}{||\chi_i - \xi_j||} \qquad i = 1, N_{DH}$$

where:

N_D is the number of chordwise panels on the duct.

N_H is the number of chordwise panels on the hub.

M_D is the number of circumferential panels on both the duct and hub.

N_{WD} is the number of chordwise panels in the wake of the duct.

$N_{DH} = (N_D + N_H) \times M_D/2$ is the total number of panels on the duct and hub of unknown strength.

$||\chi_i - \xi_j||$ is the distance between the point source at ξ_j and the control point of panel i.

$a_{i,n,m}$ is the influence coefficient for the potential induced by a unit dipole distribution on duct/hub panel n, m at the control point of panel i

$W_{i,n,m}$ is the influence coefficient for the potential induced by a unit dipole distribution on the n^{th} duct wake panel on the m^{th} circumferential duct wake strip at the control point of panel i.

The coefficients $a_{i,n,m}$ and $W_{i,n,m}$ are obtained by the same procedure used to compute the unbounded flow influence coefficients for the propeller solution described in Section 3.2. In this case, however, the influence coefficients only have to be calculated for a single circumferential duct and hub strip. Since the duct and hub geometries are axisymmetric, all of the other influence coefficients can be determined by rotating the values for the coefficients computed on a single strip. The value of $\Delta\tilde{G}^j_m$ is determined by the following equation:

$$\Delta\tilde{G}^j_m = \tilde{G}^j_{1,m} - \tilde{G}^j_{N_D,m} \tag{3.15}$$

where $\tilde{G}^j_{1,m}$ and $\tilde{G}^j_{N_D,m}$ are the values of $\tilde{G}$ on the upper and lower trailing edge panels, respectively, for the m^{th} circumferential duct strip. This is an example of Morino's Kutta condition in steady flow [35]. When solving for the generalized image, the duct is solved as a steady problem. When obtaining the solution for the potential and forces on the duct, an unsteady iterative pressure Kutta condition will be used. Since there is no inflow present, there will be no source terms in the equation. Equations (3.15) form a system of N_{DH} linear equations for the potential $\tilde{G}^j_{nm}$ on the surface of the duct and hub in the presence of a point source at ξ_j. This system is inverted N_S times, to obtain $\tilde{G}^j_{nm}$ for each of the N_S source locations, ξ_j.

Once the solution for $\tilde{G}^j_{nm}$ has been obtained for a given source point location, $\boldsymbol{\xi}_j$, the generalized image, $G_I(\mathbf{x}_i, \boldsymbol{\xi}_j)$, corresponding to that source can be computed at a set of field points, $\mathbf{x}_i$. This consists of solving the discretized form of equation (2.22) which is shown below.

$$G_I(\mathbf{x}_i, \boldsymbol{\xi}_j) = \sum_{m=1}^{M_D/2} \sum_{n=1}^{N_D} (a'_{i,n,m} + a'_{i,n,m'}) \tilde{G}_{n,m} + \sum_{m=1}^{M_D/2} \sum_{n=N_D+1}^{N_D+N_H} (a'_{i,n,m} + a'_{i,n,m'}) \tilde{G}_{n,m} + \sum_{m=1}^{M_D/2} \sum_{n=1}^{N_{WD}} (W'_{i,n,m} + W'_{i,n,m'}) \Delta \tilde{G}^j_m \tag{3.16}$$

where:

$a'_{i,n,m}$ is the influence coefficient for the potential induced by a unit dipole distribution on duct/hub panel n, m at the field point $\mathbf{x}_i$

$W'_{i,n,m}$ is the influence coefficient for the potential induced by a unit dipole distribution on the n^{th} duct wake panel on the m^{th} circumferential duct wake strip at the field point $\mathbf{x}_i$.

The primes on the influence coefficients correspond to the influence at a field point in the flow field as opposed to at a panel control point. The coefficients $a'_{i,n,m}$ and $W'_{i,n,m}$ are determined using the same method used to compute $a_{i,n,m}$ and $W_{i,n,m}$ for equation (3.15). After these coefficients are computed, all of the terms on the right hand side of equation (3.16) are known. Therefore, $G_I(\mathbf{x}_i, \boldsymbol{\xi}_j)$ can be calculated directly by summing all of the terms on the right hand side of this equation, and it is not necessary to invert a system of equations. For the solution on the duct corresponding to each of the N_S source locations, equation (3.16) will be evaluated N_{FP} times to obtain the value of $G_I(\mathbf{x}_i, \boldsymbol{\xi}_j)$ at every field point $\mathbf{x}_i$. The total number of generalized images computed directly to represent this function is, therefore, $(N_S \times N_{FP})$. Since the field points at which the generalized image is computed are the same for each source location, the coefficients $a'_{i,n,m}$ and $W'_{i,n,m}$ only have to be computed once.

Since $G_I(\mathbf{x}_i, \boldsymbol{\xi}_j)$ is a function of five variables, visualizing the shape of this function is difficult. It is important to determine the behavior of the generalized image,

however, in order to create an efficient interpolation procedure. In order to better understand the properties of the generalized image, its value was examined for the case where the location of the source point was fixed. This was done for a multitude of point source locations to produce 2-D plots of the generalized image where all of the variables except for one are held constant. Examples of these plots are contained in the remainder of this chapter. Figures 3-4 and 3-5 show schematically the coordinate system and arrangement of source and field points used to examine the generalized image. A cylindrical coordinate system is used where the origin is located on the centerline at the same axial location as the leading edge of the duct. All lengths are non-dimensionalized with respect to the propeller radius. The the radius of the duct inner surface at its midchord is 1.0 for the duct used for the examples shown in this chapter. The chordlength of the duct is also 1.0, and the hub is a constant radius cylinder of radius 0.25. A complete description of the duct geometry is given in Table 6.2. The source will be fixed at a location on the $\theta = 0$ plane at $\boldsymbol{\xi} = (x_i, r_i, \theta_i = 0)$. A set of field points is then arranged where all the field point variables except for one are held constant. This produces the "Theta-Cut," "R-Cut" and "X-Cut" arrangements depicted in Figures 3-4 and 3-5.

The convergence of the generalized image with the number of panels on the duct is shown in Figures 3-6 and 3-7. For this particular geometry, 60 chordwise and 80 circumferential panels were adequate on the duct for convergence, which is the configuration shown in Figure 3-3. Figures 3-6 and 3-7 show the generalized image resulting from a point source placed at $\boldsymbol{\xi}_j(x_j = 0.5, r_j = 0.95, \theta_j = 0.0)$ calculated at a set of field points inside the duct where radius of the field points is also 0.95. This represents an extreme case where both the source and field points approach the inner surface of the duct. In Figure 3-6 the generalized image is examined with respect to the θ position of the field point, where the axial and radial locations of the field point are fixed at $x_i = 0.5$ and $r_i = 0.95$. Since the generalized image depends only on the relative angle between the source and field point, this can be viewed as examining the behavior of the generalized image with respect to angular position of either the source point, $\boldsymbol{\xi}$, or the field point, $\mathbf{x}$. Using the terminology of equation (3.9), the figure

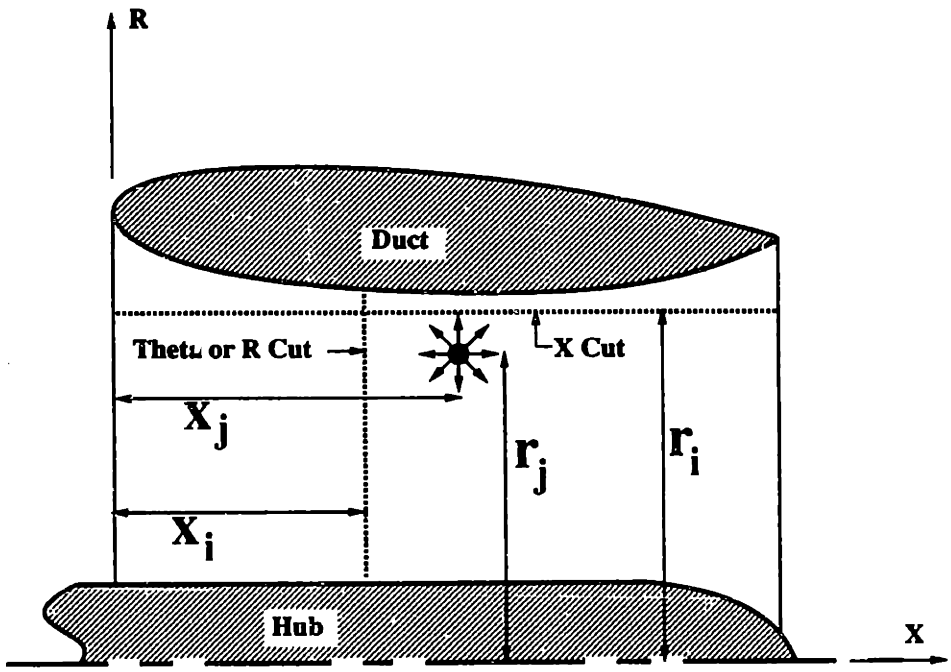

Figure 3-4: Locations of the source and field points used to examine the generalized image of a point source with respect to a duct and hub. The dashed lines represent the locations of a series of field points where θ_i of the field points is held constant.

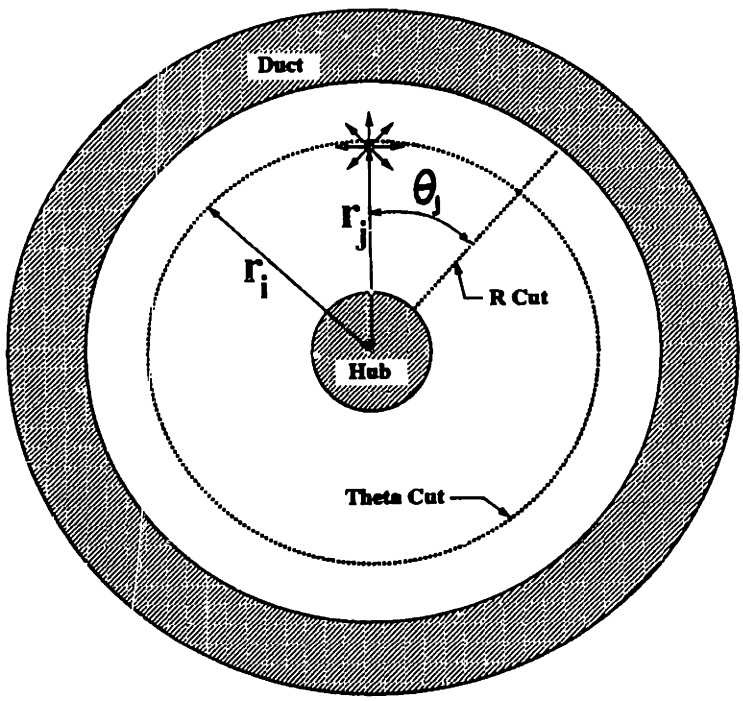

Figure 3-5: Locations of the source and field points used to examine the generalized image of a point source with respect to a duct and hub. The dashed lines represent the locations of a series of field points where x_i of the field points is held constant.

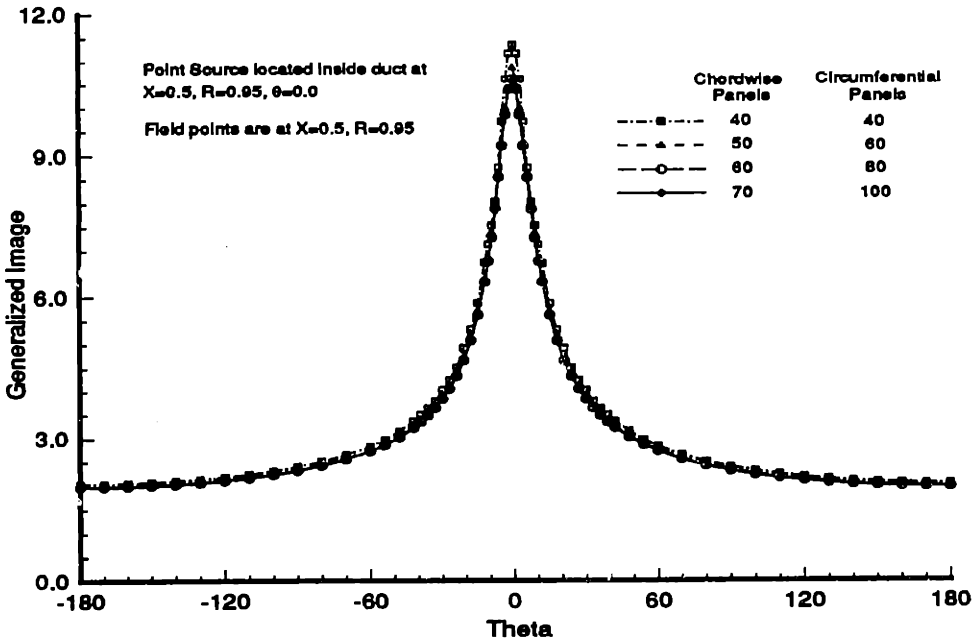

Figure 3-6: Convergence of the generalized image with respect to duct/hub paneling. All variables held constant except for θ_i of the field point.

shows a plot of $G_I(0.5, 0.95|0.5, 0.95, \theta')$. It can be seen that the generalized image is symmetrical with respect to θ in accordance with equation (3.11). In addition, it can be seen that the function has a sharp peak as both the source and field points approach the inner surface of the duct. Figure 3-7 examines the behavior of the generalized image with respect to the axial location of the field point where $r_i = 0.95$ and $\theta_i = 0$. This also shows the effects of both the source and field points approaching the duct, although the function appears to vary more sharply with respect to the angular position of the source and field points. There is actually a singularity in the generalized image where both the source and field point are located at the same point on the duct surface.

3.3.2 The simplified image

The spike which occurs in the generalized image as the source and field point approach the surface of the duct and hub will cause difficulties when developing a multivariate polynomial approximation to the generalized image. For this reason, a simplified

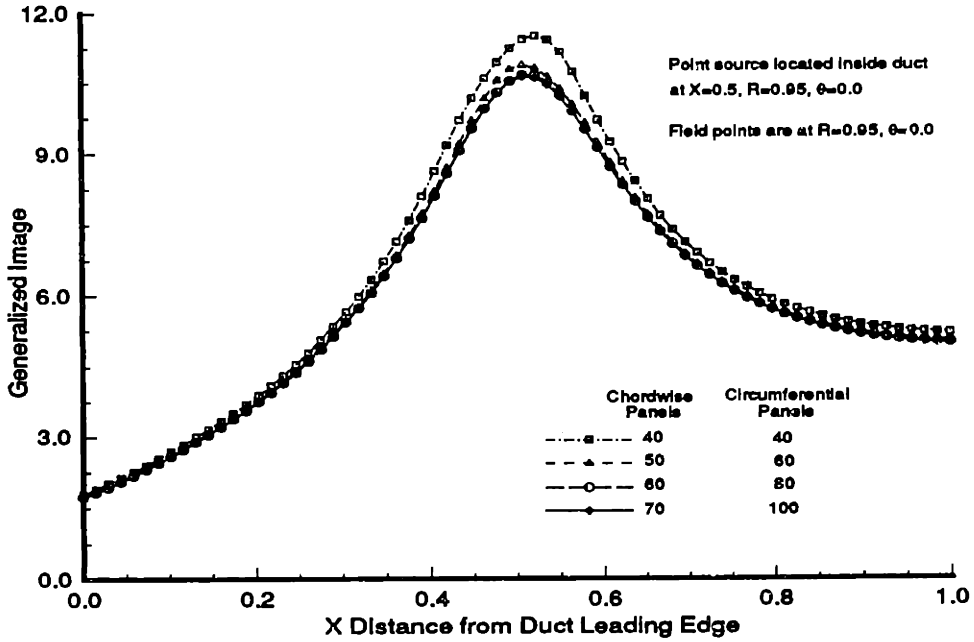

Figure 3-7: Convergence of the generalized image with respect to duct/hub paneling. All variables held constant except for x_i of the field point.

image, $G_{SI}(\mathbf{x}, \boldsymbol{\xi})$, is developed which can be subtracted from the generalized image or by which the generalized image can be divided in order to eliminate the singular behavior in this region. The desired properties of the function representing the simplified image are as follows: (1) the function should closely approximate the behavior of the generalized image in the region of the singularity; (2) the function should be smooth away from this region; (3) the function should be "simple," that is, since the simplified image is created to make the interpolation procedure more efficient, this function should not be computationally expensive to obtain. Ideally, the simplified image should consist of the potential from a few point singularities.

A simple function which models the duct and hub as infinite cylinders would seem to be a good choice for the simplified image. This function would have to satisfy the boundary condition of zero normal velocity on a cylinder in the presence of a point source. In two dimensions, the condition of zero normal velocity on a circle of radius R in the presence of a point source of strength q at radius R_s can be satisfied by the addition of an additional source, also of strength q, located above the source at radius

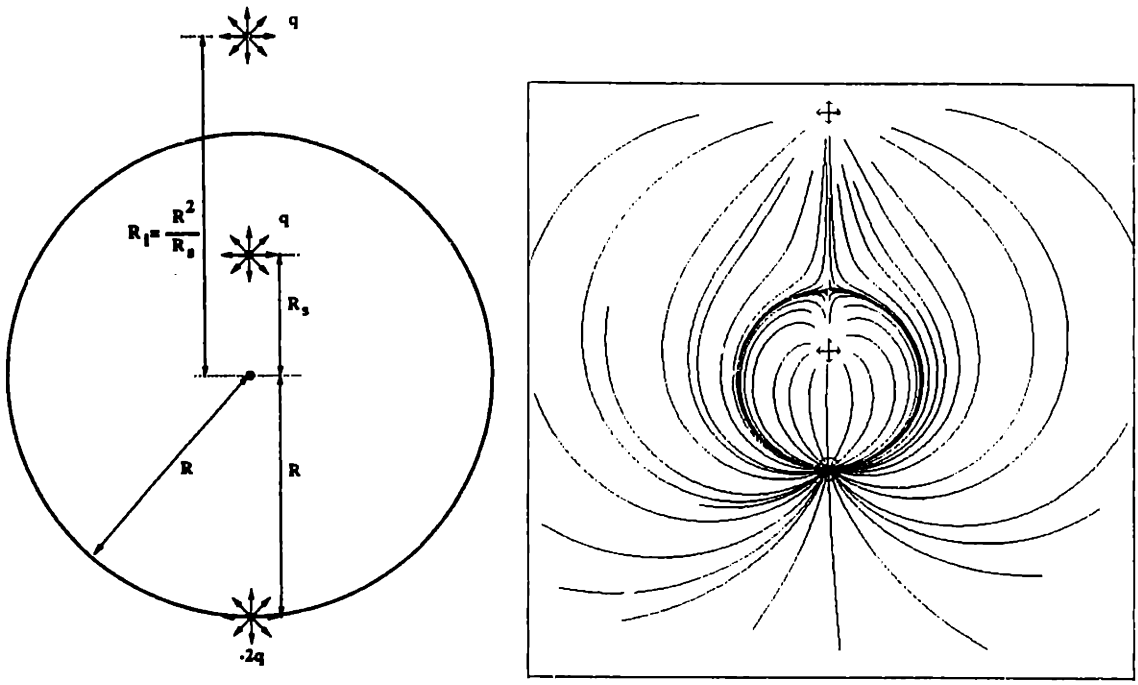

Figure 3-8: Two dimensional distribution of singularities satisfying boundary condition on a circle in the presence of a point source and the resulting streamlines.

$R_i = R^2/R_s$ and a sink of strength $2q$ located on the circle directly below the source, as shown in Figure 3-8. Unfortunately, this arrangement can not be extended to three dimensions to model an infinite cylinder in the presence of a source. In addition, the sink located on the bottom of the circle will result in a singular behavior in the simplified image away from the location of the singular region of the generalized image. Keeping only the source at R_i, however, should capture the local behavior of the generalized image near the singularity and be smooth everywhere else inside the duct. This is all that is required for the simplified image! In this case the simplified image models the duct as an infinite wall located midway between the source and image source. Near the singularity, the generalized image should behave locally as a point source near an infinite wall, so the generalized image should approach the simplified image in this region. Therefore, the simplified image chosen consists of two additional point sources placed at the same axial and angular position as the real source: one placed at radius $R_I = R_D^2/R_S$ representing the duct and the other

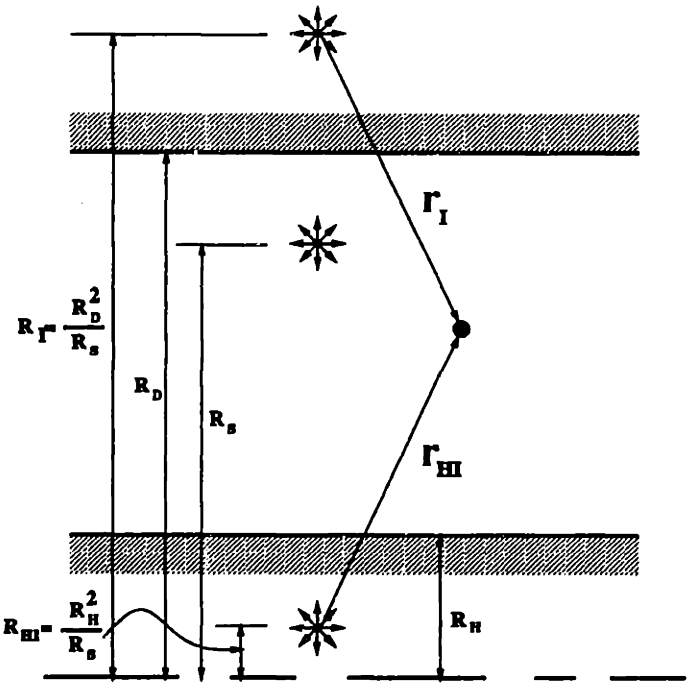

Figure 3-9: The simplified image

placed at radius $R_{HI} = R_H^2/R_S$ representing the hub, where R_D, R_H and R_S are the radii of the duct, hub and real source respectively. The simplified image is shown schematically in Figure 3-9.

The simplified image, $G_{SI}(\mathbf{x}, \boldsymbol{\xi})$, with respect to the duct and hub of a point source at $\boldsymbol{\xi} = (x_j, r_j, \theta_j)$ at a field point, $\mathbf{x} = (x_i, r_i, \theta_i)$, can be expressed as:

$$G_{SI}(\mathbf{x}, \boldsymbol{\xi}) = \frac{1}{||\boldsymbol{\xi}^I - \mathbf{x}||} + \frac{1}{||\boldsymbol{\xi}^{HI} - \mathbf{x}||} \tag{3.17}$$

where:

$\boldsymbol{\xi}^I = (x_j, \frac{R_D^2}{r_j}, \theta_j)$ and $\boldsymbol{\xi}^{HI} = (x_j, \frac{R_H^2}{r_j}, \theta_j)$ are the locations of point sources used to represent the duct and hub respectively,

R_D and R_H are the local radii of the duct and hub respectively at the location of the source,

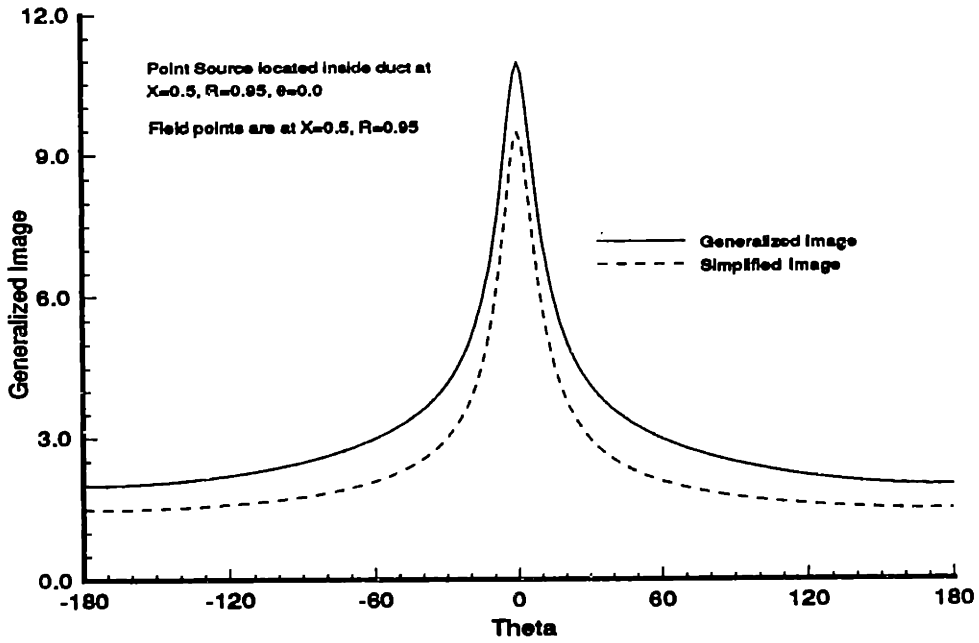

Figure 3-10: Comparison of the generalized image and the simplified image vs. θ_i of the field point.

$||\boldsymbol{\xi}^I - \mathbf{x}||$ and $||\boldsymbol{\xi}^{HI} - \mathbf{x}||$ refer to the radial distances between the field point and image sources representing the duct and hub respectively.

The comparison between the generalized and simplified images is shown in Figures 3-10 through 3-12. The point source is located at the same location as in Figures 3-6 and 3-7. Figure 3-10 shows a comparison of the two functions with respect to the relative angle between the source and field point. Figure 3-11 shows the comparison as the field point radially approaches the inner surface of the duct directly above the source. Figure 3-12 compares the function with respect to the axial location of the filed point. In all three plots it appears that the simplified image exhibits the same local behavior as the generalized image in the region where both the source and field point are near the same location on the duct. The next step is to use the simplified image to define an "image factor" which can be more easily approximated by a polynomial expansion than the generalized image and from which the generalized image can be easily obtained. There are two possibilities for using the simplified image to remove the singular behavior of the generalized image. A function could be

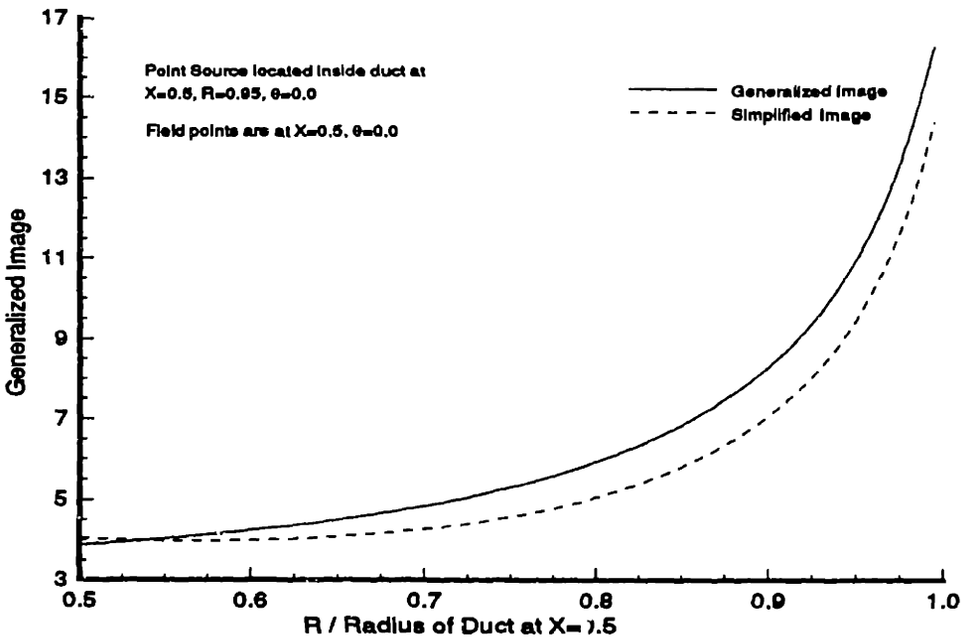

Figure 3-11: Comparison of the generalized image and the simplified image vs. r_i of the field point.

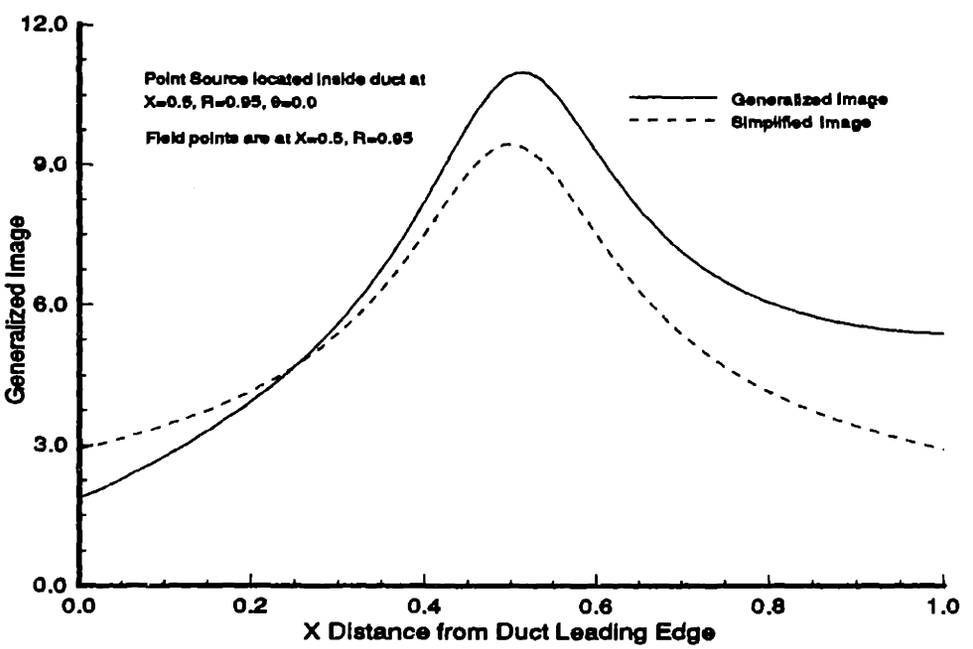

Figure 3-12: Comparison of the generalized image and the simplified image vs. x_i of the field point.

defined as either the difference between the generalized image and simplified image (the difference image factor) or as the ratio of the generalized and simplified images (the ratio image factor). Figures 3-13 through 3-15 show a comparison for these two possible image factors for the same source and field point arrangements examined by Figures 3-10 through 3-12. Figures 3-13 through 3-15seem to indicate that the image factor based on the ratio of the images is somewhat more effective at smoothing out the generalized image than is the image factor based on difference between the images. After a Chebyshev polynomial expansion was set up for both possible image factors, it was found that both possibilities require about the same number of terms in the expansion to adequately represent the generalized image. Although, the ratio image factor provides a smoother function for interpolation, it must be evaluated to a higher degree of accuracy than the difference image in order to achieve the same level of accuracy for the value of the generalized image.

Some small fluctuations appear near $\theta' = 0$ in the difference image factor shown in Figure 3-13. These can be attributed to the "saw-tooth" effect from the constant strength panels used on the duct. As will be discussed in Section 3.4.2, the points at which the image factor must be computed directly will be set up in such a way as to leave a gap of at least half the width of a panel between the duct and hub surfaces and the location of the source or field point in order to avoid discretization errors. When computing the image factors from the expansions, however, the image factor will be determined from extrapolation for points in this gap. Therefore, a trade off exists between the desire for the gap to be as small as possible to avoid errors from this extrapolation, and the need to have the gap large enough to avoid errors from discretization when using a reasonable number of panels to represent the duct and hub. Attempts to replace the constant strength dipole panels on the chordwise strips near the top of the duct with linear strength panels had little effect on narrowing the allowable size of this gap. These attempts applied linear strengths to these panels after the constant strength panel solution had been obtained. Perhaps better results could be obtained from a more complete higher order panel method. The small fluctuations seem to appear only in the circumferential direction. Note that Figures 3-13 through

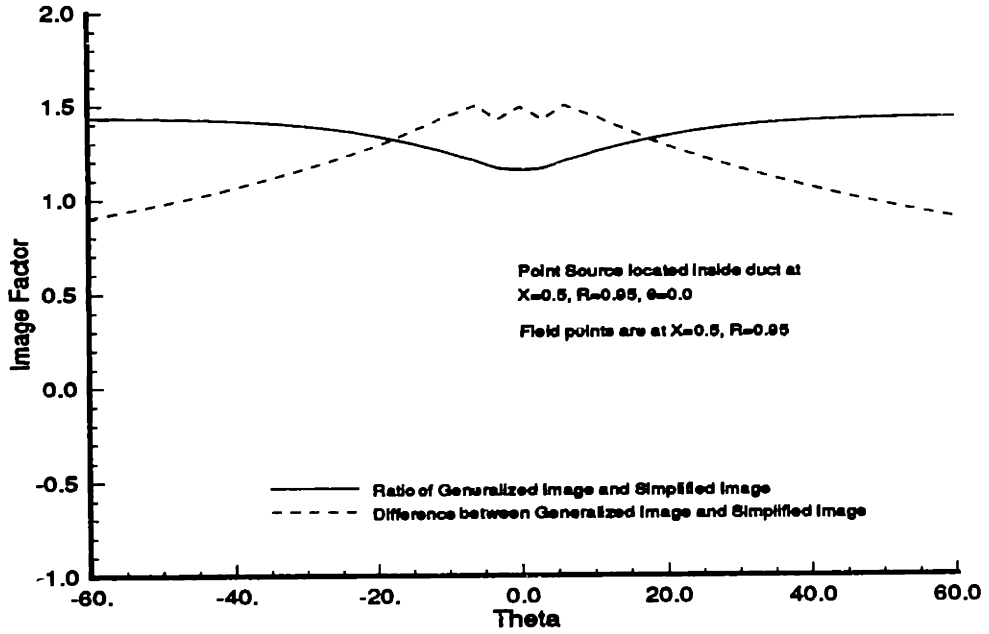

Figure 3-13: Comparison of the ratio and difference image factors vs. θ_i of the field point.

3-15 are for an extreme case, with both the source and the field points located about one-half a panel width from the duct inner surface. The panel discetization on the duct seems to have a much larger overall effect on the difference image factor than on the ratio image factor as shown by Figure 3-13.

The singularity is removed almost completely in the axial and radial directions. There is still, however, some variation in the image factor with respect to the relative angle between the source and field points, although it is still smoother than the generalized image itself. In this thesis, the ratio between the generalized image and the simplified image is used to define the image factor. Therefore, the image factor, $\mathcal{I}(\mathbf{x}, \boldsymbol{\xi})$, is defined as:

$$\mathcal{I}(\mathbf{x}, \boldsymbol{\xi}) = \frac{G_I(\mathbf{x}, \boldsymbol{\xi})}{G_{SI}(\mathbf{x}, \boldsymbol{\xi})} \tag{3.18}$$

The value of $\mathcal{I}(\mathbf{x}, \boldsymbol{\xi})$ will be computed directly for all possible combinations of the N_S source points and N_{FP} field points. The coefficients, defined by equation (3.8), which are used to modify the unbounded flow influence coefficients for a panel with a unit source distribution when solving for $\tilde{\phi}_{ij}$ on the propeller can be expressed as a

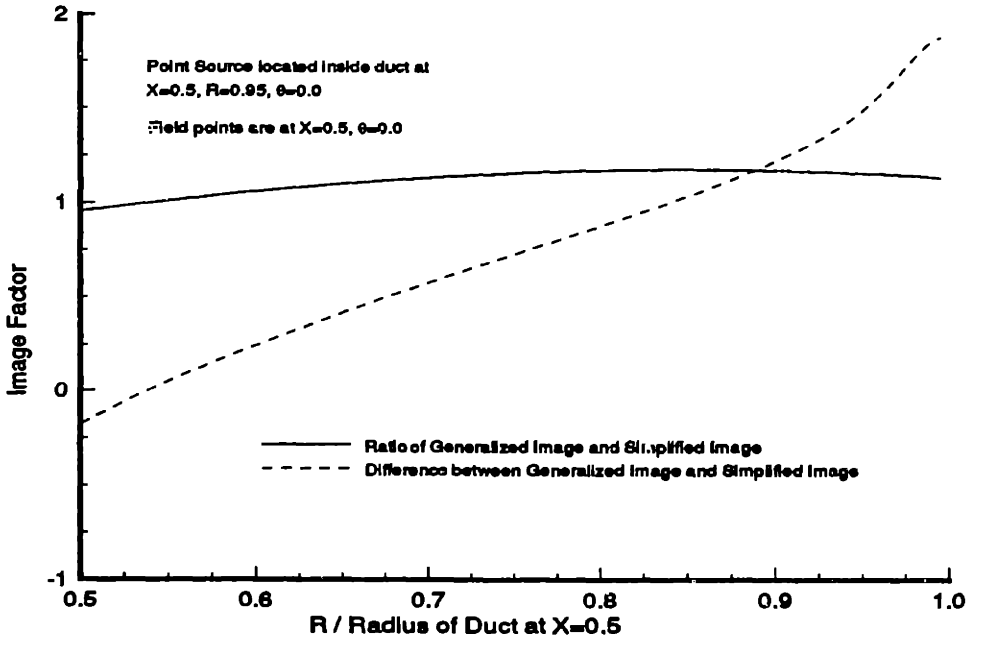

Figure 3-14: Comparison of the ratio and difference image factors vs. r_i of the field point.

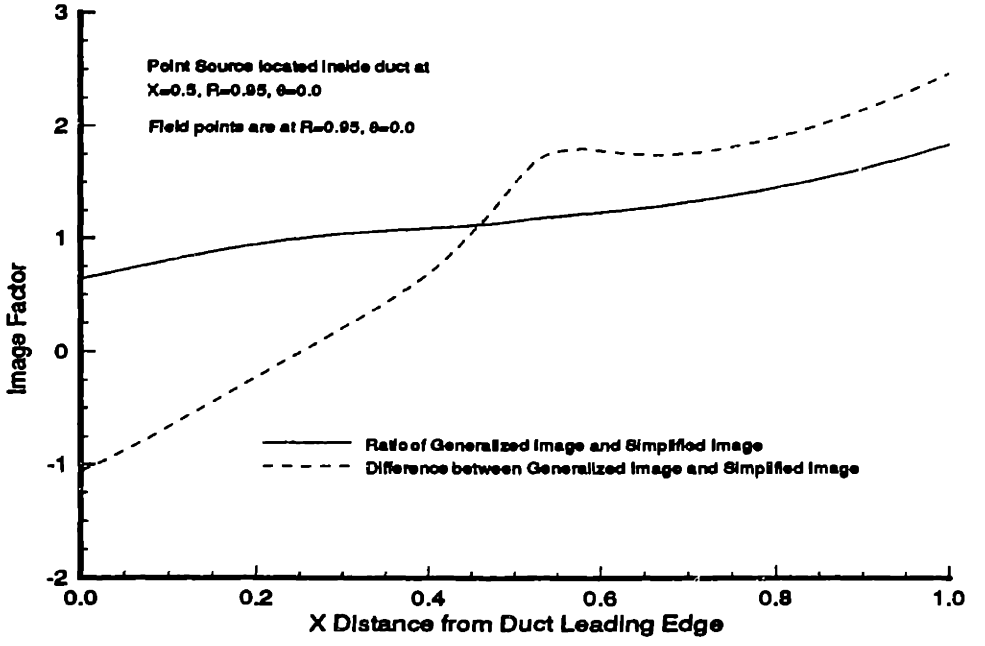

Figure 3-15: Comparison of the ratio and difference image factors vs. x_i of the field point.

function of the simplified image and the image factor.

$$\bar{b}_{ij} = \mathcal{I}(\mathbf{x}, \boldsymbol{\xi}) G_{SI}(\mathbf{x}, \boldsymbol{\xi}) \tag{3.19}$$

By substituting equation (3.19) into equation (3.8) and applying the chain rule appropriately to each term, the modification to the dipole influence coefficients which account for the presence of the duct and hub can also be expressed in terms of the simplified image and the image factor.

$$\begin{aligned} \bar{a}_{ij} &= \left[\left(\frac{\partial \mathcal{I}(\mathbf{x}_i, \boldsymbol{\xi}_j)}{\partial x_j} G_{SI}(\mathbf{x}_i, \boldsymbol{\xi}_j) + \frac{\partial G_{SI}(\mathbf{x}_i, \boldsymbol{\xi}_j)}{\partial x_j} \mathcal{I}(\mathbf{x}_i, \boldsymbol{\xi}_j) \right) \hat{i} \right. \\ &+ \left(\frac{\partial \mathcal{I}(\mathbf{x}_i, \boldsymbol{\xi}_j)}{\partial y_j} G_{SI}(\mathbf{x}_i, \boldsymbol{\xi}_j) + \frac{\partial G_{SI}(\mathbf{x}_i, \boldsymbol{\xi}_j)}{\partial y_j} \mathcal{I}(\mathbf{x}_i, \boldsymbol{\xi}_j) \right) \hat{j} \\ &+ \left. \left(\frac{\partial \mathcal{I}(\mathbf{x}_i, \boldsymbol{\xi}_j)}{\partial z_j} G_{SI}(\mathbf{x}_i, \boldsymbol{\xi}_j) + \frac{\partial G_{SI}(\mathbf{x}_i, \boldsymbol{\xi}_j)}{\partial z_j} \mathcal{I}(\mathbf{x}_i, \boldsymbol{\xi}_j) \right) \hat{k} \right] \cdot \hat{n}_j \end{aligned} \tag{3.20}$$

The derivatives of the simplified image can be expressed analytically. The image factor derivatives will be obtained from the differentiating the multivariate Chebyshev expansion for the image factor which is described in the next section.

3.4 Interpolation Scheme

The image factor of a point source with respect to the duct and hub at a specified field point can be expressed using a minimum of five variables. In this form, the image factor, $\mathcal{I}$, is expressed as shown below:

$$\mathcal{I}(\mathbf{x}_i, \boldsymbol{\xi}_j) \rightarrow \mathcal{I}(\theta', x_{fp}, r_{fp}, X_s, R_s) \tag{3.21}$$

where x_{fp} and r_{fp} are the axial and radial location of the field point, x_S and r_S are the axial and radial location of the source point, and θ' is the relative angle between the field and source points. Various methods are available from numerical analysis for approximating this function. The objectives of the interpolation scheme are to be computationally efficient, and able to produce both the value of the image factor as

well as the first derivative of the image factor with respect to each of the source point coordinates within acceptable accuracy. Since the image factor is continuous and smooth, it is reasonable to express this function in terms of a multivariate Chebyshev polynomial expansion, particularly for the approximation with respect to the axial and radial locations of both the source and field points. Chebyshev polynomials are generally the most efficient choice for a polynomial expansion of an arbitrary smooth and continuous function[3]. Expansions in terms of Chebyshev polynomials are commonly used in numerical analysis as an efficient means for approximating functions with near minimax accuracy or "equal-ripple" errors. They are particularly applicable to approximating a function, such as the image factor, where the greatest variation in the function occurs near the edges of the interpolation region. Multivariate Chebyshev polynomial expansions were used successfully by Newman [37] to accurately approximate the three-dimensional wave-resistance Green function (the potential induced from a point source traveling at a constant speed below a free surface) using a procedure similar to that which will be described here. In [37] a three variable Chebyshev polynomial expansion was utilized. In order to approximate the image factor, a five variable expansion will be required. The larger number of variables will increase the computational cost of the approximation, although it is still expected to be reasonably efficient and accurate.

The choice of the best approximation scheme for the image factor with respect to the relative angle, θ', between the source and field points is less obvious. It would appear that a Fourier cosine series could be used in this direction. This would take advantage of the fact that the image factor is even and periodic with respect to θ'. This was the method that was originally implemented. A FFT was used to obtain the coefficients of the Fourier series. Due to the sharp variation in the image factor near $\theta' = 0$, however, a large number of terms had to be retained in order for this series to adequately converge. In order to obtain a more compact series for the image factor, the interpolation region was subdivided into two separate regions with respect to θ'. One region covers the interval where $|\theta'| \leq \theta_{sub}$, where θ_{sub} is typically specified between 15° and 20°, and the other region covers the interval where $|\theta'| > \theta_{sub}$. This

subdivision is shown by Figure 3-17. In this way, a denser spacing of interpolation points can be used in the region where the sharpest variation in the image factor occurs. The image factor will then be expanded in terms of $\bar{\theta}$ which is defined as:

$$\bar{\theta} = \begin{cases} \theta_A = \theta' & \text{if } |\theta'| \leq \theta_{sub} \\ \theta_B = 180° - \theta' & \text{if } |\theta'| > \theta_{sub} \end{cases} \tag{3.22}$$

By defining $\bar{\theta}$ in this manner, the image factor will be symmetrical about $\theta_A = 0$ in the first region and symmetrical about $\theta_B = 0$ in the second region. The Chebyshev polynomial expansion can take advantage of this symmetry by using only the Chebyshev polynomials of even order. The resulting expansion for the image factor in a given region is shown below:

$$\mathcal{I}(\bar{\theta}, x_{fp}, r_{fp}, X_s, R_s) = \sum_{i=0}^{N_1}\sum_{j=0}^{N_2}\sum_{k=0}^{N_3}\sum_{l=0}^{N_4}\sum_{m=0}^{N_5} c_{ijklm} T_{2i}(\bar{\theta}) T_j^*(\xi_{fp}) T_k^*(\eta_{fp}) T_l^*(\xi_S) T_m^*(\eta_S), \tag{3.23}$$

where $T_m^*(x)$ is the m_{th} order shifted Chebyshev polynomial and $T_{2i}(x)$ is the $(2i)^{th}$ order Chebyshev polynomial of the first kind. These polynomials will be discussed in the next section. The normalized variables $\bar{\theta}$, ξ_{fp}, η_{fp}, ξ_S and η_S are functions of $\bar{\theta}$, x_{fp}, r_{fp}, X_s and R_s respectively, which are used to map the points in the duct coordinates system onto a square grid as will be described in Section 3.4.2. N_1, N_2, N_3, N_4 and N_5 refer to the number of terms retained in the expansion for each direction.

3.4.1 Chebyshev polynomial interpolation

The use of Chebyshev polynomials to approximate a function is very common, particularly for the case of single variable functions. Descriptions of this technique can be found in any basic numerical analysis textbook, and many books have been written specifically on this topic. A brief review of some of the important properties involved will be given here. A function $f(x)$ which is regular over the interval $-1 \leq x \leq 1$,

may be represented by a Chebyshev expansion in the form:

$$f(x) = \sum_{n=0}^{\infty} c_n T_n(x), \tag{3.24}$$

where $T_n(x)$ is the n^{th} order Chebyshev polynomial of the first kind. The coefficients, c_n, will converge exponentially to zero. The Chebyshev polynomials of the first kind are a family of orthogonal polynomials which are defined over the interval $-1 \leq x \leq 1$ by the formula:

$$T_n(x) = \cos(n \arccos x) \tag{3.25}$$

For the current application, it is convenient to use the shifted Chebyshev polynomials, $T_n^*(x)$ which are defined over the interval $0 \leq x \leq 1$, and are related to the Chebyshev polynomials of the first kind as follows:

$$T_n^*(x) = T_n(2x - 1) \tag{3.26}$$

The shifted Chebyshev polynomials are simply the Chebyshev polynomials of the first kind mapped onto the interval $0 \leq x \leq 1$, and they retain all of the useful properties of the Chebyshev polynomials of the first kind. If $f(x)$ is an even function, it is more efficient to form the expansion using only the even order Chebyshev polynomials, $T_{2n}(x)$, where

$$T_{2n}(x) = T_n^*(x^2). \tag{3.27}$$

The first several polynomials for both $T_n^*(x)$ and $T_{2n}(x)$, are shown in Table 3.1. The remainder of the Chebyshev polynomials can be obtained easily from the following recursion formula:

$$T_{n+1}^*(x) = 2(2x - 1)T_n^*(x) - T_{n-1}^*(x) \quad \text{for} \quad n > 1. \tag{3.28}$$

This recursion relation is very useful in evaluating the expansion as will be seen in Section 3.4.3.

The Chebyshev polynomials have many useful properties. One of the most impor-

$T_0^*(x) = 1$	$T_0(x) = 1$
$T_1^*(x) = 2x - 1$	$T_2(x) = 2x^2 - 1$
$T_2^*(x) = 8x^2 - 8x + 1$	$T_4(x) = 8x^4 - 8x^2 + 1$
$T_3^*(x) = 32x^3 - 48x^2 + 18^x - 1$	$T_6(x) = 32x^6 - 48x^4 + 18x^2 - 1$

Table 3.1: First four members of the shifted and second order Chebyshev polynomials.

tant is that their magnitude over the interval on which they are defined is bounded by 1:

$$|T_n^*(x)| \leq 1 \quad \text{for } 0 \leq x \leq 1 \tag{3.29}$$

In practice the series expansion shown in equation (3.24) will have to be truncated after the summation of a finite number of terms. The property specified in equation (3.29) means that the error resulting from this truncation will be bounded by the sum of the truncated coefficients. The Chebyshev polynomials also satisfy a discrete orthogonality relation which is useful in computing the coefficients for the expansion (see Section 3.4.2).

The use of Chebyshev polynomials is typically described for approximating a single real variable, but the extension to multiple variables is straightforward. A function $f(x, y)$ which is regular in the domain $0 \leq x \leq 1$, $0 \leq y \leq 1$ can be expressed in the form:

$$f(x, y) = \sum_{n=0}^{\infty} \sum_{m=0}^{\infty} c_{nm} T_m^*(y) T_n^*(x) \tag{3.30}$$

This can be thought of as a single variable Chebyshev expansion in x, where the Chebyshev coefficients are a function of y, which can themselves be expressed as an expansion of Chebyshev polynomials.

$$f(x, y) = \sum_{n=0}^{\infty} c_n'(y) T_n^*(x) \tag{3.31}$$

where:

$$c_n'(y) = \sum_{m=0}^{\infty} c_{nm} T_m^*(y) \tag{3.32}$$

As will be seen in Section 3.4.3, this way of looking at multivariate Chebyshev poly-

nomials is particularly useful when applying these expansions to the image factor.

3.4.2 Computation of Chebyshev polynomial coefficients

The domain in which the image factor must be computed will be divided into three regions. A separate multivariate Chebyshev polynomial expansion will then be set up for evaluating the image factor in each of these regions. Each of these expansions will be in the form of equation (3.23); however, a different set of coefficients will be required to define the generalized image in each region. The Chebyshev coefficients corresponding to each region can be determined from the values of the image factor which are calculated directly by using the discrete orthogonality relation. In order to do this, the image factor must be computed directly at a specific set of points. The selection of these points for each region will first be discussed, and then the method for computing the coefficients will be developed.

When calculating the modifications to the propeller influence coefficients needed to solve equation (3.4), the coefficients $\bar{a}_{ij}$ and $\bar{b}_{ij}$ must be obtained for various combinations of panels. These coefficients correspond to the modification to the influence of a point source or dipole placed at the centroid of panel j at the control point of panel i to account for the presence of the duct and hub. The panels on which the source and dipoles are placed, the panel j's, consist of both the panels on the blade surfaces and the blade wake surfaces. The panels at which the influence of these sources and dipoles is computed, however, consists only of the panels on the blade surfaces and do not include the wake panels. Therefore, the domain for which the image factor must be computed with respect to the location of the field points, x_{fp} and r_{fp}, need only cover the region inside of the duct in which blades may be located. For the case demonstrated here, this region extends from the duct trailing edge, located at $x = X_{TE}$, forward to some axial location X_1, in front of which no stator or propeller blades will be located. To allow the same set of coefficients to be applied to many different propeller and stator geometries during a design procedure, this region should be made large enough to include all conceivable configurations of propeller and stator blades. With respect to the relative angular position between the source and field

points, θ', this region is split at $\theta' = \theta_{sub}$ into two subregions in order to concentrate more interpolating points near $\theta' = 0$ as specified by equation (3.22). The domain for the source points, X_S and R_S, must cover the possible panel locations for both the blade surface and wake panels. This domain is also split into two subregions. One region covers the same volume inside the duct specified by the field point domain. The second region covers the volume aft of the duct trailing edge in which there are no blade surfaces, but in which panels representing the blade wakes will exist. It must be decided *a priori* at what point downstream the propeller wake will be truncated. The second region will extend downstream to this point ($x = X_W$). The field points domain will be subdivided with respect to θ' only for the case corresponding to the source point region inside of the duct. This results in total of three five-dimensional regions in which the expansion of the image factor will be defined. These regions are shown schematically in Figures 3-16 and 3-17. The resulting three regions are listed below:

Region A: Both the source points and field points are located inside of the duct, and the relative angle between the source and field points is less than θ_{sub}.

$$\begin{aligned} X_1 \leq x_{fp} &\leq X_{TE} \\ r_H(x_{fp}) + g \leq r_{fp} &\leq r_D(x_{fp}) - g \\ X_1 \leq X_S &\leq X_{TE} \\ r_H(X_S) + g \leq R_S &\leq r_D(X_S) - g \\ -\theta_{sub} \leq \theta' &\leq \theta_{sub} \end{aligned} \tag{3.33}$$

Region B: Both the source points and field points are located inside of the duct, and the relative angle between the source and field points is greater than θ_{sub}.

$$\begin{aligned} X_1 \leq x_{fp} &\leq X_{TE} \\ r_H(x_{fp}) + g \leq r_{fp} &\leq r_D(x_{fp}) - g \\ X_1 \leq X_S &\leq X_{TE} \end{aligned}$$

$$r_H(X_S) + g \leq R_S \leq r_D(X_S) - g$$
$$\theta_{sub} \leq \theta' \leq 360° - \theta_{sub} \tag{3.34}$$

Region W: The source point is located aft of the duct trailing edge, and field point is located inside of the duct.

$$X_1 \leq x_{fp} \leq X_{TE}$$
$$r_H(x_{fp}) + g \leq r_{fp} \leq r_D(x_{fp}) - g$$
$$X_{TE} \leq X_S \leq X_W$$
$$r_H(X_S) + g \leq R_S \leq R_{DWAKE} - g$$
$$-180° \leq \theta' \leq 180° \tag{3.35}$$

In the above equations, $r_H(x)$ is the local radius of the hub or hub vortex, $r_D(x)$ is the local radius of the duct inner surface, R_{DWAKE} is the radius of the duct wake, and g is the thickness of the thin gap layer between the interpolation region and the surface of the duct or hub. It is not possible to compute the solution on the duct and hub for the case where a source is located directly on the duct or hub surface using the procedure described in Section 3.3.1. Therefore, it is not possible to compute the image factor directly for points on the surface of the duct and hub. For this reason, the interpolation regions are cut off short of these surfaces, leaving a thin layer of thickness g, which is set to be about 1-2% of the propeller radius, between the interpolation region and the duct and hub surfaces. If values of the image factor are required in this layer when computing the modified influence coefficients, they will be obtained by extrapolation of the values inside the interpolation region. Although there is no guarantee as to the bounds on the error for these extrapolated values, they should be acceptable since the layer is thin and the image factor approaches a constant smoothly as the source approaches the duct, as shown in Fig. 3-14.

The shifted Chebyshev polynomials, $T_n^*(x)$ are defined over the interval [0,1], and the Chebyshev polynomials of the first kind are defined over the interval [-1,1]. There-

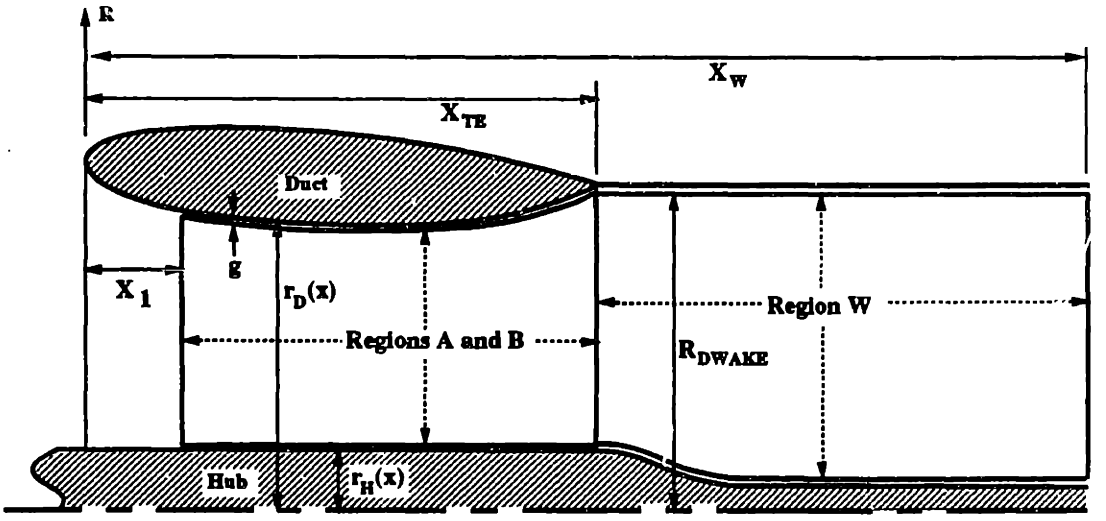

Figure 3-16: Description of the source point locations for the three interpolation regions. For Regions A and B, the field point is located in the same axial interval as the source. For Region W, the source is located in the area indicated but the field point is located inside the duct.

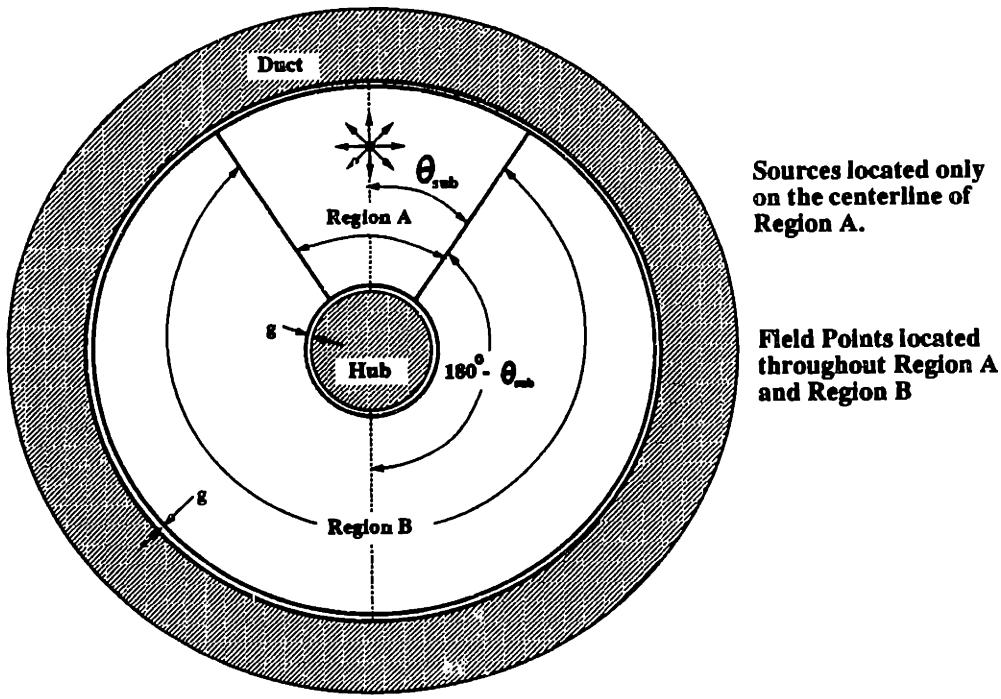

Figure 3-17: Description of the angular position for the field points in Regions A and B. The image factor is defined with respect to the relative distance between the field point and a source placed at $\theta = 0$.

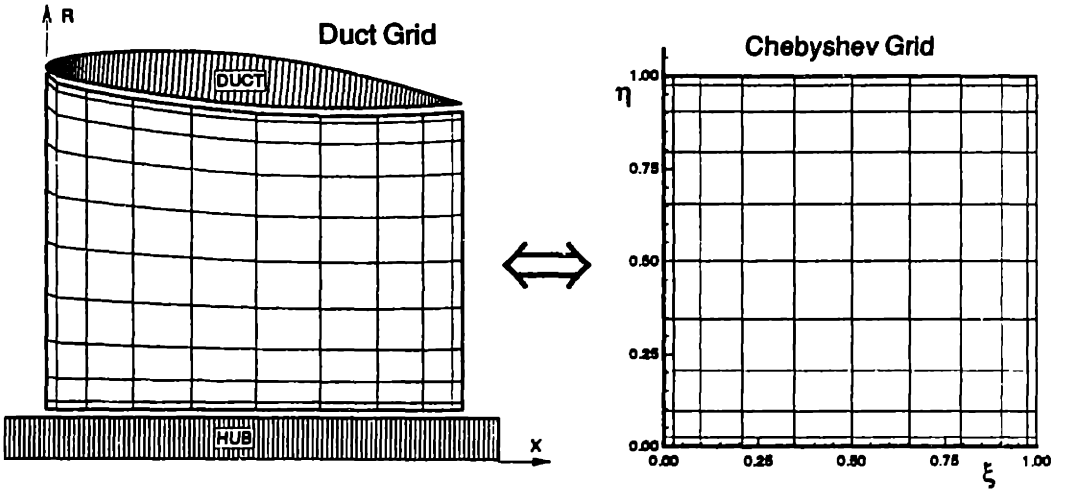

Figure 3-18: The mapping relationship for between the axial and radial location of a source or field point and a point on the rectangular grid used for the Chebyshev polynomial interpolation.

fore, the source and field point locations in each region as specified by equations (3.33) through (3.35) must be mapped onto the appropriate intervals. This will be done by mapping each point in the five-dimensional domain specified by $(\theta', x_{fp}, r_{fp}, X_S, R_S)$ to a point in the five-dimensional rectangular domain specified by $(\tilde{\theta}, \xi_{fp}, \eta_{fp}, \xi_S, \eta_S)$, where ξ_{fp}, η_{fp}, ξ_S and η_S vary from 0 to 1, and $\tilde{\theta}$ varies from -1 to 1. This mapping is shown schematically in Figure 3-18 for the axial and radial directions inside the duct. The appropriate mapping relations for each variable are given below:

$$\xi_{fp}(x_{fp}) = \frac{x_{fp} - X_1}{X_{TE} - X_1} \tag{3.36}$$

$$\eta_{fp}(x_{fp}, r_{fp}) = \frac{r_{fp} - [r_H(x_{fp}) + g]}{[r_D(x_{fp}) - g] - [r_H(x_{fp}) + g]} \tag{3.37}$$

$$\xi_S(X_S) = \begin{cases} \frac{X_S - X_1}{X_{TE} - X_1} & \text{for } X_S \leq X_{TE} \\ \frac{X_S - X_{TE}}{X_W - X_{TE}} & \text{for } X_S > X_{TE} \end{cases} \tag{3.38}$$

$$\eta_S(X_S, R_S) = \begin{cases} \frac{R_S - [r_H(X_S)+g]}{[r_D(X_S)-g]-[r_H(X_S)+g]} & \text{for } X_S \leq X_{TE} \\ \frac{R_S - [r_H(X_S)+g]}{[R_{DWAKE}-g]-[r_H(X_S)+g]} & \text{for } X_S > X_{TE} \end{cases} \tag{3.39}$$

$$\tilde{\theta}(\theta') = \begin{cases} \frac{\theta'}{\theta_{sub}} & \text{for } X_S \leq X_{TE};\ |\theta'| \leq \theta_{sub} \\ \frac{\pi - \theta'}{\pi - \theta_{sub}} & \text{for } X_S \leq X_{TE};\ |\theta'| > \theta_{sub} \\ \frac{\theta'}{\pi} & \text{for } X_S > X_{TE} \end{cases} \tag{3.40}$$

For each of the three regions, a separate set of Chebyshev coefficients c^A_{ijklm}, c^B_{ijklm} and c^W_{ijklm}, must be computed. In order to compute the coefficients for a given region, the image factor must be computed directly at a specific grid of points using the procedure described in Section 3.3. In terms of the normalized coordinates, the required locations in each direction are shown below:

$$\tilde{\theta}^i = \cos\left(\frac{i\pi}{2N_1}\right) \quad \text{for } i = 0, N_1 \tag{3.41}$$

$$\xi^j_{fp} = \frac{1}{2}\left(\cos(\frac{j\pi}{N_2}) + 1\right) \quad \text{for } j = 0, N_2 \tag{3.42}$$

$$\eta^k_{fp} = \frac{1}{2}\left(\cos(\frac{k\pi}{N_3}) + 1\right) \quad \text{for } k = 0, N_3 \tag{3.43}$$

$$\xi^l_S = \frac{1}{2}\left(\cos(\frac{l\pi}{N_4}) + 1\right) \quad \text{for } l = 0, N_4 \tag{3.44}$$

$$\eta^m_S = \frac{1}{2}\left(\cos(\frac{m\pi}{N_5}) + 1\right) \quad \text{for } m = 0, N_5 \tag{3.45}$$

where, $(N_1 + 1)$, $(N_2 + 1)$, $(N_3 + 1)$, $(N_4 + 1)$ and $(N_5 + 1)$ are the number of points which are used to represent the image factor with respect to θ', x_{fp}, r_{fp}, X_S and R_S respectively. These values must be decided upon before the coefficients are computed. An examination of the resulting coefficients will indicate whether these values are adequate, as will be shown shortly. For the case examined in this chapter, values of $N_1 = 16$, $N_2 = N_4 = 10$ and $N_3 = N_5 = 12$ were used for all three regions. The image factor must be obtained directly for all possible combinations of

the five normalized variables in each region. Therefore, the total number of image factor values, $\mathcal{I}(\tilde{\theta}, \xi_{fp}, \eta_{fp}, \xi_S, \eta_S)$, required to compute the coefficients for a given region will be $[(N_1+1)\times(N_2+1)\times(N_3+1)\times(N_4+1)\times(N_5+1)]$, which is equal to 347,633 for the case examined here. The required positions for the sources and field points in the duct coordinate system can be obtained from equations (3.36)-(3.40).

The values of the image factor with respect to the relative angle between the source and field points, θ', will be obtained by solving directly for the image factor for a source located at $\theta = 0$ and a field point located at $\theta = \theta'$. Therefore the total number of source point locations used to represent each region will be $[(N_4+1)\times(N_5+1)]$, and the total number of field points in each region at which the image factor will be computed will be $[(N_1+1)\times(N_2+1)\times(N_3+1)]$. The directly computed values of the image factor, $\mathcal{I}(\tilde{\theta}^i, \xi^j_{fp}, \eta^k_{fp}, \xi^l_S, \eta^m_S)$, are obtained by first inverting the system of equations (3.15) to obtain the potential on the surface of the duct and hub in the presence of a point source at a location corresponding to (ξ^l_S, η^m_S), and then computing the image factors using equations (3.16) and (3.18) at a field point corresponding to $(\tilde{\theta}^i, \xi^j_{fp}, \eta^k_{fp})$. The source point locations will be identical for Regions A and B so that the image factor may be computed at the field points for both of these regions using the same duct/hub solution for each source. Therefore, the total number of times which the boundary value problem of the duct and hub in the presence of a point source must be solved to compute the coefficients for all three regions is equal to $N_S = 2\times[(N_4+1)\times(N_5+1)]$, which is equal to 286 for the case demonstrated here. A different set of image factors, $\mathcal{I}^A(\tilde{\theta}^i, \xi^j_{fp}, \eta^k_{fp}, \xi^l_S, \eta^m_S)$, $\mathcal{I}^B(\tilde{\theta}^i, \xi^j_{fp}, \eta^k_{fp}, \xi^l_S, \eta^m_S)$ and $\mathcal{I}^W(\tilde{\theta}^i, \xi^j_{fp}, \eta^k_{fp}, \xi^l_S, \eta^m_S)$, will directly computed to obtain the coefficients in the three regions, c^A_{ijklm}, c^B_{ijklm} and c^W_{ijklm} respectively.

After the directly computed image factors are obtained at the specified grid points in each region, the coefficients corresponding to each region can be computed using the discrete orthogonality relation of Chebyshev polynomials. This process is described in detail by Fox and Parker [8]. For the case of a single variable defined on the interval $[-1, 1]$, the coefficients for the expansion shown in equation (3.24) can be obtained

from the following expression:

$$c_m = \frac{\epsilon_m}{N} \sum_{n=0}^{N}{}'' f(x_n) T_m(x_n), \tag{3.46}$$

where $\epsilon_0 = 1$, and $\epsilon_m = 2$ for $m > 0$. The double prime indicates that the first and last terms in the summation are divided in half. The points x_n, are similar to the required locations specified by equations (3.41) through (3.45), and in this case are specified as:

$$x_n = \cos\left(\frac{n\pi}{N}\right). \tag{3.47}$$

The values of the Chebyshev polynomials can be determined from equation (3.25) to be

$$T_m(x_n) = cos\left(\frac{nm\pi}{N}\right) \tag{3.48}$$

The expansion for the image factor will be in terms of five variables and utilize a combination of both shifted and even order Chebyshev polynomials. When the method described above is extended to this case, the formula for determining the coefficients is as follows:

$$\begin{aligned} c_{ijklm} = \quad & \frac{\epsilon_i}{2N_1}\frac{\epsilon_j}{N_2}\frac{\epsilon_k}{N_3}\frac{\epsilon_l}{N_4}\frac{\epsilon_m}{N_5} \sum_{I=0}^{N_1}{}'' \sum_{J=0}^{N_2}{}'' \sum_{K=0}^{N_3}{}'' \sum_{L=0}^{N_4}{}'' \sum_{M=0}^{N_5}{}'' \\ & T_{2i}(\tilde{\theta}^I) T_j^*(\xi_{fp}^J) T_k^*(\eta_{fp}^K) T_l^*(\xi_S^L) T_m^*(\eta_S^M) \mathcal{I}(\tilde{\theta}^I, \xi_{fp}^J, \eta_{fp}^K, \xi_S^L, \eta_S^M) \end{aligned} \tag{3.49}$$

The values of the Chebyshev polynomials in this expression can be obtained by substituting equations (3.26) and (3.27) into equation (3.25). The resulting values are:

$$\begin{aligned} T_{2i}(\tilde{\theta}^I) = \cos\left(\frac{iI\pi}{N_1}\right) \quad T_j^*(\xi_{fp}^J) = \cos\left(\frac{jJ\pi}{N_2}\right) \quad T_k^*(\eta_{fp}^K) = \cos\left(\frac{kK\pi}{N_3}\right) \\ T_l^*(\xi_S^L) = \cos\left(\frac{lL\pi}{N_4}\right) \quad T_m^*(\eta_S^M) = \cos\left(\frac{mM\pi}{N_5}\right). \end{aligned} \tag{3.50}$$

Equation (3.49) will have to be evaluated $[(N_1 + 1)(N_2 + 1)(N_3 + 1)(N_4 + 1)(N_5 + 1)]$ times to obtain the entire set of coefficients for a given region. This process will

consist of ten nested loops, and will have to be performed three times to obtain the coefficients for all three regions, c^A_{ijklm}, c^B_{ijklm} and c^W_{ijklm}. These computations required over twelve hours on a VAX-9000 for the case demonstrated in this chapter. However, these calculations are well suited for vectorization. In addition, once the coefficients for a given duct and hub geometry are obtained, they may be used for any propeller and stator blade geometries and any inflow condition in connection with the given duct and hub.

The resulting Chebyshev polynomial expansions will agree exactly at the representative points at which the image factor was computed directly. In order for the expansion to be accurate throughout the interpolation region, the values of N_1, N_2, N_3, N_4 and N_5 must be large enough to allow the coefficients, c_{ijklm} to converge sufficiently to zero in each direction [37]. The coefficients must be examined to ensure that the coefficients at the edge of each interval are below the desired tolerance.

$$\begin{aligned}
c_{N_1jklm} &< \delta \quad \text{for all } j,k,l,m \\
c_{iN_2klm} &< \delta \quad \text{for all } i,k,l,m \\
c_{ijN_3lm} &< \delta \quad \text{for all } i,j,l,m \\
c_{ijkN_4m} &< \delta \quad \text{for all } i,j,k,m \\
c_{ijklN_5} &< \delta \quad \text{for all } i,j,k,l
\end{aligned} \tag{3.51}$$

The value of the tolerance δ was specified as 1×10^{-5} for the cases studied for this thesis. If one of the conditions specified by equation (3.51) is not met, either the value for N which corresponds to that direction has to be increased or the domain must be further subdivided. It was this condition, which resulted in the region for the field points inside the duct being subdivided with respect to θ'. In general, the most efficient arrangement is a compromise between having many subregions with a smaller number of coefficients required to represent each subregion, and modeling the entire domain with a single expansion using a much larger number of coefficients. A more complete discussion on the error which results using a finite number of terms in the expansion is provided in [8].

3.4.3 Efficient evaluation of image factor expansions

In this section, the method is discussed for obtaining the image factors and its derivatives for arbitrary source and field locations from the Chebyshev polynomial expansions. This is required for computing the coefficients, $\bar{b}_{ij}$ and $\bar{a}_{ij}$, as specified by equations (3.19) and (3.20). For the general case of the image factor, $\mathcal{I}(\mathbf{x}_i, \boldsymbol{\xi}_j)$, corresponding to the modification to the influence of a point source placed at the centroid of panel j, $\boldsymbol{\xi}_j = (X_S, R_S, \theta_S)$, at the control point of panel i, $\mathbf{x}_i = (x_{fp}, r_{fp}, \theta_{fp})$, the following quintuple summation must be evaluated:

$$\mathcal{I}(\theta', x_{fp}, r_{fp}, X_S, R_S) = \sum_{i=0}^{N_1}\sum_{j=0}^{N_2}\sum_{k=0}^{N_3}\sum_{l=0}^{N_4}\sum_{m=0}^{N_5} c_{ijklm} T_{2i}(\tilde{\theta}) T_j^*(\xi_{fp}) T_k^*(\eta_{fp}) T_l^*(\xi_S) T_m^*(\eta_S) \tag{3.52}$$

where $\tilde{\theta}$, ξ_{fp}, η_{fp}, ξ_S and η_S are the normalized forms of θ', x_{fp}, r_{fp}, X_S and X_S respectively, as specified by equations (3.36) through (3.40), and $\theta' = \theta_{fp} - \theta_S$. In order to avoid confusion with the subscripts used for the Chebyshev coefficients, the subscripts fp and S are used to refer to the points on panels i and j respectively in this section. The coefficients, c_{ijklm}, correspond to the set of coefficients computed by the method developed in Section 3.4.2 for the region containing the source and field point locations of interest.

The most efficient method of evaluating this summation is by taking advantage of the recursion relation specified by equation (3.28). Both the image factor and its derivatives can then be evaluated by backwards recursion. For clarity, this will first be demonstrated for the case of a single variable function expanded using a series of Chebyshev polynomials. For the single variable case, more complete details on the methods presented here can be found in [8] and [31]. Consider a function, $f(x)$, defined in terms of a finite series of shifted Chebyshev polynomials:

$$f(x) = \sum_{n=0}^{N} c_n T_n^*(x) \quad 0 \le x \le 1 \tag{3.53}$$

To evaluate $f(x)$ by backwards recursion it is first necessary to define an array $b_n(x)$

where:

$$\begin{aligned} b_{N+2} &= b_{N+1} = 0 \\ b_n &= (4x-2)b_{n+1} - b_{n+2} + c_n \end{aligned} \tag{3.54}$$

For a given value of x, the values of b_n are obtained by first computing b_N, and then stepping down until b_0 is obtained. The value of the function may then be expressed as:

$$f(x) = b_0 - (2x-1)b_1 \tag{3.55}$$

For a function, $g(x)$, defined in terms of even order Chebyshev polynomials,

$$g(x) = \sum_{n=0}^{N} a_n T_{2n}(x) \qquad -1 \leq x \leq 1, \tag{3.56}$$

the procedure is the same, except that the expression for $b_n(x)$ is now,

$$b_n = (4x^2-2)b_{n+1} - b_{n+2} + a_n, \tag{3.57}$$

and the value of $g(x)$ is expressed as:

$$g(x) = b_0 - (2x^2-2)b_1. \tag{3.58}$$

The derivatives of equation (3.53) can be obtained by recursively modifying the coefficients, c_n. In this manner, $\frac{df(x)}{dx}$, is evaluated using the same procedure used to evaluate $f(x)$, except that the coefficients c_n will be replaced by a new set of coefficients, d_n, which are defined as:

$$\begin{aligned} d_N &= d_{N+1} = 0 \\ d_{n-1} &= d_{n+1} + 4nc_n \quad (n = N, N-1, ..., 2) \\ d_0 &= 2c_n + \frac{1}{2}d_2. \end{aligned} \tag{3.59}$$

A slightly different method is used for finding the derivative of $g(x)$. A separate

array $b'_n(x)$ is defined, which is computed along with the $b_n(x)$ array when evaluating the function. $b'_n(x)$ is defined by:

$$\begin{aligned} b'_N &= b'_{N+1} = 0 \\ b'_n &= (4x^2 - 2)b'_{n+1} - b'_{n+2} - 8xb_{n+1}. \end{aligned} \tag{3.60}$$

The derivative of $g(x)$ is then expressed as:

$$\frac{\mathrm{d}g(x)}{\mathrm{d}x} = -4xb_1 - b'_0 + (2x^2 - 1)b'_1. \tag{3.61}$$

The extension to five dimensions is easily understood by evaluating the summation with respect to one variable at a time. In this way, equation (3.52) for a given source and field point location breaks down into five nested single variable summations. In this case, the summation will first be evaluated with respect to the radial position of the source, R_S:

$$c^R_{ijkl}(R_S) = \sum_{i=0}^{N_1}\sum_{j=0}^{N_2}\sum_{k=0}^{N_3}\sum_{l=0}^{N_4}\sum_{m=0}^{N_5} c_{ijklm}T^*_m(\eta_S) \tag{3.62}$$

Then with respect to X_S

$$c^X_{ijk}(X_S, R_S) = \sum_{i=0}^{N_1}\sum_{j=0}^{N_2}\sum_{k=0}^{N_3}\sum_{l=0}^{N_4} c^R_{ijkl}(R_S)T^*_l(\xi_S). \tag{3.63}$$

Then with respect to r_{fp},

$$c^r_{ij}(r_{fp}, X_S, R_S) = \sum_{i=0}^{N_1}\sum_{j=0}^{N_2}\sum_{k=0}^{N_3} c^X_{ijk}(X_S, R_S)T^*_k(\eta_{fp}). \tag{3.64}$$

Similarly with respect to x_{fp},

$$c^x_i(x_{fp}, r_{fp}, X_S, R_S) = \sum_{i=0}^{N_1}\sum_{j=0}^{N_2} c^r_{ij}(r_{fp}, X_S, R_S)T^*_j(\xi_{fp}). \tag{3.65}$$

Finally, the image factor is evaluated from the one dimensional expansion in terms of

θ' as shown below:

$$\mathcal{I}(\theta', x_{fp}, r_{fp}, X_S, R_S) = \sum_{i=0}^{N_1} c_i^x(x_{fp}, r_{fp}, X_S, R_S) T_{2i}(\tilde{\theta}). \tag{3.66}$$

The innermost summation in each of the previous equations will be evaluated using the backwards recursion method described by equations (3.54) through (3.58). Equations (3.62) through (3.65) can be evaluated together in a nested manner as shown below:

$$\mathcal{I}(\theta', x_{fp}, r_{fp}, X_S, R_S) =$$
$$\sum_{i=0}^{N_1} T_{2i}(\tilde{\theta}) \left[\sum_{j=0}^{N_2} T_j^*(\xi_{fp}) \left\{ \sum_{k=0}^{N_3} T_k^*(\eta_{fp}) \left(\sum_{l=0}^{N_4} T_l^*(\xi_S) \left\langle \sum_{m=0}^{N_5} c_{ijklm} T_m^*(\eta_S) \right\rangle \right) \right\} \right]. \tag{3.67}$$

The partial derivatives of the image factor with respect to the normalized source locations, ξ_S and η_S, can be evaluated by first determining two new sets of coefficients for each region using equation (3.59). The partial derivatives are then evaluated in the same manner as described above, but using the "differentiated" coefficients. The partial derivative with respect to $\tilde{\theta}$ is evaluated during the last summation, equation (3.65), using the method described by equations (3.60) and (3.61). In order to obtain the partial derivatives with respect to the non-normalized variables, the chain rule is applied as follows:

$$\frac{\partial \mathcal{I}}{\partial X_S} = \frac{\partial \mathcal{I}}{\partial \xi_S} \frac{\partial \xi_S}{\partial X_S} + \frac{\partial \mathcal{I}}{\partial \eta_S} \frac{\partial \eta_S}{\partial X_S} \tag{3.68}$$

$$\frac{\partial \mathcal{I}}{\partial R_S} = \frac{\partial \mathcal{I}}{\partial \eta_S} \frac{\partial \eta_S}{\partial R_S} \tag{3.69}$$

$$\frac{\partial \mathcal{I}}{\partial \theta'} = \frac{\partial \mathcal{I}}{\partial \tilde{\theta}} \frac{\partial \tilde{\theta}}{\partial \theta'} \tag{3.70}$$

The partial derivatives with respect to the cartesian coordinates of the source, $\boldsymbol{\xi}_j = (x_j, y_j, z_j)$, can then be obtained as follows:

$$\frac{\partial \mathcal{I}}{\partial x_j} = \frac{\partial \mathcal{I}}{\partial X_S} \tag{3.71}$$

$$\frac{\partial \mathcal{I}}{\partial y_j} = \frac{\partial \mathcal{I}}{\partial R_S}\cos(\theta_j) + R_S\frac{\partial \mathcal{I}}{\partial \theta'}\sin(\theta_j) \tag{3.72}$$

$$\frac{\partial \mathcal{I}}{\partial z_j} = \frac{\partial \mathcal{I}}{\partial R_S}\sin(\theta_j) - R_S\frac{\partial \mathcal{I}}{\partial \theta'}\cos(\theta_j) \tag{3.73}$$

The value of the image factor, $\mathcal{I}(\mathbf{x}_i, \boldsymbol{\xi}_j)$ is then substituted into equation (3.19) to obtain the modifications to the source influence coefficients, $\bar{b}_{ij}$, used when obtaining the propeller solution. Both the image factor and its partial derivatives, $\frac{\partial \mathcal{I}}{\partial x_j}$, $\frac{\partial \mathcal{I}}{\partial y_j}$ and $\frac{\partial \mathcal{I}}{\partial z_j}$, are substituted into equation (3.20) in order to obtain the modifications to the dipole influence coefficients, $\bar{a}_{ij}$.

The image factor must be computed for a source on every blade and blade wake panel at the control point of every blade panel. Therefore, for a single component case with N_B blades, N_P panels on the key blade and N_W panels in the key blade wake, equation (3.67) will have to be evaluated $(N_P \times N_B \times (N_P + N_W))$ times. This process can be made more efficient by solving for the image factors at the control points on all of the blade panels for a source on a single blade or blade wake panel, and proceeding one source panel at a time. In this manner, the quintuple summation in equation (3.67) can be broken down into a triple summation for each source location. This works as follows: For each blade and blade wake panel, a three dimensional set of coefficients is defined by:

$$c'_{ijk}(\xi_S, \eta_S) = \sum_{i=0}^{N_1}\sum_{j=0}^{N_2}\sum_{k=0}^{N_3}\sum_{l=0}^{N_4}\sum_{m=0}^{N_5} c_{ijklm}T^*_l(\xi_S)T^*_m(\eta_S), \tag{3.74}$$

where ξ_S and η_S are the normalized radius and axial location of the panel. These coefficients are then used to compute the image factor for a source on that panel, at the control points of all the other panels as follows:

$$\mathcal{I}(\tilde{\theta}, \xi_{fp}, \eta_{fp}, \xi_S, \eta_S) = \sum_{i=0}^{N_1}\sum_{j=0}^{N_2}\sum_{k=0}^{N_3} c'_{ijk}(\xi_S, \eta_S)T^*_{2i}(\tilde{\theta})T^*_j(\xi_{fp})T^*_k(\eta_{fp}) \tag{3.75}$$

where ξ_{fp} and η_{fp} are the normalized axial and radial location of the control point, and $\tilde{\theta}$ is the normalized relative angle between the two panels. In this way, the quintuple summation shown in equation (3.74) only has to be evaluated $(N_P + N_W)$

times, and only the triple summation shown in equation (3.75) must be evaluated $(N_P \times N_B \times (N_P + N_W))$ times.

For a multi-component propulsor, the influence coefficients corresponding to the influence of the propeller on the stators and the stators on the propeller will be time dependent, due to the relative motion between these two components. The image factors corresponding to these coefficients will, therefore, also change with each timestep. However, for each coefficient only the relative angle between the two panels involved, θ', will change with time, and the radial and axial locations will remain constant for both the source and field points. It is more efficient, therefore, to obtain the values for these image factors for all timesteps at the same time. This is done by further breaking down equation (3.75) for every combination of panels by defining a one dimensional set of coefficients, c_i'', which are defined as follows for each combination of panels:

$$c_i''(\xi_{fp}, \eta_{fp}, \xi_S, \eta_S) = \sum_{i=0}^{N_1} \sum_{j=0}^{N_2} \sum_{k=0}^{N_3} c'_{ijk}(\xi_S, \eta_S) T_j^*(\xi_{fp}) T_k^*(\eta_{fp}) \tag{3.76}$$

The image factor at timestep n, can then be evaluated using the following one dimensional expansion:

$$\mathcal{I}(\theta'(n), x_{fp}, r_{fp}, X_S, R_S) = \sum_{i=0}^{N_1} c_i''(\xi_{fp}, \eta_{fp}, \xi_S, \eta_S) T_{2i}\left(\tilde{\theta}(n)\right). \tag{3.77}$$

There is a tradeoff between the computational efficiency and the amount of disk storage required, however, in that by computing the the propeller on stator influence coefficients and the stator on propeller influence coefficients using equations (3.76) and (3.77), these coefficients must be computed for all timesteps before the time-marching begins. Therefore, a large amount of disk memory is required to store all of the time dependent coefficients.

3.4.4 Validation of generalized image interpolation

In order to test the effectiveness of the generalized image interpolation, comparisons were made between the values of the generalized images calculated directly, using the procedure described in Section 3.3.1, and those obtained using the interpolation procedure described in the previous section. These tests were performed for the generalized images corresponding to both point sources and point dipoles. Tests were performed for a large variety of source, dipole, and field locations, and only a sampling of these results are shown here. The arrangement of source and field point locations is the same as those used to examine the generalized image in Section 3.3.1 and is shown in Figure 3-5. In the cases shown here, the point source or point dipole is located at $\boldsymbol{\xi} = (X_S = 0.5, R_S = 0.85, \theta_S = 0.0)$, and the field points are located at $\mathbf{x} = (x_{fp} = 0.5, r_{fp} = 0.85, \theta_{fp})$, where θ_{fp} varies from $-180°$ to $180°$. The duct and hub geometries are the same as that used in Section 3.3.1 and are described in Table 6.2. Figure 3-19 shows the comparison for the generalized image of a point source. The comparisons for point dipoles oriented in the x, y, and z directions are shown in Figures 3-20, 3-21 and 3-22 respectively. It can be seen that the interpolation procedure is able to accurately produce the value of the generalized image for all of these cases.

3.4.5 Truncation of the Chebyshev polynomial expansions

In order to improve the efficiency of the algorithm for evaluating the Chebyshev polynomial expansions of the image factor, a procedure is implemented to avoid the summation of negligible terms in the series. Since the magnitude of the Chebyshev polynomials is bounded by 1, $|T_n^*(x)| \leq 1$, the magnitude of each term in the expansion is bounded by the magnitude of the coefficient, $|c_{ijklm}|$, corresponding to that term. Therefore, the efficiency can be improved by avoiding the computation of terms where $|c_{ijklm}|$ is less than a specified tolerance. This is done by adjusting the upper limits of the summations in equation (3.52). The expansion with the adjusted limits

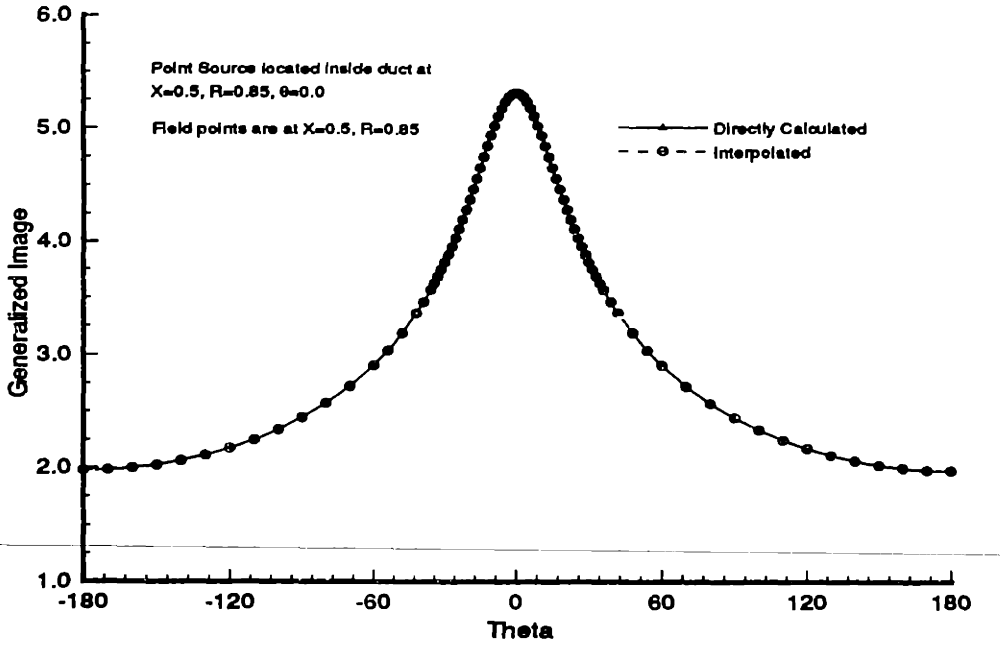

Figure 3-19: Comparison of interpolated and directly calculated values of the generalized image of a point source with respect to the duct and hub. All variables are held constant except for θ_i of the field point.

can be written as follows:

$$\mathcal{I}(\theta', x_{fp}, r_{fp}, X_S, R_S) = \sum_{i=0}^{M_1} \sum_{j=0}^{M_2^i} \sum_{k=0}^{M_3^{ij}} \sum_{l=0}^{M_4^{ijk}} \sum_{m=0}^{M_5^{ijkl}} c_{ijklm} T_{2i}(\tilde{\theta}) T_j^*(\xi_{fp}) T_k^*(\eta_{fp}) T_l^*(\xi_S) T_m^*(\eta_S) \tag{3.78}$$

where the new coefficients, M_1, M_2^i, M_3^{ij}, M_4^{ijk} and M_5^{ijkl}, are computed to truncate the expansion before the inclusion of terms where $|c_{ijklm}|$ is below the specified tolerance. A more conservative approach was used by Newman [38], in which the sum of the absolute values of all the coefficients is computed in reverse order from large upper limits. All of the terms in the sum are then eliminated if the sum of the coefficients is below a specified tolerance. This was done for a two-dimensional expansion, and it was found that various combinations of terms could be eliminated to produce the same total maximum truncation error. This procedure is much more difficult in five dimensions, however, and it was decided to go with the simpler approach. The effect of the truncation of the expansion on the evaluation of the generalized image of a

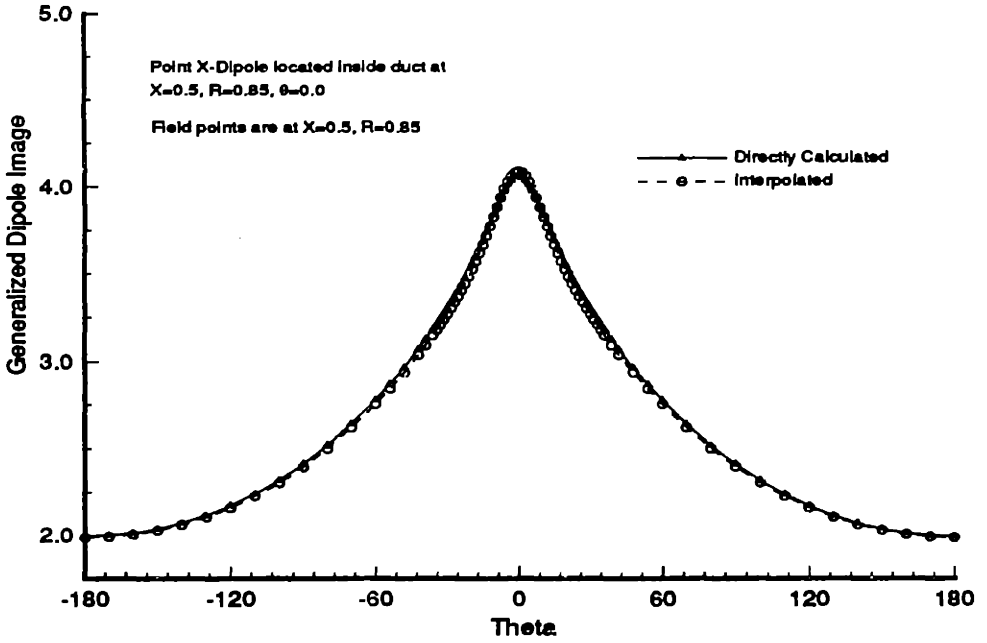

Figure 3-20: Comparison of interpolated and directly calculated values of the generalized image of a point dipole oriented in the axial direction with respect to the duct and hub. All variables are held constant except for θ_i of the field point.

point source is shown in Figure (3-23) for various values of the truncation tolerance. The effect of the truncation on the generalized image of a point dipole oriented in the θ direction, is shown in Figure (3-24). It can be seen that the truncation has a much greater effect on the generalized image for the dipole, since this value in computed using the derivative of the image factor. It appears that a truncation level of 1×10^{-4} would be adequate for computing the generalized image for a point source, but that a truncation level of 1×10^{-5} is required to accurately evaluate the generalized image for a point dipole. The effects of the truncation level on the accuracy of the solution on the propeller and the computation time required to compute the image factors will be shown in Chapter 7.

Another possible means of accelerating the evaluation of the image factor expansions is to convert the Chebyshev polynomials to equivalent ordinary polynomials. The coefficients for the ordinary polynomials can be obtained from the set of Chebyshev coefficients computed using the method discussed in Section 3.4.2 by a process

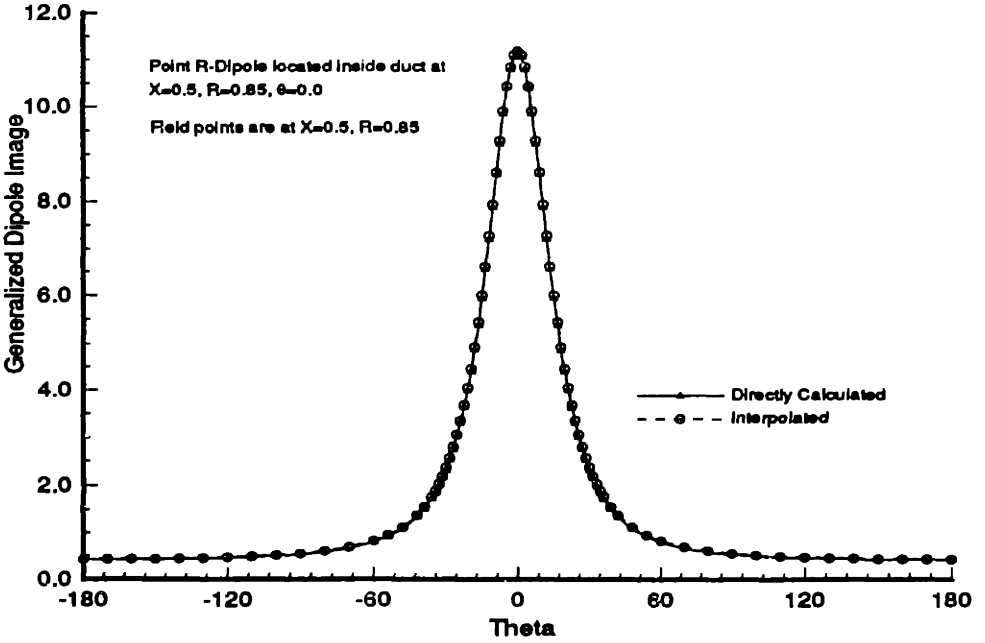

Figure 3-21: Comparison of interpolated and directly calculated values of the generalized image of a point dipole oriented in the radial direction with respect to the duct and hub. All variables are held constant except for θ_i of the field point.

described in [37]. The recursion formulas used to evaluate the Chebyshev polynomials eliminates the ability to vectorize these routines. The evaluation of the ordinary polynomials, however, is well suited for vectorization. In addition, the number of computations required per coefficient is less for the evaluation of an expansion of ordinary polynomials. This procedure was not implemented in the current method because the computer on which the method was developed was not capable of vectorization.

3.5 Calculation of the Duct Potentials and Velocities in the Absence of the Propeller

The solution for the potential on the propeller is decomposed as $\phi = \phi_D + \tilde{\phi}_{PS}$ from equation (2.23). In Section 3.2 the method used to compute $\tilde{\phi}_{PS}$ was described. This section will discuss the method used to obtain ϕ_D. In addition, when solving for $\tilde{\phi}_{PS}$ the values of the source strengths on the propeller blade panels, $\tilde{\sigma}$, are obtained from

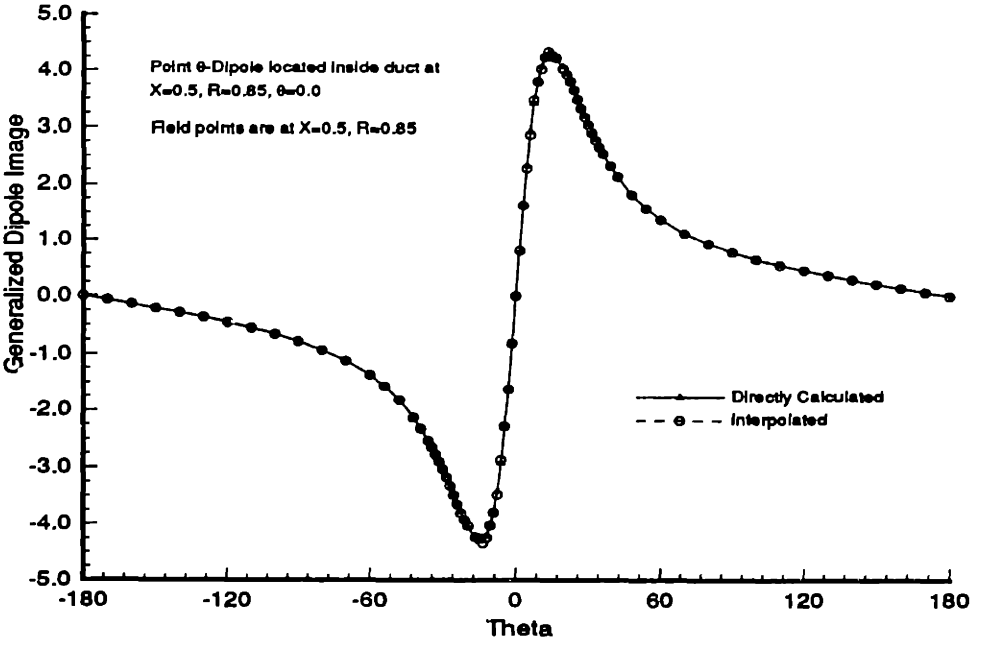

Figure 3-22: Comparison of interpolated and directly calculated values of the generalized image of a point dipole oriented in the theta direction with respect to the duct and hub. All variables are held constant except for θ_i of the field point.

equation (3.3) which requires the value of $\nabla\phi_D$. The method used to obtain $\nabla\phi_D$ will also be discussed in this section. Both ϕ_D and $\nabla\phi_D$ relate to the solution for the flow past the duct and hub in the prescribed inflow, $\boldsymbol{U}_W(x_S, r_S, \theta_S)$, but in the absence of the propeller and stator blades. Although the inflow is spatially nonuniform, the solution to ϕ_D will be steady since the duct and hub geometries are stationary. This solution is obtained from the discretized form of equation (2.24) which is shown below.

$$\sum_{j=1}^{N_{DH}} a_{i,j}\phi_D^j + \sum_{m=1}^{M_D}\sum_{n=1}^{N_{WD}} W_{i,n,m}\Delta\phi_D^m = \sum_{j=1}^{N_{DH}} b_{i,j}\sigma_D^j \qquad i = 1, N_{DH} \tag{3.79}$$

where:

ϕ_D^j is the potential on duct/hub panel j.

M_D is the number of circumferential panels on the duct.

N_{WD} is the number of chordwise panels in the wake of the duct.

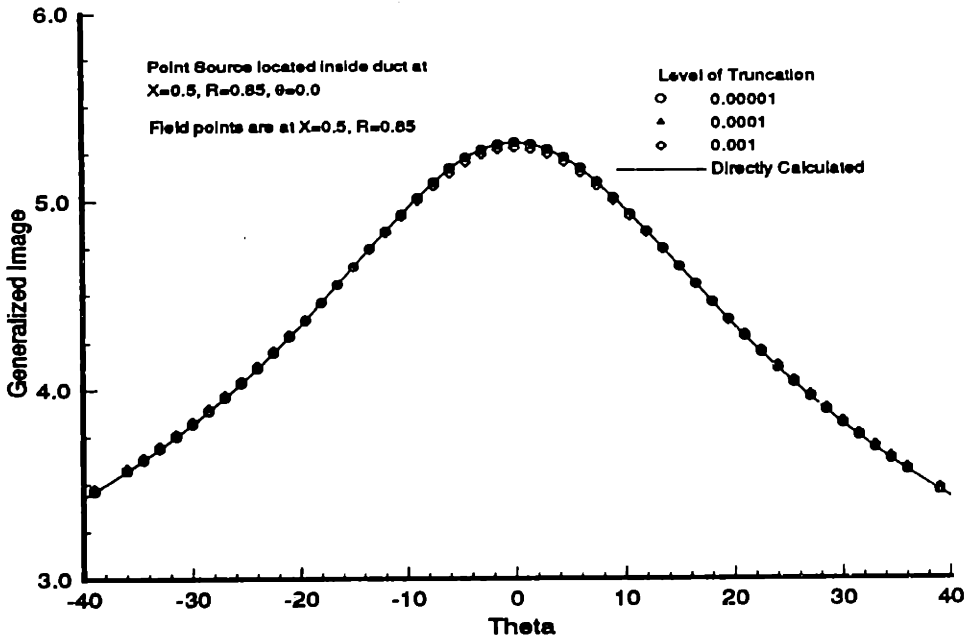

Figure 3-23: Effect of truncation on the interpolated values of the generalized image of a point source with respect to the duct and hub. All variables are held constant except for θ_i of the field point.

N_{DH} is the total number of panels on the duct and hub.

$a_{i,j}$ is the influence coefficient for the potential induced by a unit dipole distribution on duct/hub panel j at the control point of panel i

$b_{i,j}$ is the influence coefficient for the potential induced by a unit source distribution on duct/hub panel j at the control point of panel i

$W_{i,n,m}$ is the influence coefficient for the potential induced by a unit dipole distribution on the n^{th} duct wake panel on the m^{th} circumferential duct wake strip at the control point of panel i.

The procedure used to solve the linear system formed by equation (3.79) is nearly identical to the method used to solve for $\tilde{G}$ from equation (3.15) in Section 3.3.1. The solution in this case is not symmetrical about $\theta = 0$, however, so it is necessary to solve for the strengths of the panels on the entire duct. The panel discretization is the same as used for that problem and is shown in Figure 3-3. The coefficients $a_{i,j}$, $b_{i,j}$,

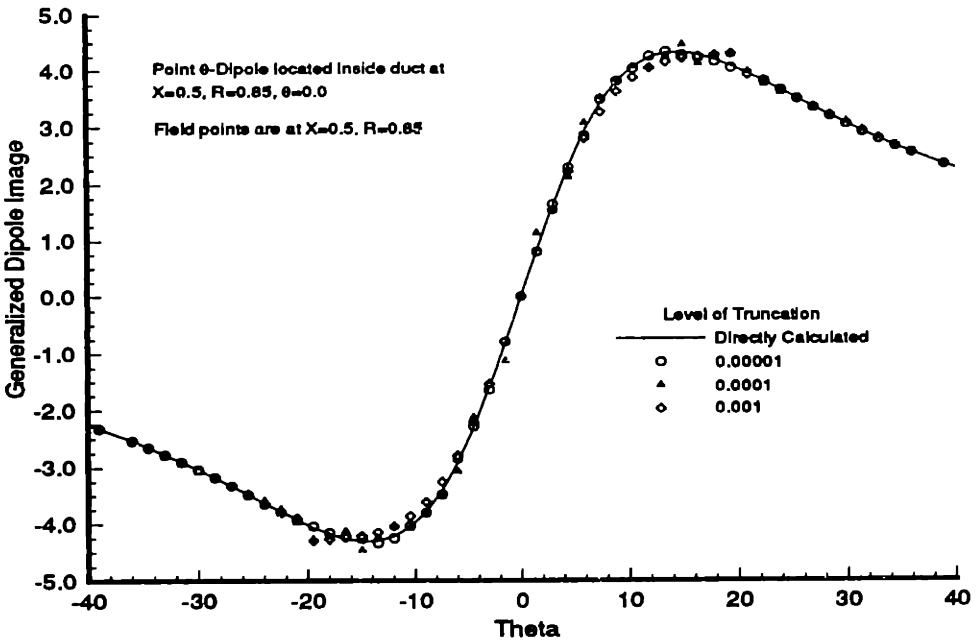

Figure 3-24: Effect of truncation on the interpolated values of the generalized image of a point dipole oriented in the theta direction with respect to the duct and hub. All variables are held constant except for θ_i of the field point.

and $W_{i,n,m}$ are computed using the same routines used to compute the unbounded flow influence coefficients for the propeller solution as described in Section 3.2 and for the generalized image solution as described in Section 3.3.1. As was the case when computing $\tilde{G}$, these influence coefficients only have to be computed for a single chordwise strip on the duct and hub, because the duct and hub geometries are axisymmetric. The source strength, σ_D^j, is defined from equation (2.24) to equal to the negative of the normal component of the inflow at duct/hub panel j.

$$\sigma_D^j = -\boldsymbol{U}_W(x_S, r_S, \theta_S) \cdot \hat{n}_j \tag{3.80}$$

An iterative pressure Kutta condition is applied at the trailing edge of the duct to obtain the jump in potential across the duct wake, $\Delta\phi_D^m$, using a method described in [23] which is similar to that used to apply the Kutta condition for the propeller solution. Equation (3.79) forms a system of N_{DH} linear equations which are inverted to obtain the values of ϕ_D^j on the duct and hub surface.

After the solution for ϕ_D is obtained on the surface of the duct and hub, the values of ϕ_D are computed at a set of field points inside of the duct and hub, $\boldsymbol{x}_i = (x_i, r_i, \theta_i)$, in order to set up a expansion similar to that used to interpolate the image factor. These computations use the following discretized equation:

$$\phi_D(\boldsymbol{x}_i) = \sum_{j=1}^{N_{DH}} a'_{i,j}\phi_D^j + \sum_{j=1}^{N_{DH}} b'_{i,j}\sigma_D^j + \sum_{m=1}^{M_D}\sum_{n=1}^{N_{WD}} W'_{i,n,m}\Delta\phi_D^m \qquad (3.81)$$

where:

$a'_{i,j}$ is the influence coefficient for the potential induced by a unit dipole distribution on duct/hub panel j at the field point $\boldsymbol{x}_i$

$b'_{i,j}$ is the influence coefficient for the potential induced by a unit source distribution on duct/hub panel j at the field point $\boldsymbol{x}_i$

$W'_{i,n,m}$ is the influence coefficient for the potential induced by a unit dipole distribution on the n^{th} duct wake panel on the m^{th} circumferential duct wake strip at the field point $\boldsymbol{x}_i$.

The coefficients $a'_{i,j}$, $b'_{i,j}$ and $W'_{i,n,m}$ are determined using the same method used to compute $a_{i,j}$, $b_{i,j}$ and $W_{i,n,m}$ for equation (3.79). After these coefficients are computed, all of the terms on the right hand side of equation (3.81) are known. Therefore, the values can be obtained at the required field point locations by summing all of the terms on the right hand side of this equation.

The required axial and radial locations for the field points, x_i and r_i, are the same as those required to compute the coefficients for the image factor expansions, x_{fp} and r_{fp}. Therefore, the axial locations, x_i, are specified by equations (3.42) and (3.36), and the radial locations, r_i, are specified by equations (3.43) and (3.37). The inflow $\boldsymbol{U}_W$ is specified in terms of a Fourier series as shown in equation (2.4). The solution for ϕ_D will be periodic in θ, and there is no singular behavior requiring that the region be subdivided in θ as was the case with the image factor. Therefore, it is logical to expand ϕ_D in a Fourier series with respect to θ. The field points used to determine the coefficients of these series will be uniformly spaced in the θ direction over the

interval from $-180°$ to $180°$. The combined Chebyshev polynomial and Fourier series expansion for ϕ_D inside of the duct is shown below:

$$\phi_D(x,r,\theta) = \sum_{i=0}^{N_1}\sum_{j=0}^{N_2} T_i^*(\xi)T_j^*(\eta)\left[\alpha_{ij0} + \sum_{k=1}^{N_3}\left(\alpha_{ijk}\cos(k\theta) + \beta_{ijk}\sin(k\theta)\right)\right] \qquad (3.82)$$

where ξ and η are the normalized forms of x and r respectively, as specified by equations (3.36) and (3.37). The values of N_1, N_2, and N_3 represent the number of terms used to compute the expansion in the x, r and θ directions respectively. These must be set large enough to allow the resulting coefficients to converge adequately to zero in each direction. For the inflows and duct/hub geometries examined in this thesis, $N_1 = 8$, $N_2 = 8$ and $N_3 = 16$ easily satisfied this condition. The value of N_3 should be at least as high as the number of harmonics used to define the inflow, U_W, in equation (2.4). The coefficients, α_{ijk} and β_{ijk} are obtained by first applying a Fast Fourier Transfrom (FFT) algorithm to determine the coefficients for a Fourier series related to the value of ϕ_D at each of the required axial and radial field point locations. The procedure described in Section 3.4.2 is then applied to compute α_{ijk} and β_{ijk} from these Fourier coefficients. The Fourier series coefficients will converge to zero in a similar manner to the convergence for the Chebyshev coefficients. Therefore, since $|\cos(k\theta)| \leq 1$ and $|\sin(k\theta)| \leq 1$, the method of truncating the expansion described in Section 3.4.5 can be used to avoid unnecessary computations when $\alpha_{ijk} \approx 0$ or $\beta_{ijk} \approx 0$. In general, it has been found that the coefficients for this series converge much more quickly than the coefficients for the image factor expansions. The expansion for ϕ_D is then evaluated using the same method used to evaluate the expansion for the image factor as described in Section 3.4.3.

The gradient, $\nabla\phi_D$, is defined as follows:

$$\nabla\phi_D = \frac{\partial\phi_D}{\partial x}\hat{i} + \frac{\partial\phi_D}{\partial r}\hat{r} + \frac{\partial\phi_D}{r\partial\theta}\hat{t} \qquad (3.83)$$

This can be obtained by computing the partial derivatives of ϕ_D in each direction. These partial derivatives can be computed directly from the combined Chebyshev

polynomial, Fourier series expansion. For the partial derivatives with respect to x and r, the procedure is the same as that used to compute the partial derivatives of the image factor with respect to X_S and R_S as described in Section (3.4.3). The partial derivative with respect to θ is computed by differentiating the terms of the Fourier series:

$$\frac{\partial \phi_D}{\partial \theta}(x,r,\theta) = \sum_{i=0}^{N_1}\sum_{j=0}^{N_2} T_i^*(\xi)T_j^*(\eta)\sum_{k=1}^{N_3}\Big(-\alpha_{ijk}k\sin(k\theta) + \beta_{ijk}k\cos(k\theta)\Big) \qquad (3.84)$$

The values of ϕ_D and the components of its gradient, $\frac{\partial \phi_D}{\partial x}$, $\frac{\partial \phi_D}{\partial r}$ and $\frac{\partial \phi_D}{\partial \theta}$, are computed at the control points for all of the propeller and stator blade panels. This computation is performed at each timestep for the propeller blade panels but only once for the stator blade panels.

3.6 Implementation for Multi-Component Propulsors

Two methods were studied for modeling the interaction between the blade row components when both a propeller and stator blades are present. The first was an extension of the method used to model the interaction between a propeller and pre-swirl stator blades by Hughes and Kinnas [19]. In this method, two separate systems of linear equations are used for the propeller and stator blades with the interaction being accounted for in an iterative manner by modifying the right hand side of each problem. This process can easily be extended to unsteady flows. The advantage of this method is that the use of influence coefficients which change at each timestep can be avoided, since the geometry used within each of the systems of equations is constant. However, a computationally expensive iterative process must be performed at each timestep.

The second approach obtains the solution on both the propeller and stator blades by solving a single system of equations. In this way, there is no need to iterate between solutions and only a single system of equations has to be inverted at each timestep. However, since the geometries of the propeller and stator blades move

relative to each other, the coefficients for the influence of the stator blade panels on the propeller and the influence of the propeller panels on the stator blades will change at each timestep. On the other hand, the image factors corresponding to these coefficients can be computed efficiently using equations (3.76) and (3.77). After performing rough calculations for the computational time required by each method, it was determined that the second approach, which models the propeller and stators as one problem, is more efficient, and this method was implemented.

One of the difficulties involved in this formulation concerns how to model the interaction between the blade of the downstream component and the wake from the upstream component. For the case of pre-swirl stators, the propeller key blade will intersect the wake from each stator blade as it rotates behind the stators. This situation is shown schematically in Figures 3-25 and 3-26. This will be treated by allowing the downstream blade to pass through the wake without altering the wake geometry. The influence from the upstream wake panels which touch the blade of the downstream component are set to zero. Similar methods have been employed to model the interaction between blade rows for contra-rotating propellers by Maskew [33] and Yang et. al. [42]. A time dependent function $h_{lm}(n)$ is created which is set equal to 0 when the l^{th} panel on m^{th} wake strip intersects one of the component blades at timestep n and is set equal to 1 otherwise. This procedure is shown schematically in Figure 3-25.

The stators and propeller are then solved simultaneously using the same procedure described in Section 3.2. Figure 3-26 shows the panel discretization used for the stator blades, propeller, and their wakes for the case of a two bladed propeller with three stator blades. The wake geometry is only shown for one of the stator blades and the key propeller blade. Fixed wake geometries are used for both the propeller and stator blades. The spacing of the panels along the propeller wake was discussed in Section 3.2. The panels along the stator wake will be placed along the prescribed stator wake surface using constant axial spacing which is related to the time step, $\Delta X_W = (\bar{U_W})_x(r)\Delta t$, where Δt is the timestep and $(\bar{U_W})_x(r)$ is the circumferential average of the axial component of the inflow, $\boldsymbol{U}_W$, at radius r. The discrete form of

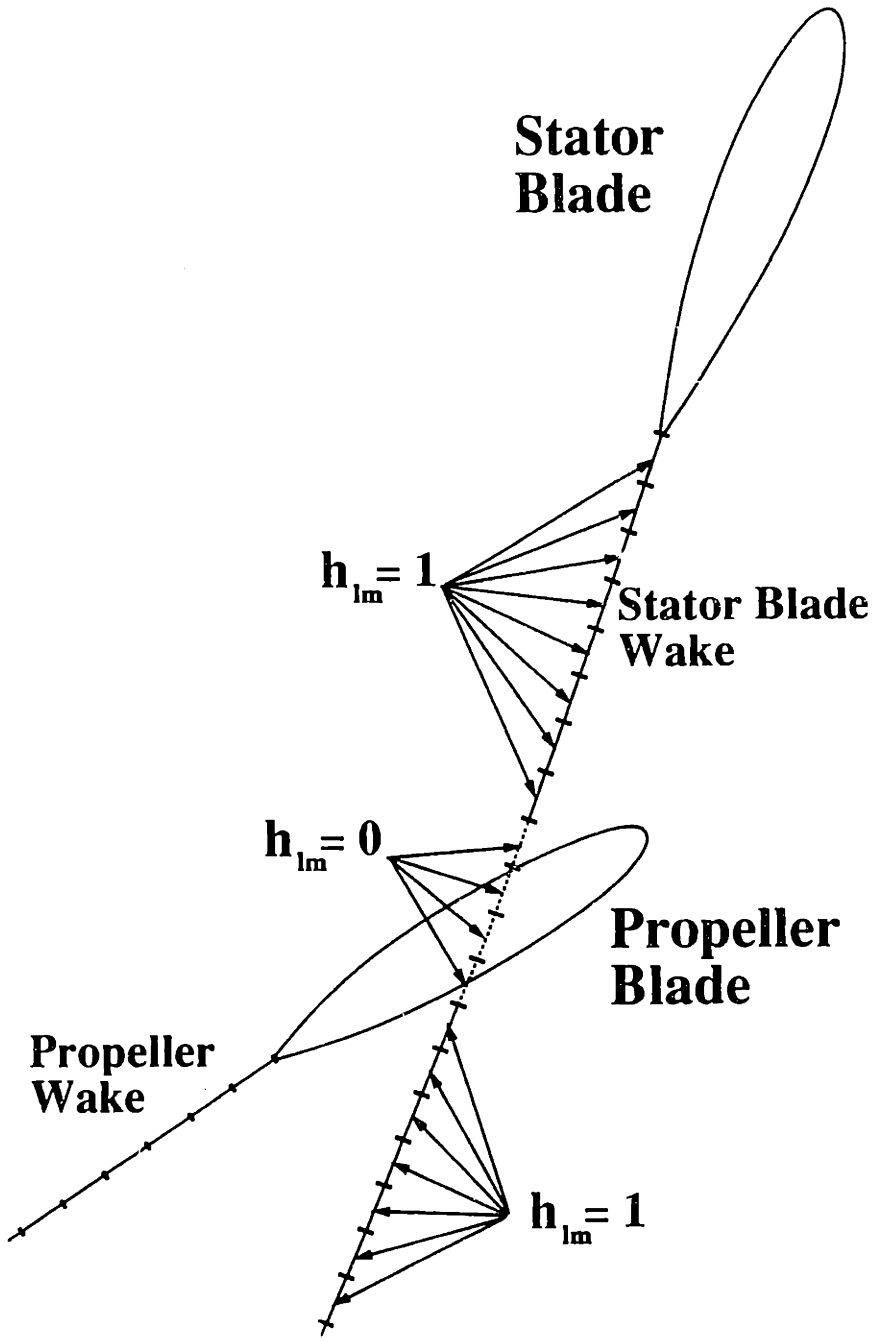

Figure 3-25: Interaction between wake of the upstream component and the blade of the downstream component.

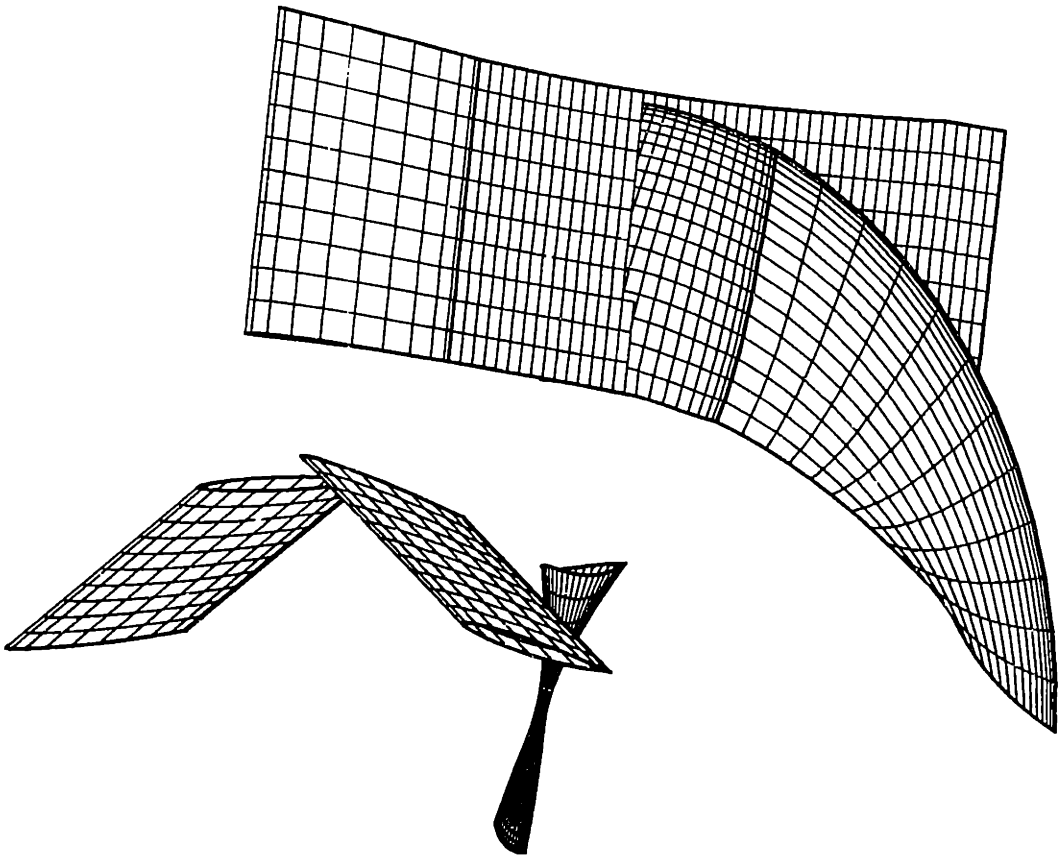

Figure 3-26: Geometry and panelization of two component ducted propulsor. The duct and hub are not shown.

equation (2.25) which includes the stator blades is shown in equations (3.85) through (3.88). Panels indexed from 1 through N_P are on the propeller blade surface, and panels indexed from $N_P + 1$ through $N_P + N_{ST}$ are on the stator blade surfaces. The influence coefficients which change with each timestep are underlined.

For the panels on the propeller blades:

$$\sum_{j=1}^{N_P} \tilde{a}_{ij}\tilde{\phi}_j(n) + \sum_{j=N_P+1}^{N_P+N_{ST}} \underline{\tilde{a}_{ij}(n)}\tilde{\phi}_j(n) + \sum_{m=1}^{M} \tilde{T}^L_{im}\Gamma_m(n) + \sum_{m=M+1}^{M+M_{ST}} \underline{\tilde{T}^L_{im}(n)}\Gamma_m(n) = RHS_i(n); \quad i = 1, N_P \tag{3.85}$$

where,

$$
\begin{aligned}
RHS_i(n) &= \sum_{k=1}^{N_B}\sum_{j=1}^{N_P} \tilde{b}_{ij}^k \tilde{\sigma}_j^k(n) - \sum_{k=2}^{N_B}\sum_{j=1}^{N_P} \tilde{a}_{ij}^k \tilde{\phi}_j^k(n) \\
&- \sum_{k=2}^{N_B}\sum_{m=1}^{M}\sum_{l=1}^{N_W} \tilde{W}_{ilm}^k \Delta\tilde{\phi}_{lm}^k(n) - \sum_{m=1}^{M}\sum_{l=2}^{N_W} \tilde{W}_{ilm}\Delta\tilde{\phi}_{lm}(n) \\
&+ \sum_{j=N_P+1}^{N_P+N_{ST}} \underline{\tilde{b}_{ij}(n)}\tilde{\sigma}_j - \sum_{m=M+1}^{M+M_{ST}}\sum_{l=2}^{N_{WST}} \underline{\tilde{W}_{ilm}(n)}\,\underline{h_{lm}(n)}\Delta\tilde{\phi}_{lm}(n) \\
&- \sum_{m=1}^{M} \tilde{T}_{im}^R \Gamma_m(n-1) - \sum_{m=M+1}^{M+M_{ST}} \underline{\tilde{T}_{im}^R(n)}\Gamma_m(n-1)
\end{aligned} \tag{3.86}
$$

For the panels on the stator blades the equations will be:

$$
\begin{aligned}
&\sum_{j=1}^{N_P} \underline{\tilde{a}_{ij}(n)}\tilde{\phi}_j(n) + \sum_{j=N_P+1}^{N_P+N_{ST}} \tilde{a}_{ij}\tilde{\phi}_j(n) + \sum_{m=1}^{M} \underline{\tilde{T}_{im}^L(n)}\Gamma_m(n) \\
&+ \sum_{m=M+1}^{M+M_{ST}} \tilde{T}_{im}^L \Gamma_m(n) = RHS_i(n); \quad i = N_P+1, N_P+N_{ST}
\end{aligned} \tag{3.87}
$$

where,

$$
\begin{aligned}
RHS_i(n) &= \sum_{k=1}^{N_B}\sum_{j=1}^{N_P} \underline{\tilde{b}_{ij}^k(n)}\tilde{\sigma}_j^k(n) - \sum_{k=2}^{N_B}\sum_{j=1}^{N_P} \underline{\tilde{a}_{ij}^k(n)}\tilde{\phi}_j^k(n) \\
&- \sum_{k=2}^{N_B}\sum_{m=1}^{M}\sum_{l=1}^{N_W} \underline{\tilde{W}_{ilm}^k(n)}\,\underline{h_{lm}^k(n)}\Delta\tilde{\phi}_{lm}^k(n) - \sum_{m=1}^{M}\sum_{l=2}^{N_W} \underline{\tilde{W}_{ilm}(n)}\,\underline{h_{lm}(n)}\Delta\tilde{\phi}_{lm}(n) \\
&+ \sum_{j=N_P+1}^{N_P+N_{ST}} \tilde{b}_{ij}\tilde{\sigma}_j - \sum_{m=M+1}^{M+M_{ST}}\sum_{l=2}^{N_{WST}} \tilde{W}_{ilm}\Delta\tilde{\phi}_{lm}(n) \\
&- \sum_{m=1}^{M} \underline{\tilde{T}_{im}^R(n)}\Gamma_m(n-1) - \sum_{m=M+1}^{M+M_{ST}} \tilde{T}_{im}^R\Gamma_m(n-1)
\end{aligned} \tag{3.88}
$$

where:

N_B is the number of propeller blades

M is the number of spanwise panels on the propeller blade

N_P is the total number of panels on the key blade

N_W is the number of chordwise panels in the propeller wake

N_{ST} is the total number of panels on *all* of the stator blades.

M_{ST} is the combined number of spanwise panels on *all* the stator blades.

N_{WST} is the number of chordwise panels in the stator blade wake.

The influence coefficients $\tilde{a}_{ij}$, $\tilde{b}_{ij}$, $\tilde{W}_{ilm}$, $\tilde{T}^R_{im}$, and $\tilde{T}^L_{im}$, are defined in the same manner used for the single component case for equation (3.4) in Section 3.2. The only difference in this case is that the underlined coefficients now change at each time step. The function $h_{lm}(n)$ is used to "turn off" the wake panels which intersect downstream blades as discussed earlier. The value for $\tilde{\sigma}^k_j(n)$ on the propeller blade panels is given by equation (3.3). The value for $\tilde{\sigma}_j$ on the stator blades is not time dependent and is computed in a similar manner as shown below:

$$\tilde{\sigma}_j = -\left(\boldsymbol{U}_W(x_j, y_j, z_j) + \nabla\phi_D\right) \cdot \hat{n}_j \tag{3.89}$$

Equations (3.85) and (3.87) are combined to form a linear system of $N_P + N_{ST}$ equations for the potential $\tilde{\phi}$ on both the propeller and stator blade surfaces. This system of equations is inverted at each time step n. The right hand side is then updated before solving the system at the next time step. The procedure continues until a steady state oscillatory solution is obtained which usually requires several propeller revolutions. The value for ϕ_D and $\nabla\phi_D$ are obtained from the procedure described in Section 3.5. The complete perturbation potential is then expressed as $\phi_D + \tilde{\phi}$. Only the propeller is modeled using a *key blade*; each stator blade is solved individually, since the geometries for all the stator blades may not be identical and each stator blade will see a different inflow. The jump in potential across the wake panels, $\Delta\tilde{\phi}_{l,m}(n)$, can be obtained from equations (2.8) and (2.9) for the propeller and equations (2.10) and (2.12) for the stator blades. The circulation at the trailing edge of the blade, $\Gamma_m(n)$, is determined from the implementation of an iterative pressure Kutta condition. The circulation is first approximated by Morino's Kutta condition as specified by equation (3.6), and a solution for $\tilde{\phi}$ is obtained from equations (3.85) and (3.87). This solution is then modified by varying $\Gamma_m(n)$ in an iterative manner

at each time step in order to satisfy the condition that the jump in pressure across the blade goes to zero at the blade trailing edge. The pressure Kutta condition is set up separately for the propeller blade and for each stator blade. In other words, $\Gamma_m(n)$ is varied separately on each blade to satisfy the equal pressure condition only for that blade, and the effect of this variation is computed only on the blade for which $\Gamma_m(n)$ is varied. In this way, the base problems which must be solved to compute the effect of varying $\Gamma_m(n)$ will not be time dependent. In addition, this procedure for applying the iterative pressure Kutta condition is much more efficient than applying the condition to all blades simultaneously and will have negligible effects on the results. The iterative pressure Kutta condition is described in detail in [15].

Chapter 4

Calculation of Duct Potentials and Forces

In Chapter 3, the procedure used to compute the solution on the propeller and stator blades was developed. The generalized image model was implemented to accurately account for the influence of the duct and hub, without having to solve for the potential on the duct and hub as part of the solution matrix at each timestep. In this chapter, it is shown how the solution on the duct and hub can be obtained from: (1) the solution history of the potential and circulation on the propeller and stator blades, and (2) the solutions for the potential distribution on the duct and hub computed when calculating the generalized images directly at a representative set of points.

The potentials on the duct obtained using this method will represent the "quasi-steady duct" (QSD) solution. In the QSD solution, the vorticity shed at the duct trailing edge is not convected downstream. This results in a duct wake sheet whose strength varies circumferentially and changes at each timestep, but is invariant in the streamwise direction. A method is presented to recover the "fully-unsteady duct" (FUD) solution from the history of the QSD solution. This method is first developed for a two-dimensional analog problem and then extended to the problem of a three-dimensional duct. The procedure used to compute the pressures and forces on the duct is then developed, including the implementation of an iterative pressure Kutta condition at the duct trailing edge.

4.1 Obtaining Duct Potentials from the Propeller Potentials - The Inverse Generalized Image

If a direct panel method is used to solve for the flow past a ducted propulsor, the integral equation for the perturbation potential is given by equation (2.5) for the FUD duct solution and equation (2.15) for the QSD duct solution. In this section we will first obtain the QSD duct potential, $\phi(\mathbf{x},t)^{QSD}$ on the duct surface. It will then be shown how after $\phi(\mathbf{x},t)^{QSD}$ is computed at all timesteps, the fully unsteady duct perturbation potential, $\phi(\mathbf{x},t)$, can be recovered. It is assumed that the differences between the QSD and FUD solutions are negligible on the hub surface. This is the same approximation as was made for the propeller and will be justified in Section 4.3.4.

When solving for the potential on the propeller and stator blades it is first necessary to solve for the ϕ_D, which is the perturbation potential on the duct and hub surface in the presence of the prescribed inflow, $\boldsymbol{U}_W$, but in the absence of the propeller and stator blades. The expression for ϕ_D is given by equation (2.24), and its value at the control points of all the duct and hub panels, ϕ_D^j, is computed in order to obtain the solution on the propeller and stators using the procedure described in Section 3.5. This can be used to decompose the the QSD perturbation potential on the duct and hub surface in a manner similar to the decomposition used for the propeller.

$$\phi^{QSD} = \phi_D + \tilde{\phi}_D \tag{4.1}$$

The expression for $\tilde{\phi}_D$ can be obtained by subtracting equation (2.24) from equation (2.15). The resulting equation for $\tilde{\phi}_D$ on the surface of the duct and hub is shown below:

$$\begin{aligned} 2\pi\tilde{\phi}_D(\mathbf{x},t) \;=\; & \int_{S_D} \tilde{\phi}_D(\boldsymbol{\xi},t)\frac{\partial G(\mathbf{x},\boldsymbol{\xi})}{\partial n_D}\,dS(\boldsymbol{\xi}) + \int_{S_{PS}} \phi(\boldsymbol{\xi},t)\frac{\partial G(\mathbf{x},\boldsymbol{\xi})}{\partial n_{PS}}\,dS(\boldsymbol{\xi}) \\ & - \int_{S_{PS}} G(\mathbf{x},\boldsymbol{\xi})(-\boldsymbol{U}_{\text{in}}\cdot\boldsymbol{n}_{PS})\,dS(\boldsymbol{\xi}) \\ & + \int_{W_D} \Delta\tilde{\phi}_D^T(\theta,t)\frac{\partial G(\mathbf{x},\boldsymbol{\xi})}{\partial n_{W_D}}\,dS(\boldsymbol{\xi}) \end{aligned}$$

$$+\int_{W_{PS}} \Delta\phi_{PS}(\boldsymbol{\xi},t)\frac{\partial G(\mathbf{x},\boldsymbol{\xi})}{\partial n_{W_{PS}}}\,dS(\boldsymbol{\xi}) \tag{4.2}$$

The terms shown in the above equation are the same as those used for equation (2.5) The perturbation potential on the surface of the propeller and stator blade panels, $\phi(\boldsymbol{\xi},t)$, is now known from the solution procedure described in Chapter 3. The source strengths, $(-\boldsymbol{U}_{in}\cdot\boldsymbol{n}_{PS})$ are also known. The potential $\tilde{\phi}_D$ can be further decomposed as shown below.

$$\tilde{\phi}_D = \tilde{\phi}^A + \tilde{\phi}^B \tag{4.3}$$

where:

$$\begin{aligned} 2\pi\tilde{\phi}^A(\mathbf{x},t) &= \int_{S_D} \tilde{\phi}^A(\boldsymbol{\xi},t)\frac{\partial G(\mathbf{x},\boldsymbol{\xi})}{\partial n_D}\,dS(\boldsymbol{\xi}) + \int_{S_{PS}} \phi(\boldsymbol{\xi},t)\frac{\partial G(\mathbf{x},\boldsymbol{\xi})}{\partial n_{PS}}\,dS(\boldsymbol{\xi}) \\ &\quad + \int_{W_D} (\Delta\tilde{\phi}^A)^T(\theta,t)\frac{\partial G(\mathbf{x},\boldsymbol{\xi})}{\partial n_{W_D}}\,dS(\boldsymbol{\xi}) \\ &\quad + \int_{W_{PS}} \Delta\phi_{PS}(\boldsymbol{\xi},t)\frac{\partial G(\mathbf{x},\boldsymbol{\xi})}{\partial n_{W_{PS}}}\,dS(\boldsymbol{\xi}) \end{aligned} \tag{4.4}$$

and,

$$\begin{aligned} 2\pi\tilde{\phi}^B(\mathbf{x},t) &= \int_{S_D} \tilde{\phi}^B(\boldsymbol{\xi},t)\frac{\partial G(\mathbf{x},\boldsymbol{\xi})}{\partial n_D}\,dS(\boldsymbol{\xi}) - \int_{S_{PS}} G(\mathbf{x},\boldsymbol{\xi})(-\boldsymbol{U}_{in}\cdot\boldsymbol{n}_{PS})\,dS(\boldsymbol{\xi}) \\ &\quad + \int_{W_D} (\Delta\tilde{\phi}^B)^T(\theta,t)\frac{\partial G(\mathbf{x},\boldsymbol{\xi})}{\partial n_{W_D}}\,dS(\boldsymbol{\xi}) \end{aligned} \tag{4.5}$$

It is possible to solve equations (4.4) and (4.4) numerically by discretizing all of the component and wake surfaces and applying a panel method similar to that used in Section 3.2. The discretized form of equation (4.5) is shown below:

$$\sum_{j=1}^{N_{DH}} a_{i,j}\tilde{\phi}^B_j(n) + \sum_{m=1}^{M_D}\sum_{l=1}^{N_{WD}} W_{i,l,m}\Delta\tilde{\phi}^B_m(n) = \sum_{k=1}^{N_{PS}} b'_{ik}\sigma_k(n) \qquad i = 1, N_{DH} \tag{4.6}$$

where:

N_{DH} is the total number of panels on the duct and hub.

M_D is the number of circumferential panels on the duct.

N_{WD} is the number of chordwise panels in the duct wake.

N_{PS} is the total number of panels on all of the stator blades and *all* of the propeller blades combined.

$a_{i,j}$ is the influence coefficient for the potential induced by a unit dipole distribution on duct/hub panel j at the control point of duct/hub panel i

$W_{i,n,m}$ is the influence coefficient for the potential induced by a unit dipole distribution on the l^{th} duct wake panel on the m^{th} circumferential duct wake strip at the control point of duct/hub panel i.

$b'_{i,k}$ is the influence coefficient for the potential induced by a unit source distribution on *propeller/stator* panel k at the control point of duct/hub panel i

In the remainder of this section, the subscript k will refer to the index of panels representing the propeller and stator blades, and the subscripts i and j will refer to index of panels representing the duct and hub. The value of $\sigma_k(n)$ represents the source strength on panel k and is defined as:

$$\sigma_k(n) = -\mathbf{U}_{P_{in}}(x_k, y_k, z_k, n\Delta t) \cdot \hat{n}_k \tag{4.7}$$

These are different from the source strengths, $\tilde{\sigma}_k$, used when solving for $\tilde{\phi}_{PS}$ which include the duct modifications to the inflow. The influence coefficients $b'_{i,k}$ are now approximated with their far field values.

$$b'_{i,k} = \int_{S_k} G\, dS \approx \frac{A_k}{||\mathbf{x}_i - \boldsymbol{\xi}_k||} \tag{4.8}$$

where A_k is the area of panel k, S_k represents the surface of panel k, and $||\mathbf{x}_i - \boldsymbol{\xi}_k||$ is the distance between the control points of propeller/stator panel k and duct/hub panel i. The effect of this assumption on the duct solution is expected to be small and will be examined in Section 6.2.2. Substituting this approximation into equation (4.6)

gives the following expression:

$$\sum_{j=1}^{N_{DH}} a_{i,j}\tilde{\phi}_j^B(n) + \sum_{m=1}^{M_D}\sum_{l=1}^{N_{WD}} W_{i,l,m}\Delta\tilde{\phi}_m^B(n) = \sum_{k=1}^{N_{PS}} \left(\frac{A_k}{||\mathbf{x}_i - \boldsymbol{\xi}_k||}\right)\sigma_k(n) \qquad i = 1, N_{DH} \tag{4.9}$$

Equation (4.9) can be further decomposed as the sum of the effects from the source distributions on each individual propeller and stator panel.

$$\tilde{\phi}_j^B(n) = \sum_{k=1}^{N_{PS}} \left[\tilde{\phi}^b(\mathbf{x}_j, \boldsymbol{\xi}_k)\left(A_k\sigma_k(n)\right)\right] \tag{4.10}$$

where,

$$\sum_{j=1}^{N_{DH}} a_{i,j}\tilde{\phi}^b(\mathbf{x}_j, \boldsymbol{\xi}_k) + \sum_{m=1}^{M_D}\sum_{l=1}^{N_{WD}} W_{i,l,m}\Delta\tilde{\phi}_{m,k}^b(n) = \frac{1}{||\mathbf{x}_i - \boldsymbol{\xi}_k||} \qquad i = 1, N_{DH} \tag{4.11}$$

The value of $\tilde{\phi}^b(\mathbf{x}_j, \boldsymbol{\xi}_k)$ represents the potential on the surface on the duct and hub surface in the presence of point source of strength 4π located inside the duct at $\boldsymbol{\xi}_k$. This is identical to the problems which had to be solved to directly compute the values the generalized images! Therefore, the value for $\tilde{\phi}^b(\mathbf{x}_j, \boldsymbol{\xi}_k)$ is equal to $\tilde{G}(\boldsymbol{\chi}, \boldsymbol{\xi})$ where $\boldsymbol{\chi} = \mathbf{x}_i$ and $\boldsymbol{\xi} = \boldsymbol{\xi}_k$. Representative values of $\tilde{G}(\boldsymbol{\chi}, \boldsymbol{\xi})$ are computed on the complete duct/hub surface for all the source locations inside of the duct required to set up the Chebyshev polynomial expansion for the image factor. The values of $\tilde{G}(\boldsymbol{\chi}, \boldsymbol{\xi})$ are obtained by inverting the system of equations formed by equation (3.15). These same solutions can now be used to set up another Chebyshev polynomial expansion for the value of $\tilde{\phi}^b$ on the surface of the duct and hub.

Equation (4.4) can be broken down in a similar manner in order to obtain $\tilde{\phi}^A$. The discretized form of equation (4.4) is:

$$\sum_{j=1}^{N_{DH}} a_{i,j}\tilde{\phi}_j^A(n) + \sum_{m=1}^{M_D}\sum_{l=1}^{N_{WD}} W_{i,l,m}\Delta\tilde{\phi}_m^A(n) = \sum_{k=1}^{N_{PS}} a'_{i,k}\phi_k(n) + \sum_{h=1}^{N_{WPS}} W'_{i,h}\Delta\phi_h(n) \qquad i = 1, N_{DH} \tag{4.12}$$

where N_{WPS} is the total number of panels used to form the wakes for all of the propeller and stator blades. The coefficients $a'_{i,k}$ and $W'_{i,h}$ represent the influence

from a unit dipole distribution on blade panel k and wake panel h respectively at the control point of duct/hub panel i. These will be replaced with their far-field approximations as follows:

$$a'_{i,k} \approx \frac{\partial}{\partial n_k}\left(\frac{1}{||\mathbf{x}_i - \boldsymbol{\xi}_k||}\right) A_k \quad W'_{i,k} \approx \frac{\partial}{\partial n_h}\left(\frac{1}{||\mathbf{x}_i - \boldsymbol{\xi}_h||}\right) A_h. \tag{4.13}$$

Equation (4.12) is then broken down to obtain the value of $\tilde{\phi}^A$ corresponding to each individual blade and wake panel.

$$\tilde{\phi}^A_j(n) = \sum_{k=1}^{N_{PS}} \left[\tilde{\phi}^a(\mathbf{x}_j, \boldsymbol{\xi}_k)\left(A_k \phi_k(n)\right)\right] + \sum_{h=1}^{N_{WPS}} \left[\tilde{\phi}^a(\mathbf{x}_j, \boldsymbol{\xi}_h)\left(A_h \Delta\phi_h(n)\right)\right] \tag{4.14}$$

where,

$$\sum_{j=1}^{N_{DH}} a_{i,j}\tilde{\phi}^a(\mathbf{x}_j, \boldsymbol{\xi}_k) + \sum_{m=1}^{M_D}\sum_{l=1}^{N_{WD}} W_{i,l,m}\Delta\tilde{\phi}^a_{m,k}(n) = \frac{\partial}{\partial n_k}\left(\frac{1}{||\mathbf{x}_i - \boldsymbol{\xi}_k||}\right) \qquad i = 1, N_{DH} \tag{4.15}$$

By comparing equation (4.15) with equation (4.11), it follows that $\tilde{\phi}^a(\mathbf{x}, \boldsymbol{\xi})$ is simply the derivative of $\tilde{\phi}^b(\mathbf{x}, \boldsymbol{\xi})$ with respect to the location of the point $\boldsymbol{\xi}$.

$$\tilde{\phi}^a(\mathbf{x}, \boldsymbol{\xi}) = \frac{\partial \tilde{\phi}^b(\mathbf{x}, \boldsymbol{\xi})}{\partial n_{\boldsymbol{\xi}}} \tag{4.16}$$

Therefore, the value of $\tilde{\phi}^a$ can also be obtained from the Chebyshev polynomial expansion for $\tilde{\phi}^b$, by differentiating the expansion using the same procedure used to obtain the derivatives of the image factor in Section 3.4.3. By combining equations (4.1), (4.11) and (4.15), an expression can be formed for the complete QSD perturbation potential, $\phi^{QSD}_j(n)$, on duct/hub panel j as shown below:

$$\begin{aligned} \phi^{QSD}_j(n) &= \phi^j_D + \sum_{k=1}^{N_{PS}} \left(\tilde{\phi}^a(\mathbf{x}_j, \boldsymbol{\xi}_k)\phi_k(n) + \tilde{\phi}^b(\mathbf{x}_j, \boldsymbol{\xi}_k)\sigma_k(n)\right) A_k \\ &+ \sum_{h=1}^{N_{WPS}} \tilde{\phi}^a(\mathbf{x}_j, \boldsymbol{\xi}_h) A_h \Delta\phi_h(n) \end{aligned} \tag{4.17}$$

The values $\tilde{\phi}^a(\mathbf{x}_j, \boldsymbol{\xi}_k)$ and $\tilde{\phi}^b(\mathbf{x}_j, \boldsymbol{\xi}_k)$ can be thought of as coefficients which represent

the potential on duct/hub panel j due to the presence of a point source or point dipole located at the centroid of propeller/stator panel k respectively. These coefficients are both determined from the Chebyshev polynomial expansion developed for $\tilde{\phi}^b$. The potential $\tilde{\phi}^b(\mathbf{x}, \boldsymbol{\xi})$ is actually the sum of the generalized image and the potential induced directly by a point source placed at $\boldsymbol{\xi}$ for the case where the field point $\mathbf{x}$ coincides with the surface of the duct.

$$\tilde{\phi}^b(\mathbf{x}, \boldsymbol{\xi}) = G_I(\mathbf{x}, \boldsymbol{\xi}) + G(\mathbf{x}, \boldsymbol{\xi}) \tag{4.18}$$

On the surface of the duct, $\tilde{\phi}^b(\mathbf{x}, \boldsymbol{\xi})$ can be expressed as a function of four variables.

$$\tilde{\phi}^b(\mathbf{x}, \boldsymbol{\xi}) \longrightarrow \tilde{\phi}^b(\theta', s_D, X_S, R_S) \tag{4.19}$$

where X_S and R_S are the axial and radial positions of the source point, $\boldsymbol{\xi}$, and θ' is the relative angle between $\mathbf{x}$ and $\boldsymbol{\xi}$. These variables are the same as those used to expand the image factor in Chapter 3. The variable s_D refers to the chordwise arc length of a point along the surface of the duct from the duct leading edge as shown schematically in Figure 4-1. By using this variable instead of the axial and radial position of $\mathbf{x}$, the function can be expressed in terms of four variables instead of five. Separate expansions are used for $\tilde{\phi}^b$ on the inner and outer surfaces of the duct.

The procedure used to set up the Chebyshev polynomial expansion for $\tilde{\phi}^b$ is the same as the procedure used to set up the expansion for the image factor. Currently this is performed only for $\tilde{\phi}^b$ on the duct. The procedure for $\tilde{\phi}^b$ on the hub would be identical and is left for future development. The resulting Chebyshev polynomial expansion is shown below:

$$\tilde{\phi}^b(\theta', s_D, X_S, R_S) = \sum_{i=0}^{N_1} \sum_{j=0}^{N_2} \sum_{k=0}^{N_3} \sum_{l=0}^{N_4} c^D_{ijkl} T_{2i}(\tilde{\theta}) T^*_j(\tilde{s}) T^*_k(\xi_S) T^*_l(\eta_S) \tag{4.20}$$

where $\tilde{\theta}$, ξ_S and η_S, are the normalized forms of θ', X_S, and R_S respectively as defined

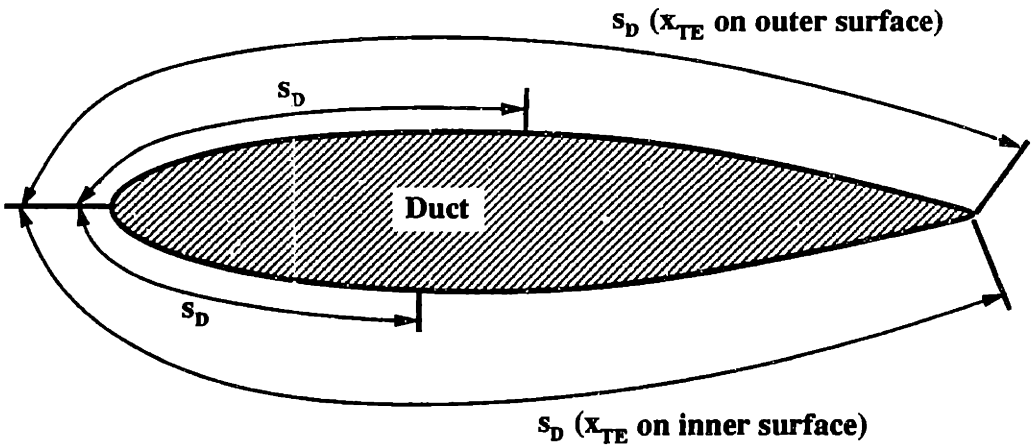

Figure 4-1: Definition of the variable s_D.

in Section 3.4.2. $\tilde{s}$ is the normalized form of s_D and is defined as follows:

$$\tilde{s} = \frac{s_D}{s_D(x_{TE})}, \tag{4.21}$$

where $s_D(x_{TE})$ is the arc length along the duct from the leading edge of the duct to the trailing edge of the duct. The value of $s_D(x_{TE})$ will be different depending on whether the point is on the inner or outer surface of the duct as shown in Figure 4-1.

As was the case for the image factor, separate expansions are established to represent $\tilde{\phi}^b$ in different regions. In this case a total of six regions are used. The domain is divided with respect to θ' and X_S in the same manner used to divide the domain when computing the image factor. Separate expansions are also created to compute $\tilde{\phi}^b$ on the inner and outer surfaces of the duct. A summary of the resulting regions is shown below.

Region 1: The source point is located inside of the duct, the field point is on the inner duct surface, and the relative angle between the source and field point is less than

θ_{sub}.

$$s_D \text{ is on the inner duct surface}$$
$$X_1 \leq X_S \leq X_{TE}$$
$$r_H(X_S) + g \leq R_S \leq r_D(X_S) - g$$
$$-\theta_{sub} \leq \theta' \leq \theta_{sub} \tag{4.22}$$

Region 2: The source point is located inside of the duct, the field point is on the inner duct surface, and the relative angle between the source and field point is greater than θ_{sub}.

$$s_D \text{ is on the inner duct surface}$$
$$X_1 \leq X_S \leq X_{TE}$$
$$r_H(X_S) + g \leq R_S \leq r_D(X_S) - g$$
$$\theta_{sub} \leq \theta' \leq 360° - \theta_{sub} \tag{4.23}$$

Region 3: The source point is located aft of the duct trailing edge, the field point is on the inner duct surface, and the relative angle between the source and field point is less than θ_{sub}.

$$s_D \text{ is on the inner duct surface}$$
$$X_{TE} \leq X_S \leq X_W$$
$$r_H(X_S) + g \leq R_S \leq R_{DWAKE} - g$$
$$-\theta_{sub} \leq \theta' \leq \theta_{sub} \tag{4.24}$$

Region 4: The source point is located aft of the duct trailing edge, the field point is on the inner duct surface, and the relative angle between the source and field point is greater than θ_{sub}.

$$s_D \text{ is on the inner duct surface}$$

$$X_{TE} \leq X_S \leq X_W$$
$$r_H(X_S) + g \leq R_S \leq R_{DWAKE} - g$$
$$\theta_{sub} \leq \theta' \leq 360° - \theta_{sub} \tag{4.25}$$

Region 5: The source point is located inside of the duct and the field point is on the outer duct surface.

$$s_D \text{ is on the outer duct surface}$$
$$X_1 \leq X_S \leq X_{TE}$$
$$r_H(X_S) + g \leq R_S \leq r_D(X_S) - g$$
$$-180° \leq \theta' \leq 180° \tag{4.26}$$

Region 6: The source point is located aft of the duct trailing edge and the field point is on the outer duct surface.

$$s_D \text{ is on the outer duct surface}$$
$$X_{TE} \leq X_S \leq X_W$$
$$r_H(X_S) + g \leq R_S \leq R_{DWAKE} - g$$
$$-180° \leq \theta' \leq 180° \tag{4.27}$$

Four regions are used for the inner surface of the duct and only two regions for the outer surface. This is done because $\tilde{\phi}^b$ varies much more sharply on the inner duct surface than on the outer duct surface. On the inner surface, Regions 1-4, $\tilde{\phi}^b$ is first divided by the value of the duct simplified image before computing the coefficients for the expansion. The expansion is then formed in terms of a function $\mathcal{G}$ which is defined below.

$$\mathcal{G}(\mathbf{x}, \boldsymbol{\xi}) = \frac{\tilde{\phi}^b(\mathbf{x}, \boldsymbol{\xi})}{G_{SID}(\mathbf{x}, \boldsymbol{\xi})}, \tag{4.28}$$

where

$$G_{SID}(\mathbf{x}, \boldsymbol{\xi}) = \frac{1}{||\boldsymbol{\xi}^I - \mathbf{x}||} + \frac{1}{||\boldsymbol{\xi} - \mathbf{x}||} \tag{4.29}$$

where $\boldsymbol{\xi}^I$ is the location of the image source used to represent the inner surface of the duct as an infinite wall as shown in Figure 3-9. The duct simplified image is the same as the simplified image, G_{SI}, defined in Section 3.3.2, except that here the potential induced directly by the source in included, and there is no image source used for the hub. G_{SID} is used to smooth out the singular behavior of $\tilde{\phi}^b$ which occurs when the source approaches a point on the duct inner surface. The idea is the same as that used to smooth out the generalized image using the image factor. This is only necessary on the inner surface of the duct, and on the outer surface, Regions 5 and 6, $\tilde{\phi}^b$ is interpolated directly. The outer surface of the duct sees no singular behavior in $\tilde{\phi}^b$. In addition, it is possible that the simplified image source might fall close to the duct outer surface, creating a singularity in $\mathcal{G}$ when none exists in $\tilde{\phi}^b$ for this case.

A separate set of coefficients are computed for each region using the procedure set forth in Section 3.4.2. After these coefficients are computed they can be used to compute the potential on the duct for any propeller and stator configuration or inflow condition. The coefficients are used both to evaluate $\tilde{\phi}^b$ and compute its derivatives for every propeller, stator, and blade wake panel. This is done using the procedure described in Section 3.4.3. The coefficients $\tilde{\phi}^b$ and $\tilde{\phi}^a$ only have to be computed for the first timestep. Equation (4.17) can then be evaluated using the stored values of $\phi_k(n)$, $\sigma_k(n)$, and $\Delta\phi_h(n)$ to obtain $\phi_j^{QSD}(n)$ at each timestep.

4.2 Correction of Duct Circulation to Account for Vortex Shedding

4.2.1 Generalized image model in steady vs. unsteady flow

As discussed at the start of this Chapter, the potentials obtained from equation (4.17) represent the "quasi-steady duct" solution. Since this equation expresses the solution on the duct in terms of a series of different steady solutions at each timestep, no mechanism exists for convecting the vorticity shed at each timestep into wake of the duct. When the generalized image model was first introduced by Kinnas and Coney

[27], it was used to accurately model the steady flow past a ducted propeller. For this steady problem, the duct coordinate system rotates along with the propeller, and the strength of the dipole sheet representing the vorticity in the duct wake is constant along the wake strips in the streamwise direction. Therefore, the generalized image model may be used without modification.

When the values of $\tilde{G}$ are calculated in order to create the Chebyshev expansions for both the image factor, $\mathcal{I}$, and the duct potential, $\tilde{\phi}^b$, the problem of the flow past the duct and hub in the absence of any inflow, but in the presence of an individual singularity is solved. When solving these problems it is assumed that the strength of the vorticity in the duct wake varies only circumferentially and does not change in the streamwise direction. This is acceptable for solving the steady problem. However, when these same values are applied to the unsteady problem, it will result in a duct wake sheet which has a different strength at each timestep, but whose strength does not change in the streamwise direction. In the actual unsteady solution, the duct will shed vorticity at each timestep. Therefore, the dipole sheet representing the duct wake will both change at each timestep and vary in the streamwise direction. The difference between the quasi-steady duct solution and the fully unsteady duct solution is shown schematically in Figure 4-3. In this chapter the method developed to account for this difference will be described.

4.3 Two Dimensional Analog Problem

4.3.1 Formulation

In order to study the problem described above and test various solutions, a two dimensional problem was developed which is analogous to a propeller operating inside of a duct in a spatially non-uniform inflow. This problem consists of two foils: a "smaller" foil which represents the propeller and a "larger" foil which represents the duct. The propeller foil is subject to the steady inflow plus a sinusoidal gust velocity. The duct foil is subject only the steady inflow, but its loading will still be unsteady

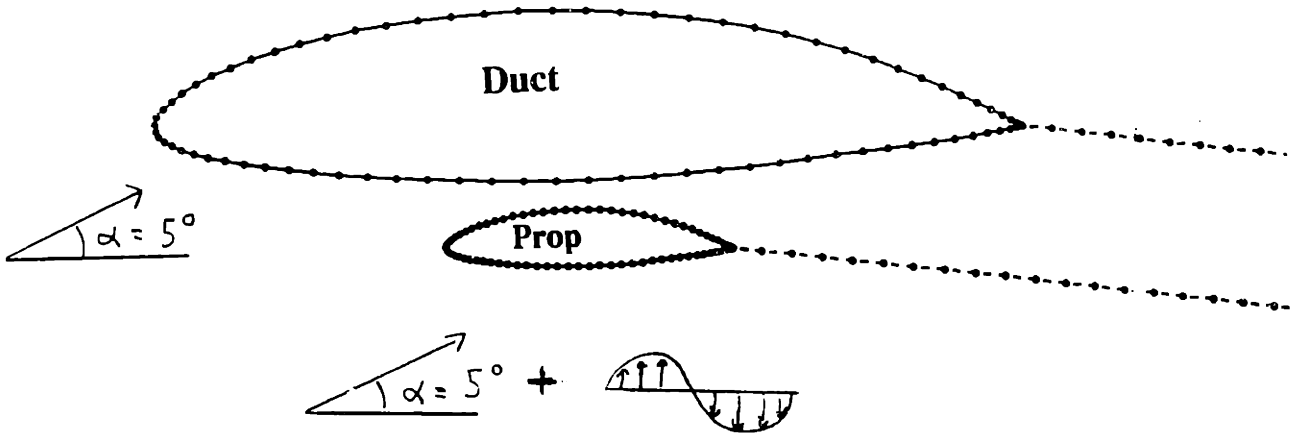

Figure 4-2: Geometry of Two Dimensional Foils Used to Examine Unsteady Duct Wake.

due to its interaction with the propeller foil. The geometry of the two foils which were used along with part of their wakes is shown in Figure 4-2.

This should accurately model the aspects of the ducted propeller problem which are of interest. In the actual problem of a ducted propeller operating in a spatially non-uniform inflow, the propeller blade will see a time-varying velocity as it rotates through wake. In the absence of the propeller, however, the duct would see a velocity field which does not vary with time, and the duct loading is unsteady only because of its interaction with the propeller blades.

This geometry and inflow condition is solved using two different methods. The problem is first solved where the strength of the duct wake is constant in the streamwise direction. This strength is allowed to change at each timestep, however, and is set equal to the difference in the potential on the upper and lower trailing edge panels of the duct foil. In two dimensions, this is equivalent to placing a point vortex at the trailing edge of the duct foil (there is also a starting vortex infinitely far downstream). This case is called the "quasi-steady duct" solution. In the second case, which is called the "fully unsteady duct" solution, the strength of the first panel of

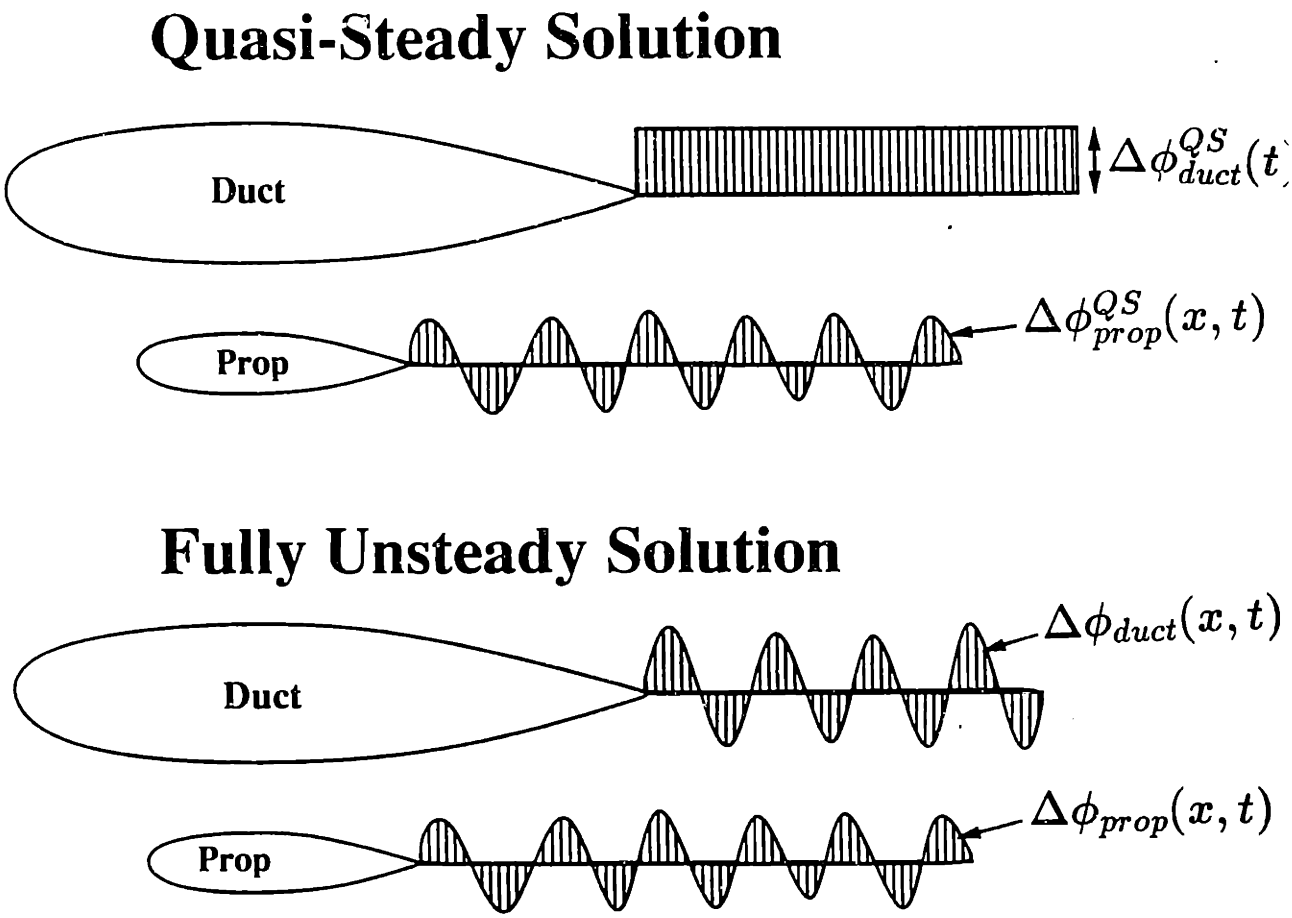

Figure 4-3: Difference between quasi-steady duct and fully unsteady duct solution for two dimensional analog problem.

the duct foil wake is set equal to the difference in potential at the trailing edge for current timestep. This value is then convected downstream producing a duct wake whose strength both changes at each timestep and varies in the streamwise direction. In both cases the smaller (propeller) foil is treated as fully unsteady. The geometry of the wakes are fixed in time. The difference between these two methods is depicted in Figure 4-3. The question addressed in the following sections is: *Can the fully unsteady duct solution be recovered from the time history of the quasi-steady duct solution?*

4.3.2 Mathematical Formulation

By applying Greens formula in the usual manner, the velocity potential on the foil surfaces for the quasi-steady duct case, ϕ^{QSD}, will satisfy the following equation:

$$\begin{aligned}\phi^{QSD} &= \int_{S_{duct}} \phi^{QSD} \frac{\partial G}{\partial n}\, dS + \int_{S_{prop}} \phi^{QSD} \frac{\partial G}{\partial n}\, dS + \Delta\phi^{QSD}_{duct}(t) \int_{W_{duct}} \frac{\partial G}{\partial n}\, dS \\ &\quad + \int_{W_{prop}} \Delta\phi^{QSD}_{prop}(x,t) \frac{\partial G}{\partial n}\, dS - \int_{S_{duct}+S_{prop}} G(-\vec{V}_{in} \cdot \hat{n})\, dS \end{aligned} \tag{4.30}$$

where:

- G is the Greens function, which in two dimensions is equal to $\ln R$, where R is the distance between the point of integration and the point at which the potential is being evaluated.
- S_{duct} is the surface of the duct foil.
- W_{duct} is the surface of the wake of the duct foil.
- S_{prop} is the surface of the propeller foil.
- W_{prop} is the surface of the wake of the propeller foil.
- $\hat{n}$ is the normal vector.
- $\Delta\phi_{duct}$ is the strength of the duct foil wake.
- $\Delta\phi_{prop}$ is the strength of the propeller foil wake.
- $\vec{V}_{in}$ is the inflow velocity, which includes a sinusoidal gust velocity on the propeller foil.

Notice that the dipole strength in the duct wake, $\Delta\phi_{duct}$, varies only with time and can, therefore, be written outside of the integral over the duct wake surface. However, the strength of the propeller foil wake, $\Delta\phi_{prop}$, varies with both time and streamwise location and must be included inside of the integral over the propeller wake.

Using the same procedure, the potential on the foils for the "fully unsteady duct" case, ϕ, satisfies the equation given below:

$$\begin{aligned}\phi &= \int_{S_{duct}} \phi \frac{\partial G}{\partial n}\, dS + \int_{S_{prop}} \phi \frac{\partial G}{\partial n}\, dS + \int_{W_{duct}} \Delta\phi_{duct}(x,t) \frac{\partial G}{\partial n}\, dS \\ &\quad + \int_{W_{prop}} \Delta\phi_{prop}(x,t) \frac{\partial G}{\partial n}\, dS - \int_{S_{duct}+S_{prop}} G(-\vec{V}_{in} \cdot \hat{n})\, dS \end{aligned} \tag{4.31}$$

Note that the strength of the duct wake, $\Delta\phi_{duct}(x,t)$, varies both in time and in the streamwise direction and must, therefore, be included inside of the integral over the duct wake surface. By subtracting equation (1) from equation (2), we get the expression for the term which must be added to the "quasi-steady duct" solution potentials to give the correct potential distribution for the fully unsteady duct case. This term will be called ϕ^{BP}, since it will eventually be expressed as the summation of a series of "Base Problem" solutions.

$$\phi^{BP} = \phi - \phi^{QSD} \tag{4.32}$$

$$\begin{aligned}\phi^{BP} &= \int_{S_{duct}} \phi^{BP} \frac{\partial G}{\partial n}\, dS + \int_{S_{prop}} \phi^{BP} \frac{\partial G}{\partial n}\, dS + \int_{W_{duct}} \left[\Delta\phi_{duct}(x,t) - \Delta\phi^{QSD}_{duct}(t)\right] \frac{\partial G}{\partial n}\, dS \\ &\quad + \int_{W_{prop}} \Delta\phi^{BP}_{prop}(x,t) \frac{\partial G}{\partial n}\, dS \end{aligned} \tag{4.33}$$

Two of the terms in the expression for ϕ^{BP} are often very small and can usually be ignored, particularly at higher frequencies and when the propeller is not close to the duct trailing edge. These terms are the integral of the potential on the propeller foil surface and the integral over the propeller foil wake sheet. For cases where the propeller is not close to the trailing edge of the duct, the inclusion of these terms is not expected to have a significant effect on the overall solution for the potential on the duct surface. This will be better understood in Section 4.3.4. In addition, the value of ϕ^{BP} on the propeller should be negligible. The expression for the correction which must be applied to the duct solution then consists of an integral over only the

duct foil surface and its wake.

$$\phi^{BP} \approx \int_{S_{duct}} \phi^{BP} \frac{\partial G}{\partial n}\, dS + \int_{W_{duct}} \left[\Delta\phi_{duct}(x,t) - \Delta\phi^{QSD}_{duct}(t)\right] \frac{\partial G}{\partial n}\, dS \qquad (4.34)$$

This is important when extending this method to three dimensions since in order to obtain the correction terms one must solve an equation only over the surface of duct without including the propeller geometry. When equation (4) is used to obtain ϕ^{BP}, the solution will be called the "full base problem" solution. When equation (5) is used, it will be called the "partial base problem" solution.

4.3.3 Implementation

The correction potential , ϕ^{BP}, may be obtained by discretizing equation (4) or (5) and solving for ϕ^{BP} at each timestep. This is done after the quasi-steady duct solution on the foil is obtained for the given timestep, so that ϕ^{QSD} and $\Delta\phi^{QSD}(t)$ are known. In addition, at a given timestep, the correction has already been applied at the previous timesteps, so that the correct fully unsteady values for the duct foil potential and wake strength, ϕ and $\Delta\phi(x,t)$, are known for all timesteps prior to the current one. For a given timestep, therefore, the difference between the correct fully unsteady duct wake strength and the quasi-steady duct wake strength, $[\Delta\phi_{duct}(x,t) - \Delta\phi^{QSD}_{duct}(t)]$, will be known over the entire wake surface except for the point right at the trailing edge of the duct foil. At the trailing edge, however, this value is equal to the jump in potential at the trailing edge of the duct foil, $(\phi^{BP}_{+} - \phi^{BP}_{-})$, obtained using equation (4) or (5). This then breaks down to form a system of linear equations which can be solved at each timestep using the same procedure which is used to obtain the quasi-steady duct solution. The terms which must be solved for at each timestep are shown schematically in Figure 4-4.

The solution to the correction potential, ϕ^{BP}, can easily be decomposed into the summation of a series of time independent base problem solutions. The base problem solutions will only have to be computed once at the first timestep. These solutions are then stored and used to modify the quasi-steady duct solution at all of the following

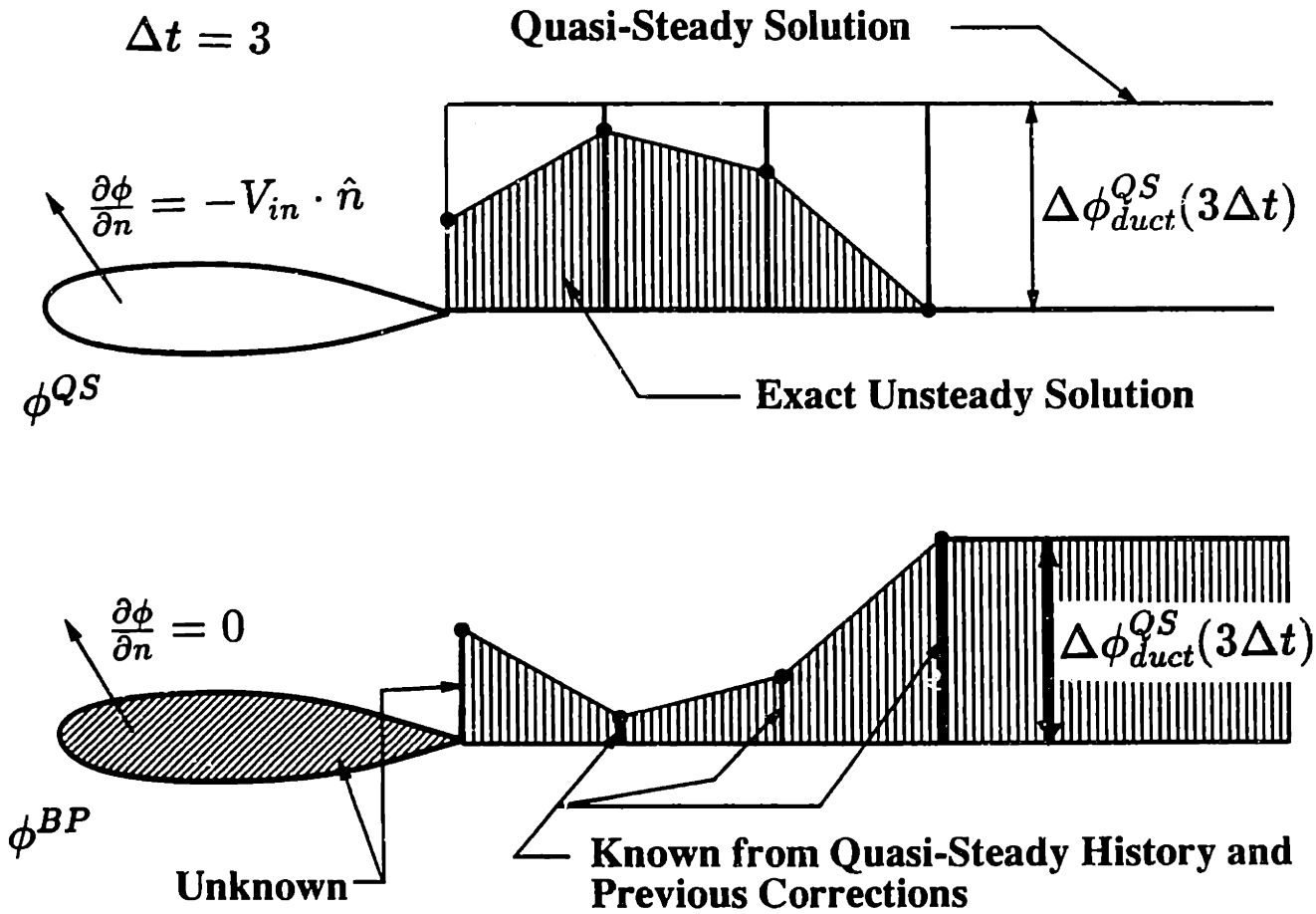

Figure 4-4: Modification to quasi-steady duct potential on foil required to produce fully unsteady duct potential.

timesteps. This process is shown schematically in Figure 4-5. For the partial base problem solution, only the duct foil geometry is used. The solution for the potential on the duct foil is obtained for the case where the inflow velocity and the dipole strength of the wake panels are both set equal to zero, except for one duct wake panel which has a strength equal to unity. This is repeated for each duct wake panel. On the first wake panel, a linear dipole distribution is used which is set equal to the jump in potential on the duct foil at the trailing edge at the left edge of the panel and set equal to zero at the right edge of the panel. The solution for the correction potential, ϕ^{BP}, can then be expressed as the summation of these base problem solutions, multiplied by the difference in the duct wake strength between the fully unsteady duct solution and the quasi-steady duct solution at the corresponding streamwise location in the wake as shown in equation (6). The first two base problems must be treated in a special way in order to handle the linear dipole distribution on the first duct wake panel.

$$\begin{aligned}\phi^{BP} &= \varphi_0\left[\Delta\phi^{QSD}(t) - \Delta\phi(x_1,t)\right] + \varphi_1\frac{1}{2}\left[\Delta\phi(x_1,t) - \Delta\phi(x_2,t)\right] \\ &\quad +\varphi_2\left[\Delta\phi^{QSD}(t) - \frac{1}{2}\left(\Delta\phi(x_2,t) + \Delta\phi(x_3,t)\right)\right] + \cdots \\ &\quad +\varphi_N\left[\Delta\phi^{QSD}(t) - \frac{1}{2}\left(\Delta\phi(x_N,t) + \Delta\phi(x_{N+1},t)\right)\right] \qquad (4.35)\end{aligned}$$

where φ_n is the potential on the duct foil from the base problem solution for the n^{th} duct wake panel. The values for ϕ, ϕ^{QSD}, ϕ^{BP}, and φ_n are all solved for the same grid of duct control points.

The correct value for the vorticity shed by the duct foil at this timestep is then equal to the difference in the jump in the corrected potential, $(\phi^{QSD} + \phi^{BP})$, at the trailing edge. This can also be obtained by correcting the quasi-steady duct wake strength directly, using the shed vorticity at the trailing edge from each of the base problem solutions.

$$\Delta\phi(x_0,t) = \Delta\phi^{QSD}(t) + D_0\left[\Delta\phi^{QSD}(t) - \Delta\phi(x_1,t)\right] + D_1\frac{1}{2}\left[\Delta\phi(x_1,t) - \Delta\phi(x_2,t)\right]$$

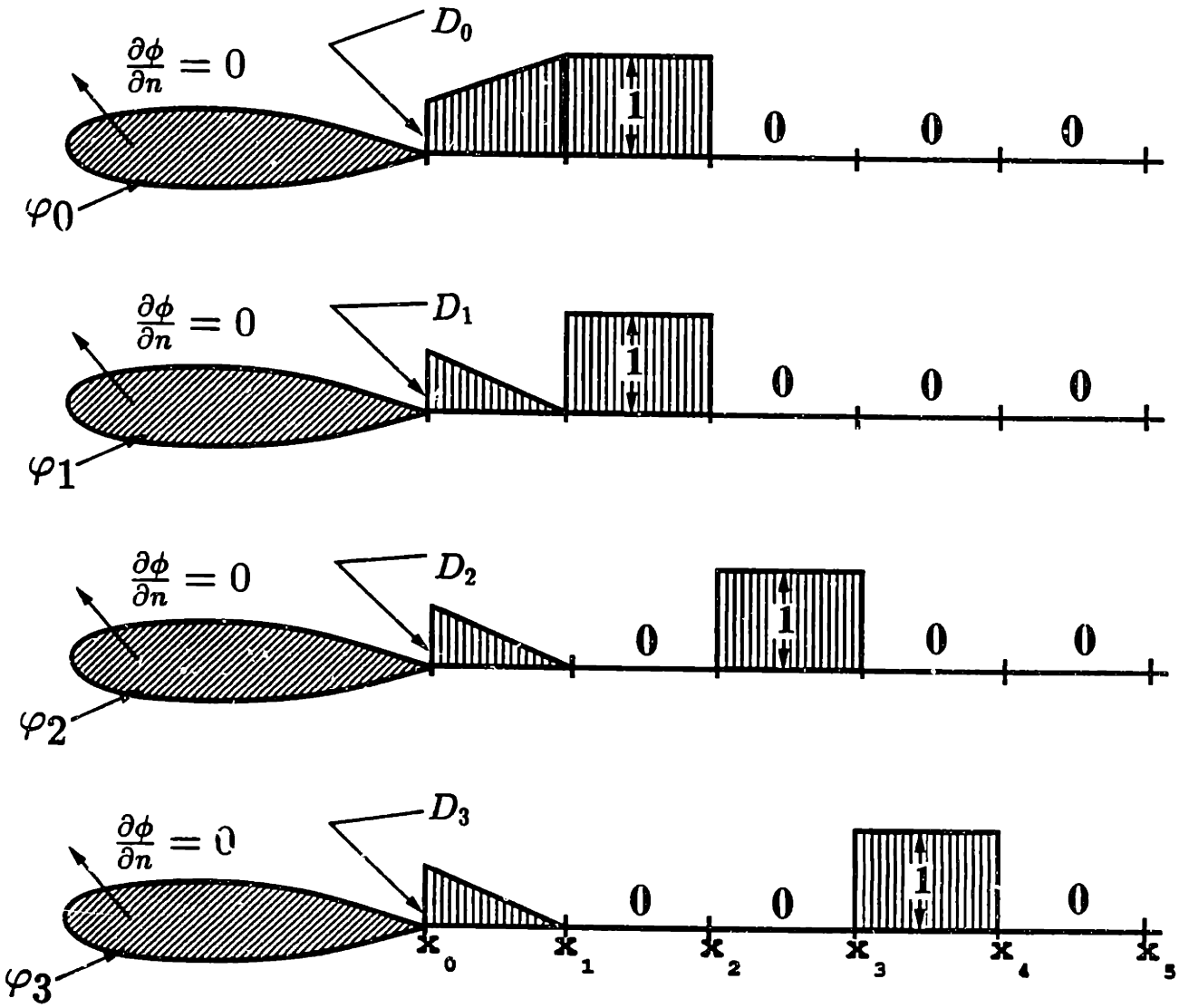

Figure 4-5: Correction potential expressed in terms of base problem solutions.

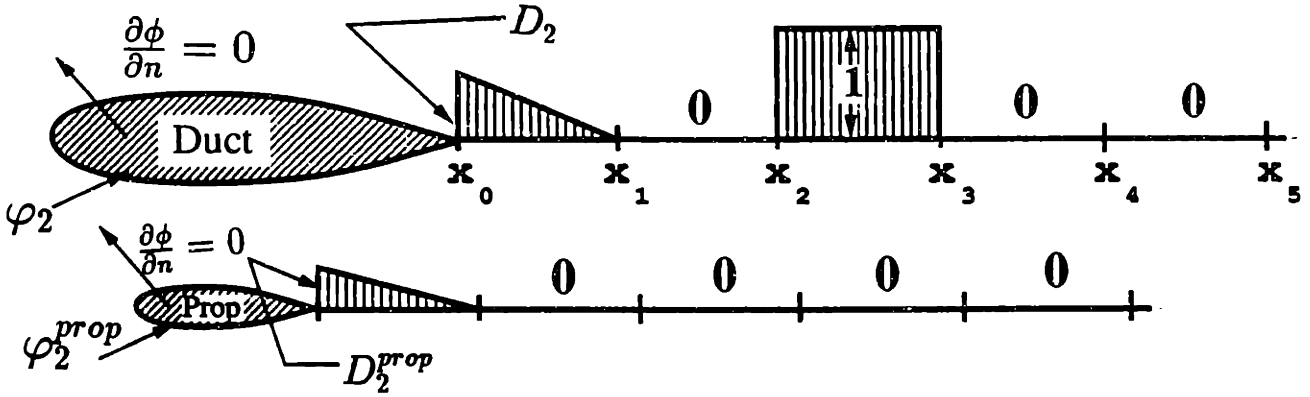

Figure 4-6: The full base problem solution.

$$+D_2\left[\Delta\phi^{QSD}(t) - \frac{1}{2}\left(\Delta\phi(x_2,t) + \Delta\phi(x_3,t)\right)\right] + \cdots$$
$$+D_N\left[\Delta\phi^{QSD}(t) - \frac{1}{2}\left(\Delta\phi(x_N,t) + \Delta\phi(x_{N+1},t)\right)\right] \qquad (4.36)$$

where D_n is the jump in potential at the trailing edge of the duct foil from the base problem solution for the n^{th} duct wake panel.

The procedure works the same way for the "full base problem" solution except that the kinematic boundary condition must also be satisfied on the propeller foil for each of the base problem solutions. This is shown schematically in Figure 4-6. The base problems only have to be computed for the duct wake panels. The strength of the propeller wake panels are set to zero, except for the first propeller wake panel which has a linear dipole distribution, equal to zero at the right end of the panel and the potential jump at the trailing edge of the propeller foil at the left end of the panel.

4.3.4 Results

The flow past the test geometry shown in Figure 4-2 was solved using both the method producing the quasi-steady duct solution and the fully unsteady duct solution. The results shown are for a reduced frequency, $k = \frac{\omega c}{2U}$, of 4.0, based on the chord length of the propeller foil, and a gust amplitude equal to 20% of the inflow velocity. The

quasi-steady duct solutions were then corrected using both the full base problem solution and the partial base problem solution. Figure 4-7 shows the results for the lift coefficient on the duct foil over a complete period. The results are compared for the fully unsteady duct solution, the quasi-steady duct solution, and the quasi-steady duct solution modified by the partial base problem solution. This shows that there is a relatively large discrepancy in the lift coefficient obtained from the quasi-steady duct and fully unsteady duct solutions, and that this discrepancy is nearly eliminated through the addition of the partial base problem solution. Figure 4-8 shows the same comparison, except that this time full base problem solution is used to correct the quasi-steady duct results. In this case the discrepancy between the fully unsteady duct and quasi-steady duct solutions is *completely* eliminated by the addition of the full base problem solution. This was expected, since the full base problem solution is defined to be difference between the fully unsteady duct and quasi-steady duct solutions. The partial base problem, however, is generally adequate in accounting for the vorticity shed by the duct foil. In addition, the partial base problem solution is more efficient when the procedure is extended to three dimensions, since knowledge of the propeller geometry is not required.

Figure 4-9 shows the results for the lift coefficient on the propeller foil over one period. A comparison is given between the fully unsteady duct and quasi-steady duct solutions and the quasi-steady duct solution corrected with the full base problem solution. The partial base problem solution will have no effect on the propeller foil, as in that case the potentials will only be modified on the duct foil. The figure shows that virtually no discrepancy exists between the lift coefficients on the propeller foil obtained using the quasi-steady duct and fully unsteady duct solutions. What little discrepancy does exist is eliminated completely by the addition of the full base problem solution.

4.3.5 Extension to Three Dimensions

The extension of the method to treat the vorticity shed by the duct in the ducted propulsor problem has been implemented in a straightforward manner. Currently only

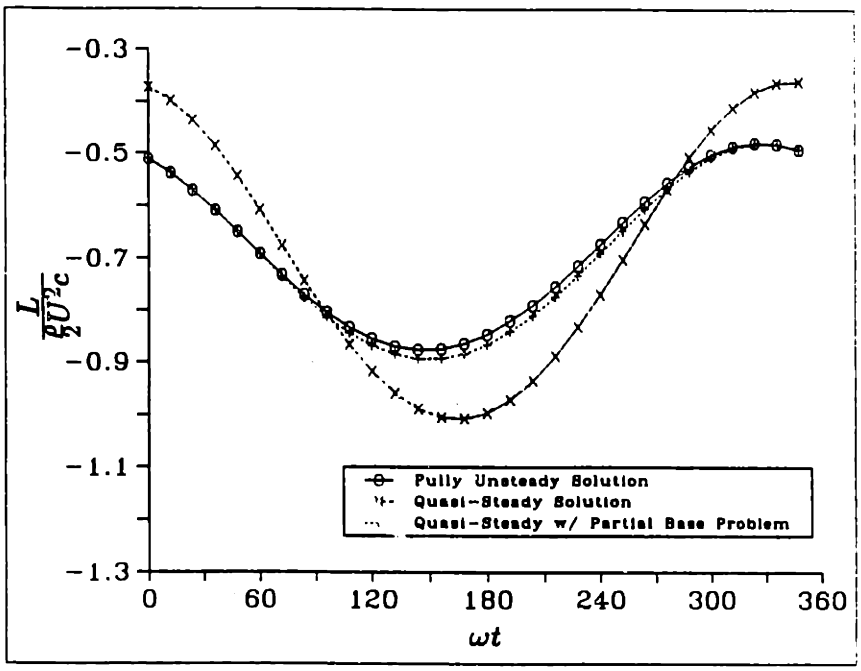

Figure 4-7: Lift coefficient on duct foil over one period with partial base problem correction.

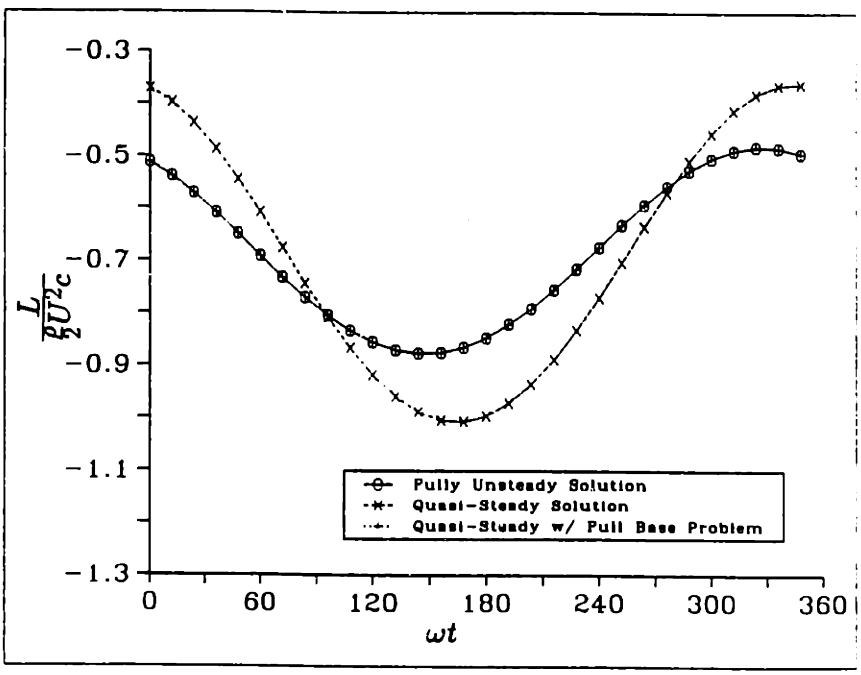

Figure 4-8: Lift coefficient on duct foil over one period with full base problem correction.

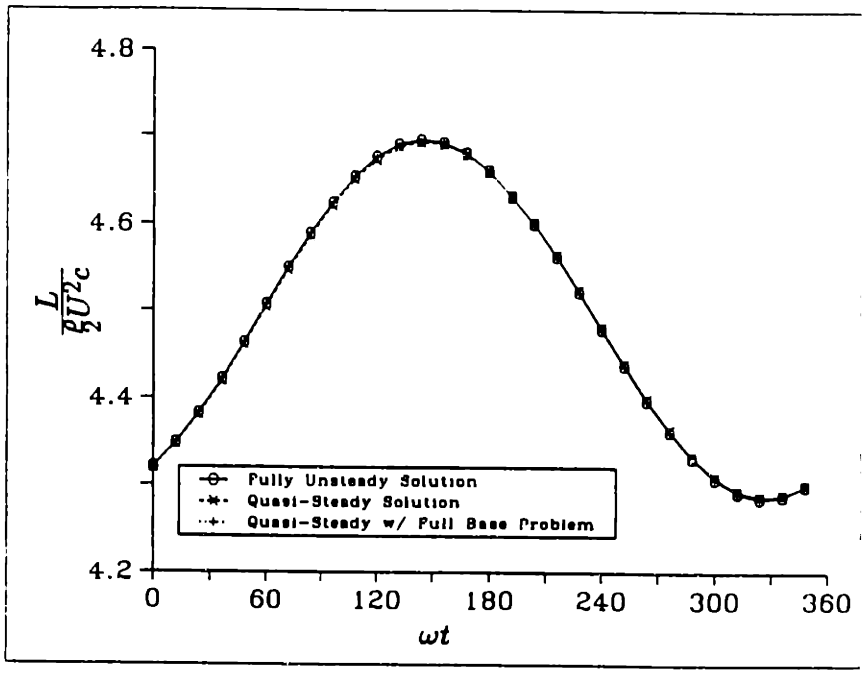

Figure 4-9: Lift coefficient on propeller foil over one period with full base problem correction.

the partial base problem solution is used. By taking advantage of the axisymmetry of the duct geometry, the base problems have to be solved only for the panels along a single chordwise duct strip, and the propeller and stator geometries are not involved. The first several base problems are solved using triangular panels in order to better represent the direction of the vorticity in the duct wake. It has been found that only the base problems representing the section of the duct wake corresponding to about half a propeller revolution have a significant impact on the solution. Therefore, after this point one additional base problem is used which applies the steady duct wake strength to remainder of the duct wake. The first several base problems are shown schematically in Figure 4-10. The length of the duct wake panels is determined from the timestep. The base problems will consist of solving for the potential on the duct with zero inflow, and with all of the duct wake panel strengths set equal to zero except for one wake panel which will have a strength of unity. The first wake panel at each circumferential position will have a linear dipole distribution set equal to zero at the right edge and equal to the jump in potential on the duct surface at the trailing edge at the left edge. A typical example is shown in Figure 4-11.

For cases where the propeller or stators are very close to the duct trailing edge and the reduced frequency is low, the full base problem solution may need to be

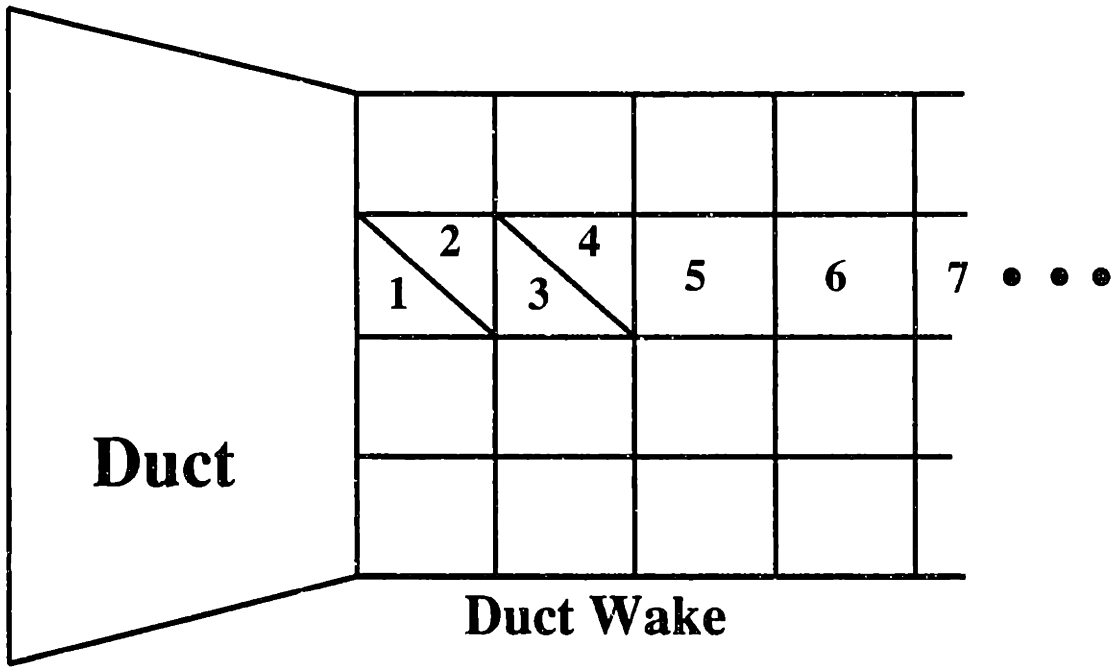

Figure 4-10: Base problems used to correct for duct shed vorticity.

used. In this case the problem will no longer be axisymmetric due to the presence of the propeller and stator blades. Therefore, this will require the base problems to be solved for all of the duct wake panels. As in the two dimensional case, however, each of these base problems will only have to be solved once before the first timestep. The base problem solutions are then stored and used to modify the quasi-steady duct solution at each timestep.

Since the perturbation potential on the duct is now expressed partly in terms of an expansion of Chebyshev polynomials, it is possible to obtain the perturbation velocity by differentiating these polynomials directly, rather than applying a finite difference method to the values of the potential computed at the duct control points. This would be done by differentiating both $\tilde{\phi}^b$ and $\tilde{\phi}^a$ with respect θ' and s_D. This method might have some advantages, in that the alignment of the panels on the duct might be less critical. However, the component of the perturbation velocity from ϕ_D would still have to be computed using finite differences. In addition, this approach will make it more difficult to perturb the solution when applying the iterative pressure Kutta condition. In the current model, the perturbation velocity is obtained by first fitting a piecewise

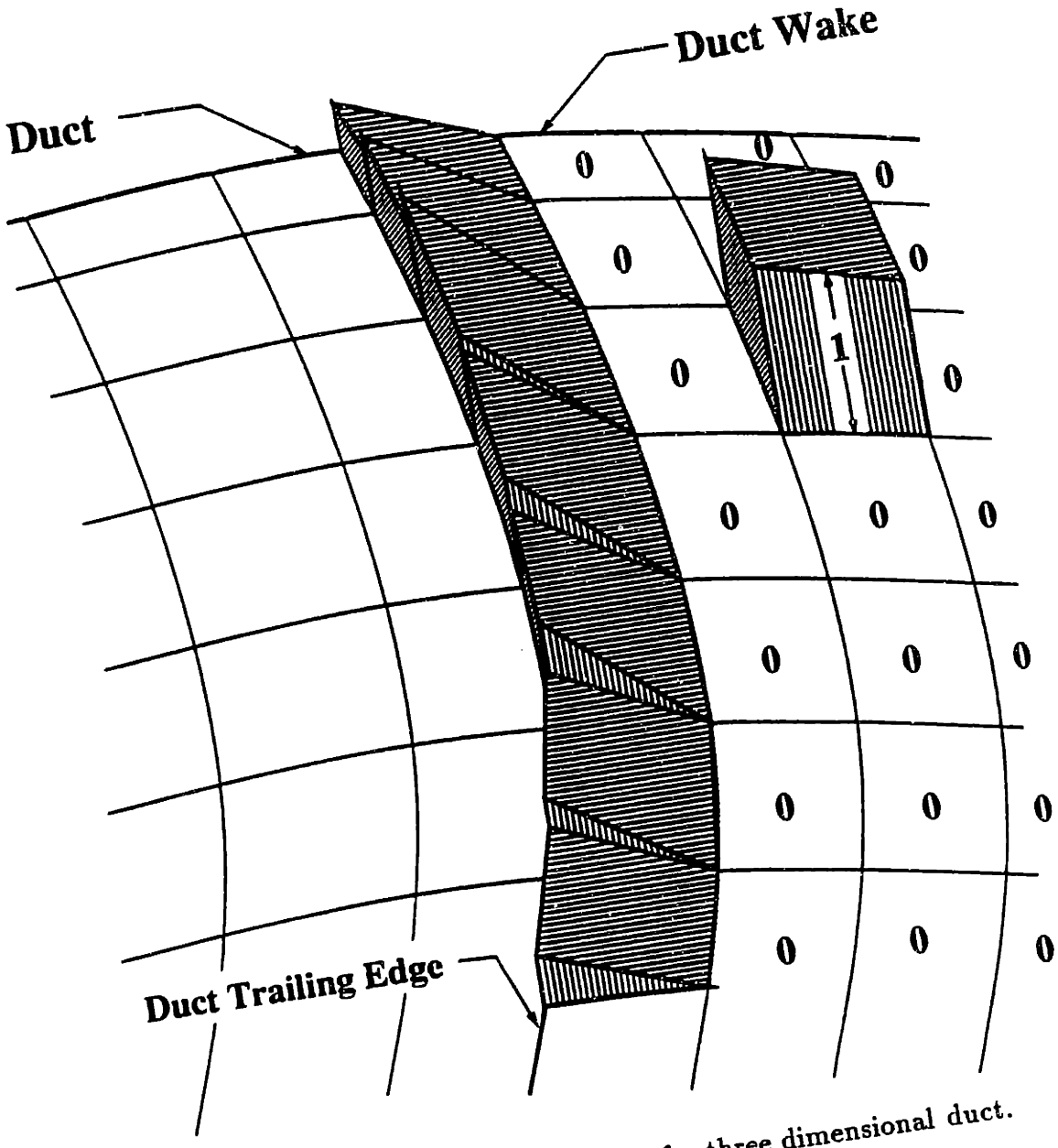

Figure 4-11: Base problem solution for three dimensional duct.

cubic spline through the potentials in the circumferential direction at each chordwise control point position. This spline is used to shift the potentials onto a control point grid which uses the same chordwise spacing but is aligned with the propeller and propeller wake. This is done carefully, using a separate spline between each set of blades. The circumferential perturbation velocity is obtained directly from the cubic spline used to shift the potentials onto the aligned grid. The chordwise perturbation velocity is obtained using a centered difference method along the aligned chordwise strips. This procedure was found necessary to avoid errors which occurred when applying a finite difference method using the straight grid where the control points used for the centered difference lied on opposite sides of the trace of the propeller wake along the duct surface. Observations of the velocity vectors computed along the duct surface show a sharp increase in the velocity across the trace of the propeller wake on the duct surface as shown by Figure 6-21 in Section 6.3.1. The difference between the aligned and straight duct grids are similar to those shown in Figures 6-1 and 6-3.

Chapter 5

Analysis of the Flow in the Tip Clearance Region

5.1 Special characteristic of the flow through the tip clearance

One of the difficulties in the analysis of ducted propellers is the accurate treatment of the flow through the clearance between the interior surface of the duct and the tip of the propeller. This flow is termed the gap flow, tip clearance flow, or leakage flow. For a typical ducted propeller, the gap is only a fraction of a percent of the propeller diameter. This raises some concern as to whether viscous effects are important in this region. Even in the case where the clearance flow is primarily inviscid, a more detailed local solution is required in order to accurately represent the flow through this gap. The huge difference in length scale causes an error for the local flow through the gap when solving for the flow past the propulsor using potential flow analysis. Unfortunately, this error in the local gap flow has a major influence on the global flow and must be accounted for.

A similar problem occurs in the analysis of axial flow turbomachinery, and significant work has been done in that field with regard to this problem. Several investigators of this problem have concluded that this leakage flow is largely inviscid in

nature at normal gap clearance levels [41] [1]. In addition, the leakage volume rate is not heavily dependent on the chordwise flow [39]. This allows for the use of simple two dimensional experiments to investigate the flow in this region.

Experimental work concerning the flow in the tip clearance region has been carried out by Shalnev [40], Gearhart [10], Booth, Dodge and Hepworth [1], and Wadia and Booth [41]. A review of these experiments has been made by Van Houten [39]. These experiments showed that the flow through the gap is highly dependent upon the geometry of the tip. For the case of a square tip, it was found that the corner at the entrance of the gap causes a separation bubble which reattaches to the blade tip. This separation bubble results in the leakage flow being less than would otherwise be predicted. In addition, the jet at the exit of the gap results in the rolling up of a vortex on the suction side of the blade. Wadia and Booth [41] concluded that the leakage flow was dominated by balance of pressure and convection and could be modeled as a special kind of orifice.

The effect of the tip clearance flow on the global potential flow solution was studied by Kerwin et al. [23] by examining the flow past a lifting line of span s and constant downwash $w^* = 1$ traveling near an infinite wall. It was shown that as the distance between the tip of the lifting line and the wall, h, becomes very small ($h/s = 0.0025$), the velocities produced inside the gap exceed 50 times the downwash velocity. Furthermore, these unrealistically large gap velocities significantly affect the global solution for the circulation on the lifting line. In this thesis, the goal is not to obtain an accurate local solution for the detailed flow in the clearance region, but rather to capture the effect of this flow on the global solution. A simple empirical model will be applied to predict the correct mean velocity and flow volume through the clearance region. This will then be coupled with the potential flow solution for the global flow through the propulsor. It may be presumed that the major impact of the clearance gap on the global flow solution is the resulting leakage flow volume [39].

5.2 Rectangular foil next to an infinite wall

The effect of the clearance flow on the global solution may be examined by considering a rectangular foil traveling near an infinite wall. For the foil examined in this work, the maximum thickness of the cross section is 10% of the chord length and the maximum camber is 4% of the chord length. The foil has an aspect ratio of 2.9. The foil lies in the $z = 0$ plane and the wall is formed by the $y = 0$ plane. The distance between the foil and the wall is h, and the foil has a span of about $s = 1.0$ (The actual span is equal to $1.0 - h$). The incoming flow, U_∞ is inclined at an angle of attack α with respect to the foil.

The potential flow solution is first obtained using a potential based panel method. The grid used to obtain this solution for the case $h = 0.02$ is shown in Figure 5-1. Cosine spacing is used in both the chordwise and spanwise directions. There are 40 panels placed around the foil in the chordwise direction and 20 in the spanwise direction. The presence of the wall is accounted for by including a simple image foil which is also shown in Figure 5-1. The image foil geometry and grid are identical to that of the real foil geometry and grid, except the y coordinates for all of the image foil grid points are the negative of their counterparts on the real foil. Since the resulting solution will be symmetrical about the $y = 0$ plane, it is only necessary to solve for the potential on the real foil. Figure 5-2 shows the spanwise distribution of circulation computed on the foil for various gap ratios at $\alpha = 4$ degrees. The lowest curve represents a relatively large gap, $h = 0.04$, while the next three curves show the effect on the circulation as the gap is successively halved. The top curve shows the circulation resulting from the zero gap case, where the wall has the effect of creating the same flow that would result around a foil of twice the span in the absence of the wall. This figure shows that even for extremely small gaps, the potential flow solution produces a large loss in the lift at the tip of the blade compared with the zero gap solution, and that an infinitesimal change in the gap results in a large change in the global solution. The potential flow solution also results in a huge velocity through the tip clearance region which will not occur in a real flow. It is this unrealistically large

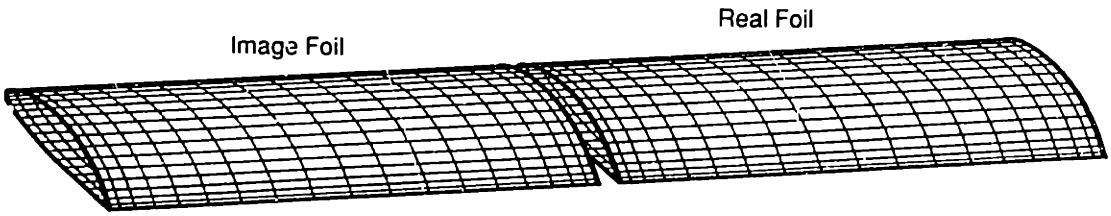

Figure 5-1: Panel arrangement for a rectangular foil together with its image, $h = 0.02$

velocity through the clearance region which causes the error in the global solution for the distribution of loading on the blade.

5.3 Treating the gap as a porous foil

The first step in incorporating the clearance flow model into a panel method solution for the flow past a ducted propeller is to obtain an expression for the correct leakage volume flow though the clearance. This can be obtained by treating the local flow in this region as that of a two-dimensional orifice. The velocity can be related to the difference in pressure across the tip of the blade using Bernoulli's equation. The reduction in the flow from losses in the orifice is generally expressed in terms of an empirically determined discharge coefficient, which is defined as:

$$C_Q = \frac{Q}{h}\sqrt{\frac{\rho}{2\Delta p}} \tag{5.1}$$

where:

- Q is the total volume flow through the gap
- Δp is the difference in pressure across the gap
- ρ is the fluid density
- h is the clearance height.

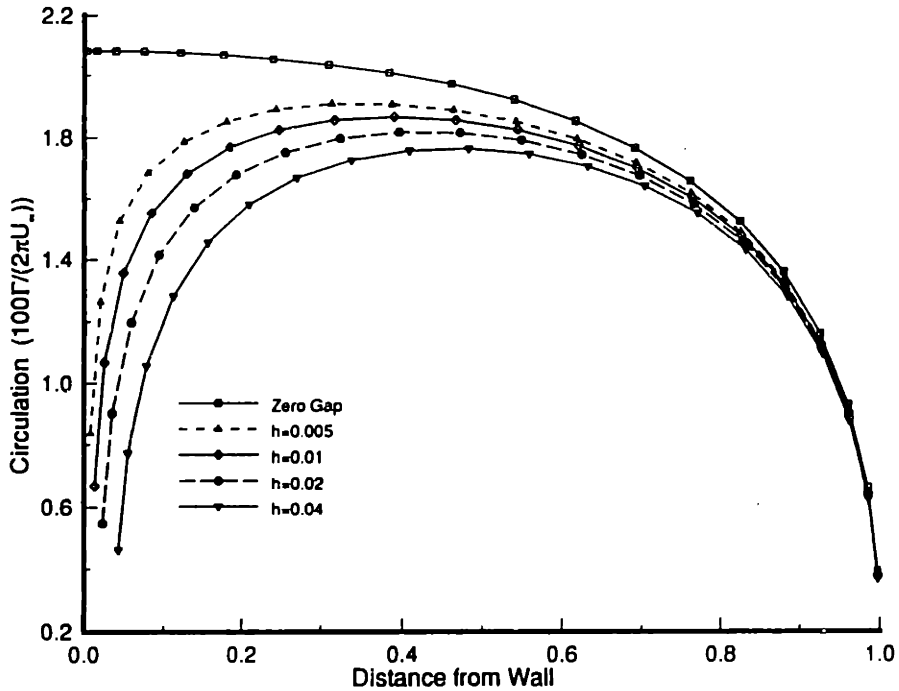

Figure 5-2: Spanwise distribution of circulation for a set of foils with varying gap distances from an infinite wall. The circulation is obtained from potential flow for $\alpha = 4°$.

It was shown through a series of experiments by Booth et al. [1] that C_Q is independent of the gap clearance height, h, and the chordwise velocity along the blade. However, C_Q is a strong function of the blade tip shape. The pressure side of the blade tip is often rounded off which may eliminate flow separation in the gap resulting in a higher value of C_Q. The boundary layer on the surface of the duct and the relative motion of the duct surface with respect to the blade tip may also have a strong influence on the value of C_Q. For the analysis shown in the following examples, a value of $C_Q = 0.84$ is used. This represents the mean of the values extracted from the turbomachinery literature by Van Houten [39]. It is conceivable that the value for the discharge coefficient could be obtained using a two-dimensional Navier-Stokes solution for the local clearance flow of a desired tip geometry. An example of this type of solution is described in [41].

Using equation 5.1, the mean velocity through the gap at a given chordwise location can be expressed in terms of the difference in pressure between the pressure and

suction sides of the blade at that location:

$$w_R = C_Q \sqrt{\frac{2\Delta p}{\rho}} = |\mathbf{U}_{in}| \, C_Q \sqrt{\Delta C_P} \tag{5.2}$$

where:

- w_R is the mean relative flow velocity through the gap
- $\mathbf{U}_{in}$ is the local inflow velocity relative to the blade as defined in Chapter 2.
- C_P is the pressure coefficient on the blade at the tip, which is defined as:

$$C_P = \frac{p - p_\infty}{\frac{1}{2}\rho \mathbf{U}_{in}^2} \tag{5.3}$$

To incorporate this expression for the mean velocity into the panel method scheme, an additional row of panels is introduced which closes the gap. In the case of the foil traveling near an infinite wall, these panels connect the foil with its image. The resulting paneling for the same geometry described earlier is shown in Figure 5-3. The additional panels which close the gap are shown as the shaded panels in this figure. An additional row of wake panels is added as well, which connect the real foil wake with the wake of the image foil. This has the effect of adding some loading in the clearance region which does not exist in the potential flow solution and indicates that the fluid in the clearance does some work on the propeller blade. This is similar to the "retained lift theory" used by Lakshminarayana [29], where the drop in pressure (or total enthalpy) across the gap is taken as a fraction of the drop in pressure across the blade. In support of this theory, it has been noted that some of the fluid which exits the gap has actually passed through part of the blade region and over the blade tip, leaving the gap in the form of a rolled up tip vortex. This fluid has done some work on the blade. By introducing the fictitious blade in the gap, this work is accounted for [9].

As discussed in Chapter 2, the boundary condition on the foil is typically satisfied by setting the source distribution on each panel, $\frac{\partial \phi}{\partial n}$, to cancel the normal component

of the inflow velocity.

$$\frac{\partial \phi}{\partial n} = -\mathbf{U}_{in} \cdot \hat{n} \tag{5.4}$$

This satisfies the kinematic boundary condition of zero normal velocity on the foil surface. For the panels in the gap region, this is no longer the desired boundary condition. The new boundary condition for these panels should be that the velocity normal to the panel surface equal the normal component of w_R at the same chordwise location along the blade tip. It is assumed that the direction of w_R is normal to the mean camber surface of the blade section at the tip. The new boundary condition for the gap panels can be satisfied by specifying the source distribution on these panels using the following expression:

$$\frac{\partial \phi}{\partial n} = |\mathbf{U}_{in}| \, C_Q \sqrt{\Delta C_P} \hat{n} \cdot \hat{n}_c - \mathbf{U}_{in} \cdot \hat{n} \tag{5.5}$$

where $\hat{n}$ is the unit normal vector to the panel surface, and $\hat{n}_c$ is the unit normal vector to the mean camber surface at the blade tip at the same chordwise location as the panel. The value for ΔC_P is obtained by an iterative procedure. The problem for the potential distribution on the foil is first solved as if the gap were completely sealed by using Equation 5.4 to specify the source strengths for the gap panels. The pressure distribution is then computed by differentiating these potentials using a finite difference scheme. The value for ΔC_P is taken to be the difference between C_P on the blade tip panel adjacent to the gap panel and C_P on the blade tip panel on the opposite side of the blade at the same chordwise location. The problem for the potential on the foil is then solved again with the boundary condition on the gap panels now specified by Equation 5.5. The pressures on the foil are then recomputed and used to update the boundary condition on the gap panels. The solution converges within several iterations. Figure 5-4 shows the effect of implementing the gap model for the foil geometry shown in Figures 5-1 and 5-3 for the same range of gap sizes studied in Figure 5-2. These results show a continuous trend from large gap to zero gap which is more consistent with experimental findings than the pure potential flow results shown in Figure 5-2. The results for the smallest gap studied ($h = 0.005$)

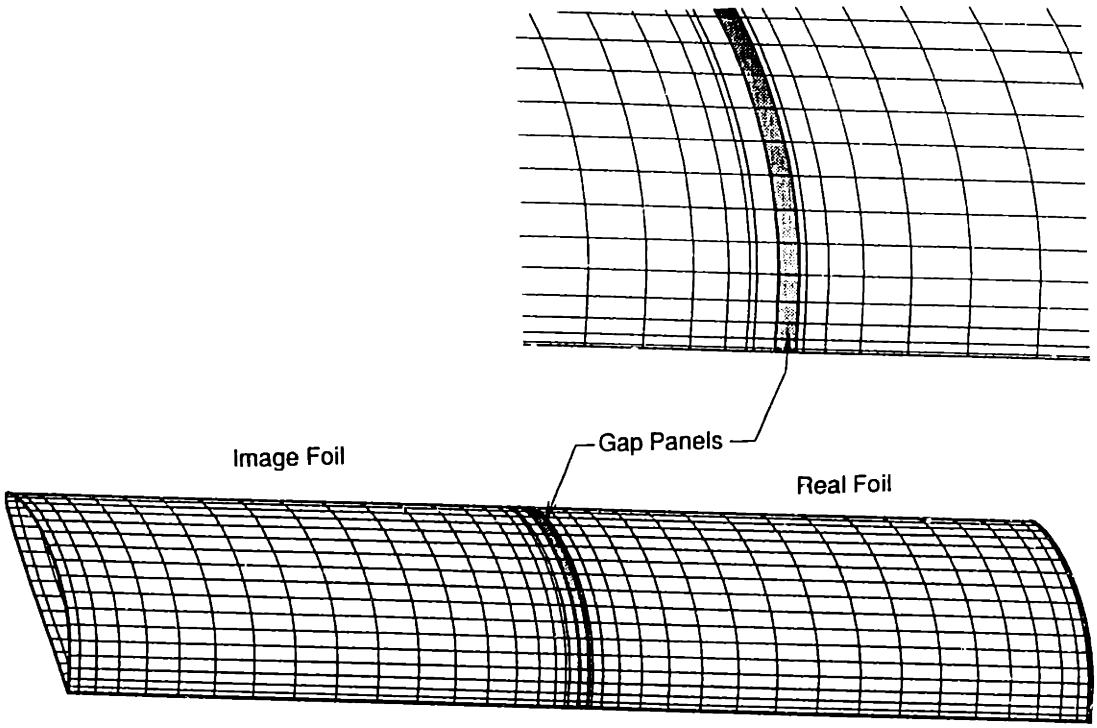

Figure 5-3: Panel arrangement for a rectangular foil together with its image, including the additional gap panels, $h = 0.02$

are almost identical to the zero gap results, while the results for the largest gap ($h = 0.04$) approach the potential flow solution. This is the desired outcome, as the potential flow solution should be adequate for large gap sizes, while at the same time, the idealization of representing the clearance flow as that through a two-dimensional orifice becomes less realistic for large gaps.

The sensitivity of the solution to the discharge coefficient, C_Q is shown in Figure 5-5. This comparison is done for a constant gap size of $h = 0.02$. The foil geometry is the same as that used earlier. The value of C_Q is varied from 0.6 to 1.0. The lower values of C_Q are closer to the zero gap solution as expected. In fact, the zero gap solution can be produced by setting $C_Q = 0$, since this will apply the zero normal velocity boundary condition on the gap panels. $C_Q = 1$ represents the case where there is no energy lost by the fluid as it passes through the gap, and the velocity is obtained by a direct application of Bernoulli's equation. It is evident from Figure 5-5 that a wide variation in C_Q has a relatively small effect on the global solution. This is a fortunate result, because it means that any reasonable estimate for the discharge

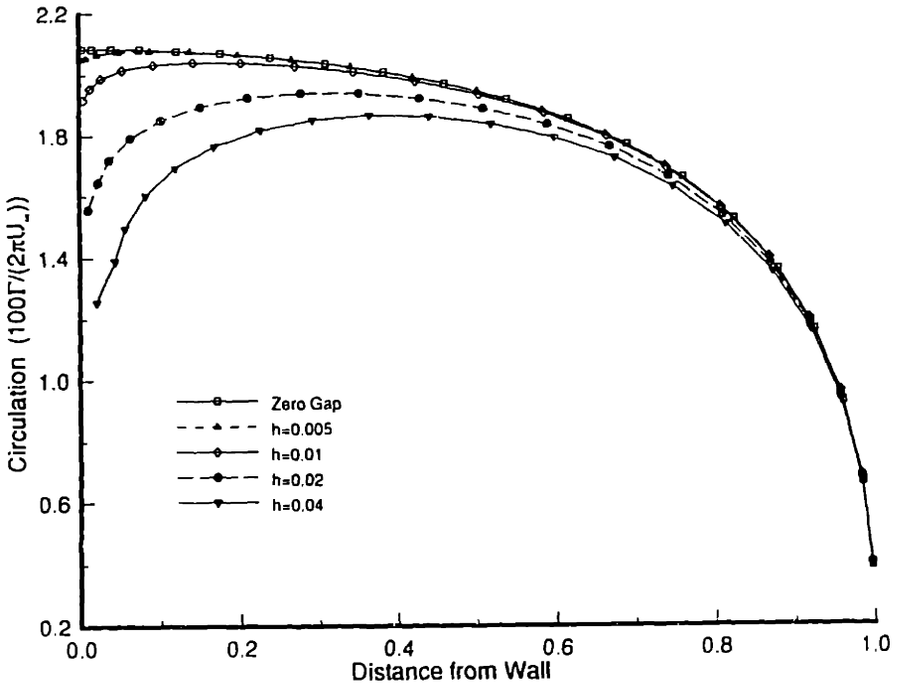

Figure 5-4: Spanwise distribution of circulation for a set of foils with varying gap distances from an infinite wall. The angle of attack is 4 degrees. The gap flow is controlled using a discharge coefficient of $C_Q = 0.84$.

coefficient will produce a substantial improvement in the accuracy of the method when compared to the potential flow solution.

Figure 5-6 demonstrates the effect of loading on the solution after the gap model has been incorporated. This plot is identical to Figure 5-4 except the loading has been roughly doubled by increasing the angle of attack from 4 to 8 degrees. It can be seen that the increase in loading has the effect of creating a slightly more "sealed" gap. This suggests that the influence of the clearance flow has the undesirable effect of augmenting unsteady forces, since as the loading increases, the gap will appear more sealed, thus further increasing the loading.

Finally, a convergence test was made to study the effect of panel density on the solution for the spanwise distribution of circulation on the blade after the inclusion of the gap model. This test was made for $h = 0.02$ and $\alpha = 4°$. Figure 5-7 shows the results of this convergence test. The convergence of the solution with panel density does not appear to be affected by the inclusion of the gap model.

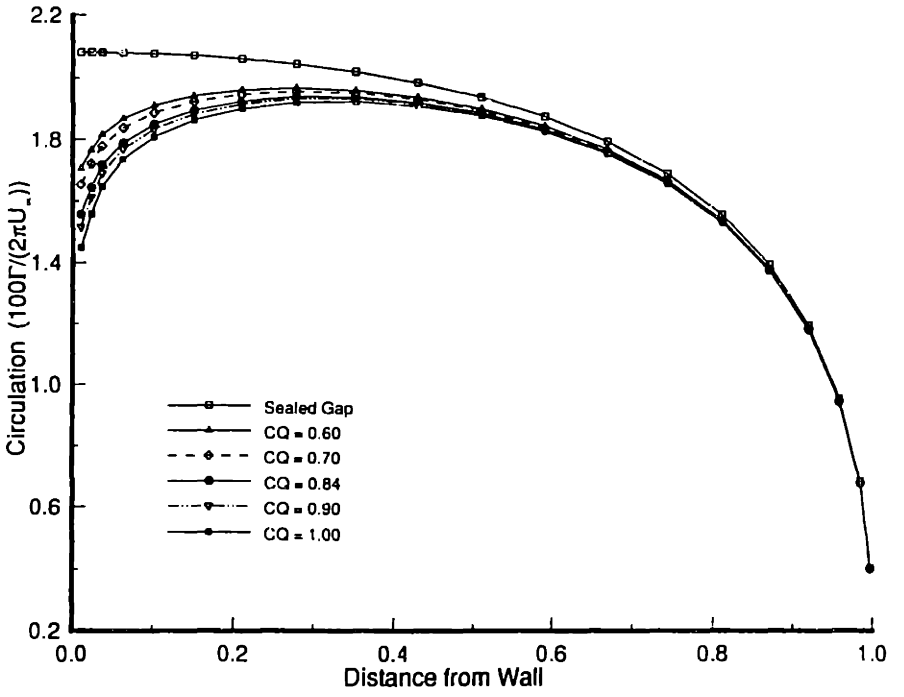

Figure 5-5: Sensitivity of the circulation distribution on the foil to the discharge coefficient, C_Q. $h = 0.02$ and $\alpha = 4°$.

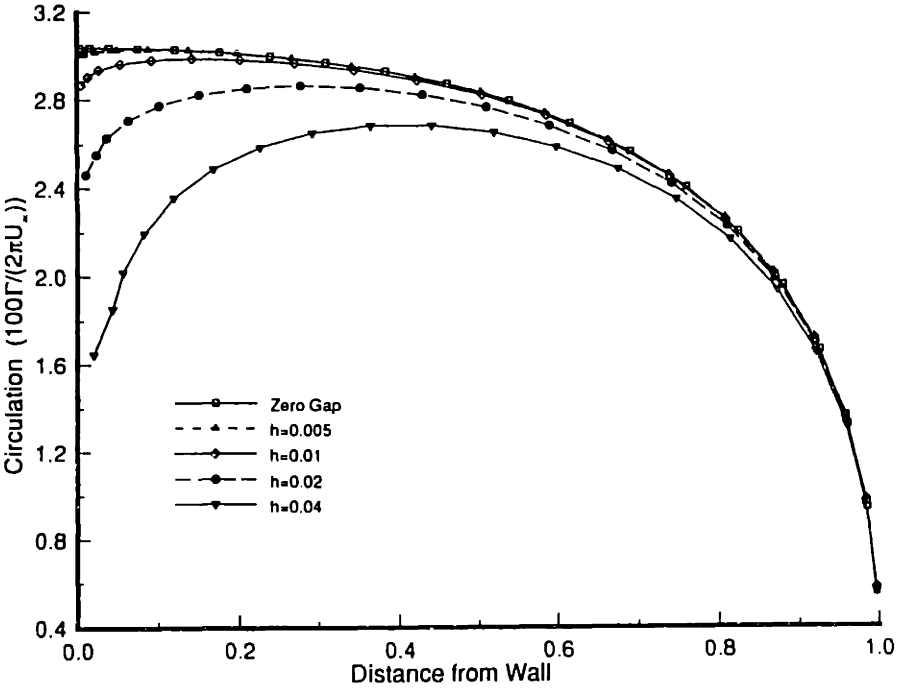

Figure 5-6: Spanwise distribution of circulation for a set of foils with varying gap distances from an infinite wall. The angle of attack is 8 degrees. The gap flow is controlled using a discharge coefficient of $C_Q = 0.84$.

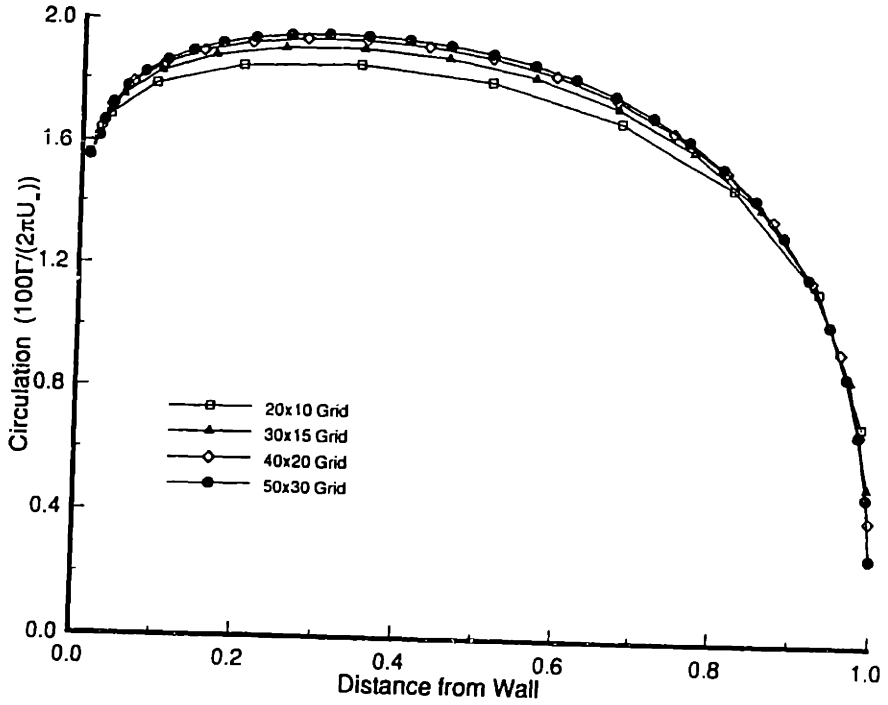

Figure 5-7: Convergence of the spanwise distribution of circulation for a foil near an infinite wall. $h = 0.02$ and $\alpha = 4°$.

5.4 Implementation of the gap model in a steady ducted propeller panel method

The model described in the previous section was also implemented into a steady flow ducted propeller panel method. This method was then applied to the three bladed ducted propeller whose geometry is described in Section 6.1. The grid and geometry used is shown in Figure 5-8. Note that only a third of the duct and hub and one of the propeller blades are shown. The additional panels used to model the gap are the shaded panels in this figure. The grid on the duct surface is aligned both with the propeller blade and its wake. In this case, the pressure difference across the gap, which is used to apply the boundary condition to the gap panels, is determined using only the pressure distribution computed on the blade surface. The pressure distribution on the duct surface is not incorporated into the gap model. The wake strip connected to the row of gap panels fills the gap between the duct inner surface and the top row of wake panels on the real blade wake. This wake strip continues past the duct

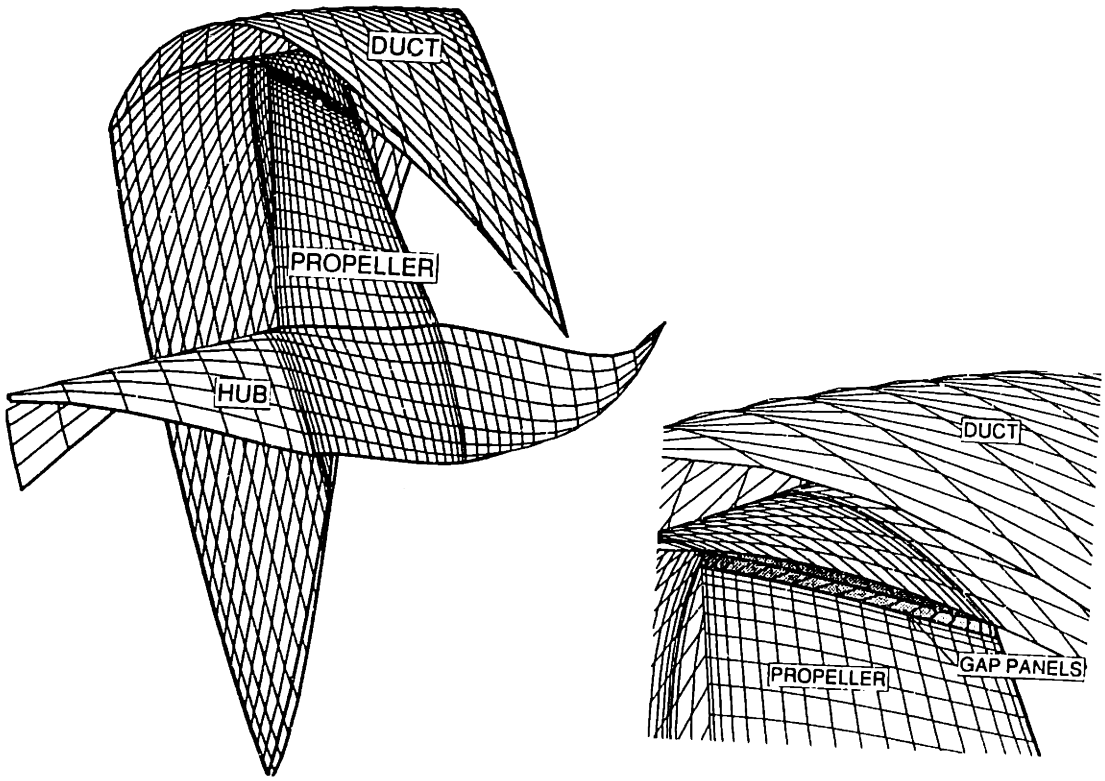

Figure 5-8: Geometry and grid for the panel method solution for a ducted propeller incorporating an additional row of panels to model the gap.

trailing edge, filling the gap between the duct wake and the real blade wake. The solution is obtained in an iterative manner using the same procedure described for the foil traveling near an infinite wall. In this case, some damping is required for the solution to converge quickly. The results for the spanwise distribution of circulation on the propeller blade at an advance coefficient of 0.833 are shown in Figure 5-9. This is compared with the results for the same geometry where the gap is completely sealed and with the results from the potential flow solution in the absence of the gap model. The size of the gap is 1.8% of the propeller radius, and a value of $C_Q = 0.84$ was used. It can be seen that the pure potential flow solution produces zero loading at the propeller tip while the loading is near its maximum at the tip for the zero gap solution. The solution which incorporates the gap model produces what appears to be a very realistic result, with some reduction in loading at the tip due to presence of the gap. The gap model has the same effect as it had in the case of the foil traveling near an infinite wall.

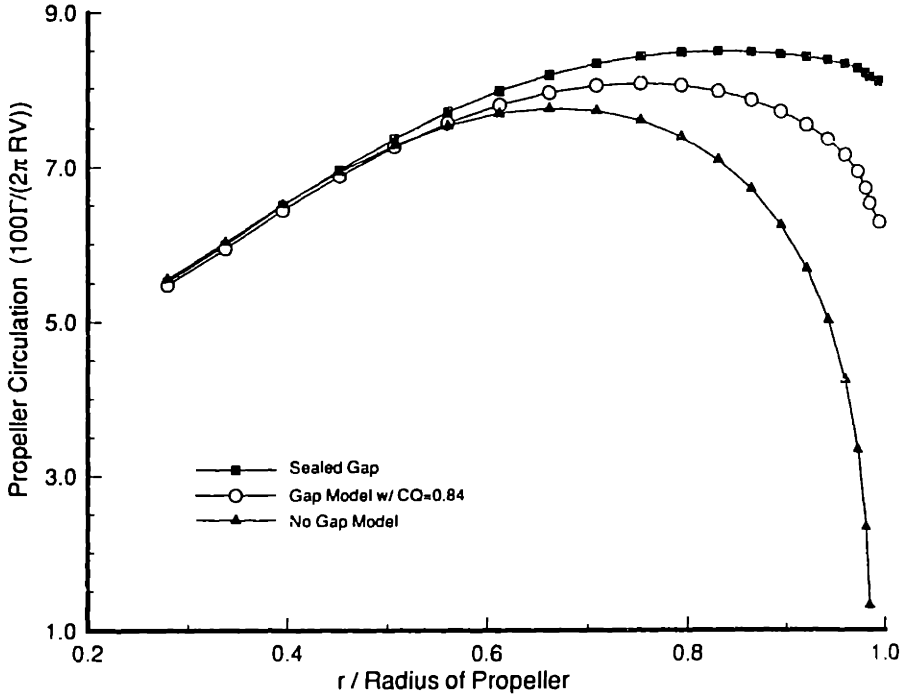

Figure 5-9: Spanwise distribution of circulation on the propeller blade with zero gap, 1.8% gap with orifice equation applied to gap flow, and 1.8% gap pure potential flow.

The circumferential distribution of circulation on the duct is shown in Figure 5-10. These results are also compared with the zero gap solution and pure potential flow solution. The results are shown for the section of the duct which lies between two propeller blades. In the potential flow solution there is no jump in the circulation on the duct due to the propeller blade. The zero gap solution and the solution which incorporates the gap model produce a jump in the circulation distribution on the duct which equals the circulation at the tip of the propeller blade (or at the tip of the fictitious blade inside the gap for the gap model solution). This is the expected result, since if the gap is very small, some of the circulation on the propeller should be transfered onto the duct.

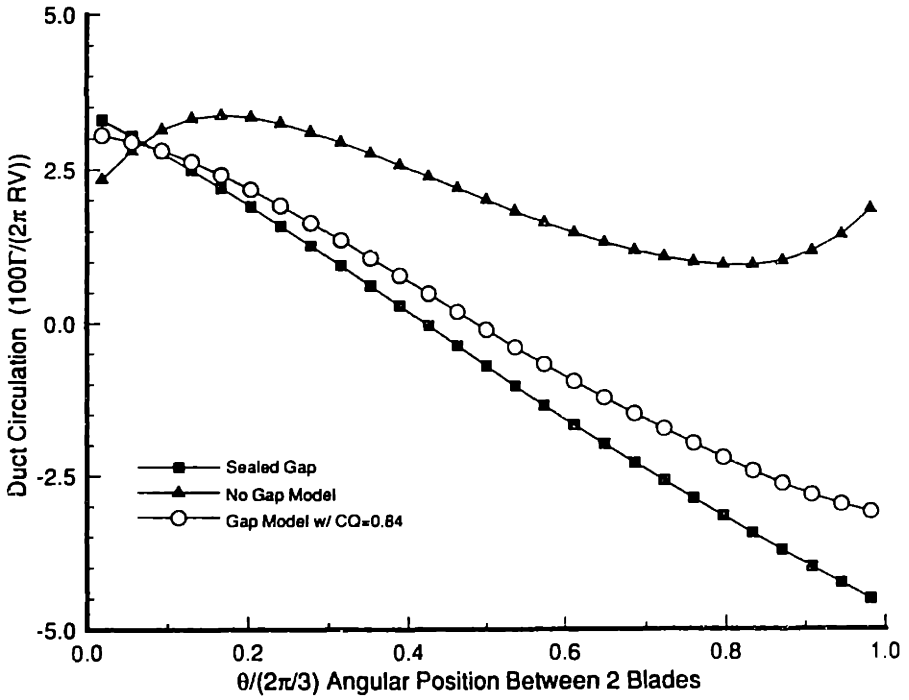

Figure 5-10: Circumferential distribution of circulation on the duct with zero gap, 1.8% gap with orifice equation applied to gap flow, and 1.8% gap pure potential flow.

Chapter 6

Analysis of Computational Results

In this chapter the results of the computational method presented in Chapters 2 through 4 are analyzed. Ideally, in order to validate the complete model, a comparison between the results produced by this method and the results from an unsteady panel method which models all components directly would be made. However, no such model was available to us at the time of this work. A method was available for computing the steady flow past a single component ducted propeller using a direct panel method. Therefore, the results are first discussed for a single component ducted propeller in steady flow. These results are obtained from the current method by examining the propulsor in a uniform inflow. The distributions of circulation on both the propeller and duct are examined. For the purpose of this comparison the code name "PSF10T" will be used to represent the direct panel method and the code name "DPUF10" will be used to represent the method presented in this thesis. The PSF10T code [16] was developed at MIT originally to examine propellers with attached tip sections and has been slightly modified in order to solve for the steady potential flow past a ducted propeller. The results for a ducted propeller with a set of pre-swirl stator blades operating in a uniform inflow are also examined using the current method.

A exhaustive analysis of the convergence and consistency of the open propeller analysis method PUF10, on which DPUF10 is based, is given in [15]. In [15], the convergence is analyzed with respect to the number of panels used in both the span-

wise and chordwise directions as well as the size of the timestep and number of propeller revolutions. It is expected that the convergence properties of the current method should be similar in this respect, although the far field approximation used when computing the generalized images may have an effect on the required number of panels. The convergence of the generalized image with respect to the number of panels used on the duct and hub and the number of terms retained in the Chebyshev polynomial expansion of the image factor was demonstrated in Chapter 3. A brief examination of the effect of the generalized image model on the convergence with respect to the number of panels on the propeller is provided in this chapter.

No systematic comparison of the method with experimental results is given. Unfortunately, there is not any experimental data for the unsteady forces on multi-component ducted propulsors available in the open literature. Therefore, this thesis attempts only to show that the results of the method are convergent and consistent with existing methods for the steady flow case. Results are also shown for both a single and multiple component ducted propulsor operating in non-uniform flow, and the reasonableness of these results is investigated.

6.1 Description of Test Geometries

The method is used to predict the flow past two ducted propulsor configurations. The first configuration is a three-bladed single component ducted propeller. The blade geometry of the propeller is given in Table 6.1 and the geometry of the duct is given in Table 6.2. The hub consists of a cylinder whose radius is constant and equal to 25% of the propeller radius. The gap between the inner surface of the duct and the tip of the propeller is 3% of the propeller radius. Table 6.3 shows the terminology used in defining the propeller geometry. Figures 6-1 and 6-3 show the geometry for the single component propulsor.

The second configuration consists of a two-bladed ducted propulsor with a set of three pre-swirl stator blades. A slightly longer duct with the same basic geometry is used for this propulsor in order to fit the additional blade row. The geometry for this

Hub/Diameter ratio:	0.25
Section meanline:	NACA a=0.8
Thickness form:	modified NACA66

r/R	P/D	x_m/D	θ_m	c/D	f/c	t/D
0.25	1.50	0.00	0.00	0.244	0.0227	0.0285
0.30	1.50	0.00	0.00	0.246	0.0232	0.0266
0.40	1.50	0.00	0.00	0.249	0.0233	0.0228
0.50	1.50	0.00	0.00	0.250	0.0218	0.0190
0.60	1.50	0.00	0.00	0.249	0.0205	0.0152
0.70	1.50	0.00	0.00	0.246	0.0200	0.0114
0.80	1.50	0.00	0.00	0.241	0.0197	0.0076
0.90	1.50	0.00	0.00	0.234	0.0192	0.0038
0.95	1.50	0.00	0.00	0.230	0.0189	0.0019
1.00	1.50	0.00	0.00	0.225	0.0184	0.0000

Table 6.1: The geometry of the test propeller.

Duct Inner Surface		Duct Outer Surface	
x/R	r/R	x/R	r/R
0.000	1.100	0.000	1.100
0.052	1.072	0.050	1.124
0.102	1.061	0.099	1.131
0.154	1.052	0.150	1.136
0.202	1.044	0.198	1.138
0.296	1.030	0.306	1.139
0.401	1.017	0.396	1.136
0.494	1.009	0.504	1.127
0.603	1.003	0.597	1.114
0.707	1.002	0.701	1.094
0.801	1.004	0.807	1.068
0.849	1.005	0.853	1.056
0.900	1.007	0.903	1.041
0.948	1.010	0.950	1.027
0.996	1.013	0.996	1.013

Table 6.2: The duct offsets for the single component ducted propulsor. All distances are non-dimensionalized with respect to the propeller radius, and x/R represents the distance from the duct leading edge. The propeller midchord is located at x/R=0.5.

Dimensional	Nondimensional	Representation
R	1	propeller radius
r	r/R	local radius
ϕ	P/D $= 2\pi r \tan\phi/D$	pitch angle
x_m	x_m/D	rake
θ_m	θ_m	skew in degrees
c	c/D	chord length of section
f	f/c	maximum camber of section
t	t/D	maximum thickness of section

Table 6.3: Definition of propeller geometry terms.

duct is given in Table 6.4. The same propeller blade geometry is used for both the single and two component test cases, although for the two-component configuration only two blades are used. The gap between the tip of the propeller and the duct inner surface is still 3% of the propeller radius. The stator blades consist of three evenly spaced straight foils with NACA66 thickness forms, no rake or skew and constant thickness, camber, chord length, and pitch angle over the span. The geometry of the stator blades are summarized in Table 6.5. The geometry of the complete two component propulsor is shown in Figure 6-10. In the remainder of this chapter, the two configurations discussed in this section will be referred to as simply the single component propulsor and the two component propulsor.

6.2 Uniform Flow Results - Comparison with Steady Results

6.2.1 Solution on propeller

In order to check the consistency of the method, the single component propulsor described in the previous section, was analyzed in a uniform inflow to produce the steady solution from the unsteady analysis method. These results were then compared to the results from an existing method, PSF10T, which solves the steady problem directly, without the use of generalized images for the same geometry. The panelization used

Duct Inner Surface		Duct Outer Surface	
x/R	r/R	x/R	r/R
0.000	1.231	0.000	1.230
0.047	1.189	0.052	1.271
0.099	1.172	0.107	1.288
0.151	1.160	0.159	1.300
0.190	1.152	0.200	1.307
0.307	1.132	0.319	1.323
0.417	1.115	0.401	1.332
0.508	1.102	0.523	1.340
0.710	1.078	0.726	1.347
0.893	1.059	0.910	1.347
1.084	1.043	1.102	1.342
1.280	1.032	1.298	1.327
1.513	1.028	1.530	1.298
1.701	1.030	1.716	1.267
1.912	1.037	1.923	1.225
2.008	1.041	2.018	1.203
2.098	1.047	2.107	1.182
2.207	1.054	2.213	1.155
2.299	1.061	2.304	1.131
2.407	1.070	2.409	1.102
2.456	1.074	2.457	1.088
2.495	1.077	2.495	1.077

Table 6.4: The duct offsets for the two component ducted propulsor. All distances are non-dimensionalized with respect to the propeller radius, and x/R represents the distance from the duct leading edge. The propeller midchord is located at x/R=1.65 and the stator blades are centered at x/R=0.75

Section meanline	NACA a=0.8
Thickness form	modified NACA66
Pitch Angle	80.0°
c/D	0.30
f/c	0.01
t/D	0.02

Table 6.5: The stator geometry used for the two component ducted propulsor.

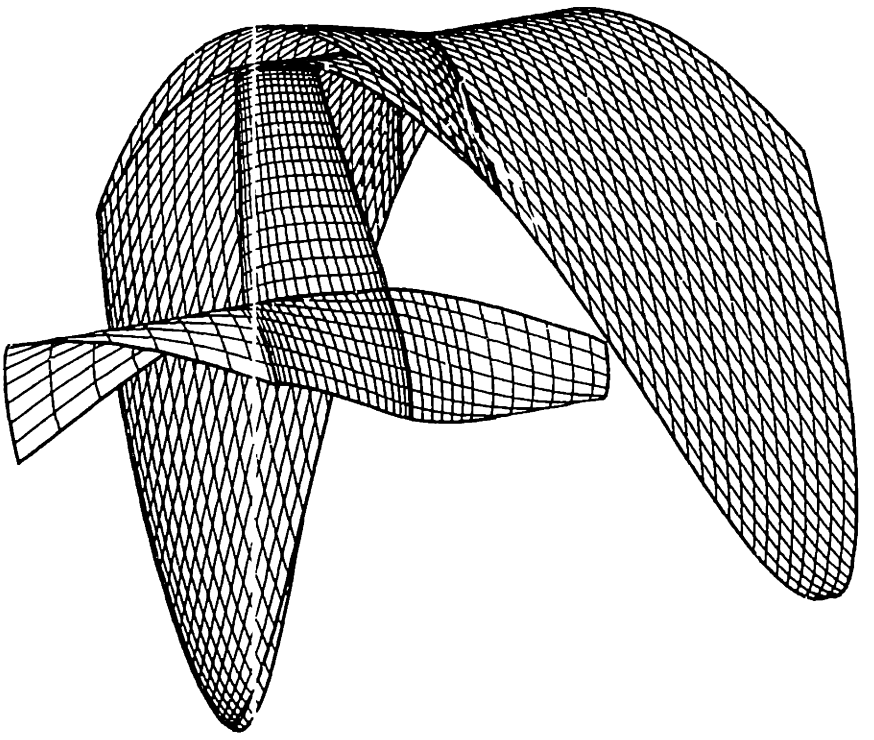

Figure 6-1: Geometry and panelization of the single component propulsor; Only one of the three blades and a third of the duct and hub is shown. The pitch of the duct and duct wake paneling is aligned with the propeller blade pitch at the tip.

for PSF10T is shown in Figure 6-1. The panelization used for DPUF10 is identical for the propeller and the propeller wake. The propeller wake geometry is shown in Figure 3-2. Figure 6-2 shows the comparison between the present method and the direct method for the spanwise distribution of circulation on the propeller blade. The small differences result from the slightly different numerical implementation used in the two methods.

In order to examine the effect of the assumption that the difference between the "quasi-steady duct" solution and "fully unsteady duct" solution is small on the propeller, PSF10T was also run using the panelization shown in Figure 6-3. Even though PSF10T produces a steady solution with respect to the rotating propeller coordinate system, if the duct is viewed from a stationary coordinate system, the circumferential distribution of circulation on the duct will vary with time as the

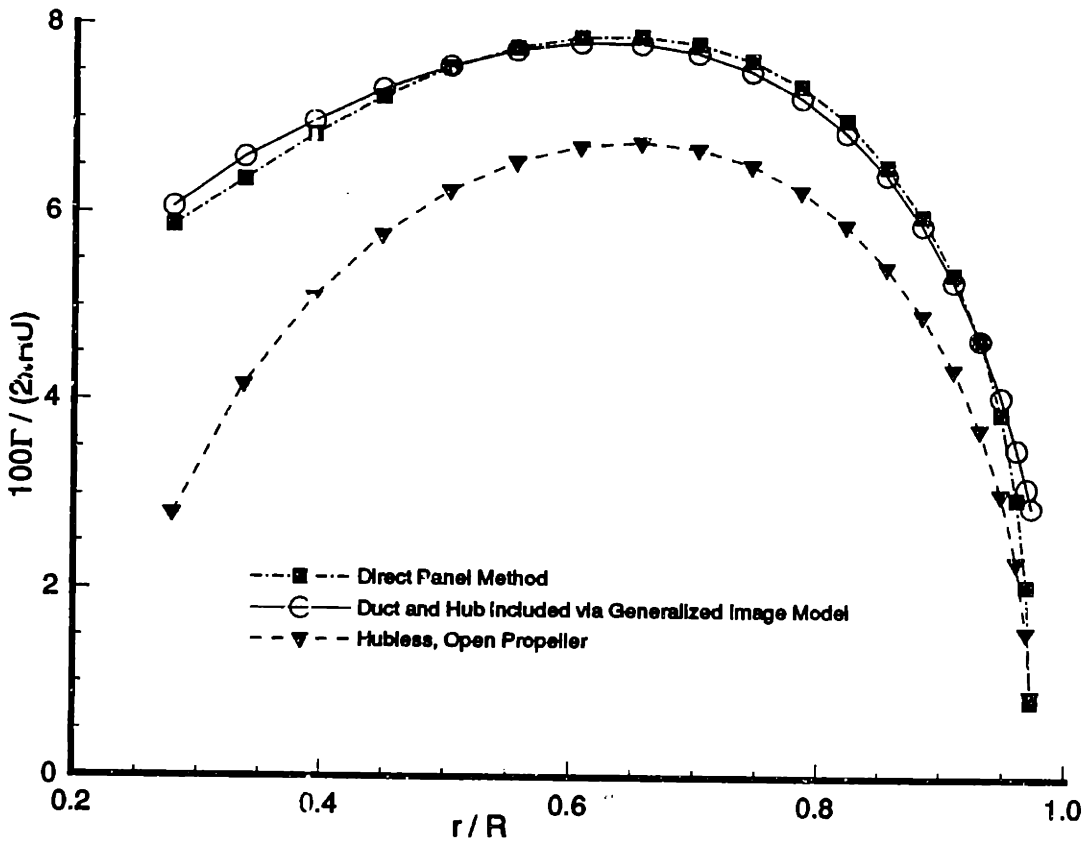

Figure 6-2: Spanwise distribution of circulation on the propeller for the single component propeller in steady flow; $J = 0.833$.

propeller rotates inside the duct. Vorticity will be shed at each point along the duct trailing edge, and this vorticity will be convected downstream producing a wake sheet on which the vorticity in constant along streamlines that rotate along with the propeller. Therefore, modeling the duct using the straight back wake shown in Figure 6-3 should have the same effect as the quasi-steady duct solution. Figure 6-4 shows that there is little difference between the steady solution for the circulation on the propeller resulting the direction of the vorticity in the duct wake. This result is for the case where the propeller is located axially in the center of the duct. The effect would likely be greater if the propeller is located close to the duct trailing edge. The convergence of the present method with number of panels is shown in Figure 6-5. It can be seen that there is a slight variation near the hub as the number of panels is increased. This may be attributable to the far-field approximation used when computing the generalized images. Since half-cosine spacing is used on the propeller blade, there are large propeller panels adjacent to the hub. Approximating the generalized images for these panels with those for point singularities at the panel centroids may lead to inaccuracies in the solution near the hub. As the number of panels increases, the size of the panels adjacent to the hub will decrease, and the far-field approximation should become more accurate.

6.2.2 Solution on the Duct

As discussed in Chapter 4 the "quasi-steady duct" solution is first computed on the duct, and then the fully unsteady duct solution is recovered from the QSD solution at all timesteps. After the fully unsteady duct solution is obtained, an iterative pressure Kutta condition is applied in order to ensure that there is no jump in pressure across the trailing edge of the duct. Since the duct is examined in the non-rotating coordinate system, the solution on the duct will be unsteady due to its interaction with the propeller, even though the inflow is uniform. As discussed in the previous section, the solution from a direct panel method which uses a straight rectangular grid on the duct wake, as shown in Figure 6-3, and obtains the solution on the duct in the rotating coordinate system, is equivalent to the quasi-steady duct solution

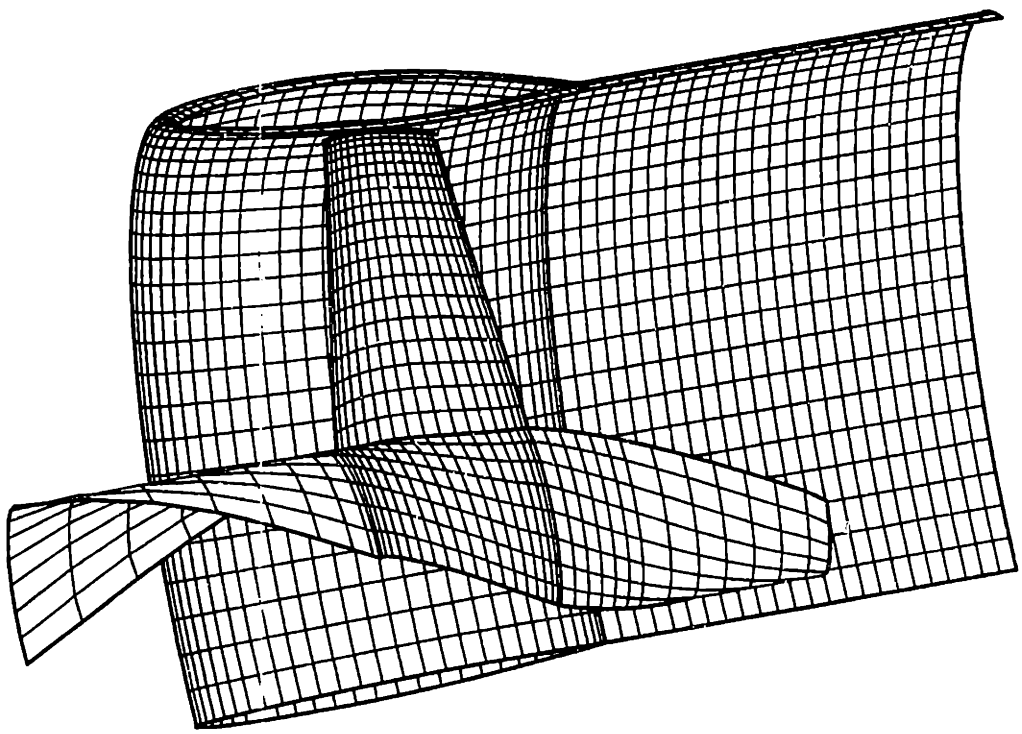

Figure 6-3: Geometry and panelization of the single component propulsor; Only one of the three blades and a third of the duct and hub is shown. The duct and duct wake paneling have infinite pitch.

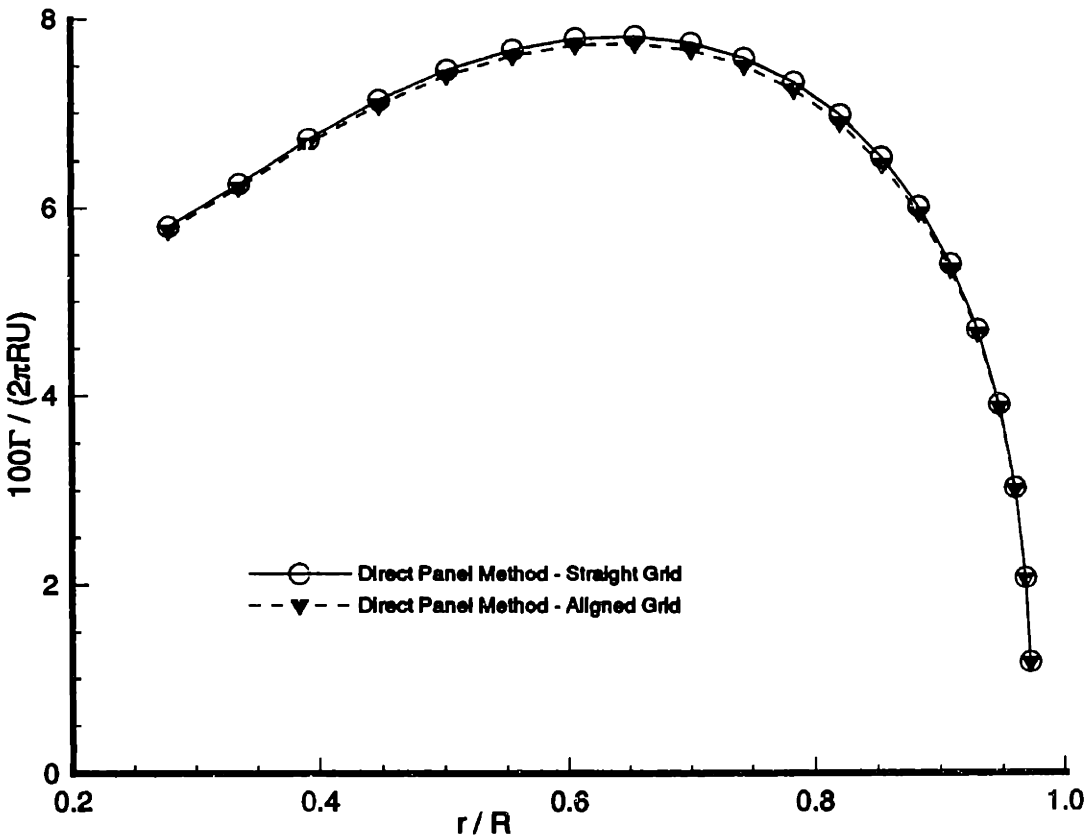

Figure 6-4: Effect of duct wake pitch angle on the spanwise distribution of circulation for the single component propeller in steady flow

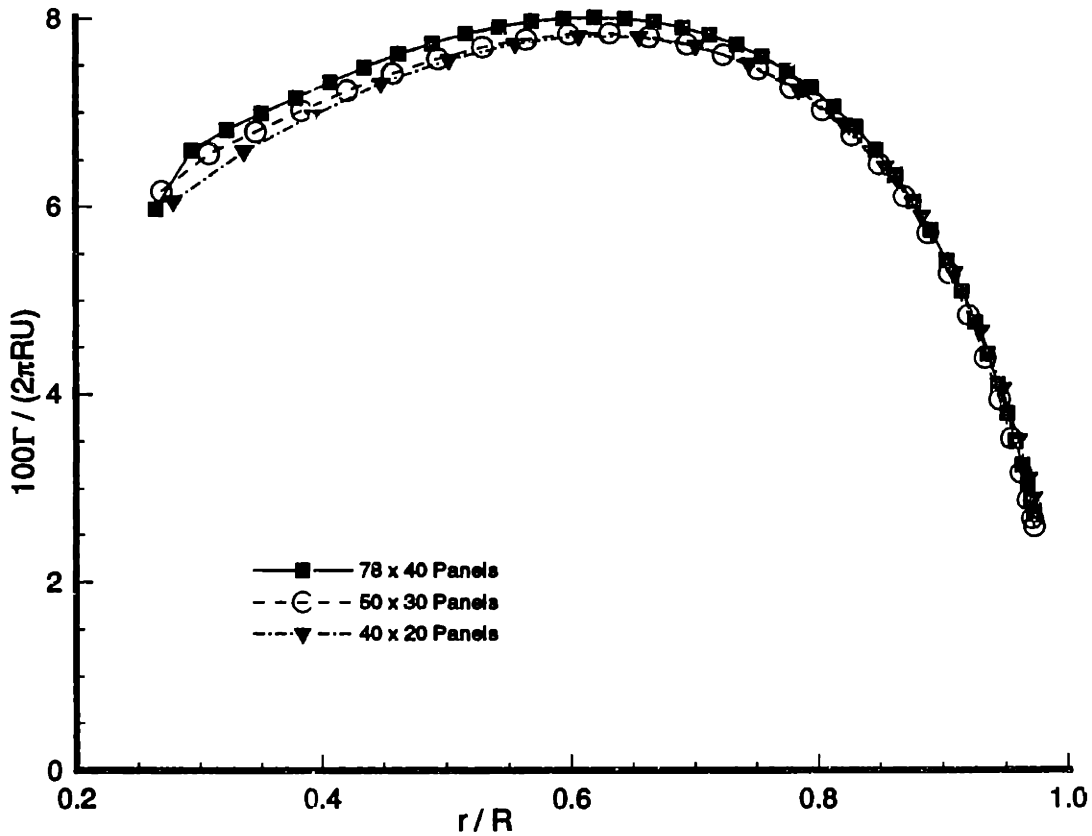

Figure 6-5: Convergence of spanwise distribution of circulation propeller for the single component propulsor in steady flow with number of panels.

obtained by the present method. Therefore, comparisons can be made with the direct panel method for the quasi-steady duct solution before the application of the base problems. This comparison is shown in Figure 6-6 for the case of the single component propulsor at the same operating point examined in the previous section. The base problems discussed in Chapter 4 are then applied to account for the vorticity shed by the duct. The fully-unsteady duct solution is obtained from PSF10T by using the correctly aligned grid shown in Figure 6-1. The resulting comparisons for the FUD duct circulation before the application of the iterative pressure Kutta condition is shown by Figure 6-7. Comparing Figures 6-6 and 6-7 shows that there is a significant difference between the QSD and FUD solutions on the duct which is comparable to the difference between the QSD and FUD solutions on the two-dimensional duct foil discussed in Chapter 4. Figure 6-7 shows that the fully-unsteady duct solution is recovered by the application of the base problems. Finally the iterative pressure Kutta condition is applied. The resulting comparison for the final duct circulation after the pressure Kutta condition is imposed is shown by Figure 6-8. The present method appears to be reasonably consistent with the direct method at each stage of the computation for the solution on the duct. In order to examine the effect of the far-field approximation specified by equation (4.8) on the duct solution a one-bladed version of the single component propulsor was analyzed using PSF10T. This same problem was then solved a second time with the propeller represented by point sources and dipoles of strength corresponding the the source and dipole panel strengths from the first solution. The results of this test are shown in Figure 6-9. There appears to be little effect from the use of the far-field approximation for this case.

6.2.3 Solution for two component propulsor

The method was also used to examine the flow past the ducted propulsor with a set of pre-swirl stator blades shown in Figure 6-10. The geometry used for the wakes is shown in Figure 3-26. The inflow for this case is uniform. However, the loading on both the stators and propeller will be unsteady due to the interaction between the components. Figure 6-11 shows the propeller circulation near $0.7R$ for the key

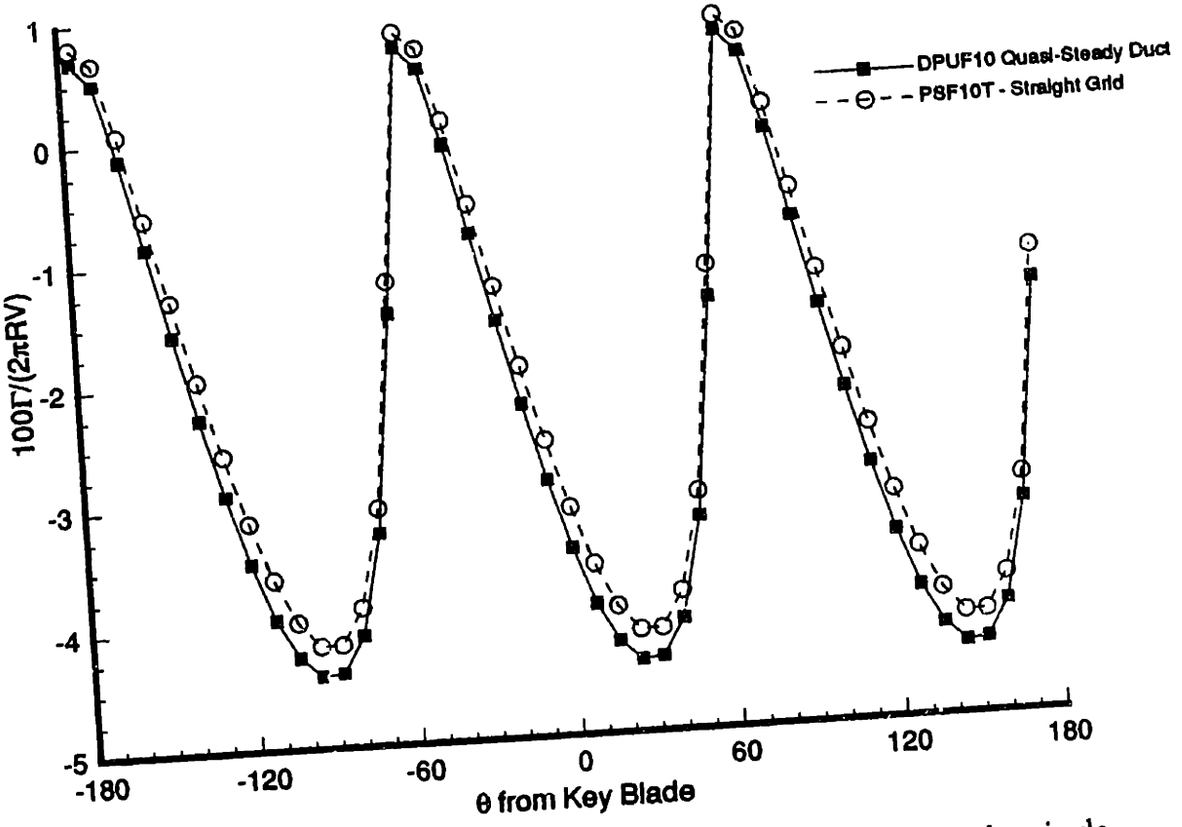

Figure 6-6: Circumferential distribution of circulation on the duct for the single component propeller in steady flow; $J = 0.833$. These curves represent the "quasi-steady duct" solution.

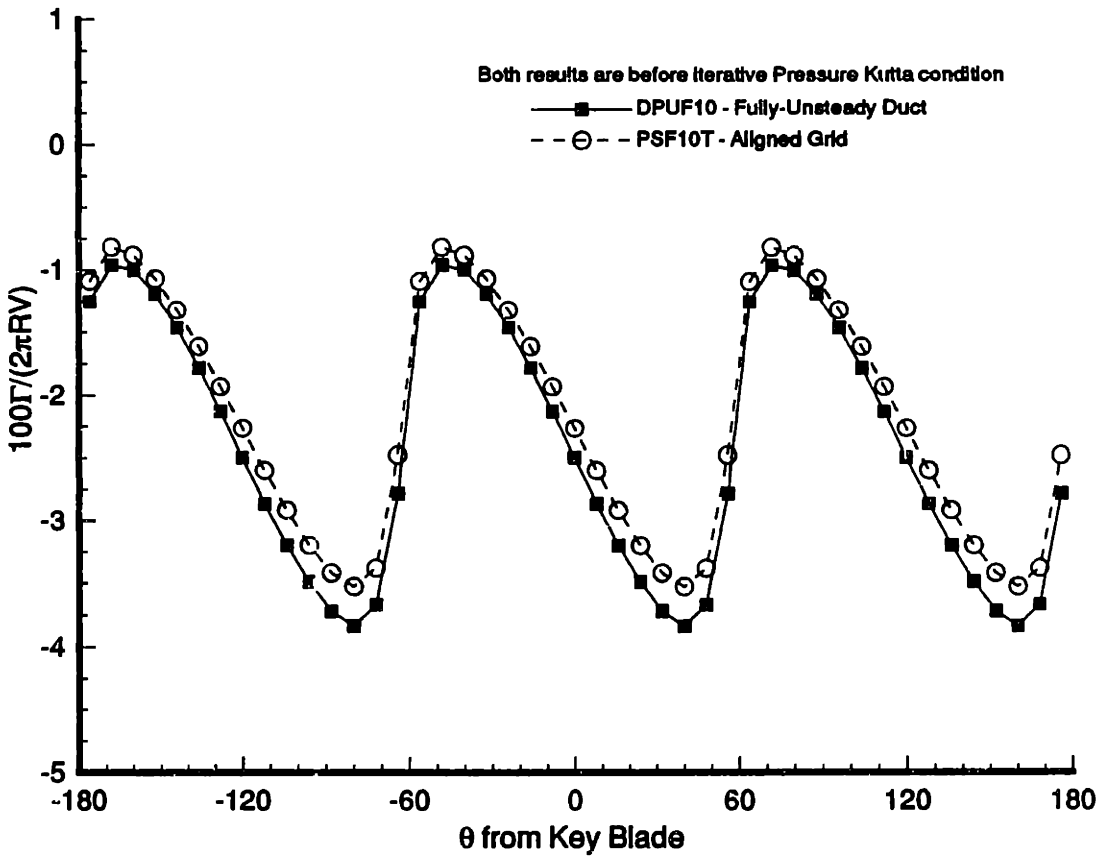

Figure 6-7: Circumferential distribution of circulation on the duct for the single component propeller in steady flow; $J = 0.833$. These curves represent the "fully-unsteady duct" solution before the application of the iterative pressure Kutta condition.

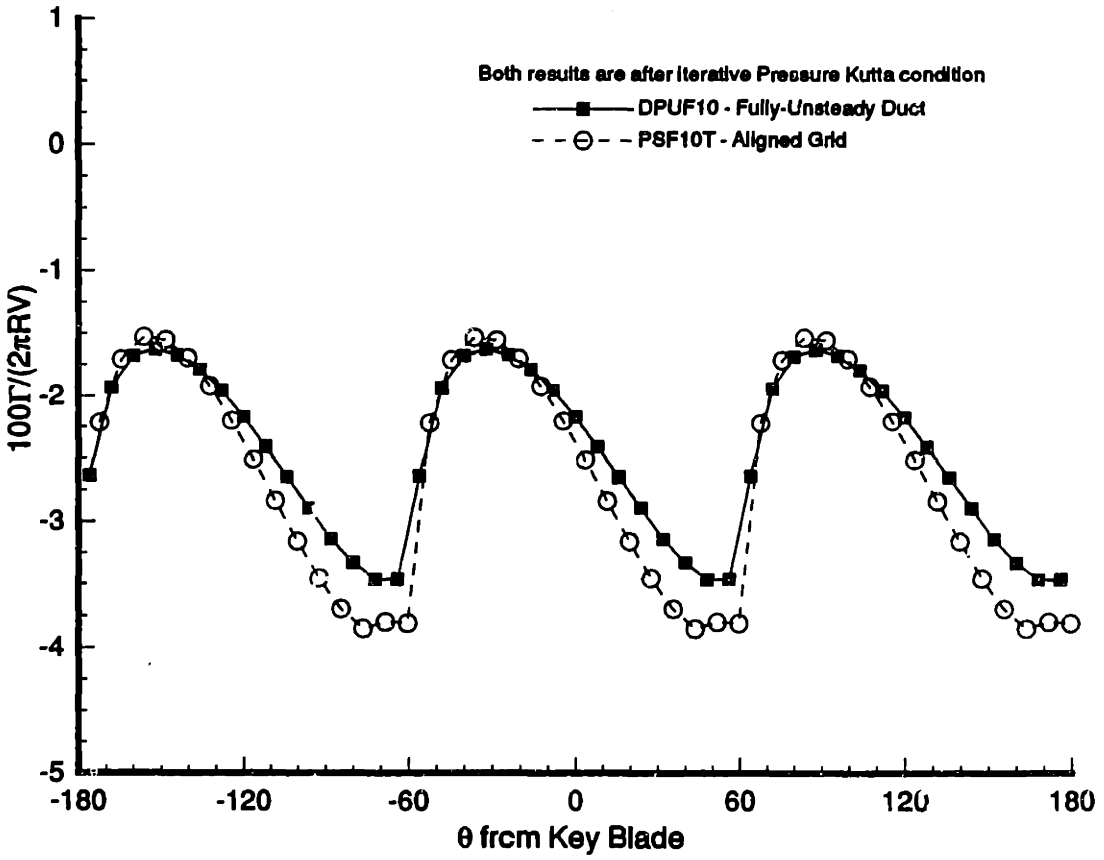

Figure 6-8: Circumferential distribution of circulation on the duct for the single component propeller in steady flow; $J = 0.833$. The values are shown after the application of the iterative pressure Kutta condition for both PSF10T and DPUF10.

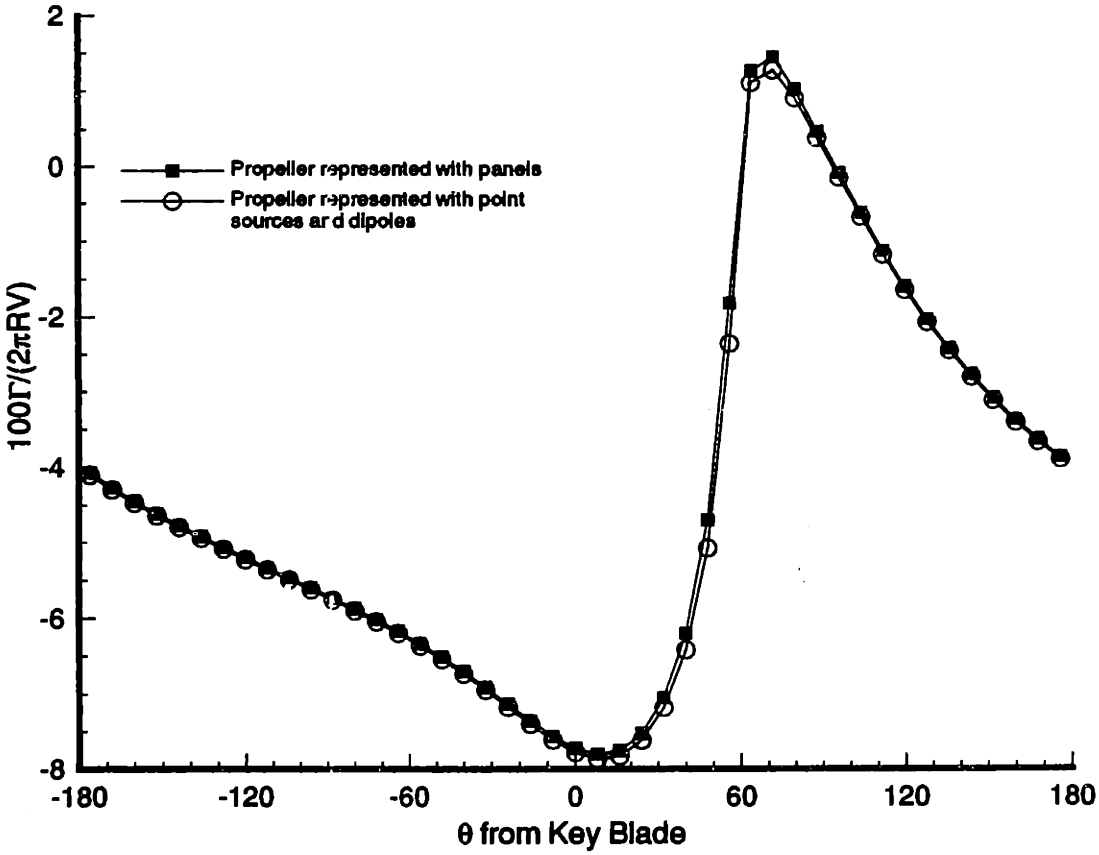

Figure 6-9: Effect of the far-field approximation on the solution on the duct.

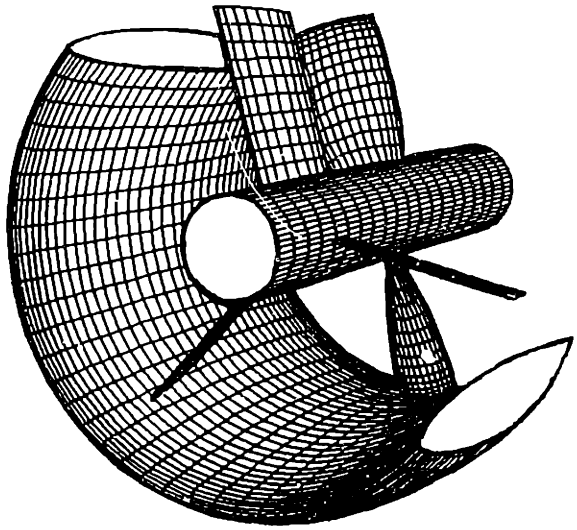

Figure 6-10: Geometry and panelization of two component ducted propulsor; Only half of the duct is shown.

propeller blade as a function of shaft rotation angle and Figure 6-12 shows the range between the maximum and minimum values for the spanwise distribution of circulation on the propeller blade during a complete revolution. Figures 6-13 and 6-14 show the same results for the stator blades. These results seem reasonable as they show that over the period of a complete rotation by the propeller, each stator blade sees two pulses as each of the two propeller blades passes behind it. Likewise, the key propeller blade experiences three pulses in its circulation as it passes behind each of the three stator blades.

6.3 Analysis of Unsteady Results

As discussed at the start of this chapter, one of the difficulties faced in attempting to validate the present method for unsteady flows is the absence of any experimental data for the unsteady forces on ducted propellers or an available alternative method for predicting the unsteady forces on multi-component ducted propellers. In this section some results obtained by the current method are shown for the flow past both the single component propulsor and the two component propulsor in a non-uniform inflow. The inflow used for both propulsors is the three cycle wake shown in

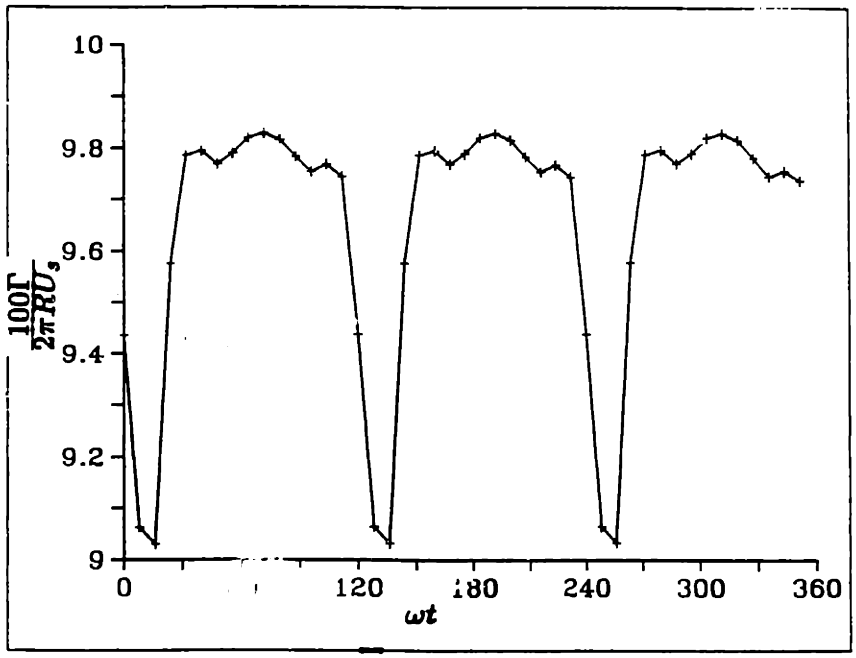

Figure 6-11: Unsteady circulation on the key propeller blade near $0.7R$.

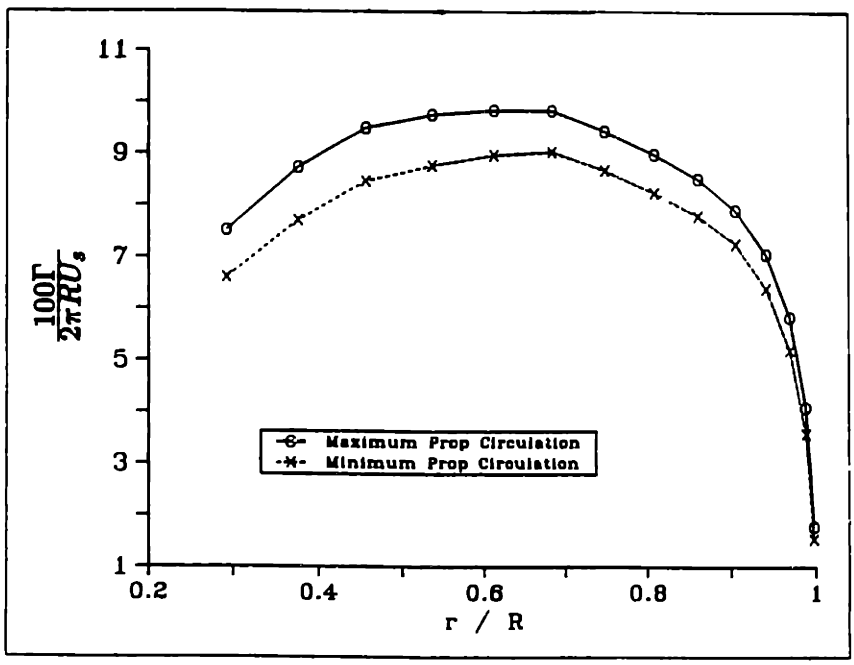

Figure 6-12: Variation the spanwise distribution of circulation on the key propeller blade for a two-component propulsor in uniform flow.

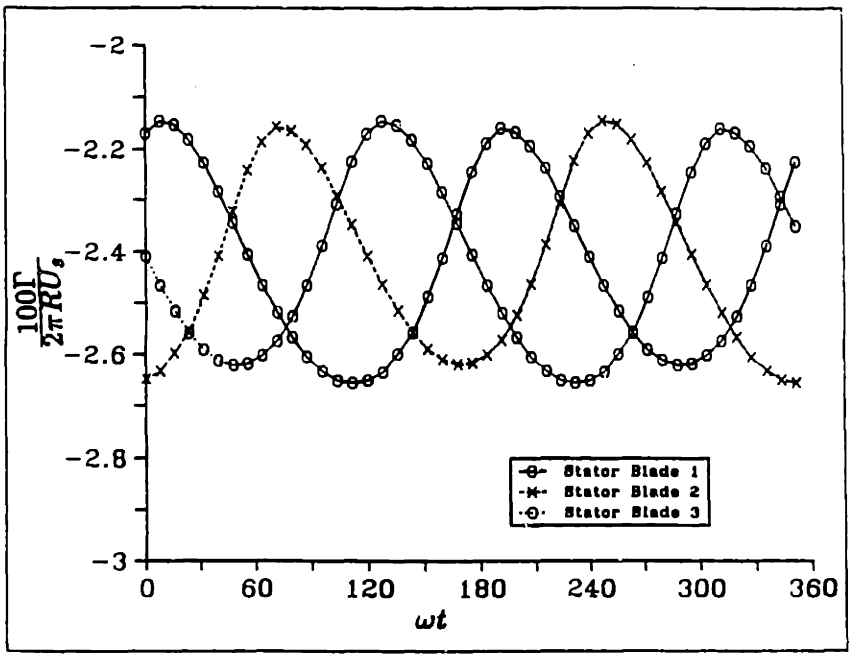

Figure 6-13: Unsteady circulation on the stator blades near $0.7R$.

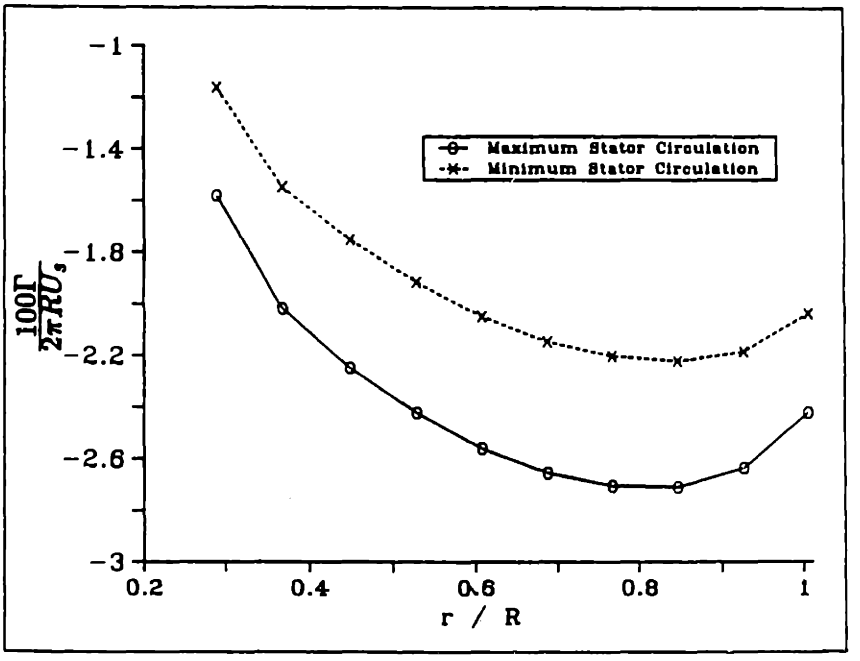

Figure 6-14: Variation the spanwise distribution of circulation on the stator blades for a two-component propulsor in uniform flow.

Figure 6-15.

6.3.1 Single component propulsor in unsteady flow

Figure 6-16 shows the unsteady circulation on the propeller for the single component propulsor as a function of shaft rotation angle, and Figure 6-17 shows the unsteady circulation on the duct at various angular locations as a function of shaft rotation angle. The results were obtained using 40 chordwise panels, 20 spanwise panels, and a timestep of 8 degrees. Figure 6-18 examines the effect of the duct on the unsteady forces by comparing the unsteady thrust coefficient, K_t, both with and without the duct and hub for the same propeller. The open propeller in solved in the inflow resulting from the solution of the duct and hub in the specified inflow in the absence of the propeller. If an unsteady ducted propulsor analysis method was unavailable, one might attempt to solve for the unsteady forces on a ducted propeller using this approach with an open propeller code. As Figure 6-18 shows, this would significantly underpredict the unsteady thrust. Figure 6-19 shows the harmonically analyzed unsteady axial force on the duct. This force is non-dimensionalized as: $C_F = F_x/(0.5\rho V_s^2 R^2)$, where R is the radius of the propeller. In the harmonic analyses shown in Figures 6-18 and 6-19, the mean (steady) values for the K_t and axial force have been subtracted out. The mean value of K_t is about 1.0 for the propeller, and the mean non-dimensionalized axial force on the duct is about 0.06. The third harmonic dominates for both the duct and the propeller since is a three bladed propeller in a three cycle wake. Figure 6-20 shows the pressure distribution on a section of the inner surface of the duct which extends from the duct leading edge to the duct trailing edge and covers about two-thirds of the duct circumference. The vertical axis shows the circumferential position in radians. Different length scales are used for the vertical and horizontal axes. The results are shown for the timestep at which the propeller key blade is at $-40°$ from the top dead center position. The pressure is non-dimensionalized as $C_p = \frac{p_\infty - p}{\frac{1}{2}\rho U^2}$. Figure 6-21 shows the velocity vectors over the same section of the duct surface at the same timestep.

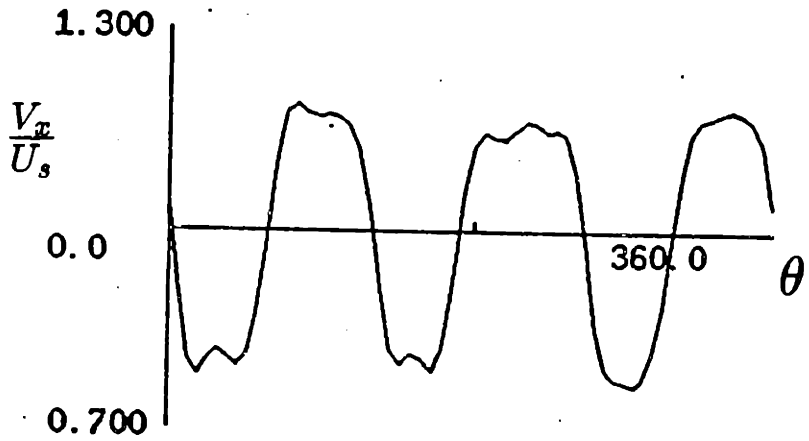

Figure 6-15: Axial component of inflow velocity near $0.7R$.

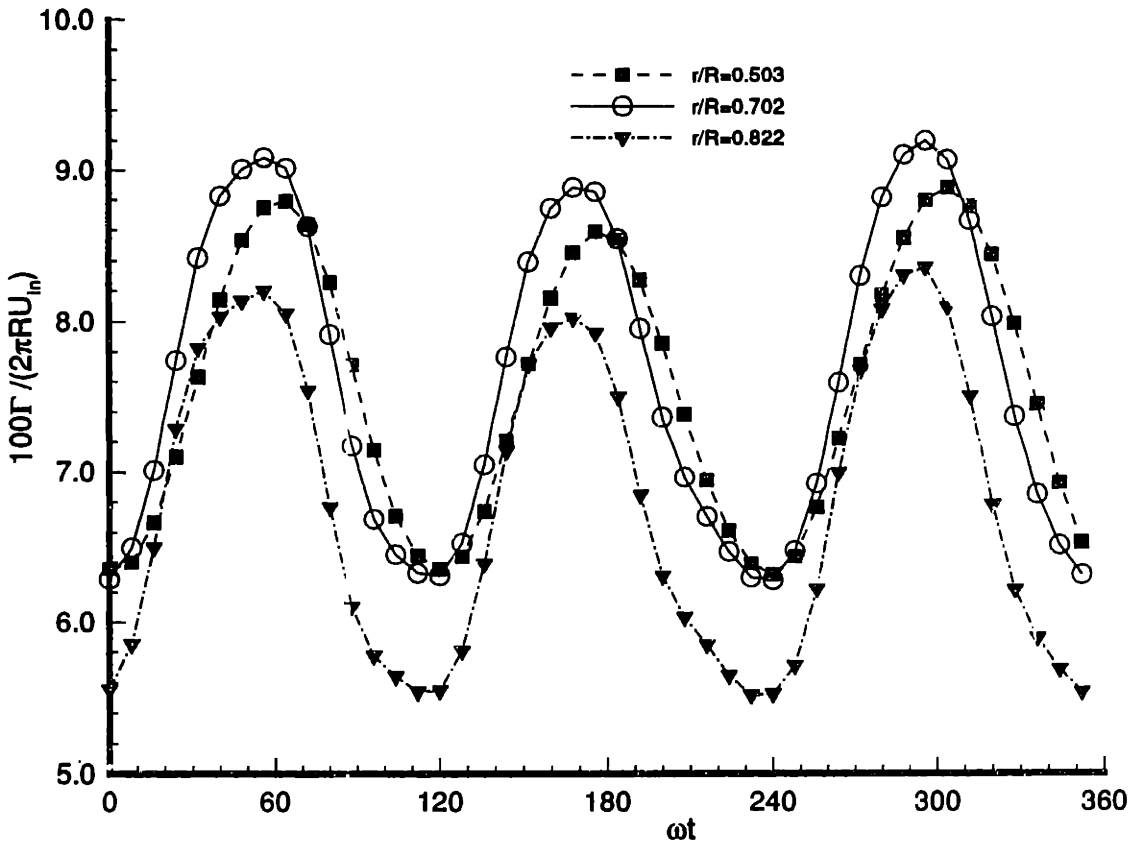

Figure 6-16: Unsteady circulation for single component ducted propulsor at various radii.

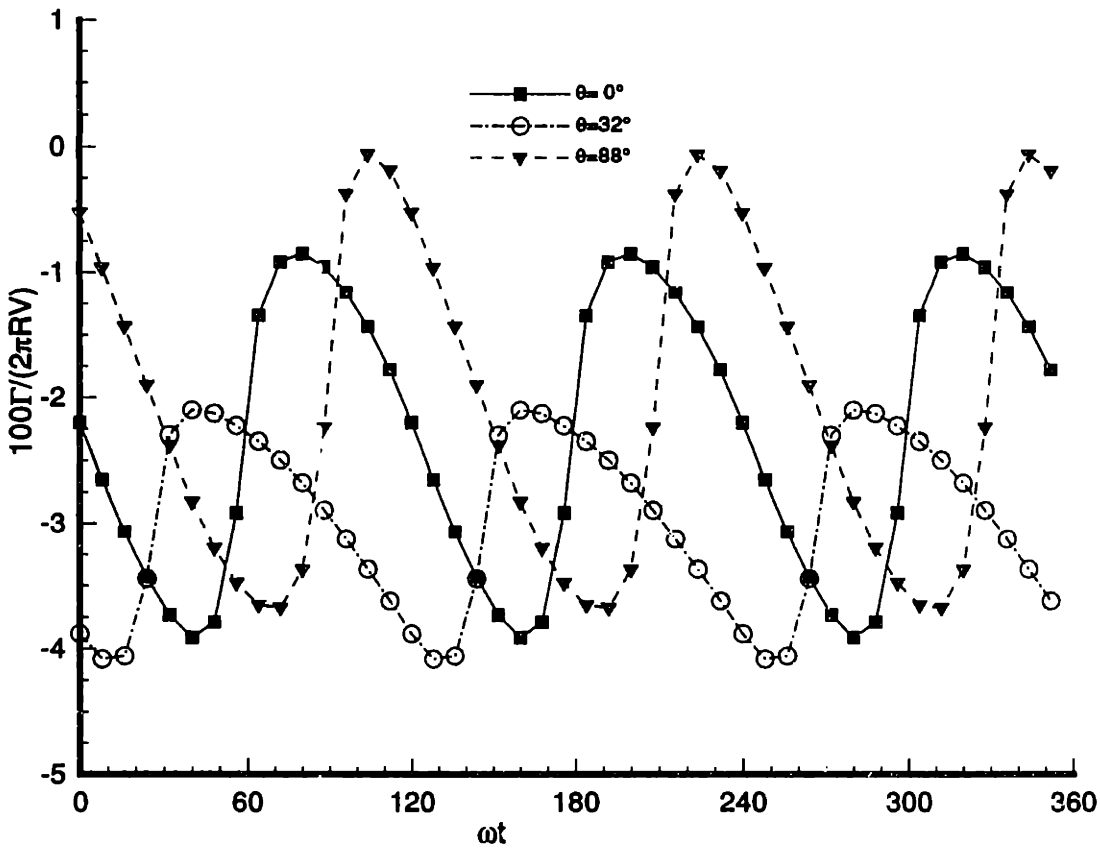

Figure 6-17: Unsteady duct circulation for the single component ducted propulsor at various angular positions. The propeller key blade is at $\theta = 0$ at time $\omega t = 0$.

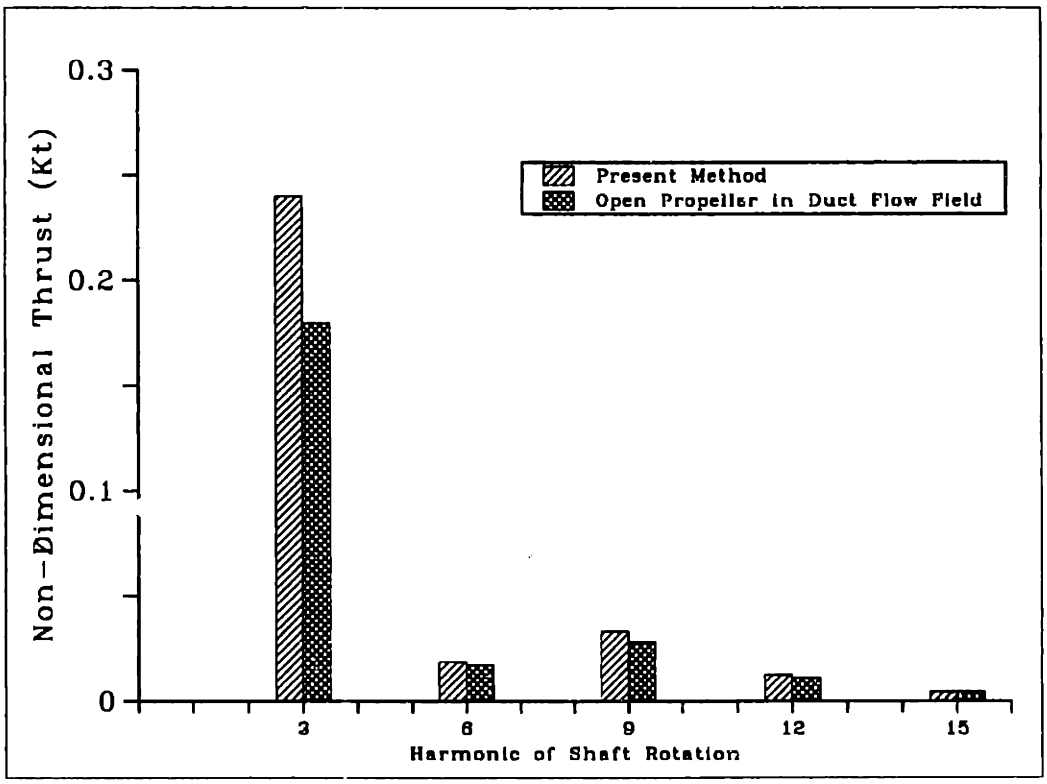

Figure 6-18: Thrust harmonics of the propeller for single component propulsor in three-cycle wake.

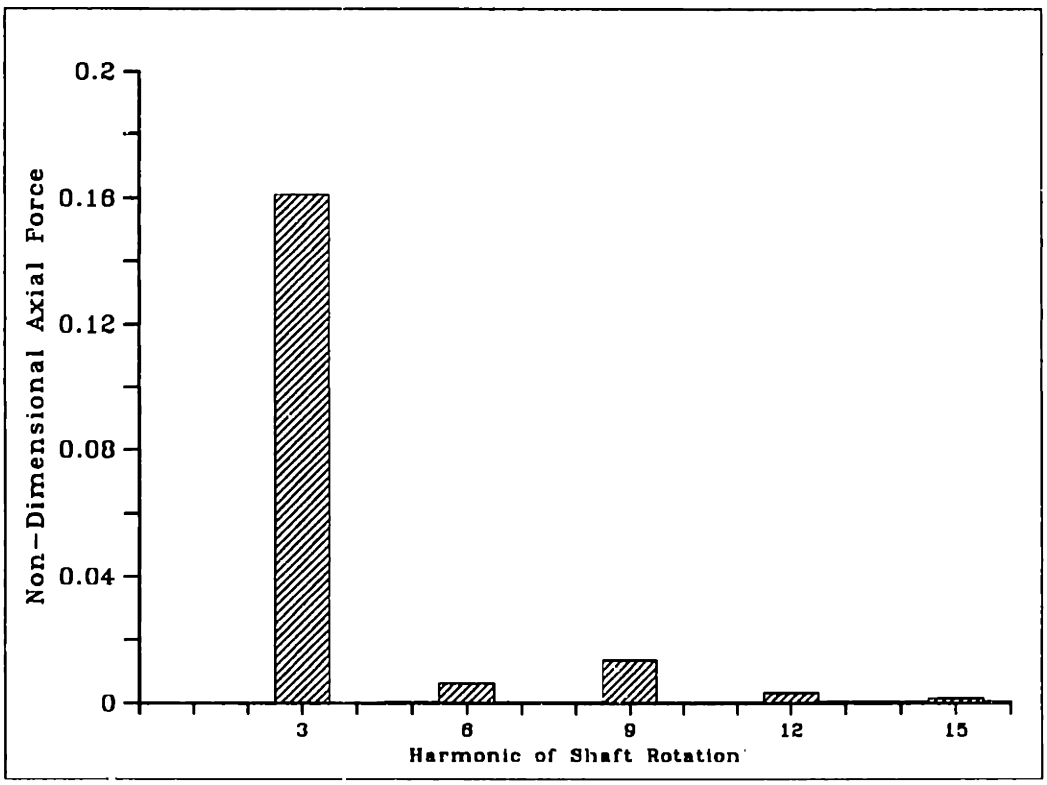

Figure 6-19: Axial force harmonics of the duct for single component propulsor in three-cycle wake.

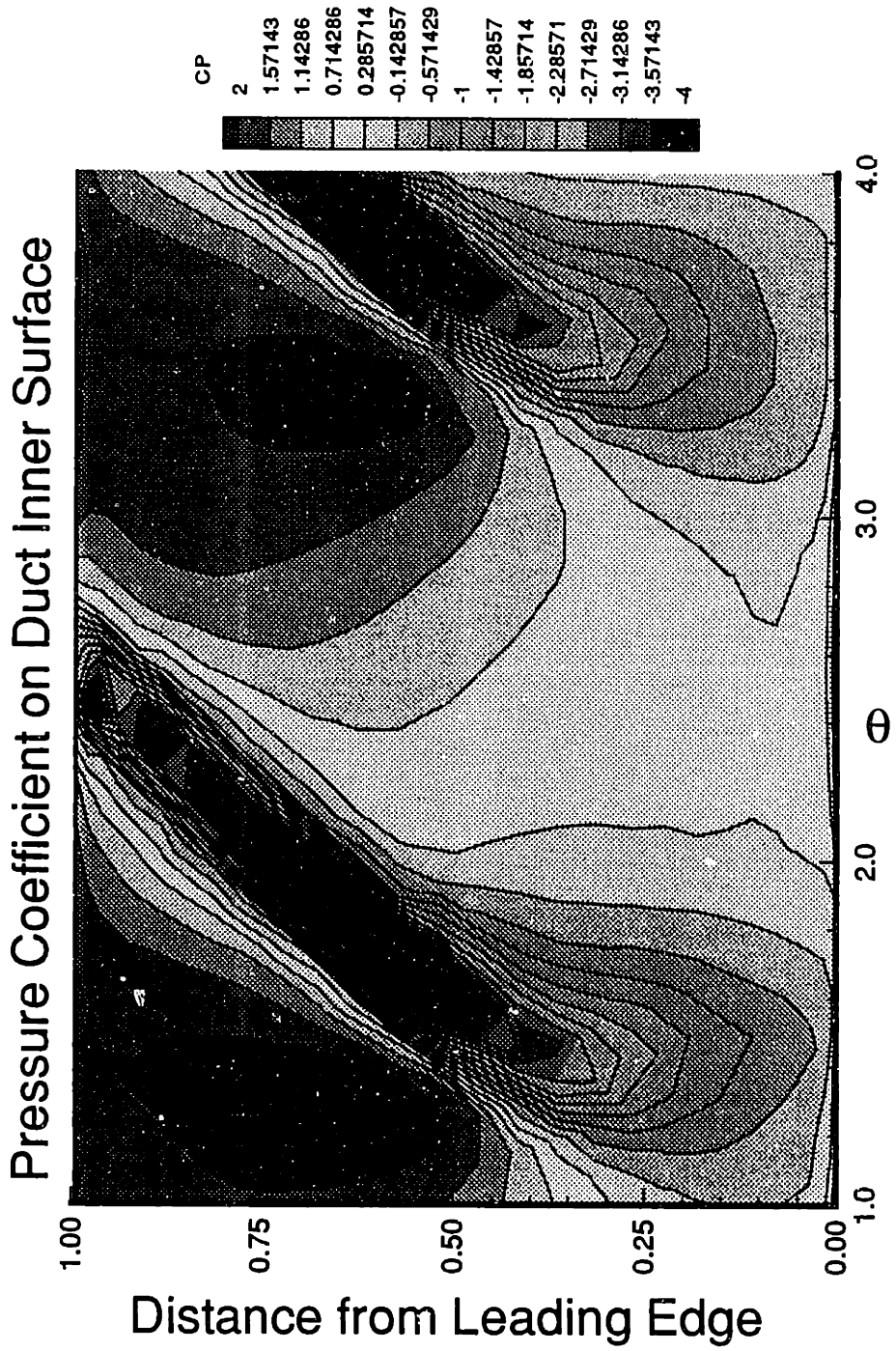

Figure 6-20: Pressure distribution on a section of the duct inner surface.

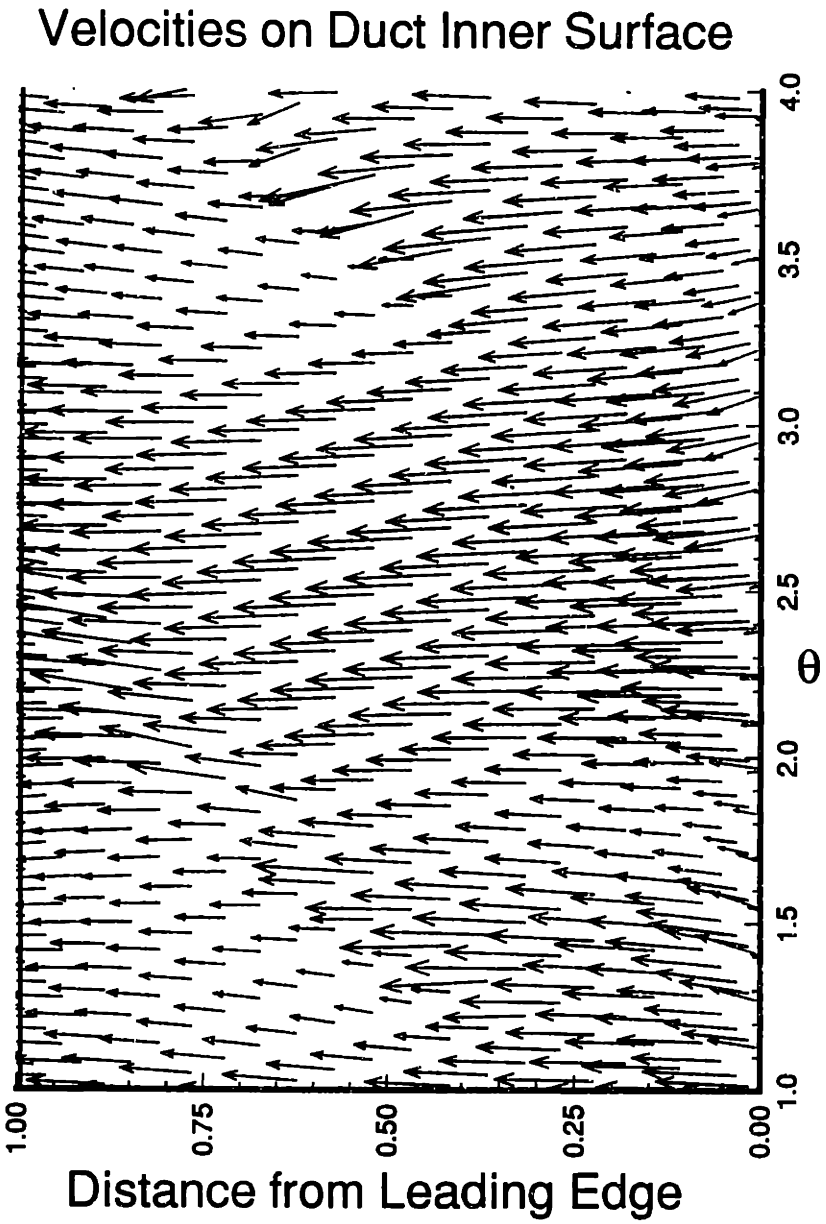

Figure 6-21: Velocity vectors on a section of the duct inner surface.

6.3.2 Two component propulsor in unsteady flow

The two component propulsor was examined in the same non-uniform inflow. The results for the unsteady circulation on the propeller as a function of shaft rotation angle are shown in Figure 6-22, and the unsteady circulation on the stator blades is shown in Figure 6-23. A harmonic analysis for the unsteady non-dimensional axial forces on each component is shown in Figure 6-24. The mean axial force on each component is subtracted out and all the forces are normalized as $C_F = F_x/(0.5\rho V_s^2 R^2)$, where R is the propeller radius. In this case the propeller only has two blades but still operates in a three cycle wake. In addition, the wakes from the stator blades add non-uniformity to the flow seen by the propeller. Unsteady forces are produced only for the even harmonics since the propeller has two blades. The mean value for the non-dimensional axial thrust on the propeller is 4.22.

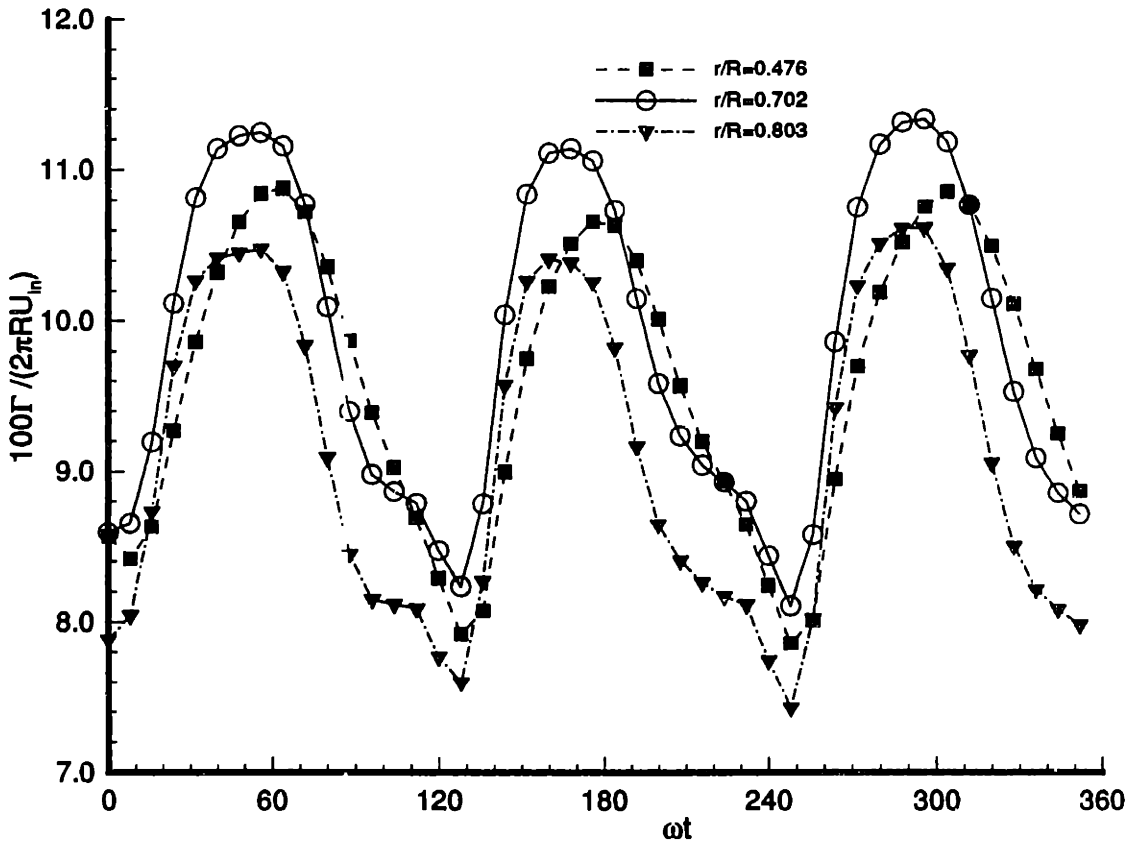

Figure 6-22: Unsteady propeller circulation at various radii for the two component propulsor.

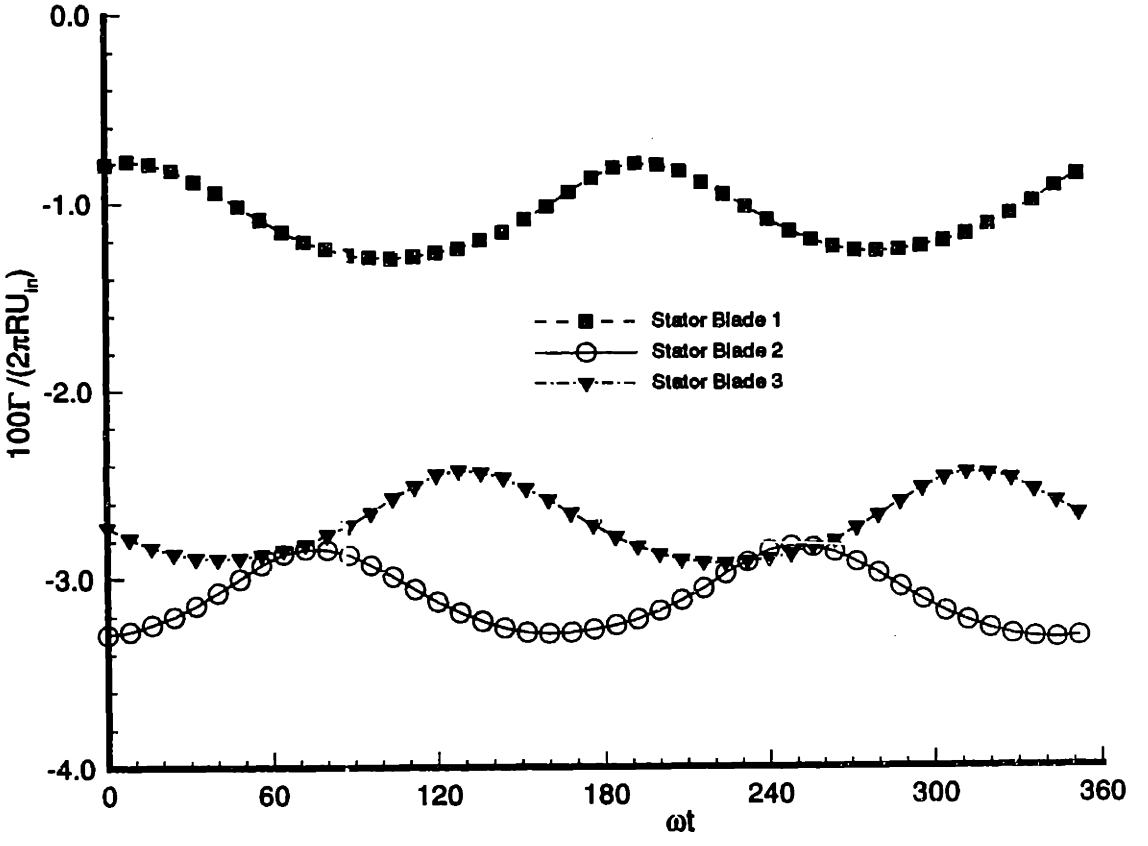

Figure 6-23: Unsteady stator blade circulation at $r/R = 0.688$ for the two component propulsor. Both the local radius and circulation are non-dimensionalized with respect to the *propeller* radius.

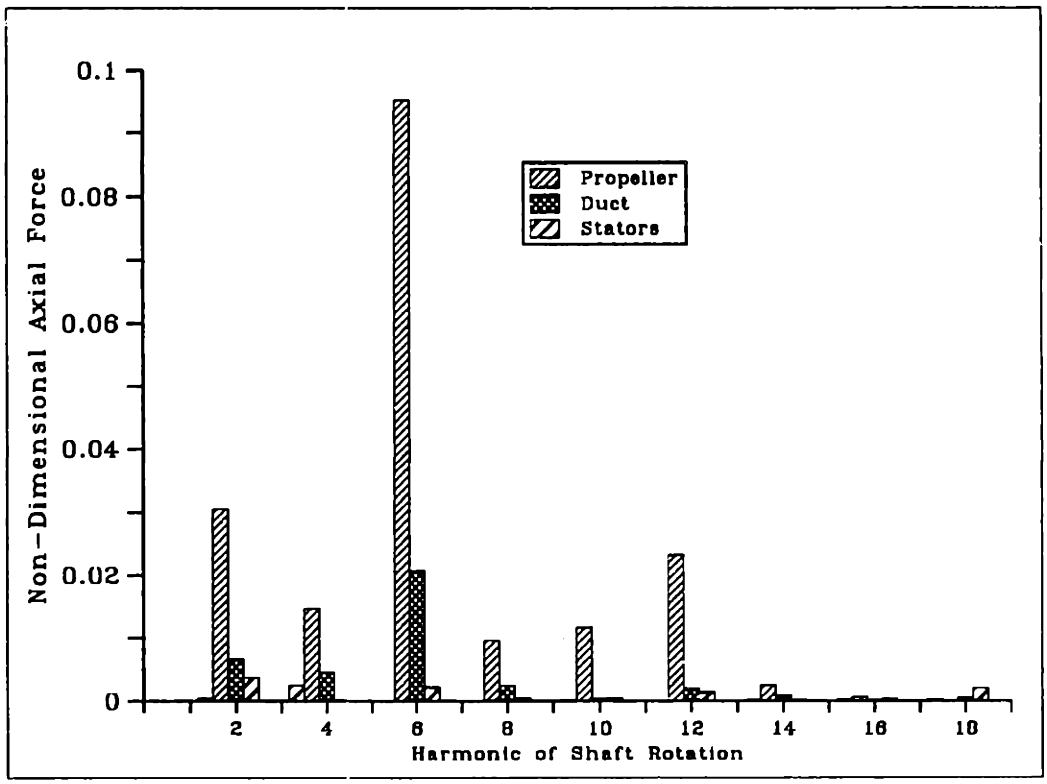

Figure 6-24: Axial force harmonics of the duct, propeller, and stator blades for a multi-component propulsor in a three-cycle wake.

Chapter 7

Computational Efficiency for Various Methods

The rational basis behind the generalized image model and the use of Chebyshev polynomial expansions to represent the generalized images is that by incorporating these procedures, an analysis method could be developed which is more efficient for modeling multi-component ducted propulsors in unsteady flow than a direct panel method applied to the same problem. In this chapter, we examine the computational efficiency of the method developed in this thesis and make comparisons with estimates of the computational efficiency of an equivalent direct panel method.

In order to obtain estimates for the computation time required by both the current method and a direct method, runs were performed on a VAX-9000, which is a mini-supercomputer located at MIT. Experiments with simple computations showed this computer to be capable of about 5-10 Mflops. Although the speed of the VAX-9000 is roughly equivalent or even slower than recent workstations, it has the advantage of having a large amount of virtual memory and disk space. This allowed for the entire matrix (consisting of about 3000 unknowns for the direct method) to be stored in virtual memory for both methods. Perhaps the biggest advantage of this computer was that its use was available to us for free at the time of this work. Runs were performed using an option which records the computational time spent in each subroutine so that the critical sections of each method could be determined.

To estimate the time which would be required for a direct panel method, the PSF10T code described in the previous Chapter was used. This code, however, is only capable of solving for the *steady* flow past a *single* component ducted propulsor. The time which would be required if this method were to be extended to unsteady flows was estimated by determining the computation time required to obtain the matrix solution for the steady case, multiplying this time by the number of timesteps needed to obtain a converged solution by the current method, and adding this value to the time used to solve the steady problem. For a fully unsteady direct panel method using a fixed wake geometry, the gridding of the duct, propeller and wake and the computation of the influence coefficients would only have to be performed once. The time required by this part of the computation should be the same regardless of whether the problem is being treated in a steady or unsteady manner. The computations which must be performed at each timestep for the unsteady case include only the solution of the system of equations, the computation of the updated right hand side, and the application of the iterative pressure Kutta condition. It is assumed that this time is dominated by the time required to obtain a solution to the system of equations. The time required to update the right hand side and apply the pressure Kutta condition at each timestep is assumed to be negligible. In this manner, an estimate was made of the time required to solve for the unsteady flow past the single component propulsor described in Section 6.1 using a direct panel method. The panelization used for this test is shown in Figure 6-1. The panelization on the propeller and propeller wake is identical to that which will be used for DPUF-10. The number of panels on the duct are determined such that the total number of panels matches the number of panels used on the duct when computing the generalized images directly. However, for a three-bladed single component propulsor, only one third of the duct needs to be included in the system of equations if the duct is modeled using a *key duct section* in the same way a *key blade* is used. This results in 800 panels on the key blade, 1600 panels on the key duct section, and 340 panels on the key hub section. The total number of unknowns is 2740. The estimated time was computed for an unsteady solution using 135 timesteps. The results of this computation are shown in Table 7.1.

Influence Coefficients	Matrix Solver	Total Time
7	35	57

Table 7.1: Estimated computational time required to compute the unsteady flow past a single component ducted propulsor using a direct panel method on a VAX-9000 computer. All times are in minutes.

It can be seen that the computational time required by the direct method is dominated by the time spent solving the matrix of equations after the coefficients have been determined.

When determining the computational time required by the method presented in this thesis, only the time required to obtain the solution on the propeller is taken into account. The time needed to compute the Chebyshev coefficients for the image factor corresponding to a given duct and hub geometry is not included. This is reasonable since it is expected that numerous propeller geometries and operating conditions will be examined for a given duct geometry. Therefore, even though the time required to develop the image factor expansion is large (roughly 12 hours on the VAX-9000), this procedure only has to be done once for a given duct and hub. The same set of coefficients may then be used for every propeller geometry and operating condition. The effect of the level of truncation used for the Chebyshev polynomial expansions on both the accuracy and efficiency of the method was also examined as part of this investigation. The truncation of the Chebyshev polynomial expansions of the image factor was discussed in Section 3.4.5. The terms in the expansion whose coefficients have an absolute value below the "level of truncation" are ignored. The error in the image factor for a given panel resulting from this truncation is bounded by the *sum* of the absolute values of coefficients which are ignored, and not simply by the level of truncation itself. Therefore, if a large number of coefficients are truncated, the potential for error might be large, even if the absolute value of each truncated coefficient is very small. In addition, since the image factor must be multiplied by the simplified image, which can be of order 10, a degree of accuracy is lost converting

Level of Truncation	Influence Coefficients	Matrix Solver	Total Time
No Truncation	85	3.6	114
1×10^{-6}	75	3.5	91
1×10^{-5}	59	3.5	79
1×10^{-4}	35	3.5	50
1×10^{-3}	11	3.4	25
1×10^{-2}	3.4	3.4	18

Table 7.2: Computational time required on a VAX-9000 computer for a single component ducted propeller using DPUF10. All times are in minutes.

the image factor to the generalized image. Another order of accuracy may be lost when computing the derivatives of the image factor as required to determine the generalized images corresponding to the dipole influence coefficients. Table 7.2 shows the computation times required to solve for the flow past the single component ducted propulsor described in Section 6.1, using the present method with various truncation levels. For these tests, a uniform inflow was used, but the solution was obtained as if the problem were unsteady using 135 timesteps. Since the solution is computed only on the propeller at each timestep, there are only 800 unknowns which must be solved for at each timestep. The effects of the level of truncation used on the accuracy of the solution on the propeller is shown in Figure 7-1. The computational time required by the current method is dominated not by the matrix solution but by the calculation of the influence coefficients, namely the evaluation of the quintuple summation used in the image factor expansion. The level of truncation, therefore, has a significant influence on the resulting computation time. The truncation level must be set between 1×10^{-4} and 1×10^{-5} for the current method to show improvements in efficiency over a direct method. However, Figure 7-1 indicates that 1×10^{-5} is about as high as the truncation level can be set before the accuracy solution on the propeller is affected.

A block iterative matrix solver is used for both methods for which the time required to obtain the solution at each timestep is roughly proportional to the square of the number of unknowns. Therefore, it makes sense that the direct method spends about

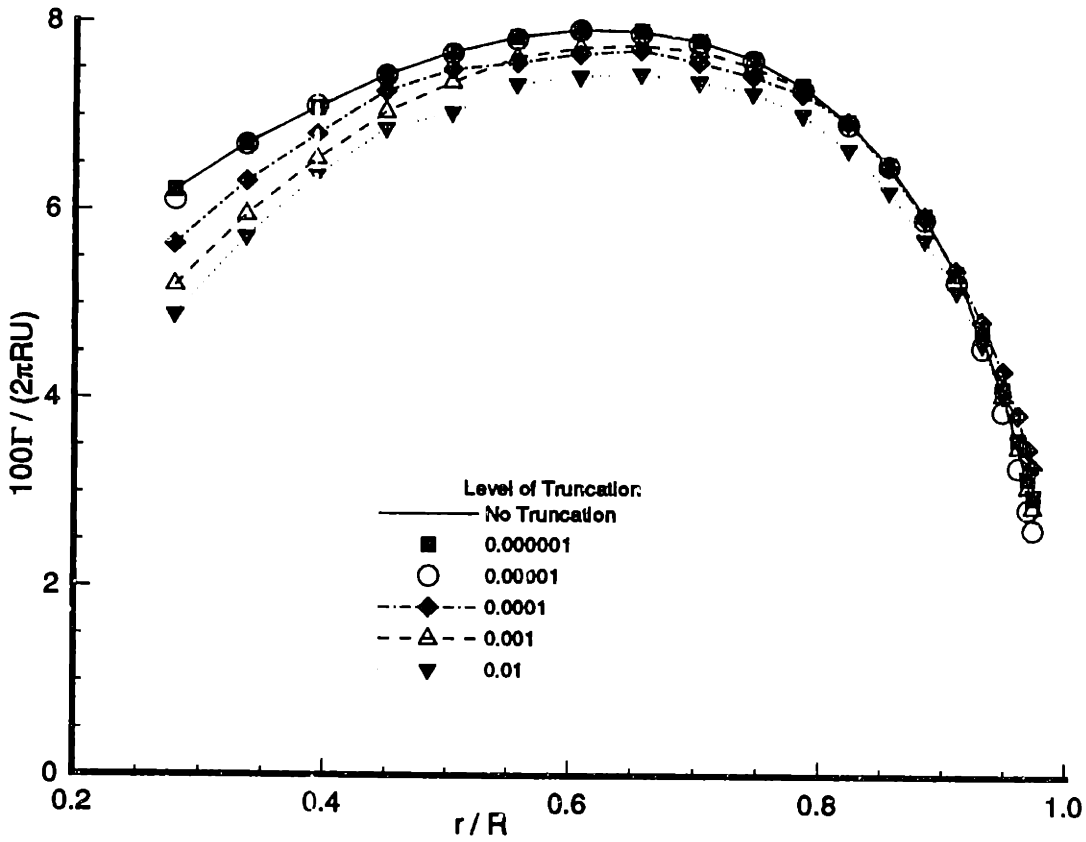

Figure 7-1: Effect of truncation level on the spanwise distribution of circulation for a single component ducted propulsor in uniform flow; $J = 0.833$.

ten times the computational effort in the matrix solver as does the current method, since the number of unknowns used in the direct method is over three times that used in the current method for the case demonstrated above. The time required to compute the influence coefficients is dependent upon the number of unknowns multiplied by the number of blade and wake panels on all blades. Since the time required by the current method is dominated by the influence coefficient computations, the time required to obtain the solution using the current method can be expressed *roughly* as:

$$\text{Comp. Time}_{\text{Current Method}} \propto (N_{PS} + N_{WPS}) \times N_B \times N_{PS} \tag{7.1}$$

where N_{PS} is the total number of panels on the key propeller blade and all of the stator blades, N_B is the number of propeller blades, and N_{WPS} is the total number of panels on the key propeller blade wake and the wake of all the stator blades. Similarly, since the time required by the direct method is dominated by the matrix solutions, the time required by this method can be expressed *roughly* as:

$$\text{Comp. Time}_{\text{Direct Method}} \propto (N_{PS} + N_{DH})^2 \tag{7.2}$$

where N_{DH} is the total number of panels used to represent the duct and hub.

From these expressions, it can be seen that the relative efficiency of the current method compared with a direct panel method is largely dependent on the ratio of the panels used to represent the duct and hub divided by the number of panels used to represent the propeller and stator blades, N_{DH}/N_{PS}. For the case of the single component propulsor examined here, this ratio is about 3, and the efficiency of the two methods are comparable. As the value of this ratio increases, the relative efficiency of the current method will improve. In this sense, the single component propulsor is not the best test of the computational efficiency of the method. The primary application for this method is the analysis of *multi-component* propulsors. In the case of the direct method for a single-component propulsor, efficiency is gained by only having to solve for the panels representing $1/N_B$ of the duct and hub. With the addition of even a single stator blade, this *key duct section* solution is no longer

possible and the number of panels required to represent the duct and hub increases by a factor equal to the number of blades. Therefore, the current method should be more efficient for a multi-component propulsor with several stator blades. However, as the number of stator blades is increased, the ratio N_{DH}/N_{PS} decreases since more panels are required to represent the higher number of stator blades. It is conceivable for a ducted propulsor design to incorporate over ten stator blades, in which case the number of panels required to represent the propeller and stator blades would be comparable to the number used to represent the duct and hub. The ratio of the number of duct/hub panels to the number of propeller/stator panels which is required to justify the current method would decrease considerably if the interpolation of the image factor was to be made more efficient. Some ideas on how to improve the efficiency of these computations are listed in the Section 8.2.

Another possible advantage of the current method concerns the required amount of virtual memory. If the matrix coefficients are all stored in virtual memory, the current method would allow for a greater number of panels used to represent the propeller and stator blades in the cases where the total matrix size is limited by the available virtual memory of the machine.

Chapter 8

Conclusions and Recommendations

8.1 Conclusions

In this thesis, a method is presented for the analysis of the unsteady flow past a multi-component ducted propulsor using a time-marching panel method for the propeller and stator blades and incorporating the duct and hub through the use of the generalized image model. The method is used to predict the unsteady pressures, forces, and circulation distributions on the propeller, duct and stator blades for two test propulsors in both uniform and non-uniform inflows. The results are shown to be reasonably consistent with a direct panel method for the case of a single component ducted propulsor in uniform flow. The method is shown to produce reasonable results for both single and multi-component propulsors operating in non-uniform flow.

An efficient method is developed to compute the generalized images which first calculates the value of the generalized image directly *only* for a representative set of points, and then sets up a Chebyshev polynomial expansion for the image factor, defined as the ratio of the generalized image and a simplified image. This expansion is used to evaluate the generalized image at all other locations. This process is shown to accurately reproduce the directly computed values for the generalized image for arbitrary locations inside of the duct. Although this procedure is far more efficient

than a direct calculation of the generalized images for all of the required panel locations, it was found that a large number of terms must be retained in the expansion in order to represent the image factor accurately. The result is that a significant amount of computational effort must be spent on the evaluation of the Chebyshev polynomial expansions of the image factor. For the case of a single component propulsor, it is found that the computational savings from the reduced number of unknowns resulting from the use of the generalized image model are largely canceled by the large computational effort required to evaluate the image factor expansions. The method presented in this thesis should still be more efficient, however, for a two-component propulsor with a limited number of stator blades. Improvements are required, however, in the efficiency of the image factor interpolation.

In order to extend the generalized image model to unsteady flows, a method is presented to account for the vorticity shed by the duct. A two dimensional analog problem is first used to examine the effect of the vorticity shed by the duct. Using this analog problem, it has been shown that:

- Representing the duct via the generalized image model is equivalent to solving the quasi-steady problem on the duct and the fully unsteady problem on the propeller.

- The forces on the propeller, especially those at high reduced frequencies, are not affected significantly by using the quasi-steady solution on the duct as opposed to the fully unsteady duct solution.

- Substantial differences exist between the forces on the duct obtained using the quasi-steady duct and fully unsteady duct solutions.

- A computationally efficient method was introduced for including the effects of the duct shed vorticity, via base problems, thereby recovering the fully unsteady duct solution from the quasi-steady duct solution.

The method developed using the analog problem is then extended to the problem of the three dimensional duct. It is shown that the fully unsteady duct solution can be

recovered from the history of the quasi-steady duct solution.

A method is also introduced to account for the effect of the flow through the tip clearance region on the global solution past the propulsor. The local flow through the tip clearance is shown to have a significant effect on the solution, particularly when the size of the clearance is small.

8.2 Recommendations for Future Research

The computational time required to solve for the unsteady flow past a propulsor using the current method is dominated by the time required to evaluate the generalized image for each propeller and stator panel with respect to the duct. The most significant improvement to the current method, therefore, would be to improve the efficiency of the generalized image interpolation. This must be done by either reducing the number of terms retained in the Chebyshev polynomial expansion for the image factor or developing a method for evaluating the expansion more quickly.

- The large number of terms required for the Chebyshev expansion for the image factor may be attributed to the small fluctuations in the directly calculated values of the generalized image near the edges of the interpolation region. These fluctuations in the generalized image result in a variation in the image factor in the order of 1×10^{-4}, which is roughly the same order as the required accuracy of the image factor interpolation. Therefore, enough terms must be used in the expansion to model these fluctuations whose frequency is determined by the spacing of the panels on the duct. These small fluctuations are not visible when observing the generalized image itself, but can be seen when the simplified image is subtracted from the generalized image. The fluctuations may be attributed to the "saw-tooth" effect from the constant strength panels on the duct. By representing the duct with a higher order panel method it may be possible to eliminate these fluctuations. Another possibility would be to smooth out the directly computed values of the image factor before determining the coefficients for the Chebyshev polynomials. Regridding the duct and hub such that there

are more panels concentrated near the position of the source and such that the panels are better aligned with the field points may also improve the smoothness of the directly computed image factors. If the fluctuations in the directly computed values for the image factor are reduced or eliminated, it may be possible to evaluate the image factor accurately using far fewer terms than are currently required, significantly improving the efficiency of the method.

- By converting the Chebyshev polynomial expansion to an equivalent series of ordinary polynomials, the number of computations which must be performed per coefficient will be reduced. This will also allow for the use of vectorization when evaluating the expansion.

In addition, the effect of the far-field approximation of the generalized image should be more closely examined, particularly with regard to the generalized images used to modify the self influence coefficients and near field influence coefficients for panels adjacent to the duct and hub. A more detailed computation of the generalized images only for the panels adjacent to the duct and hub may improve both the convergence and consistency of the method. The current method uses a fixed wake geometry for all of the components. Improvements may be attained by using a more realistic unsteady model for the geometries of the propeller and stator wakes. This would add significantly to the computation time required, however. The effects of viscosity could be incorporated through the use of an interactive viscous/inviscid boundary layer solution such as the method developed by Hufford[17]. Another possibility is to examine the effects of sheet cavitation within the propulsor by incorporating the method developed by Fine[7].

Bibliography

[1] T.S. Booth, P.R. Dodge. and H.K. Hepworth. Rotor-Tip Leakage: Part I—Basic Methodology. *ASME Journal of Engineering for Power*, vol 104:pp 154–161, January 1982.

[2] E.B. Caster. A Computer Program for Use in Designing Ducted Propellers. Technical Report 2507, NSRDC, 1967.

[3] G. Dahlquist and Å. Björck. *Numerical Methods.* Prentice-Hall, Englewood Cliffs, N.J., 1974.

[4] G. Dyne. A Method for the Design of Ducted Propellers in a Uniform Flow. Technical Report 62, Swedish State Shipbuilding Tank, Goteberg, Sweden, 1967.

[5] J.A.C. Falcão de Campos. On the calculation of ducted propeller performance in axisymmetric flows. Technical Report 696, Netherlands Ship Model Basin, Wageningen, The Netherlands, 1983.

[6] Jinzhang Feng and Shitang Dong. A Method for the Prediction of Unsteady of Unsteady Hydrodynamic Performance of the Ducted Propeller with a Finite Number of Blades. Technical Report 85006, China Ship Scientific Research Center, Wuxi,China, August 1985.

[7] N.E.. Fine. *Nonlinear Analysis of Cavitating Propellers in Nonuniform Flow.* PhD thesis, Department of Ocean Engineering, MIT, October 1992.

[8] L. Fox and Parker I.B. *Chebyshev Polynomials in Numerical Analysis.* Oxford University Press, London, 1968.

[9] R.P. Gauthier. An Investigation of Flow Field Perturbation Caused by Constant Blade Tip Clearance in a Turbine. Master's thesis, Department of Aeronautics and Astronautics, MIT, June 1990.

[10] W.S. Gearhart. Tip Clearance Cavitation in Shrouded Underwater Propulsors. *Journal of Aircraft*, 3(2), 1966.

[11] I.S. Gibson and R.I. Lewis. Ducted propeller analysis by surface vorticity and actuator disc theory. In *Proceedings of the Symposium on Ducted Propellers*, number 1–10, Teddington, England, MAY 1973. The Royal Institution of Naval Architects.

[12] E.J. Glover and P.G. Ryan. A comparison of the theoretical and experimental performance of a ducted propeller system. In *Proceedings of the Symposium on Ducted Propellers*, number 1–10, Teddington, England, MAY 1973. The Royal Institution of Naval Architects.

[13] J. L. Hess. Calculation of Potential flow About Arbitrary Three-Dimensional Lifting Bodies. Technical Report MDC J5679-01, McDonnell Douglas, October 1972.

[14] J. L. Hess and A. M. O. Smith. Calculation of Nonlifting Potential Flow About Arbitrary Three Dimensional Bodies. *Journal of Ship Research*, vol 8(no 2), September 1964.

[15] C-Y. Hsin. *Development and Analysis of Panel Method for Propellers in Unsteady Flow.* PhD thesis, Department of Ocean Engineering, MIT, September 1990.

[16] C-Y. Hsin. User's Manual of PSF10T: Release 1.0. Technical Report 92-3, Department of Ocean Engineering, MIT, September 1992.

[17] G. Hufford. Viscous Flow Around Marine Propellers Using Boundary Layer Strip Theory. Master's thesis. MIT, Department of Ocean Engineering, May 1992.

[18] M.J. Hughes. Analysis programs for a Ducted Propeller with Non-Axisymmetric Pre-Swirl Stator Blades - User's Manual. Technical report, MIT, Department of Ocean Engineering, September 1991.

[19] M.J. Hughes and S.A. Kinnas. An Analysis Method for a Ducted Propeller with Pre-swirl Stator Blades. In *Proceedings of the Propellers '91 Symposium*, number 15, Virginia Beach, VA, September 1991. SNAME.

[20] M.J. Hughes, S.A. Kinnas, and J.E. Kerwin. Experimental Validation of a Ducted Propeller Analysis Method. *Journal of Fluids Engineering*, 114:214–219, June 1992.

[21] B. Hunt. The mathematical basis and numerical principles of the boundary integral method for incompressible potential flow over 3-d aerodynamic configurations. In *Numerical Methods in Applied Fluid Dynamics*, pages pp 49–135. Academic Press, 1980.

[22] J.E Kerwin. Marine Propellers. *Ann. Rev. Fluid Mech.*, 18:pp. 387–403, 1986.

[23] J.E. Kerwin, S.A. Kinnas, J-T Lee, and W-Z Shih. A Surface Panel Method for the Hydrodynamic Analysis of Ducted Propellers. *Trans. SNAME*, 95, 1987.

[24] S.A. Kinnas and W.B. Coney. The Generalized Image Model - An Application to the Design of Ducted Propellers. *Journal of Ship Research*, Vol. 36(No. 3):pp 197–209, September 1992.

[25] S.A. Kinnas and C-Y. Hsin. Boundary Element Method for the Analysis of the Unsteady Flow around Extreme Propeller Geometries. *Journal of The American Institute for Aeronautics and Astronautics*, Vol 30(No. 3):pp 688–696, March 1992.

[26] S.A. Kinnas, C.Y. Hsin, and D.P. Keenan. Potential Based Panel Method for the Unsteady Flow Around Open and Ducted Propellers. In *Proceedings of the Eighteenth Symposium on Naval Hydrodynamics*, Ann Arbor, Michigan, August 1990.

[27] Spyros A. Kinnas and William B. Coney. On the optimum ducted propeller loading. In *Proceedings of the Propellers '88 Symposium*, number 1, Virginia Beach, VA, September 1988. SNAME.

[28] Spyros A. Kinnas and William B. Coney. A Systematic Method for the Design of Ducted Propellers. In *Proceedings of the Fourth International PRADS89 Symposium*, volume Vol. 4, Varna, October 23-28 1989.

[29] B. Lakshminarayana. Methods of Predicting the Tip Clearance Effects in Axial Flow Turbomachinery. *Journal of Basic Engineering*, pages pp 467–482, September 1970.

[30] Jin-Tae Lee. *A Potential Based Panel Method for The Analysis of Marine Propellers in Steady Flow.* PhD thesis, M.I.T., Department of Ocean Engineering, August 1987.

[31] Y.L. Luke. *The Special Functions and Their Approximations*, volume I. Academic Press, New York, 1969.

[32] B. Maskew. USAERO: A Time-stepping Analysis Method for the Flow about Multiple Bodies in General Motions, User's Manual. Technical report, Analytical Methods, Inc., Redmond, WA, 1990.

[33] B. Maskew. Private communication. In ,, 1993.

[34] W.B. Morgan. Theory of the Annular Airfoil and Ducted Propeller. In *Fourth Symposium on Naval Hydrodynamics*, number ACR-73, pages pp 151–197, 1962.

[35] Luigi Morino and Ching-Chiang Kuo. Subsonic potential aerodynamic for complex configurations : A general theory. *AIAA Journal*, vol 12(no 2):pp 191–197, February 1974.

[36] J.N. Newman. Distributions of Sources and Normal Dipoles Over a Quadrilateral Panel. *Journal of Engineering Mathematics*, vol 20:pp 113–126, 1986.

[37] J.N. Newman. Evaluation of the Wave-Resistance Green Function: Part 1 - The Double Integral. *Journal of Ship Research*, Vol. 31(No. 2):pp. 79–90, June 1987.

[38] J.N. Newman. The Approximation of the Free-Surface Green Functions. Technical report, Manuscript for the Fritz Ursell Retirement Meeting, March 1990.

[39] Van Houten R. Analysis of Ducted Propellers in Steady Flow. Technical Report 4.76-1, Airflow Research and Manufacturing Corp., Watertown, MA., February 1986.

[40] K. K. Shalnev. Cavitation in Turbomachines. *Water Power*, January 1958.

[41] A.R. Wadia and T.C. Booth. Rotor-Tip Leakage: Part II—Design Optimization Through Viscous Analysis and Experiment. *ASME Journal of Engineering for Power*, vol 104:pp 162–169, January 1982.

[42] C.-J. Yang, G. Wang, M. Tamashima, R. Yamazaki, and H. Koizuka. Prediction of the unsteady performance of contra-rotating propellers by lifting surface theory. In *Transactions*, number No. 83. The West-Japan Society of Naval Architects, March 1992.